INTERNATIONAL DOCTORAL
SCHOOL OF THE USC

Gabriel
García Jiménez

PhD Thesis

Proton-Induced Fission and Spallation Reactions in Inverse Kinematics: Insights from CALIFA Calorimeter Reconstruction

Santiago de Compostela, 2024

Doctoral Programme in Nuclear and Particles Physics

ESCOLA DE DOUTORAMENTO INTERNACIONAL DA USC

TESE DE DOUTORAMENTO

Proton-Induced Fission and Spallation Reactions in Inverse Kinematics: Insights from CALIFA Calorimeter Reconstruction

Gabriel García Jiménez

Director e titor: Héctor Álvarez Pol

Directora: Dolores Cortina Gil

ESCOLA DE DOUTORAMENTO INTERNACIONAL DA UNIVERSIDADE DE SANTIAGO DE COMPOSTELA

Programa de doutoramento en física nuclear e de partículas

Santiago de Compostela, Xuño 2024

Abstract

This thesis work focuses on the study of proton-induced reactions on ^{238}U in inverse kinematics, taking advantage of the R^{3}B/SOFIA setup to enable comprehensive kinematic measurements of the relevant reaction channels. After the beam impinged into the liquid hydrogen target at 540 AMeV, the identified channels, including spallation-evaporation and spallation-fission reactions, were selected by measuring the charge of reaction products with the use of the TWIN MUSIC detector.

Fission was induced after knockout processes, with scattered nucleons being analyzed using the CALIFA calorimeter. Innovative reconstruction algorithms, such as neural networks and a custom clustering algorithm, were developed for CALIFA to extract the energies of scattered proton pairs on an event-by-event basis. These energies were then employed to calculate the process's excitation energy through an invariant mass approach, which was subsequently correlated with fragment charge yields and compared with theoretical models like ABLA07 and INCL across various physics model configurations. From these studies, different shell energy-damping functions were examined.

Furthermore, cross-sections for spallation-evaporation and spallation-fission channels were measured. The obtained data demonstrate good agreement with previous measurements for the former and with theoretical models for the latter.

Acknowledgements

Jesus, what a journey! It has been four (and a half) long years since the first time I encountered something called *TCloneArrays*, and a new detector to be installed in Germany named CALIFA. There were so many new things to learn at the beginning, but luckily I had you, Héctor, from the start, taking care of me with a lot of patience and showing me that the devil hides in the details. I will never forget that your door was always open for me, always willing to discuss any topic with a smile, and checking for a long time even the simplest histogram, making sure that both of us understood every single aspect of the analysis. I am also grateful that you guide my work by providing me with the tools, but at the same time, allowing me to draw my own path (and in fact, I still owe you a dish of my famous black rice).

I have to also say thanks to Pepe and Lola, for giving me the opportunity to enter the field of nuclear physics, with such an interesting experiment. I also appreciate the analysis meetings that we had, where I could show my progress and discuss plans and things to check. Especially to Lola, for the useful corrections and comments to this manuscript, and all the crazy paperwork at the beginning of my thesis.

Pablo, this work also started with you. You showed me the wonderful fields around GSI, in our trips from Arheilgen to Cave C, where we mounted lots of crystals. Thanks also to David, the most precise technician I have ever met, for the friendly explanations and the meticulous and perfect work, that resulted in such a nice detector.

On my trips to GSI, I met some fabulous people, that made experiments and preparations an easier task. Andrea L., Manuel, Tomás, Simone, Eleonora, Ivana, Tobias, Lukas, Hans, Valerii, Daniel G., Daniel K. and Christian, thanks for being such a nice group of people to share a beer! Thanks also to the French group: Julien, Audrey, Laurent, Pierre, and Guillaume (I still have a metal song to sing with you).

The population at Office 7 quickly grew, but José Luis was there to take care of the children. Apart from providing us with lots of sugar, that kept our brains working, your expertise on every topic of the analysis saved us multiple times, and I will always remember the almost inaudible conversations about physics that we both had, that made me connect points quite often and guide me through this work.

Speaking about Office 7, this journey would not be the same without Martina, Antía G.,

Rubén, and in former times Juan, Dani F., Dani R., and Ali, from Office 5. These guys made it possible not to become crazy every day through the so-often frustrating analysis, with multiple pauses for coffee, merienda or just watching memes.

Help that comes with responsibility can be just work, in my opinion. Help that comes just from the inside is kindness, and that's the reason why I have to thank Bea (I've never seen such a broad view of the nuclear physics world) and Manuel (that one-nucleon cut man, that was it...)

I would like to express my gratitude and affection to my friend Antía G., for the times we have gone through. I cannot imagine a better analysis buddy, always dealing with the worst problems with courage and the best humor. Sometimes I recall our visits to GSI, especially those in the middle of COVID-19, where we fought through masks, cables, and long and cold bike rides back to our dubious-quality pension, thinking about the same situation but being alone, and I just have to give thanks that you were there (and also here, gravity falls nights are neat!). For the same reason, I would like to thank my other buddy, Martina, for the funny trips to GSI (remember, we even made Jose Luis laugh with that card game!), and for being always the first to follow when suddenly I wanted some sugar bomb in the middle of the work.

Rúa das Hortas 6, what a wonderful house in a wonderful city. There I enjoyed (for the first time) the feeling of having friends and sharing life with Juan and Antia E. in harmony. Those paella and tennis Sundays will be always some of my best memories, from a place where I enjoyed every single day and felt truly happy. I lost more tennis matches, but Juan lost more Battlefront games. Balance, they called it.

Ahora viene la parte más importante, la de mi familia. Eva y Paco, fuisteis siempre un ejemplo de trabajo duro, honesto y bien hecho, cuidando de vuestros hijos de una manera espléndida. Por vosotros estoy aquí ahora, y este trabajo es vuestro, más que mío o de nadie más. A Irene, por ser siempre mi apoyo, la persona en la que puedo confiar para cualquier cosa, y la persona más valiente que conozco. Y a David, que trajo su bondad y amabilidad para complementar a tan extraordinaria personita.

Silvia, mi compañera de vida. Tener a alguien que te apoye durante tiempos difíciles, compartiendo tu pasión, es algo incalculable. Y por eso te doy las gracias, por enseñarme que un planeta se puede hacer tan pequeño como se quiera, siempre que dos manos estén dispuestas a juntarse desde ambos extremos.

"Sulley, I am baring my soul here. The least you can do is pay attention."

Monsters Inc.

Este trabajo está dedicado a mis padres y a mi hermana, porque cruzaron conmigo la tormenta. Y aún me esperan con ilusión cuando bajo del tren.

Contents

Unless otherwise specified, all figures and pictures in this document have been obtained by the author. If a figure, picture or scheme was used from another source, the corresponding permissions and rights were kindly requested from the authors or the editorials.

List of Figures

List of Tables

Introduction

Nuclear physics is a vast field whose applications are a key part of modern society. The production of radioactive isotopes plays a major role in today's healthcare system, being one of the most used techniques for medical imaging and diagnosis. Studying these isotopes' half-lives and decay modes allows for better delivery of these isotopes to medical facilities, and the correct usage and dose for every specific medical application. In addition, the techniques that are developed daily by physicists in nuclear physics research facilities are commonly applied later to the general public. For example, particle detector design and operation, radiation shielding, simulation, and particle transport codes or reconstruction methods have a direct benefit for society.

Nuclear physics plays a major role in the explanation of how the present elements in our planet were created. Elements are created in stars and some of the parts of this stellar nucleosynthesis can be reproduced in experimental nuclear facilities. Proton capture rates, beta decay of exotic nuclei, and fusion barriers are key aspects of the hydrogen and helium burning in starts, the CNO cycle, or the p and s process. Stellar models require precise input from the experimentalists and the proposal, analysis, and interpretation of experiments serve for a better understanding of how the stellar environment was able to produce the elements that are common to our daily life.

Nuclear fission is used daily as one of the main energy sources; for many countries, this energy production method cannot be replaced by any other energy source. The safe operation and storage of nuclear waste depends on a precise knowledge of the produced fragment yields, that characterize the heat produced in such reactions and define the technical specifications of the reactors and the storage containers.

This thesis work combines two well-known reaction processes in a novel experimental procedure: proton-induced fission of ^{238}U was studied in inverse kinematics. The complete characterization of the fission fragments in mass and charge and the energy and angle reconstruction of the scattered nucleons prior to fission allowed to determine the excitation energy of the process and correlate this observable with fission fragment yields.

Motivations and Objectives of This Work

In this chapter, a general description of the fission process is presented together with an overview of spallation, knockout, and quasi-free reactions, mechanisms that will be explored in detail in the next chapters, by studying realistic simulations, experimental data, and physical models. Then, the aim of the experiment will be described in detail, together with the underlying physics of the complete reaction.

2.1 A Brief Overview of The Fission Process

Fission is a complex process where a deformed heavy nucleus splits into two smaller fragments, releasing a large amount of energy compared with other nuclear reactions, and some light products such as neutrons or gamma rays. Since its discovery in 1939 by O. Hahn and F. Strassmann [1], and the interpretation of L. Meitner and O. Frisch as the scission of the nucleus [2], nuclear fission has been an important part of society thereafter. The use of this reaction for energy production is still one of the main sources of energy supply for mankind. Using nuclear fission as a weapon also plays a major role worldwide, leading to international agreements, laws, and regulations about commerce with fissile material.

2.1.1 General Description

When a heavy nucleus deforms, a competition between the surface energy, that contributes to keeping the system together, and the Coulomb repulsion between the pre-fragments begins. For some nuclei, tunneling through the Coulomb barrier is possible even if no excitation energy is given to the system. Those nuclei undergo naturally-occurring fission, that can be observed in addition to beta and alpha decay, the most common decay modes for such heavy nuclei. Some other nuclei require some energy addition to the system to undergo fission. This excitation energy, which can be obtained via several reaction mechanisms, is transformed into

a collective motion of the nucleons, that deforms the system up to the saddle point, where the fission process is irreversible. The difference between the mass of the system in the saddle point and the mass of the system in the ground state is called *fission barrier*, an observable that defines the fission probability of the excited system.

2.1.2 The Bohr-Wheeler Model

The first approach to explain the fission process was developed by N. Bohr and J.A. Wheeler [3] using the ideas from the liquid drop model. Let's suppose that the nucleus is spherical before any reaction occurs, and let's also say that when a nucleus undergoes fission, the deformation transforms the sphere into an ellipsoid shape, with main axes a and b ($a > b$). These two values are related to the sphere radius R via the eccentricity parameter ϵ:

$$a = R(1+\epsilon), \quad b = R(1+\epsilon)^{-1/2}. \tag{2.1}$$

The pairing and symmetry terms in the semi-empirical mass formula [4, 5], are intrinsic to the nuclear species, so these terms remain intact when the system is deformed. The surface of an ellipsoid can be approximated by

$$S = 4\pi R^2(1 + \frac{2}{5}\epsilon^2 + ...), \tag{2.2}$$

so the surface term for an ellipsoid is modified by a factor $(1 + \frac{2}{5}\epsilon^2 + ...)$. By computing the change in binding energy, ΔB:

$$\Delta B = B(\text{Ellipsoid}) - B(\text{Sphere}) \sim (\frac{2}{5}a_s A^{2/3} - \frac{1}{5}a_c Z^2 A^{-1/3})\epsilon^2. \tag{2.3}$$

So, for a nucleus with $\Delta B > 0$, the stretching is favorable in terms of binding energy, if the Coulomb term is smaller than the surface term:

$$a_c Z^2 A^{-1/3} < 2a_s A^{2/3}. \tag{2.4}$$

Using the tabulated values for a_c and a_s, a *fissility* parameter can be defined as

$$x \simeq \frac{1}{50}\frac{Z^2}{A}, \tag{2.5}$$

which accounts for the stability of the nucleus against deformations.

This approach first estimated the fission barrier for many isotopes, although some problems were soon encountered. First, as can be seen in Fig. 2.1, the Bohr-Wheeler model only predicted symmetric fission, as the only descending path from the saddle point. The observed asymmetric fission, where one fragment has a larger mass than the other, and the discovery of fission isomers fired the search for a better explanation of the process.

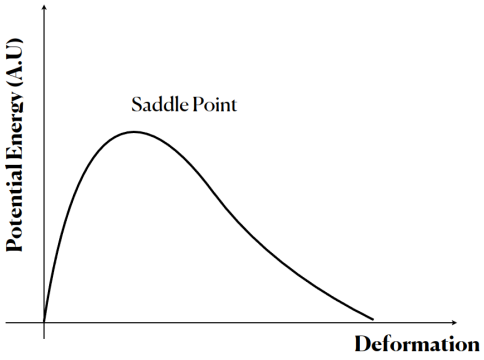

(a) Example of the potential energy as a function of the deformation for the LDM calculation.

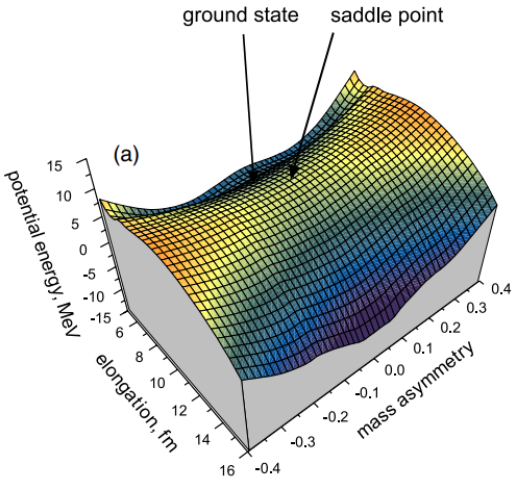

(b) Potential energy surface calculated for ^{238}U using a macroscopic calculation [6] (Copyright from IOP Publishing, 2008)

Figure 2.1: Fission barrier evolution and potential energy surface calculated using a macroscopic approach.

2.1.3 The Nilsson Diagrams and Shell Corrections

Soon after the explanation of nuclear shells by M. Goeppert-Mayer [7] and J. Jensen [8], it was natural to extend the idea to deformed nuclei. In 1955, S. Nilsson developed a method [9] that calculated single-particle energies as a function of the nuclear deformation. This method extended the calculations of the nuclear shell model, which used a central potential with spherical symmetry.

This approach was applied for calculations taking the nuclear energy as the sum of the lower levels occupied by nucleons. Although fission barriers were more or less reproduced, the method gave worse results than the LDM approach. It was Strutinsky, in 1967 who developed a method in which the shell structure of the nucleus was included as a correction to the macroscopic, LDM calculation [11]. Since this method includes information about single-particle levels and macroscopic information about the nucleus, this approach is often called the macroscopic-microscopy approach. In this way, the total energy reads as

$$E = E_{LDM} + \delta E, \tag{2.6}$$

with this last term given by the shell correction.

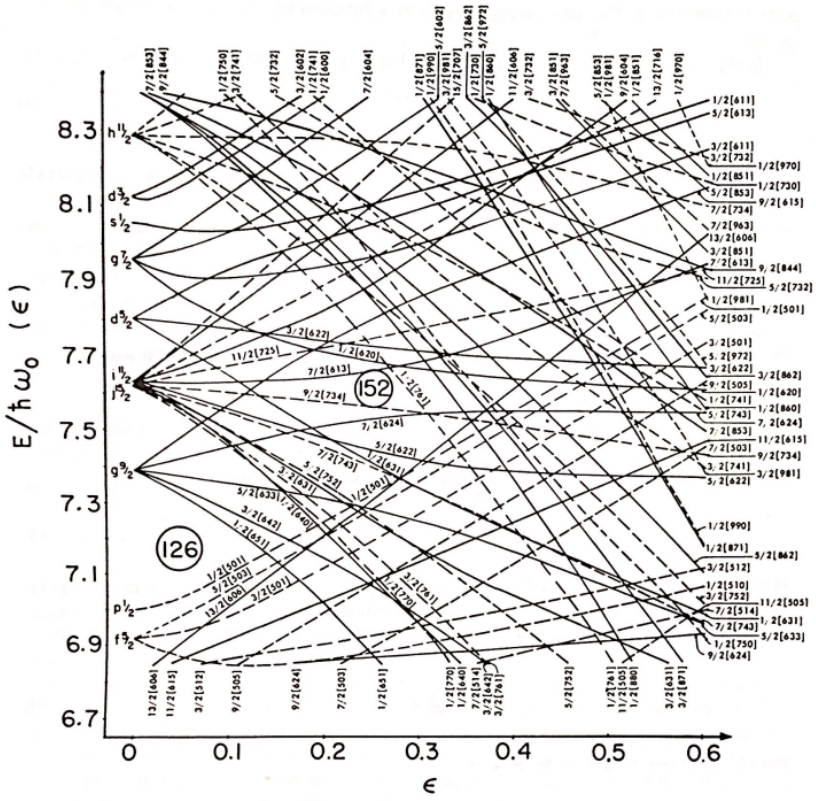

Figure 2.2: Nilsson diagram representing the evolution of single-neutron energy levels with respect to the nuclear deformation. Figure taken from [10] with open access permits.

The inclusion of the shell effects gives a modified potential surface that correctly accounts for asymmetric fission and also explains the apparition of a second, smaller fission barrier in some actinides. This double-humped barrier is associated with the apparition of fission isomers, first discovered by Polikanov [12] et al in 1962, when an isomeric state of ^{242}Am was found to have a delayed fission decay mode with a half-life of 14 ms.

2.1.4 Fission Modes

U. Brosa et al proposed in 1990 a model for explaining the observed experimental fission yields [14]. The different paths in the potential energy surface that the system can follow were called *fission channels*.

In this model, the scission point is represented by two preformed fragments sharing a neck. This neck can be split at any point when the two fragments separate, and depending on the neck length, the observed distribution in Z and A will be more or less broad. This

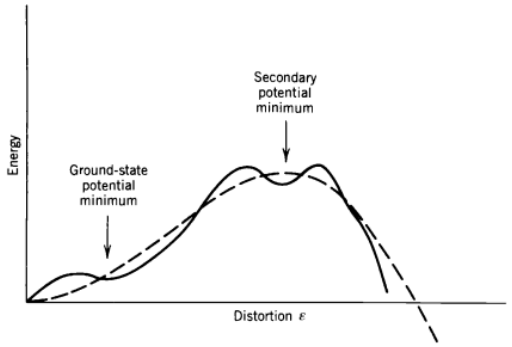

(a) Example of the potential energy as a function of the deformation for the macroscopic-microscopic calculation (solid line), compared with LDM calculations (dashed line). Figure taken from [13], with rights and permissions from Wiley (Copyright 1991)

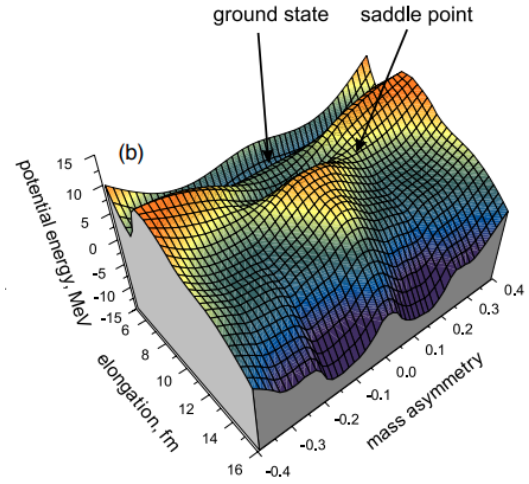

(b) Potential energy surface calculated for ^{238}U using a macroscopic-microscopic calculation. Figure taken with permissions from [6]. (Copyright from IOP Publishing, 2008)

Figure 2.3: Fission barrier evolution and potential energy surface calculated using a macroscopic-microscopic approach. The apparition of a second fission barrier accounts for the existence of fission isomers.

idea is called *random neck rupture*. Based on these ideas, five fission modes can be defined:

1. **Super Long (SL):** In the potential energy surface (Fig. 2.3), corresponds to the center part, where the system evolves up to a configuration with 0 mass asymmetry. Both fragments are highly deformed, but their kinetic energy is lower due to the longer neck at the scission point. Both fragments exhibit a large prompt neutron multiplicity, due to the deformation of the medium-mass fragments.

2. **Super Short:** In this fission mode, the two fragments are formed as quasi-spherical, sharing a short neck that translates into high kinetic energies. This short neck produces narrow fragment distributions and the spherical shape produces almost no neutron emission. This fission mode is only observed in nuclei heavier than ^{252}Cf.

3. **Standard I (S1):** A compact configuration influenced by the double magic ^{132}Sn in actinides, and a deformed light fragment. The kinetic energies of the fragments are

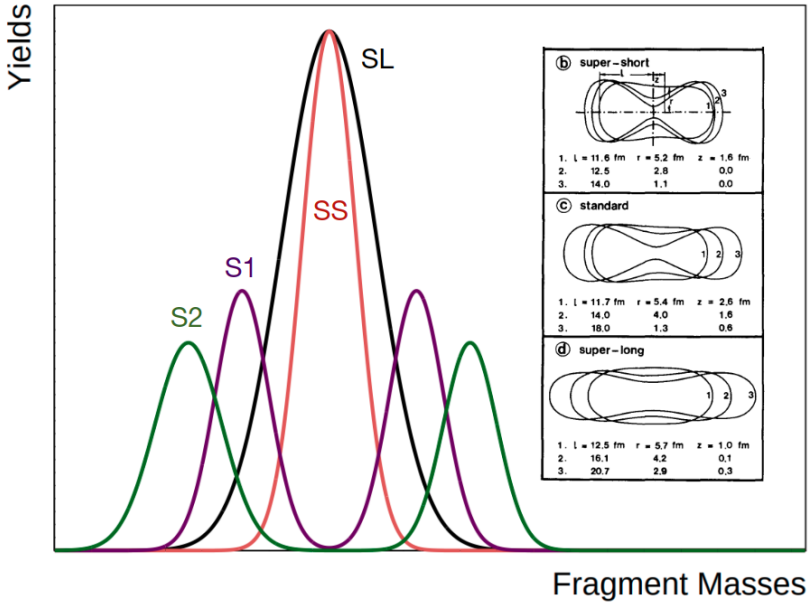

Figure 2.4: Scheme of some fission modes proposed by Brosa. The inset figure is cited from [14] with permissions (Copyright 1990 Published by Elsevier B.V.), and shows the different steps in the elongation up to the scission point. Yields and masses are only shown as a demonstration and show no particular physical system.

high, and the light fragment emits more neutrons than the heavy fragment. This mode exhibits asymmetric mass distributions.

4. **Standard II (S2):** This channel also presents asymmetric distributions, centered around mass 140 for actinides. In this case, the heavy fragment is deformed, while the lighter one has an almost spherical shape. This configuration results in larger neutron multiplicity and lower kinetic energies.

5. **Super Asymmetric:** Rarely observed, corresponds to fission where the mass of the fission fragments is highly asymmetric [15].

2.2 Spallation and Knockout Reactions

Nuclear spallation is often defined as a process in which a fast, relativistic light particle impinges on heavy nuclei, resulting in an excited remnant and the emission of several light particles or fragments, either via the multi-step reaction process or by the de-excitation stage of the recoil fragment. Spallation occurs naturally when cosmic rays collide with the nuclei

present in the earth's atmosphere and is believed to be responsible for part of the generation of Li, Be, and B in the interstellar medium [16]. This nuclear process is also the main source of neutron production for scientific purposes [17], being present at several facilities around the world, such as the European Spallation Source (ESS).

The high energy that is used in these reactions, usually $E > 100$ MeV, translates into an associated de Broglie wavelength way smaller than the nuclear size. This collision can be then modeled as consecutive nucleon-nucleon interactions that leave the fragment in an excited state. This process is often called *intranuclear cascade*. When the cascade process finishes, the excited remnant evaporates light particles (such as neutrons and gammas, and less frequently protons and alpha particles), or decays by fission.

2.2.1 Quasi-free Reactions

Knockout reactions are direct processes with the removal of a single nucleon from the target, with small or no disturbance to the remaining part of the original nucleus. A specific case of a knockout process is the removal of a single nucleon from the target, where the core of the original nucleus remains as a spectator. The excitation energy left to the remnant is then only caused by particle-hole excitations.

These direct reactions are commonly known as quasi-free reactions, and since the discovery of such a process, quasi-free scattering has been an invaluable tool for nuclear structure studies [18, 19, 20]. The momentum of the scattered particles and the remaining nucleus can be used for obtaining information about single particle occupancies and the angular momentum of the orbit from where the nucleon was removed [21].

It was around the 1950s [22, 23] when the bombardment of some light targets by protons was followed by the detection of two angular correlated proton pairs. If the incoming proton has a three-momentum $\vec{p_0}$, and the two outgoing protons carry the indices 1 and 2, then

$$\vec{p_0} = \vec{p_1} + \vec{p_2} + \vec{p}_{A-1}. \tag{2.7}$$

The opening angle shared between the two scattered protons can be calculated as

$$\alpha = \cos^{-1}\left(\frac{\vec{p_1} \cdot \vec{p_2}}{|\vec{p_1}||\vec{p_2}|}\right) \tag{2.8}$$

which in spherical coordinates happens to be

$$\alpha = \cos^{-1}\left[\sin\left(\theta_1\right)\sin\left(\theta_2\right)\cos\left(\phi_2 - \phi_1\right) + \cos\left(\theta_1\right)\cos\left(\theta_2\right)\right]. \tag{2.9}$$

This opening angle was soon discovered to be centered around 90°, reinforcing the fact that the two particles interacted as if both were free. However, the obtained distributions were spread around the expected value, due to the internal momentum of the nucleon inside the nucleus. This internal momentum can be modeled following a three-dimensional Gaussian distribution, whose width is calculated as

$$\sigma = \sigma_0\sqrt{\frac{A_r(A_p - A_r)}{A_p - 1}}, \quad \text{and} \quad \sigma_0 = \sqrt{2S_p}, \tag{2.10}$$

where A_p is the mass of the projectile, A_r is the mass of the remnant and S_p is the proton separation energy. This model, proposed by A.S. Goldhaber [24], correctly predicted the observed angular distribution widths.

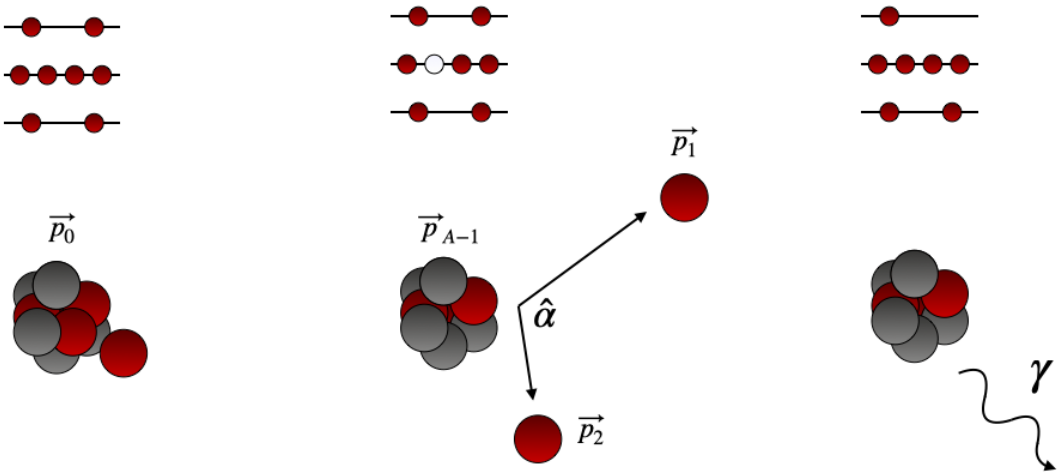

Figure 2.5: Scheme of a (p,2p) quasi-free reaction. The upper diagrams represent an example of a particle-hole excitation process, where the excited remnant emits a gamma in coincidence with the proton pair.

The power of the quasi-free reactions relies on the fact that the process is highly selective, making it possible to know from which nuclear shell the nucleon was knocked out by studying the momentum distributions of the fragment [25]. The kinetic energy of the two nucleons can be measured and the excitation energy of the recoil fragment (E^*_{A-1}) can be extracted as

$$E^*_{A-1} = E^k_0 - (E^k_1 + E^k_2 + E^k_{A-1}) - S_n, \tag{2.11}$$

assuming that the knocked-out nucleon was below the fermi surface. The terms E^k represent the kinetic energies of the incoming nucleon (0), the scattered pair (1,2), and the recoil (A-1), and S_n is the separation energy of the scattered nucleon. An schematic view of this process is displayed in Fig. 2.5.

The idea of quasi-free scattering can be extended to other nucleons or particles, so the reactions (p,pn),(p,pd),$(p,p\alpha)$... can be also studied using the same reaction scheme.

2.3 Objectives of the Experiment

2.3.1 Shell Effects Suppression and Energy Sharing of the Fission Fragments

As stated before, shell effects were introduced as a correction to the previous nuclear fission models for explaining the observed fission yields at low excitation energies. However, it is well known that shell corrections only play a major role when fission occurs at low excitation energies. If the nuclear level density rises with the addition of more excitation energy to the system, nucleons can move to more levels, hindering the effects of the shell structure. This suppression is also reinforced by the fact that for high energies (or large angular momentum), the nucleus deforms, so the central potential that was considered for shell level calculation is deformed and the energies of the different levels start to cross, as presented in Fig. 2.2.

This suppression effect must be taken into account when calculating the total energy of the system, so Equation 2.6 must be modified with the addition of a suppression factor in the form

$$E = E_{LDM} + S(E^*)\ \delta E. \tag{2.12}$$

Since this damping effect was observed and modeled, several prescriptions for this suppression function have been suggested. Ignatyuk [26], proposed a purely exponential function:

$$S(E^*) = \exp\left(-E^*/E_0\right) \tag{2.13}$$

with an E_0 value that is usually adjusted with data. The study of this damping shape by Randrup [27] and the comparison with more recent data, lead to a modification by including

two parameters to adjust:

$$S(E^*) = \frac{1 + e^{-E_1/E_0}}{1 + e^{(E^* - E_1)/E_0}}. \tag{2.14}$$

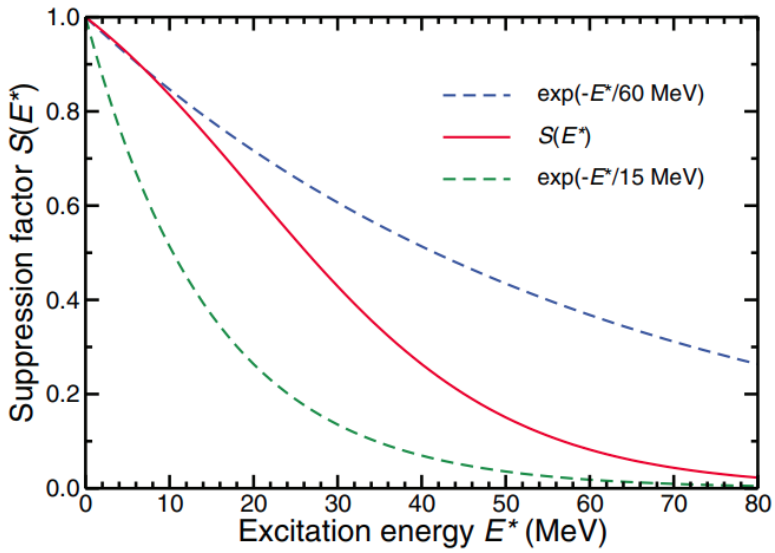

Figure 2.6: Different proposed shapes for the damping function. The red curve represents the shape proposed by Randrup, and the blue and green lines represent the pure exponential function as stated by Ignatyuk. Figure taken from [27], with permissions from the American Physical Society.

Energy sorting mechanisms have been proposed to explain the observed fission yields and evaporated neutron multiplicities with changing excitation energies. In [28], an explanation based on a net increase of the system entropy explained the observed prompt-neutron multiplicity at different excitation energies (Fig. 2.7). A study of the average prompt neutron multiplicity correlated with the excitation energy of the process would allow to characterize the point where the superfluid phase on which this theory is based has to be coupled with standard, fermi-gas model calculations. The experimental test of these ideas would require a reaction mechanism and an experimental setup by which one can:

- Measure charge and mass distributions with high precision.
- Measure the excitation energy of the process.
- Induce a wide range of excitation energies.

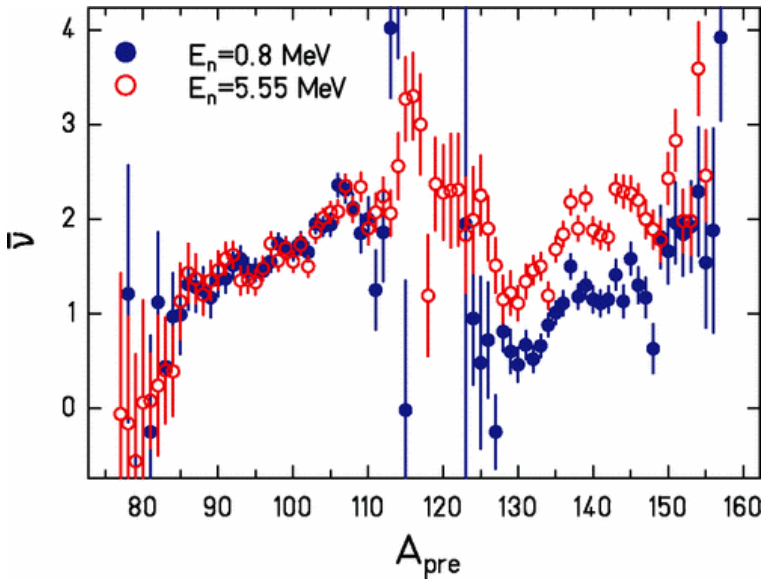

Figure 2.7: Prompt neutron multiplicity for neutron-induced fission of ^{237}Np, for different excitation energies. Figure taken from [28], with permission from the American Physical Society.

Coulomb-induced fission is expected to excite the nucleus to energies around $E^* = 10 - 15$ MeV [29], while typical transfer-induced fission experiments allow for high precision measurement of the E^*, but only up to 20-30 MeV [30] and not with highly exotic nuclei.

2.3.2 Quasi-free Knockout Reactions on Heavy Nuclei

Quasi-free reactions have been extensively studied for light and medium mass isotopes, allowing for detailed studies of the structure of exotic nuclei. However, the characterization of this reaction process has not been yet studied for unstable heavy ions, only for stable heavy targets in direct kinematics [31]. Experimental campaigns at GSI at the decade of the 90's, allowed for the study of spallation residues, but with no information on the scattered nucleons prior to evaporation or fission. The study of these reactions in heavy nuclei would give an idea of how this method could be used for studying heavy-ion properties.

These points initiated the search for a new method for studying spallation-fission and spallation-evaporation reactions in heavy ions, which is the main topic of this thesis work.

2.4 Proposed Measurement: Knockout-Induced Fission of ^{238}U

If a heavy ion is delivered at high, relativistic energies and impinges onto a proton target, then fission is induced via nucleon-nucleon collisions, which can result in a variable number of nucleons being scattered from the heavy ion. These spallation-induced fission experiments were exploited several years ago [32, 33, 34], by using the Fragment Separator (FRS) at GSI. In these experiments, only one fragment coming from the fission process was measured, making no possible the characterization of the fissioning system in Z. Later on, the SOFIA (Studies on Fission with Aladin) collaboration carried out several experiments at GSI [35, 29], using a novel experimental setup at which the masses, charges, and velocities were measured for both fission fragments for the first time, using an inverse kinematics approach. For these experiments, the excitation energy of the process was estimated using models.

The proposed measurement for this experiment consisted then in ^{238}U ions being delivered at 540 AMeV at the proton target. After a single-proton knockout process, which can be determined by measuring the two fission fragments' charge in coincidence, the relative angle between the scattered pair can be measured, and the excitation energy can be obtained using an invariant mass calculation. The excitation energy of the process can be obtained, using four-momentum notation as

$$\begin{pmatrix} E_b \\ 0 \\ 0 \\ p_{bz} \end{pmatrix} + \begin{pmatrix} m_t c^2 \\ 0 \\ 0 \\ 0 \end{pmatrix} = \begin{pmatrix} E_1 \\ p_{1x}c \\ p_{1y}c \\ p_{1z}c \end{pmatrix} + \begin{pmatrix} E_2 \\ p_{2x}c \\ p_{2y}c \\ p_{2z}c \end{pmatrix} + \begin{pmatrix} E_R \\ p_{Rx}c \\ p_{Ry}c \\ p_{Rz}c \end{pmatrix}, \tag{2.15}$$

where the subscripts denote the particle (b=beam, 1=first proton, 2=second proton, t= target, and R=recoil fragment). In this calculation, the beam is supposed to have only a momentum component in one direction. If the momentum of the two protons is measured, and the momentum of the incoming beam is known, then an invariant mass approach can be used to determine the excitation energy of the recoil nucleus:

$$\begin{aligned} I_m^2 &= \left(\sum E\right)^2 - \left|\sum pc\right|^2 \\ &= (E_b + m_p c^2 - (E_1 + E_2))^2 - (p_{1x}c + p_{2x}c)^2 - (p_{1y}c + p_{2y}c)^2 - (\sqrt{E_b^2 - m_b^2 c^4} - (p_{1z}c + p_{2z}c))^2 \end{aligned} \tag{2.16}$$

This invariant mass corresponds then to the mass of the recoil fragment after the reaction,

and the excitation energy can be then calculated by subtracting the resting mass of the recoil:

$$E^* = I_m - m_R c^2. \tag{2.17}$$

For the case of a quasi-free process, the excitation given to the remnant corresponds to single particle-hole excitations. If the knocked-out proton interacts with the rest of the nucleons, this rescattering process increases the excitation energy due to the multiple nucleon-nucleon collisions.

Although this experiment had already been proposed at RIKEN using the SAMURAI setup, the presence of delta electrons and charge states did not allow for a proper study of the fission products. For this reason, this experiment (named s455) was carried out using the SOFIA/R^{3}B setup that will be described in the next chapter. The SOFIA detectors allowed for the complete identification of both fission fragments in charge and mass. The CALIFA detector, together with the AMS silicon strip tracker, allowed for the determination of the scattered pair 4-momentums.

Methodology

Within this chapter, comprehensive details regarding the experimental apparatus employed for conducting the described experiment are outlined, along with a presentation of the subsequent analysis tools encompassing software frameworks, algorithms, and simulations.

3.1 Experimental Procedures

3.1.1 GSI Facilities and the R3B Cave

The experiment, a proof of concept which was part of the Phase-0 experimental program (Fig. 3.1), was carried out at the installations of the GSI (Gesellschaft für Schwerionenforschung) Helmholtzzentrum accelerator facility located in Darmstadt, Germany. This facility has been focused on the production of heavy ions for their use in different research fields (nuclear physics, astrophysics, biophysics, plasma physics...) since its foundation in 1969.

Neutral ^{238}U atoms were initially prepared at the ion source, the point where heavy ion production begins for each GSI experiment. These neutral atoms were then converted into partially stripped ions through the application of high voltage. After that, these ions were introduced into the UNILAC (Universal Linear Accelerator), where they underwent acceleration and had the remaining electrons removed by passing through a gaseous medium, thereby increasing their charge state. Following this pre-acceleration phase, the ions were directed to the SIS18, a heavy ion synchrotron with a circumference of 216 m. The synchrotron accelerated the ions up to 637 AMeV ($\sim$ 0,8 c). As the experiment did not require a secondary exotic beam, the ions were directly sent to the experimental cave without passing through the FRS separator. This path, together with a scheme of the GSI facility is presented in Fig. 3.2. The ^{238}U ions finally arrived at Cave C, the experimental Cave for the R^{3}B (Reactions with Radioactive Relativistic Beams) collaboration. The R^{3}B experiment is an international

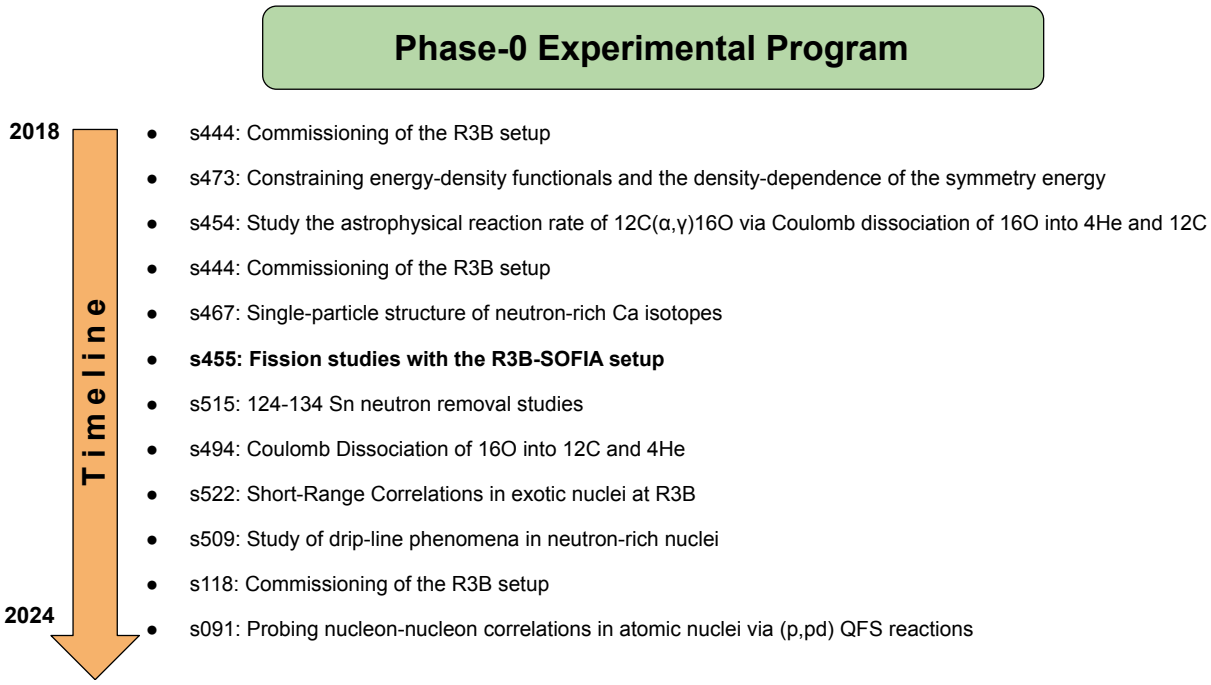

Figure 3.1: Experimental program of the R^3B Collaboration during the GSI Phase-0.

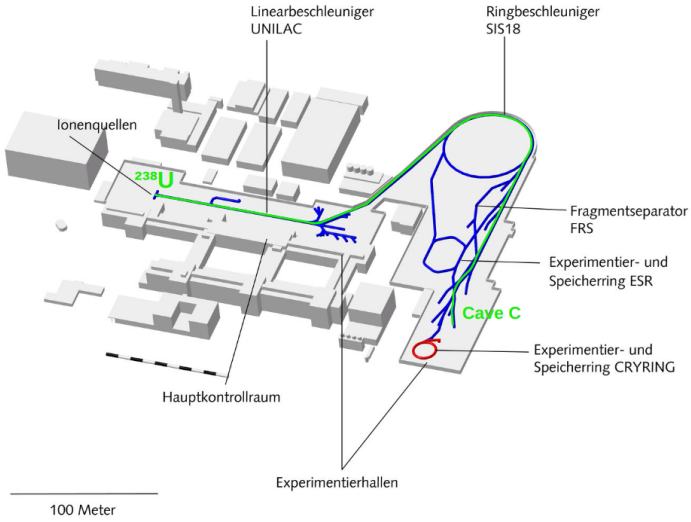

Figure 3.2: Scheme of the GSI facility. The path that the ions followed for the experiment is highlighted in green. Figure adapted from [36], with the corresponding rights and permissions.

collaboration currently composed of 255 registered members [37]. The setup, which is now under construction, is aimed at studies in inverse kinematics with exotic-fast beams, with

energies ranging from hundreds of MeVs to more than 1 GeV. The framework is designed to work as a versatile experimental setup with complete kinematic measurement capabilities, where a diverse physics program can be carried out. Experiments in nuclear astrophysics, equation of state, shell model and nuclear structure, fission, and short-range correlations have been performed.

3.1.2 R^{3}B Setup at Cave C

The experimental setup employed for the experience is presented here. Multiwire Proportional Chambers were used for tracking purposes. The time of flight of the fission fragments was obtained by using the Time of Flight detector. The scattered nucleon coordinates were measured using CALIFA and AMS. The TWIN MUSIC detector was used to reconstruct the charge of the spallation residues and the charge of the fission fragments. NeuLAND was installed at the end of the setup for neutron multiplicity measurements. With this configuration, a complete kinematic measurement of the projectile and the reaction products was possible.

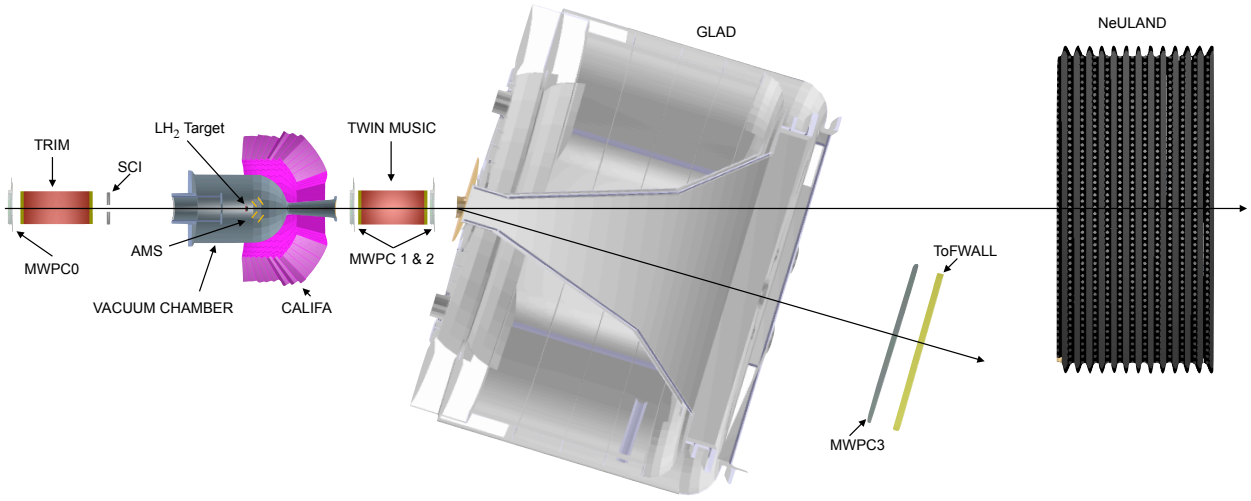

Figure 3.3: Experimental setup. Distances are not to scale.

3.1.2.1 Multiwire Proportional Chambers

Several Multiwire Proportional Chambers [38] (MWPC) were used for precise beam tracking of the beam and the reaction products. Each MWPC is composed of a plane of wires sandwiched by two parallel pad planes. The space between planes is filled with gas (84% Ar,

16% CO_2). The pad planes are set to ground and work as cathodes, while the wire plane is set to a high voltage, acting as an anode. When an ion passes through the gas volume, the ionized electrons drift into the wire plane, inducing a signal in the two pad planes. The first plane has vertical pads and gives X position, while the second plane has horizontal pads and gives Y position. The position on each plane is calculated using the distribution of induced signals for each hit.

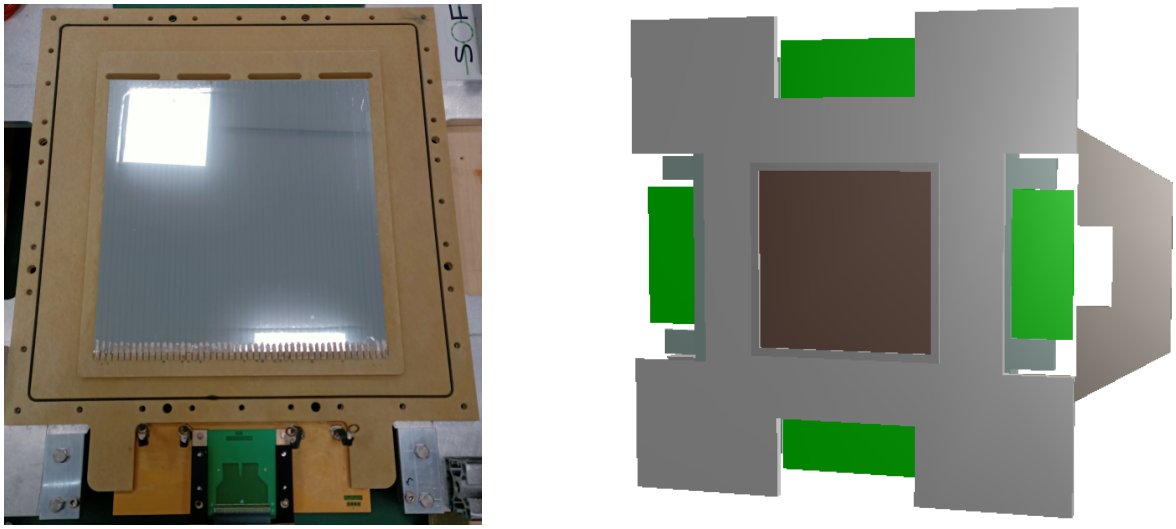

(a) Opened MWPC0.

(b) MWPC0 geometry used in simulations. The aluminum frame and the holder structure are also displayed.

Figure 3.4: The aluminum frame and the Mylar windows were removed in the picture so the pad plane is visible.

MWPC0: This detector was placed at the beginning of the beamline, at the entrance of Cave C, and used for beam tracking. The active region of 200×200 mm^2 was constituted of horizontal and vertical pad planes that were composed of 64 pads, each one 3,125 mm wide. The pads were built by evaporating Al on a 12 μm foil of Mylar. Each wire on the wire plane had a diameter of 5 μm.

MWPC1 and MWPC2: These two detectors were used for tracking the reaction products (fission fragments and spallation residues). The detectors were made of a first vertical pad plane, with 64 pads 3,125 mm wide, and segmented into two parts. Then a plane of horizontal wires, 50 μm wide, preceded a horizontal pad plane with a width of 5 mm. The only

difference between the MWPC1 and the MWPC2 was that the second one had gold evaporated in the Mylar foil instead of Al. The active region for both detectors was 200×200 mm^2.

MWPC3: This detector was the biggest one of the MWPCs, with an active region of 900×600 mm^2. Placed at the end of the setup, the X, and Y position given by this detector was used for tracking the fission and spallation fragments after the magnetic field. This MWPC had first a vertical plane of 288 pads, a wire plane, and a horizontal pad plane with 20 units.

3.1.2.2 Plastic Scintillator

A plastic scintillator (BC400) was placed at the entrance of Cave C before the target. This detector was used for time of flight (ToF) measurements and also for producing the incoming beam signal. The $50 \times 32 \times 1{,}5$ mm^3 plastic was attached to two PMTs (Hamamatsu 6533), one on each side, using optical grease. When an ion hits the plastic, light is produced and transformed into an amplitude pulse by the two PMTs on both sides.

The whole was covered by isolating tape so no light could enter from the outside. The scintillator, together with the PMTs, was then mounted into an aluminum frame so the detector could be aligned with the incoming beam axis.

3.1.2.3 CALIFA

CALIFA (CALorimeter for In-Flight detection of γ rays and light-charged pArticles) is the calorimeter-spectrometer surrounding the reaction target of the R^{3}B experiment [39], and in this experiment it was used for energy measurements of the scattered nucleons after the spallation process.

The detector is composed of 2544 CsI(Tl) scintillation units, covering a polar range from 7° to 143° and full azimuthal range. CALIFA can simultaneously detect high-energetic particles with a resolution of $\sim 1\%$ for protons, and gamma rays, with a resolution of 5% at 1 MeV [40, 41]. The huge dynamic range of the detector, along with its high granularity and the almost full solid angle covering for the typical reactions studied in R^{3}B, makes this detector a key part of every experimental setup.

3.1.2.3.1 Detector Layout The detector is divided into three different parts: the Barrel part, the iPhos part, and the CEPA part. The Barrel part contains crystals covering from

43° to 143° degrees in polar angle. The iPhos (intrinsic Phoswich) part covers from 22° to 43°. This part is more suitable for particle identification using the two different light components of CsI(Tl), hence the name. Finally, the CEPA part can detect particles emitted in an angular range of 7° to 22°. These parts are schematized in Fig. 3.5 b.

At the moment of the experiment described in this work, the iPhos part was filled with 480 crystals, and the barrel part was partially filled with 1024 crystals, from 22° to 86°. The detection units were mounted into their final holding frame in November 2019 at Cave C. The CEPA part was tested and mounted by the end of 2023.

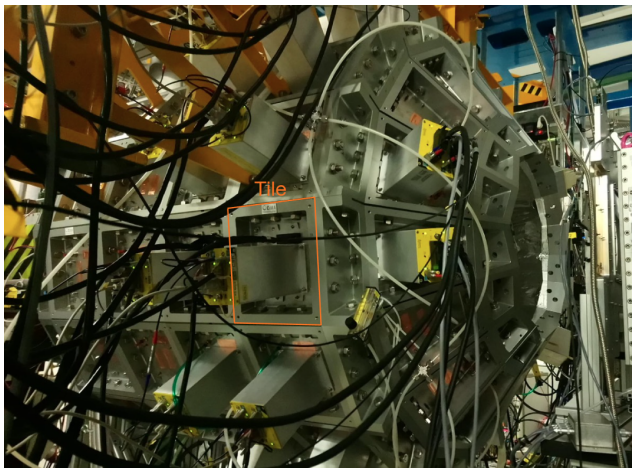

(a) CALIFA halves enclosing the reaction chamber. Each half can move independently.

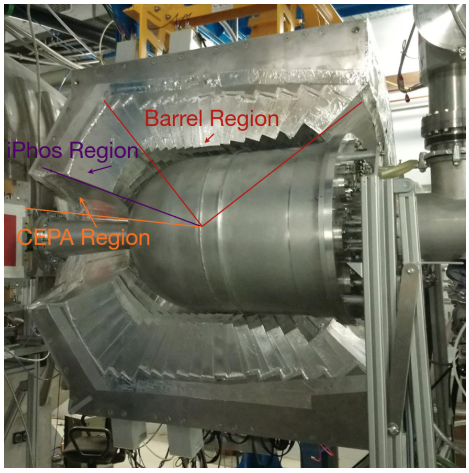

(b) CALIFA opened. The reaction chamber fits inside the carbon fiber structure. The different lines demark the Barrel, iPhos, and the future CEPA part.

Figure 3.5: CALIFA structure at the R^3B Cave.

The aluminum frame of the detector (Fig. 3.5 a) is divided into two halves. To avoid mistakes when referring to each half while people were working at the Cave, the right part of CALIFA from the beam perspective was denoted as *Wixhausen* half, while the left part was called *Messel* part. These two names refer to two close villages near GSI and provide an absolute frame of reference for the CALIFA working group. Each half frame is held by a moving frame installed on top of a set of columns on the floor of Cave C. This moving frame allows for the alignment of CALIFA with respect to the target area. Each half contains a honeycomb-like carbon fiber structure that is divided into *pockets* or *alveoli*. This structure

is displayed in Fig. 3.6. For the barrel part, each alveolus contains four crystals, that are held into position by an auxiliary device called *finger*. This device is attached to the sides of the structure. The iPhos part crystals are more irregular, and some of the big crystals are contained in a single carbon fiber pocket or in groups of two crystals per pocket. Crystal pockets are accessible from the outside by removing a square aluminum plate called *tile*. This tile isolates the crystal environment from the outside and have some connections for preamplifiers, laser calibration system, and N_2 gas pipes for humidity control.

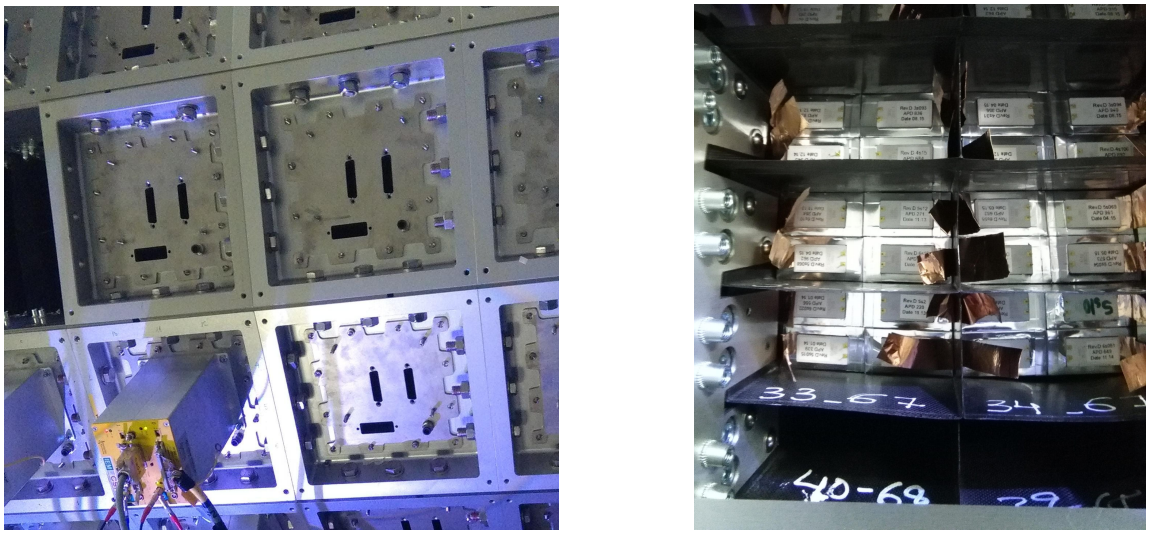

(a) CALIFA tile with and without preamp attached.

(b) Mounted crystals. Each group of four-barrel crystals fits inside a carbon fiber pocket.

Figure 3.6: CALIFA opened tile before and after filling with crystals.

3.1.2.3.2 Detection Units and Readout Each CALIFA detection unit consists of a CsI(Tl) inorganic scintillation crystal, whose basic properties are summarized in Table 3.1. The crystals have a right-pyramid frustum shape, with lengths varying from 14 to 22 cm. Barrel crystals are more regular than iPhos crystals, which close that calorimeter forming an octagonal shape.

A wrapping of ESR (Enhanced Specular Reflector) 3M Vikuiti™ [42] tightly adheres to the scintillator material, so the light can not escape and also the slightly hygroscopic material is better preserved from humidity [43]. The light produced in the crystal is then collected on the back part of the crystal by a Large Area Avalanche PhotoDiode (LAAPD or APD

E. Wavelength (Max)	Decay Constant	Density	Refractive Index	Light yield
550 nm	Fast: 0,6 us, Slow: 3,5 us	4,51 g/cm^3	1,79	54 photons/keV

Table 3.1: Basic properties of CsI(Tl) taken from [45] and [46].

from now on). This Hamamatsu S8664-1020 APD [44] consists of a double 10×10 mm^2 photodiode, a semiconductor operated in reverse voltage that is sensible to light emission, so a current is produced every time this diode is excited by the light produced in the crystal. The semiconductor carriers, which are accelerated by the high electric field, produce current proportional to the energy of the detected particle. APDs are stable in terms of operation under magnetic fields, but as they are semiconductor-based devices, temperature strongly influences the obtained gain. This APD is attached to the back of the crystals using optical cement. Two pins are mounted on top of the APD, serving at the same time for biasing the APD and also for registering the change of current generated by the ionizing particle. A picture of this mounting is shown in Fig. 3.7. The pins are then connected to a PCB, that is attached inside the tile and put together in groups of 16 channels. Every two 16-channel groups in the barrel part are read by a Mesytec preamplifier MPRB-32, so the barrel crystals can only be operated using one gain setting. iPhos two 16-group crystals are attached to MPRB-32 DR (double range) preamplifiers, so every crystal signal is split in two, one in high gain and suitable for gamma detection, and the other in low gain aimed for proton measurements. Different configurations of the detector can be arranged, depending on the experimental needs. For the present case, the full iPhos part was double read, while only the crystals behind AMS coverage were set in proton range, being the rest of them set in high gain mode.

3.1.2.3.3 Data Acquisition Chain When an ionizing particle hits the scintillator material, the generated photons arrive at the APD and produce a change in the flowing current, that is superior to the stand-by current called dark current. This change is registered by the preamp and transformed into an amplitude pulse, that can be read in high or low gain, depending on the experiment requirements.

The pulse generated by the preamp arrives at the FEBEX [47] (Front End Board with optical link EXtension, a front-end board that contains, in a simplified view, an Analog to Digital Converter(ADC) and a FPGA (Field Programmable Gate Array). The ADC first samples the generated pulse in the preamplifier, and then the FPGA performs some operations:

(a) CALIFA crystal for the CEPA part.

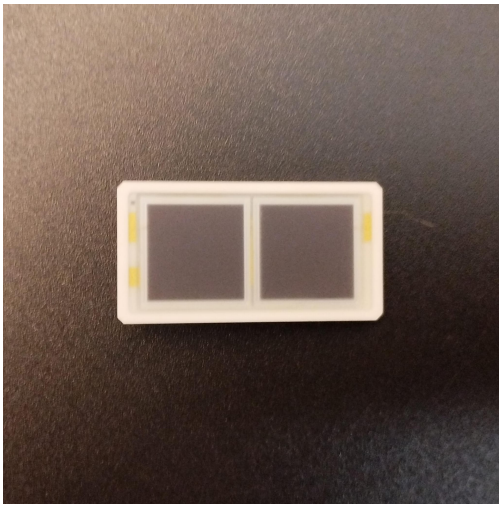

(b) Double APD Hamamatsu S8664-1020

Figure 3.7: CALIFA crystal ready to be installed at the CEPA part. The wrapping is tightly installed so every crystal fits perfectly inside the carbon fiber pocket and the light collection is optimized.

- Time Over Threshold (ToT): when a particle impinges the detector but the set gain is not low enough to process all the generated amplitude, the FPGA can measure the time that takes to go up and down the limit threshold. This quantity can be correlated with the particle energy and a ToT calibration can be performed for channels set in gamma range (high gain). The ToT procedure is not always done, as it requires recording all the pulse traces, which slows down the DAQ and induces some deadtime.
- Fast and Slow Component Separation (N_f, N_s): since the decay constant of the two components of light is quite different, an appropriate integration time can be defined so the two components are well separated.

The energy of a given event can be obtained with three different methods:

- ToT: as explained before, this value is proportional to the particle energy.
- Peak Sensing: the maximum value of the peak is stored in the event buffer as a measure of the particle energy.
- Slope Extrapolation: the peak sensing algorithm takes a few μs to find the top of the signal, so for trigger delivering, the slope at the beginning of the pulse is extrapolated

and used as an estimation of the total energy. This algorithm relies on the fact that the rise time of the signal is almost independent of the total energy.

The processed information is managed by the MBS [48] (Multibranch System), a DAQ system developed by GSI.

CALIFA can run in three different modes:

- Free Running: in this mode, CALIFA is self-triggered, so if a signal passes the internal trigger threshold then the event is recorded.
- Externally Triggered: an external trigger is sent to the MBS trigger bus, which is sent to the internal trigger bus. All channels are read without the need to pass the internal trigger threshold.
- Validated: the internal trigger generated by CALIFA is delayed. The detector signals are stored if there is a coincidence between the internal trigger from CALIFA and an external trigger.

For this experiment, CALIFA was running in free mode, so every signal recorded by the detector was stored, independently of the signals coming from the rest of the setup.

3.1.2.4 AMS

AMS (Alpha Magnetic Spectrometer) detectors are the silicon-stripped detectors installed at the International Space Station (ISS) for the tracking of high-energy cosmic rays. At the R^3B Cave, they have been mounted surrounding the reaction target at several experiments, in different configurations. For this case, the detectors were hanging from a plastic frame, together with the gold shielding used for δ-electron attenuation. This configuration was the one chosen for the experimental proposal after calculations and simulations performed in [49], where the impact of these secondary particles was studied in depth.

Each AMS detector has a size of $72 \times 42 \times 0{,}3$ mm^3 and consists of two sides, called the K side (n-dopped) and the S side (p-dopped). The S side has an implantation width of 27,5 μm, and only one out of four strips are read. If a particle hits a non-connected implantation region, then a signal is induced in the connected one, resulting in an effective strip width of 110 μm. The K side has an implantation width of 104 μm, with every strip being read out. The total number of strips is 640 for the S side (groups of four) and 384 for the K side.

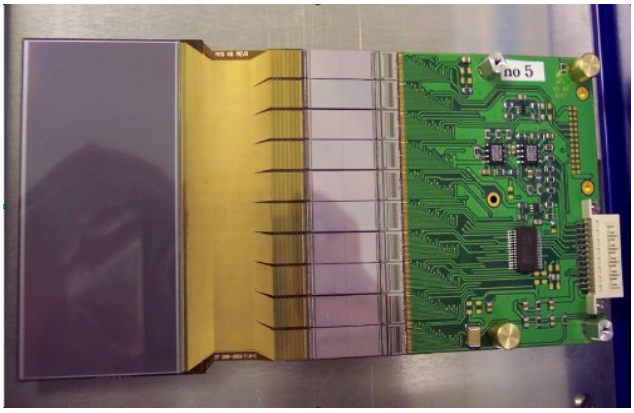

Figure 3.8: Single AMS detector. The sensitive area is on the left side, with the coupled electronics and the connections on the right part of the picture. Every group of 64 channels is read by an ASIC chip. Picture taken from [50], with open access permissions.

The readout is performed by the SIDEREM (SIlicon DEtector REadout Module), a specifically designed module for the AMS detectors at GSI.

3.1.2.4.1 Detector Configuration for the Experiment Six AMS detectors were used for tracking the scattered protons coming out from the reaction target. The spatial distribution of the detectors is sketched in Fig. 3.9 and in Fig. 3.10.

3.1.2.5 LH_2 Target

The LH_2 target was designed to perform experiments at R3B where only pure proton-incoming nucleon interactions were measured. A pure hydrogen target would allow then to study clean proton-knockout reactions without the need for target subtraction, a common procedure in previous experiments, where a measurement of the background generated from the C part of the typical CH_2 targets was performed [21].

The liquid hydrogen target has a cylindric shape ($\varnothing$ 42 mm, width= 15 mm) and consists of a cryostat installed at the upper part of the device. The hydrogen gas is liquified there at 20,3 K and 1041 mbar. The resulting liquid falls and fills the target capsule, located at the bottom part. The entrance and exit Mylar windows of the target have a width of 120 and 180 μm, respectively.

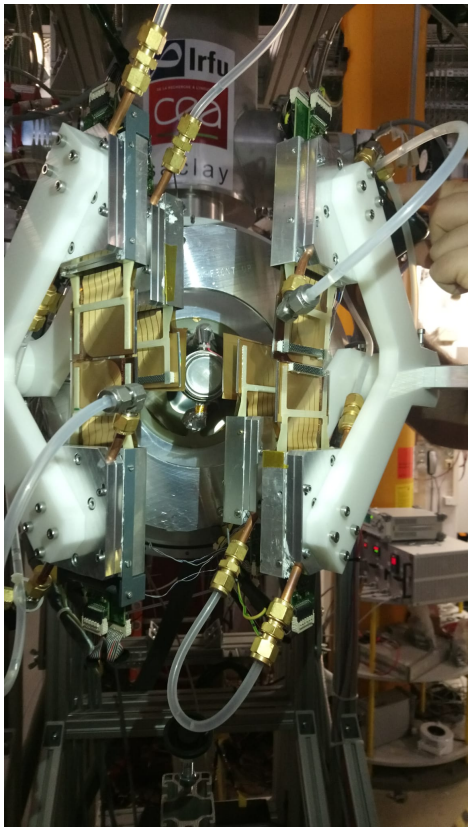

(a) Opened reaction chamber after the experiment, showing the AMS detectors and the LH_2 target.

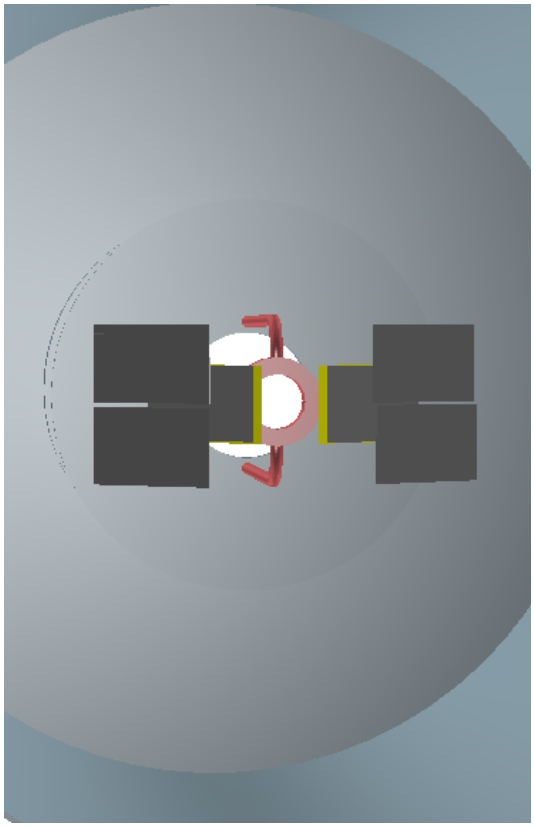

(b) AMS geometry used for simulations. Details about this geometry will be presented in subsequent sections.

Figure 3.9: AMS configuration for experiment s455. The left picture shows the plastic holding frame, the 6 AMS detectors, and the gold shielding. In the right plot, the geometry used for simulations is displayed. The target capsule and the auxiliary parts were removed from the picture for the sake of clarity.

3.1.2.6 TWIN Music

The TWIN Music [51] is a double multisampling ionization chamber used for the charge identification of the two fragments that are produced in fission reactions. The two detector sections are separated by a vertical metal plane that acts as a cathode. Each section is divided at the same time into an upper part and a bottom part, where a frisch grid and the anodes are located. Four identical sections result from this configuration. A sketch of the detector is displayed in Fig. 3.12.

Each one of the 16 anodes present in a section is read when a fragment travels through

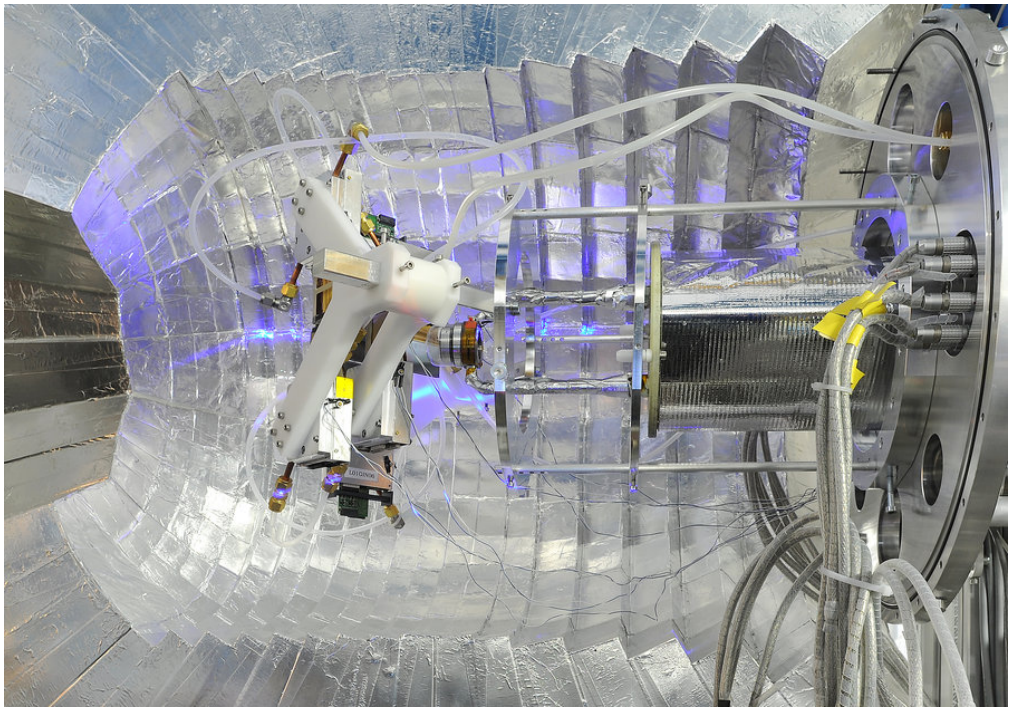

Figure 3.10: Reaction region enclosed by the CALIFA-AMS system. Credits to Gabi Otto, Copyright GSI GmbH.

the gas. The drift time on each anode allows for a trajectory reconstruction, so the angle of the entering fragment can be obtained. The charge collected on the anode is used for obtaining the charge of the fission fragment.

3.1.2.7 GLAD

GLAD is the GSI Large Acceptance Dipole of the R^3B collaboration. It was designed as a replacement for ALADIN (A Large Acceptance DIpole magNet), the old magnet of the ALADIN/LAND collaboration. This new detector was used in all of the R^3B phase-0 experiments and will be installed at the new high-energy cave of the collaboration at FAIR.

The magnet features a maximum high magnetic field integral of about 5 Tm, which allows an 18° bending of a 15 Tm beam (for example, ^{138}Sn at 1 GeV / nucleon). This high bending power and the large magnet acceptance allow for a variety of different reaction mechanisms to be studied, from fission to spallation reactions, at a wide range of incoming energies. The GLAD magnetic field is created by superconducting coils made of 16 km of NbTi cable, that can hold up to 3700 A of current. The total dimensions of the magnet, including the frame

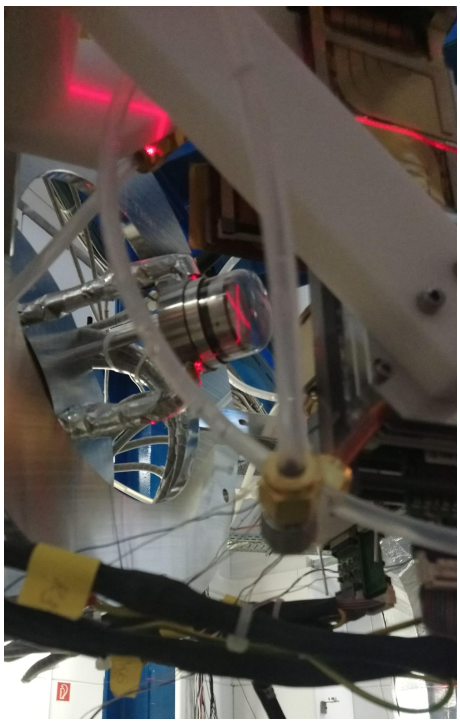

(a) Target capsule inside the reaction chamber. The laser mark helped with the alignment.

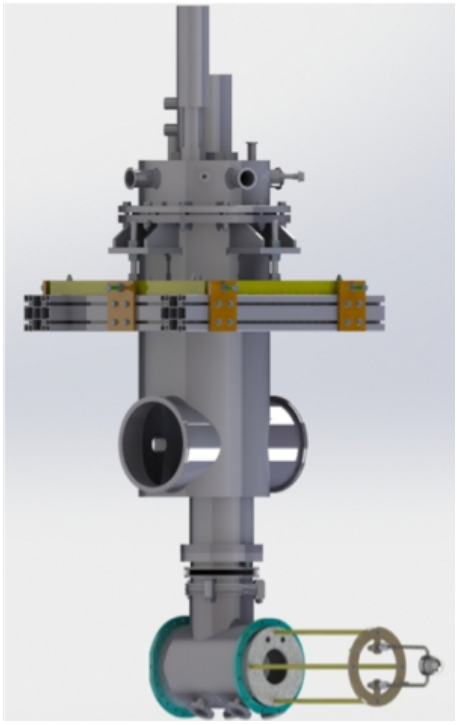

(b) CAD sketch of the cryostat + target capsule and frame system.

Figure 3.11: LH_2 Target at s455 Experiment.

and the cooling system are 3,5 m long, 7 m wide, and 4 m tall, with a weight of 50 tons.

3.1.2.8 ToF Wall

The Time of Flight Wall (ToF Wall) was located at the end of the setup and aimed for time-of-flight measurements of the fission fragments. The difference in time between this detector and the plastic scintillator located at the entrance of Cave C allows for the determination of the fragment's velocity. This velocity, along with a proper determination of the fragment's trajectories, would allow to obtain the mass of each reaction product.

The detector is made of 28 individual plastic scintillators, with a size of $32 \times 60 \times 5$ mm^3. The total active surface is, therefore, $896 \times 60 \times 5$ mm^3. Each detection unit is attached on both sides to a pair of PMTs, that measure the arrival time of the signal on both sides. With this measure, the Y position of the detected particle can be obtained, and also its time of flight. The detector is mounted in a mobile aluminum frame, that can be adjusted by a step

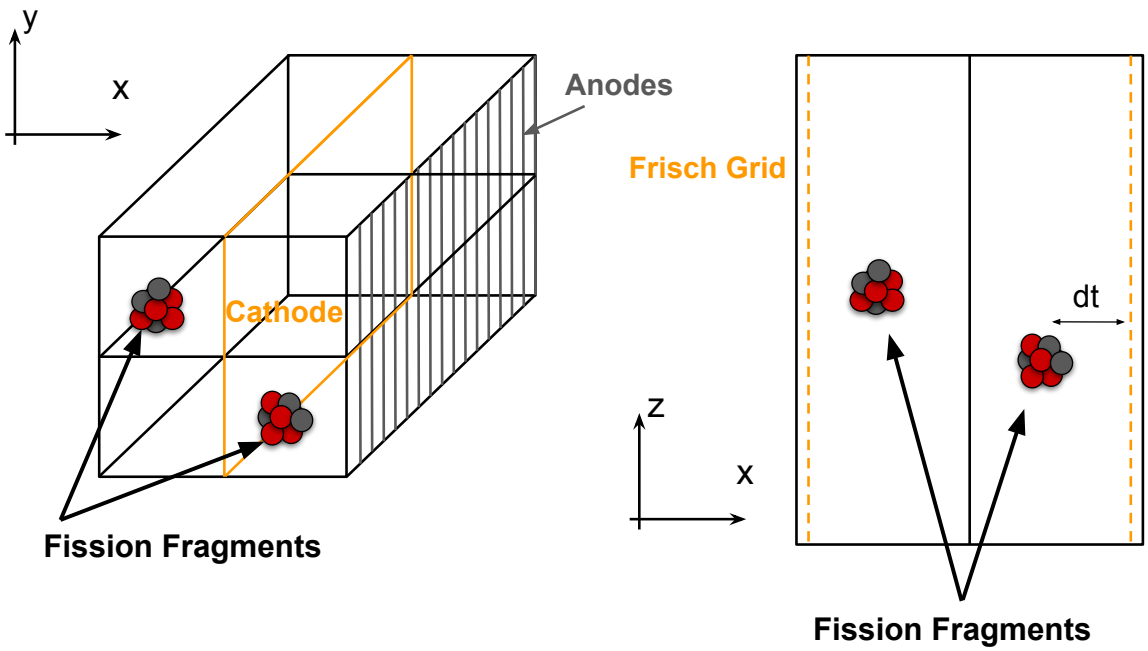

Figure 3.12: Scheme of the TWIN MUSIC experimental disposition. The left figure shows the detector from the entering beam perspective. The right picture shows a top view of the detector.

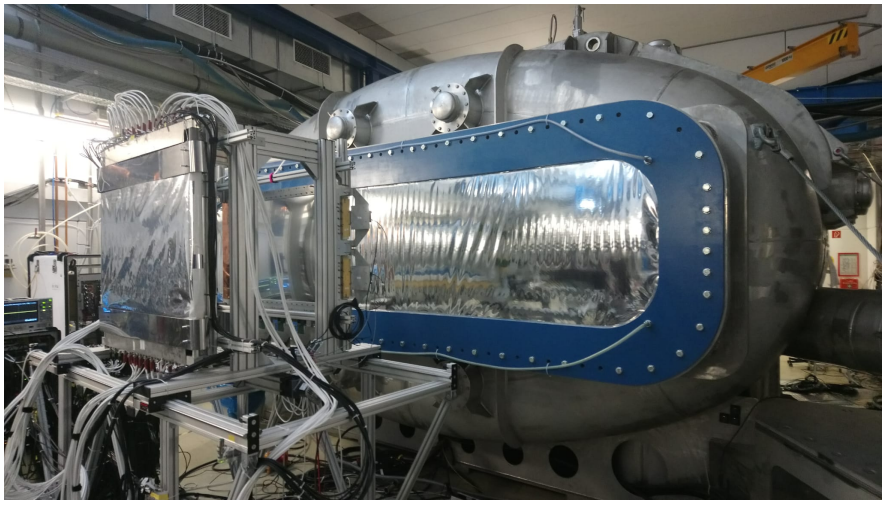

Figure 3.13: GLAD installed at Cave C.

motor. This allows for a proper alignment of the detector with respect to the GLAD bending line of reference.

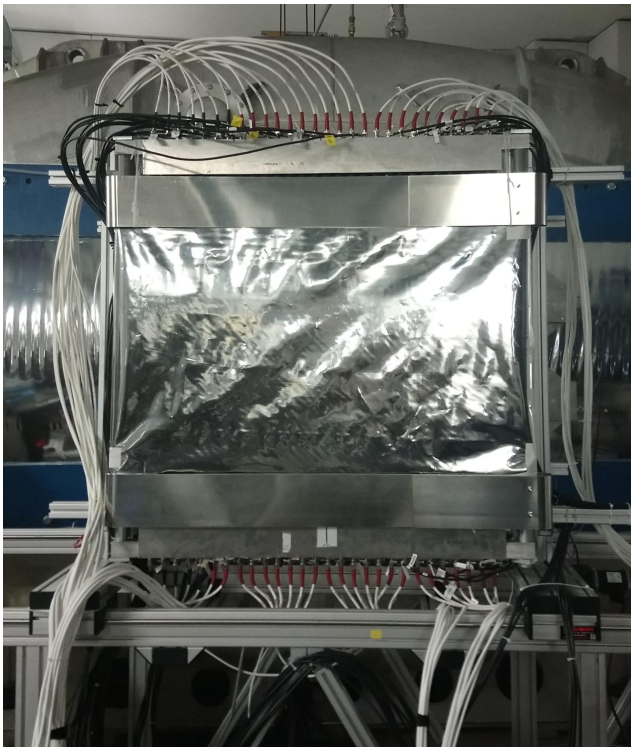

Figure 3.14: TofWall installed at the end of the beamline. The frame of the detector is shared with the MWPC3.

3.1.2.9 NeuLAND

NeuLAND [52] (New Large-Area Neutron Detector) is the neutron detector of the R^3B collaboration.

The detector design is aimed for a high resolution in time-of-flight for neutrons, multi-neutron detection capabilities, high efficiency, and a high acceptance for neutrons produced in the typical reaction mechanisms covered by the R^3B physics program. In its final configuration, the detector's active size will be $250 \times 250 \times 300$ cm^3. NeuLAND will have 3000 plastic scintillator bars, with a size of $5 \times 5 \times 250$ cm^3. The bars will be arranged forming vertical and horizontal layers, and every group of two layers will be set together in a double-plane. 30 double planes are expected to be installed in the final configuration. 6000 PMTs will be attached to both bar ends, collecting the light produced in the scintillation process. For the experiment, 12 double-planes were installed with a total of 1200 working detection units.

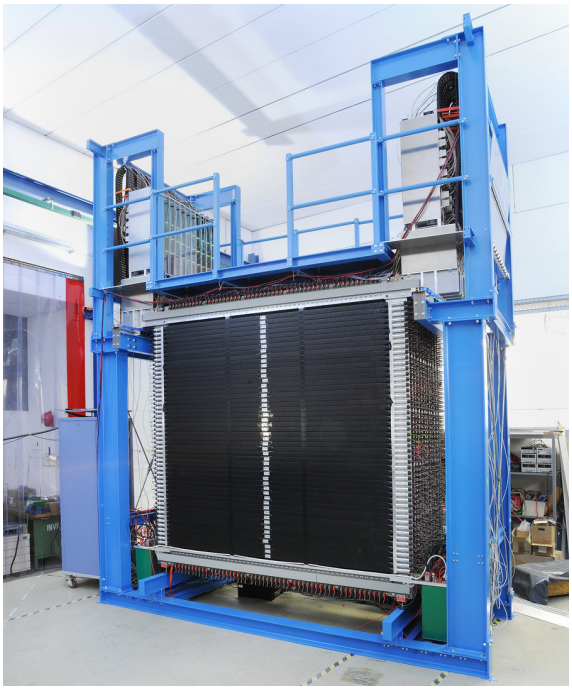

Figure 3.15: NeuLAND experimental disposition. The DAQ modules are installed on top of the blue frame. Copyright: Gabi Otto, GSI GmbH.

Detector	Active Part	Channels (I/F)	General Purpose	s455 Purpose
MWPC0	Gas	128/128	Tracking	Beam tracking
TRIM	Gas	18/18	Secondary beam Z identification	-
SCI	Plastic Scintillator	2/2	Start signal and ToF	Start signal and ToF
CALIFA	Inorganic Crystals	1504/2544	Gamma and particle detection	Proton energy measurement
AMS	Silicon Strips	6144/6144	Vertex reconstruction	Vertex reconstruction
MWPC1	Gas	168/168	Fission fragment tracking	Fission fragment tracking
TWIN	Gas	64/64	Fission fragment Z identification	Fission fragment Z identification
MWPC2	Gas	168/168	Fission fragment tracking	Fission fragment tracking
GLAD	-	-	Mass spectroscopy	Mass of fission fragments
MWPC3	Gas	408/408	Fission fragment tracking	Fission fragment tracking
ToFWALL	Plastic Scintillators	56/56	Time of Flight	Time of Flight and Fission trigger
NeuLAND	Plastic Scintillators	2400/6000	Neutron detection	Neutron detection

Table 3.2: Summary of the different detection systems used in experiment s455. The third column refers to Installed channels when the experiment was performed (I) and expected channels in the final (F) detector configuration. Double readings and reference channels are not taken into account.

3.2 Software

3.2.1 R3BRoot

The standard tool for data analysis and simulations within the R3B collaboration is R3BRoot [53]. This framework is based on FairRoot[1] [54] tasks and Geant4 [55]. Some characteristic features are :

- It is written in C++ and object-oriented. The code is well-optimized so it is fast, efficient, and trustable.
- It is supported by an active community on GitHub, where questions, issues, and new code additions are solved and checked by developers.
- It provides the same tools and data structures for simulation and experimental data. The data coming from detectors is stored in data structures, that are transformed via *tasks*. In this way comparing results from experiments and simulations is simple and straightforward.
- Calibration, mapping, and simulation parameters are managed efficiently and precisely, using tools inherited from FairRoot tasks.
- Connections with Geant4, Geant3, and other particle transport engines are provided, so the user can adapt the physical requirements of the simulation by using the supported physics lists.

A detailed description of the R3BRoot internal functioning can be found in Appendix A.

3.2.2 CALIFA Software

As this work is centered on the analysis and simulation of data using the CALIFA calorimeter, a detailed description of the software tools used for that is presented here. Despite having a similar data structure as any other detector, in the manner that is presented in Appendix A, there are some parts that are specific to this detector and others that were developed for this work.

[1] FairRoot is a framework based on ROOT and developed at FAIR, which offers a set of tools for data transport, detector simulation, and reconstruction tasks. It also provides connections with particle transport engines such as Geant4 or Geant3.

3.2.2.1 Geometry

The geometry design for simulation and reconstruction purposes was based on the original detector CAD drawings made during the development phase [41]. This geometry includes the scintillator material, the carbon fiber alveoli, the wrapping, and the air interface between all components.

There are a total of 23 different crystal geometries, that fit in different parts of the calorimeter, contained in the carbon fiber alveoli. Each alveoli is defined by eight corners, that are allocated in space. Then each crystal is rotated and translated until every detection unit is placed inside its corresponding pocket. This geometry is then loaded in the simulation and analysis macros and can be rotated, and displaced at will to match the real position of the detector during the experiment. This geometry is also customizable and mimics the configuration of the detector at the experimental Cave. In this way, the two halves can be opened, displaced with respect to the target, and rotated according to experimental measurements. A list of the installed crystals used in the experiment is given to the software that creates this object, so missing detection units are not created and therefore not taken into account while doing simulations or analysis.

3.2.2.2 The R3BCalifa class and R3BCalifaDigitizer

The management of the information created by Geant4 inside the active volume of CALIFA is handled by the **R3BCalifa** class. For every track that is propagated inside the material, this class adds all the step information (energy losses, lengths, Nf, Ns) and creates a point, that contains information on a given track inside the material. This **R3BCalifaPoint** has several data members: Track ID, Detector ID, Crystal ID, Coordinates, Momentums, times, lengths, and energy losses of the tracks inside the crystal material.

After all points have been calculated and stored, the **R3BCalifaDigitizer** class is responsible for taking all the points that were created within the active material corresponding to a single crystal, adding the energy losses, and applying, in its simplest form, the nominal resolution that is expected at the energies being reconstructed. This reconstruction gives at the end another data level, called **R3BCalifaCrystalCalData**, that contains all the energy deposited in the crystal for the current event. This data level is therefore directly comparable with experimental data and contains calibrated energy, time-over threshold (ToT), crystal ID, Nf and Ns components, and crystal time.

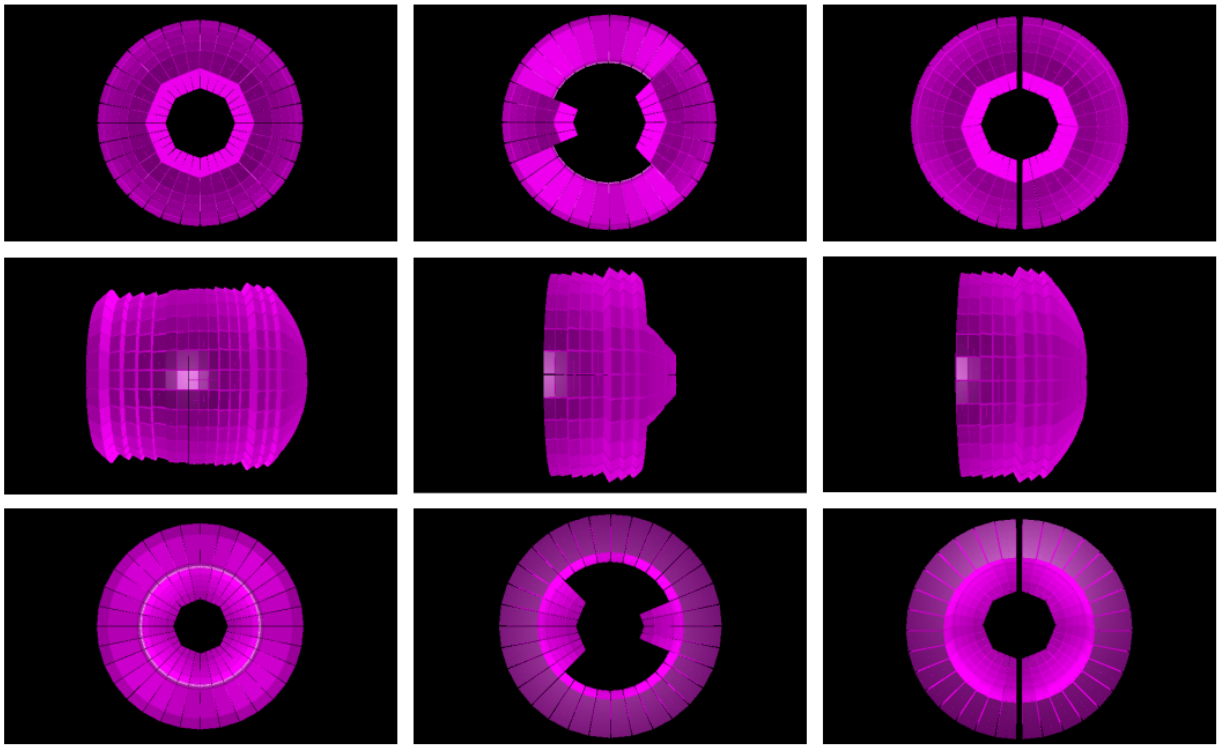

Figure 3.16: Different views of the CALIFA active volume. Columns: from left to right geometries for the complete configuration, previous experiments, and this experiment. Rows: from top to bottom front view, side view, and bottom view of the calorimeter.

Since a realistic simulation is needed not only for comparison between the experience and the simulation but also for developing novel algorithms for data reconstruction and analysis, a new set of simulation parameters was developed for this class. The parameter container is generated typically from the analysis of calibration runs with gamma sources before and after the experiment. Collected data allows to calculate crystal by crystal the experimental resolutions and thresholds at the moment of data collection. These parameters are loaded into simulation runs, so when the digitizer adds up all the energy losses in a crystal, the actual resolution of that crystal is applied before saving the calibrated energy level. If this energy does not pass the experimental threshold, it is discarded and the calibrated level is not created. The exact procedure for extracting resolutions and thresholds is explained in Chapter 4.

3.2.2.3 Clustering Algorithm

CALIFA was designed to provide energy measurement of light energy particles coming from the reaction target, together with gamma rays. Those high-energy gamma rays that can be Compton-scattered leave energy in more than one crystal, while those with enough energy to create an electron-positron pair will give another two 511 keV gammas that are back-to-back scattered. Protons that hit the calorimeter leave energy typically in one, two, or at most three crystals, even if they punch through the scintillator material. Therefore is necessary to have a method for grouping crystals in a coherent and meaningful way so the physical observables are well reconstructed in a structure called *cluster*.

The R3BRoot task that performs the clustering is intended to work in a way that for experimental data proton and gamma clusters are reconstructed using the optimal combination of crystal ranges. This algorithm works as follows:

1. The class has three data members that work as thresholds for selecting valid signals:

   - fProtonClusterThreshold: minimum energy required in a crystal for being considered as a proton cluster candidate.
   - fGammaClusterThreshold: minimum energy required in a crystal for being considered as a gamma cluster candidate.
   - fCrystalThreshold: minimum energy required in a crystal to be included in a cluster.

   All of these possibilities will be considered to asign the crystal that initiated the cluster creation. The angular information of the cluster will be provided by this crystal, and will be frequently called *mother* crystal of a cluster.

2. An algorithm is defined for grouping crystals into some angular region of the calorimeter and the values of this region are set by the user. Some typical algorithms are:

   - Rectangular window. A crystal is included inside a cluster if the differences between its polar and azimuthal angles with respect to the crystal that generated the cluster are smaller than the defined limits:

   $$|\varphi_{Mother} - \varphi_{Crystal}| \leq \Delta\varphi \quad \&\& \quad |\theta_{Mother} - \theta_{Crystal}| \leq \Delta\theta \tag{3.1}$$

   - Round window. In this case, a crystal is included inside a cluster if the opening angle between the crystal and the mother crystal is smaller than a certain value.

This opening angle is calculated as the angle between two 3D vectors in space:

$$\hat{\alpha} = cos^{-1}\left(\frac{\vec{v}_{Mother} \cdot \vec{v}_{Crystal}}{|\vec{v}_{Mother}|\,|\vec{v}_{Crystal}|}\right), \quad \hat{\alpha} \leq \Delta\hat{\alpha} \tag{3.2}$$

3. The calibrated data is read at the beginning of the event and four vectors of R3BCalifaCrystalCalData objects are created:

   - Proton candidates: for crystals above fProtonClusterThreshold and set in proton range.
   - Gamma candidates: for crystals above fGammaThreshold. If the crystal is double ranged then the high gain signal is taken into account and the low gain signal is removed from the vectors.
   - Saturated candidates: for crystals set in high gain that have energy marked as NAN, coming from a saturation of the ADC. This energy cannot be reconstructed (unless some other algorithm is performed during calibration such as ToT reconstruction) but a cluster is still built and can be used for counting purposes, for example in cross section calculations.
   - All crystal vector: every crystal that is above fCrystalThreshold is included here. These crystals are added to each cluster candidate if they are inside the defined angular window for building a cluster.

4. The four lists are sorted by energy in decreasing order.

5. For the first entry in the proton candidate list the angular difference of all crystals with respect to this candidate is calculated using some of the previously described algorithms. If this difference is below the limit, this crystal energy, Nf, and Ns are added to the cluster information, and the crystal is removed from all lists. Since the proton energy is expected to be shared between a few crystals around the mother one, the low gain energy is taken into account when adding neighbor energies and the high gain information is discarded. If the surrounding crystals are only read in high gain the energy is added only if the crystal is not saturated.

When all neighbors have been added, this first candidate for a proton cluster is removed and an R3BCalifaClusterData is created, containing:

- Total energy, as the sum of all the energies of the crystals inside the cluster.
- Nf, as the sum of all the Nf data of the crystals inside the cluster.

- Ns, in the same way as Nf.
- Time, as the time information of the mother crystal. In experimental data, this time is the White Rabbit time (the DAQ time) at which this signal was recorded.
- Polar angle. This angle is obtained from the mother crystal and read from the ROOT geometry.
- Azimuthal angle. The same as the polar angle.
- Crystal list. A list of all crystal IDs contained in the cluster. The first one is the mother crystal.
- Cluster ID. This number is set to 0 for proton clusters, 1 for gamma clusters, and 3 for saturated clusters.

6. The algorithm continues with the next element in the proton candidate list.
7. When the proton candidate list is empty, the algorithm starts with gamma clusters. The crystals are matched in the same way but the high gain range signals are preferred over low gain signals around the mother crystal. If there are no high gain signals around then the low gain ones are taken into account.
8. When the gamma candidate list is empty, the saturation clusters are constructed in the same way as proton and gamma clusters.

3.2.2.4 Angular Randomization Procedure

The angular information within the cluster object is discrete and corresponds to the angular coordinates of each crystal centroid with respect to the target. When a correlation between some observable and angular information is presented this discretization makes it difficult to interpret results and see possible failures or patterns. To address this issue, a randomization procedure was implemented at the cluster level of CALIFA, resulting in a higher granularity of the displayed angular information that allows an easier and more natural way of interpreting this data. This algorithm works as follows:

1. First a simulation is launched. The desired CALIFA geometry is loaded and millions of 50 keV gammas are simulated with multiplicity one.
2. Once the simulation is finished, the file is loaded into an analysis macro. An array of 2342 two-dimensional histograms is created for storing angular information for each crystal.

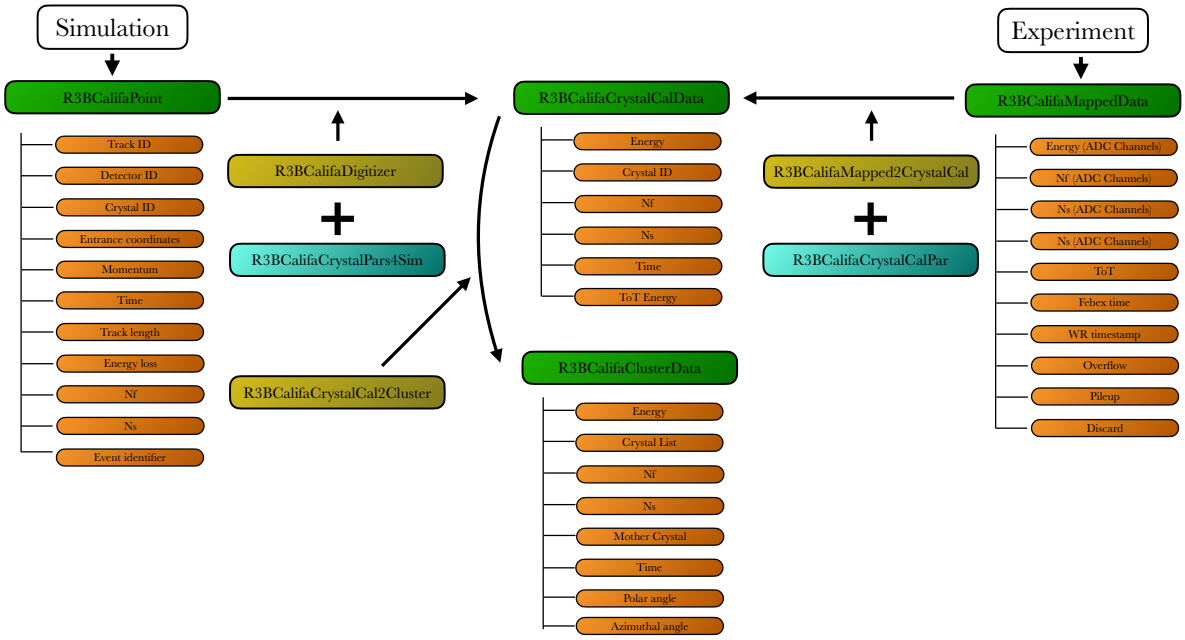

Figure 3.17: Detailed scheme of CALIFA data flow for both experimental and simulation data. Data structures are displayed in green, data members in orange, tasks in gold, and parameter containers in blue. Experimental data processing will be explained in the analysis chapter.

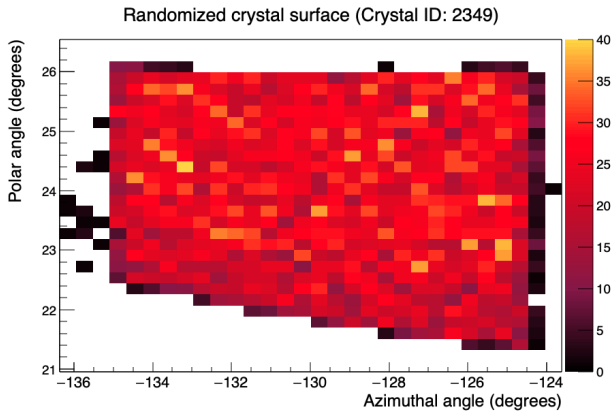

Figure 3.18: Randomized surface of the crystal. This distribution is later used by the clustering for creating random angles.

3. Every time a crystal is hit by a gamma, the angular coordinates of the primary that impinged the crystal surface are stored in its corresponding 2D histogram.

4. When the analysis is finished, every crystal surface is represented by those histograms, that are loaded into the clustering class.

5. For every created cluster, if the randomization procedure is set to true, two angular coordinates are obtained from the desired crystal histogram as random numbers that follow the crystal face angular distribution.

The reconstructed angle has a larger error in the case of the randomized one. For the discrete case, the error is the difference between the point of impact in the crystal surface and the fixed centroid of the crystal, while for the randomized case this difference is measured between two random points over the face. Taking as an example a rectangular crystal face with side length l and if the impact point is denoted as x, the expected variance in distance is

$$\sigma(x) = \sqrt{\frac{1}{l}\int_0^l x - \frac{l}{2} dx} = \frac{l}{\sqrt{12}}, \tag{3.3}$$

assuming an uniform distribution with mean $\mu = \frac{l}{2}$. For the randomized angle this difference is the difference between two uniform random positions, so the distribution is triangular with a maximum value of l centered at 0, with a variance of

$$\sigma_{Rand} = \frac{l}{\sqrt{6}} = \sqrt{2}\ \sigma_{Discr}. \tag{3.4}$$

These two cases can be calculated for angles by performing a simulation. In this case, the same procedure was used as for the randomization algorithm, so the difference in angles between the primary particle and the reconstructed angle using randomized and discrete angles can be extracted.

Angular Difference	**Mean**	**Variance**
$\Delta\theta_{Disc}$	0,034	1,198
$\Delta\theta_{Rand}$	0,003	1,693
$\Delta\varphi_{Disc}$	-0,591	3,026
$\Delta\varphi_{Rand}$	-0,005	4,283

Table 3.3: Calculated means and variances for the two modes of reconstruction using all the crystals in the calorimeter. Everything is expressed in degrees.

The results are shown in Fig 3.20 and summarized in Table 3.3. As expected, the variance in the randomized case is exactly $\sigma_{Rand} = \sqrt{2}\sigma_{Disc}$. As a result of this, the randomization procedure should be used only for studying correlations and distributions, but the discrete angle of the crystals should be used for physical calculations, such as Doppler correction of gammas or momentum calculation of protons.

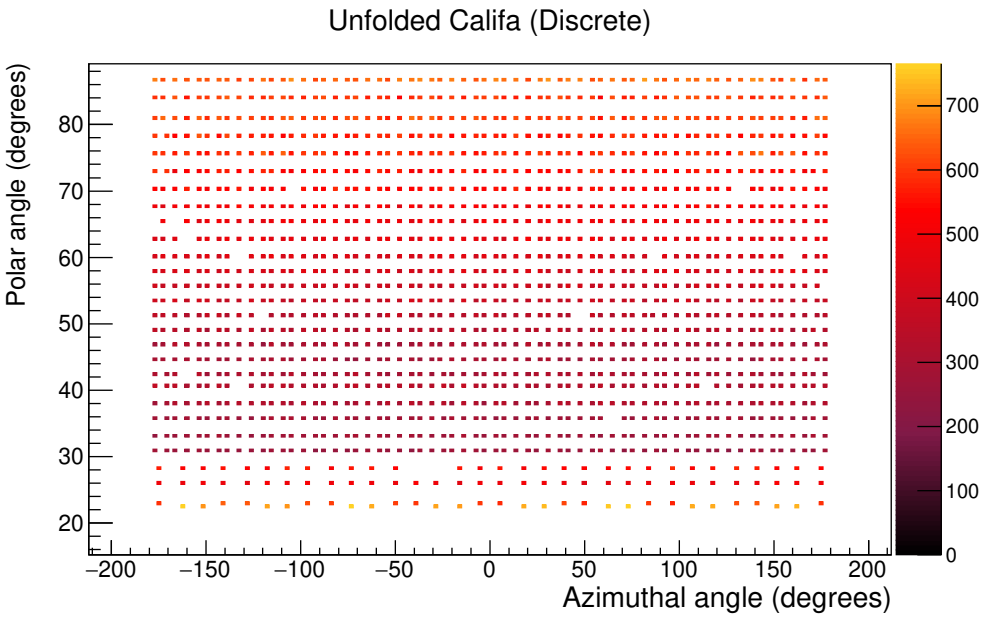

(a) Discrete angles for the nominal position of CALIFA.

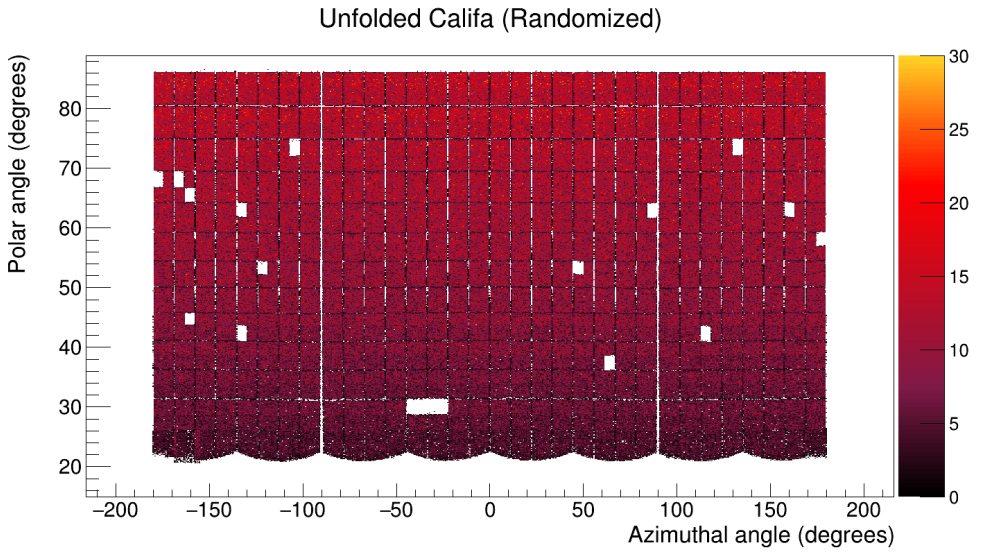

(b) Randomized angles for the experimental position of CALIFA in s455.

Figure 3.19: Angular distributions before and after randomization.

3.2.3 SoKAI

SoKAI (Some Kind of Artificial Intelligence) is a machine learning framework that was developed for this work for reconstruction purposes and as an alternative to using common Python

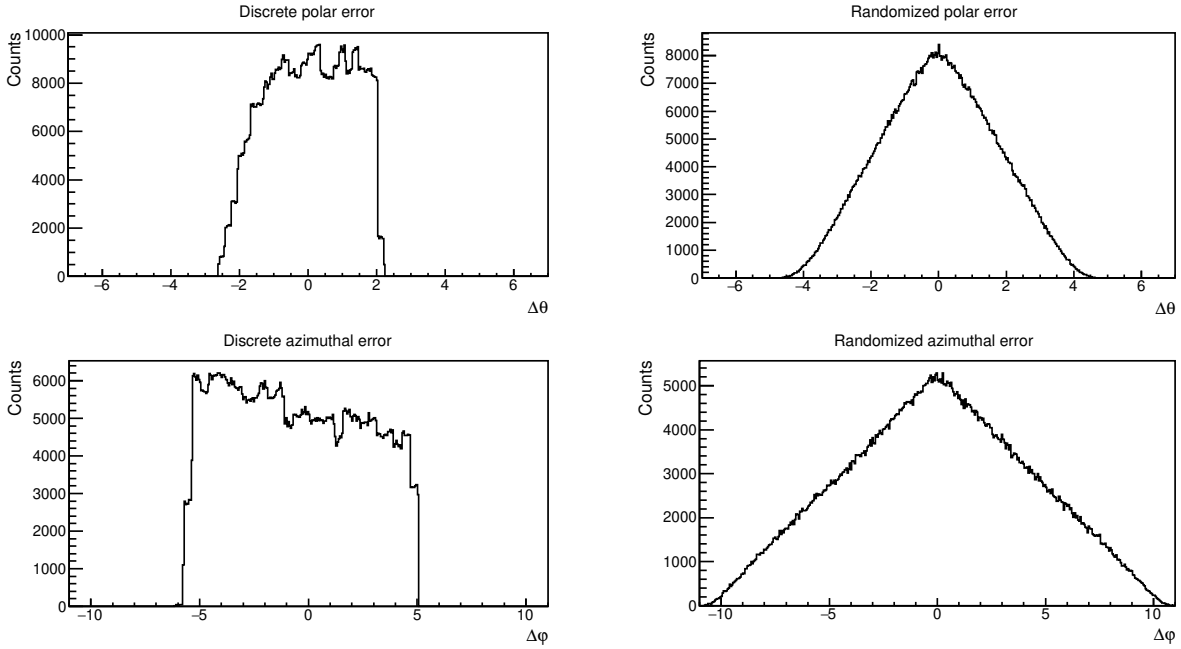

Figure 3.20: Angular errors for both polar and azimuthal coordinates. This delta difference is expressed as $\Delta\varphi = |\varphi_{Primary} - \varphi_{Reconstructed}|$ *and* $\Delta\theta = |\theta_{Primary} - \theta_{Reconstructed}|$.

frameworks such as Keras, Pytorch, or TensorFlow [2]. This framework is purely written in C++, so a complete integration with other C++ projects (R3BRoot and ROOT, mainly) is easy and direct. The idea behind this project was that the user could merge the code with the typical procedures carried out in the R3BRoot analysis, in the case of CALIFA, clustering, online reconstruction, and analysis. In this work, SoKAI will be used to reconstruct the energy of the scattered proton pair, as detailed in the next chapter.

SoKAI is built using extensively the standard methods from the C++ library (at the moment of writing, C++ 17). The information is transmitted using standard vectors, that contain custom objects designed for neural network calculations. The code has minimal dependencies (CMake, ROOT, and GLOG), and has been installed and run in a large variety of Linux and MacOS systems.

[2]Technically TensorFlow runs behind Keras, but it can be also used as a low-level framework on its own using the different existing APIs.

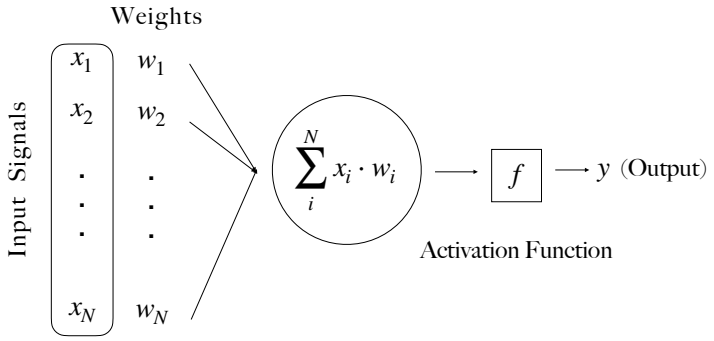

Figure 3.21: Scheme of a perceptron unit.

3.2.3.1 Neural Networks: the Basics

A neural network is a computational algorithm based on the structure and functioning of the human brain. The first works using artificial units of calculations called neurons date back to 1943 when W. McCulloch and W. Pitts [56] modeled the behavior of an ensemble of neurons by using propositional logic. Later on, in 1958, F. Rosenblatt proposed the concept of Perceptron [57], where this single unit of calculus accepted some stimuli from the outside, modeled as several input channels from where the information comes. These signals are multiplied by some *weights* before being added in the first part of the perceptron. An activation function is defined as the mathematical function that is applied to the sum of the incoming signals. The result of this function evaluation can be logical (yes/no, 0 or 1) or continue, as an amplitude pulse of the incoming signals. To update the weights, the difference between the expected output and the obtained output is computed and the parameters are changed according to:

$$w_j^{'} = w_j - \alpha(y - \hat{y})x_j, \tag{3.5}$$

where $w_j^{'}$ is the updated weight, α is the learning parameter, which modifies how much weights are changed on each iteration over the dataset, and $(y - \hat{y})$ is the difference between the expected output and the actual output. It can be proved that a single perceptron unit can only linearly separate data (Novikoff, 1962), so the perceptron has been historically used for binary classification. Some later models using multilayer perceptron were developed, but the idea of the perceptron as an artificial model was quickly forgotten. Later on, A.G. Ivakhnenko and V. Lapa developed a model based on Multilayer Perceptrons (MLP) [58]. This model was able to improve the prediction task by removing unnecessary computational nodes in the network.

The discovery of the Backpropagation algorithm, and its use over experimental data [59] marked a turning point in the development of AI models, but the algorithm was forgotten until its rediscovery at the beginning of the 21st century. The growth of the computational power available to researchers and the general public, along with the development of daily usage of AI-based technology, propelled the discovery of a plethora of different neural network models and algorithms, that are now a common tool in many scientific fields.

3.2.3.2 Neural Network Structure

A Neural Network (NN) model features a variable number of computational units called *neurons*. These neurons are identical in structure to the perceptron unit. Several neurons are grouped in a structure called *layer*, and several layers are connected using weight matrices. A model is then composed of a variable number of neuron layers, that can range from two (shallow networks) to a huge number of middle layers, called *hidden layers* that form a *deep learning* model. A general structure of a NN is displayed in Fig. 3.22.

These neurons can apply several different activation functions over the input data. The most common function is LeakyReLU, a modified version of the Rectified Linear Unit function. Sigmoid and Tahn functions are also used.

A bias value is sometimes added to the neuron's output before multiplying by the corresponding weight. This bias vector is also a tuneable parameter that is updated on each backpropagation step.

In a general way, the input for a given neuron m of a given layer P can be written as:

$$i_m = \sum_{j=1}^{N} w_{jm} o_j, \tag{3.6}$$

with N the total number of neurons in the previous layer and o_j the output of the j-th neuron of the previous layer. This value is the m-th element of the vector that results from the operation

$$I^P = O^{P-1} W^{P-1,P} = (o_1^{P-1}, o_2^{P-1} ...) \begin{pmatrix} w_{1,1}^{P-1,P} & \cdots & w_{1,M}^{P-1,P} \\ \vdots & \ddots & \vdots \\ w_{1,N}^{P-1,P} & \cdots & w_{N,M}^{P-1,P} \end{pmatrix} \tag{3.7}$$

After all data is propagated for a given event of the data sample, the *loss* function is computed. This function is a measure of how good is the network output and is computed using the *label* data, which is the correct output for a given input. This label data ($\hat{y}$) is usually obtained from simulations, human-processed, or as the output of any other algorithm

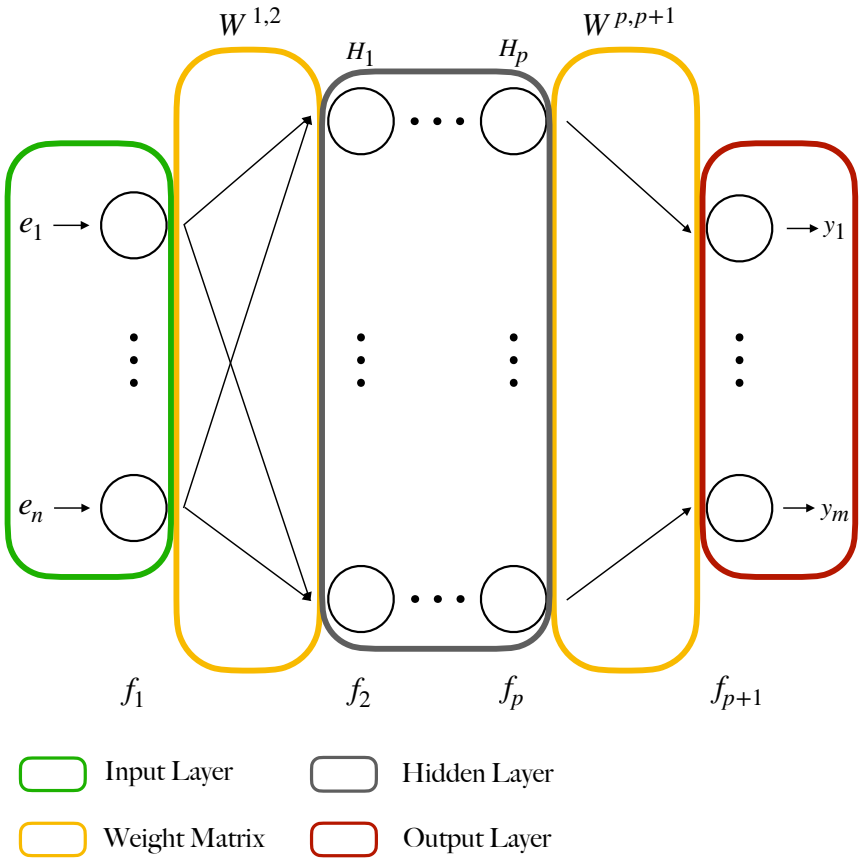

Figure 3.22: General scheme of a Neural network model, with p hidden layers, n input neurons, and m output neurons.

that is known to give good results. The loss is then calculated as

$$L \equiv L(y,\hat{y}). \tag{3.8}$$

The most common losses in regression tasks, where the network is expected to give some continuous values, are the Quadratic and Absolute loss functions:

$$L_Q = \frac{1}{N}\sum_{j=1}^{N}(y-\hat{y})^2, \quad L_A = \frac{1}{N}\sum_{j=1}^{N}|(y-\hat{y})|, \tag{3.9}$$

with N the total number of neurons in the output layer. For multi-label classification purposes, every neuron output in the output layer is transformed into a probability of belonging to one of the N classes using the softmax activation function

$$P(o_n) = \frac{e^{o_n}}{\sum_{j=1}^{N} e^{o_j}}, \tag{3.10}$$

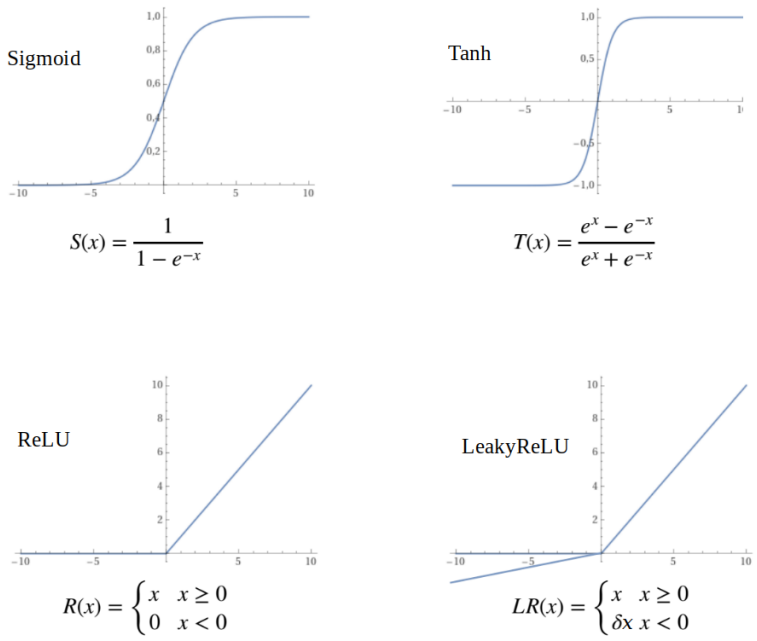

Figure 3.23: Common activation functions used in Neural Network models. The LeakyReLU function has a slight slope in the negative part, that prevents the gradients from vanishing for a given weight if the neuron output is negative. This slope has been exaggerated for better visualization.

Then, the categorical cross-entropy loss function is used:

$$L_C = -\sum_{j=1}^{N} \hat{y}_j \log P(o_j). \tag{3.11}$$

The target for the classification case is usually one-hot encoded. This means that an event that is classified as class 2 out of 4 possible classes will be labeled as

$$\hat{y} = (0,1,0,0). \tag{3.12}$$

3.2.3.3 Backpropagation

A weight joining two neurons is updated by using the loss function. The gradient of this function is calculated for the weight that has to be updated. After the calculation, the new weight will be

$$w'_{n,m} = w_{n,m} - \alpha \frac{\partial L}{\partial w_{n,m}}, \tag{3.13}$$

where α is the learning rate hyperparameter, that sets how fast the weights are updated. This value is usually set to small quantities (i.e. α = 0,01 , 0,001...). If this parameter is set to a too-large value, then the minimum region in the hypersurface defined by the loss function can be skipped from one iteration to another. If the value is too small, then the algorithm takes much time to converge and may not arrive at the global minimum. If this procedure is repeated on an event-by-event basis, the algorithm is named stochastic gradient descent.

To avoid a high fluctuation of the loss values, the weights can be updated after some pre-fixed number of iterations over the dataset. This procedure is called mini-batch learning, and the weights are updated using the mean of the gradients obtained for the events in the mini-batch.

The most common algorithm used now is Adam [60]. Adam is the short name for Adaptive moment estimation. In short, this algorithm defines a custom learning rate for every parameter in the model calculated using first (p) and second moments (q):

$$\begin{aligned} p^{'}_{n,m} &= \beta_1 \; p_{n,m} + (1-\beta_1)\frac{\partial L}{\partial w_{n,m}} \\ q^{'}_{n,m} &= \beta_2 \; q_{n,m} + (1-\beta_2)\left(\frac{\partial L}{\partial w_{n,m}}\right)^2 \end{aligned} \tag{3.14}$$

then these moments are weighted according to how many backpropagation steps (s) have been performed:

$$\begin{aligned} \hat{p}_{n,m} &= \frac{p^{'}_{n,m}}{(1-\beta_1)^s} \\ \hat{q}_{n,m} &= \frac{q^{'}_{n,m}}{(1-\beta_2)^s} \end{aligned} \tag{3.15}$$

and the weights are updated as

$$w^{'}_{n,m} = w_{n,m} - \alpha \frac{\hat{p}_{n,m}}{\sqrt{\hat{q}_{n,m}} + \epsilon} \tag{3.16}$$

with ϵ a small value used to avoid divisions by 0.

3.2.4 Structure

The code is based on the definition of C++ classes for every part of a neural network calculation. For example, a neuron (SKNeuron) is a class that accepts the information as an

input and gives an output when required. This output can be obtained via several activation functions that are chosen by the user. A layer (SKLayer) is then a class with one data member that stores a collection of neurons (a standard vector containing several instances of SKNeurons). A model (SKModel) contains several layers and performs the forward propagation of data and the backpropagation algorithm, both implemented as class methods of the SKModel class.

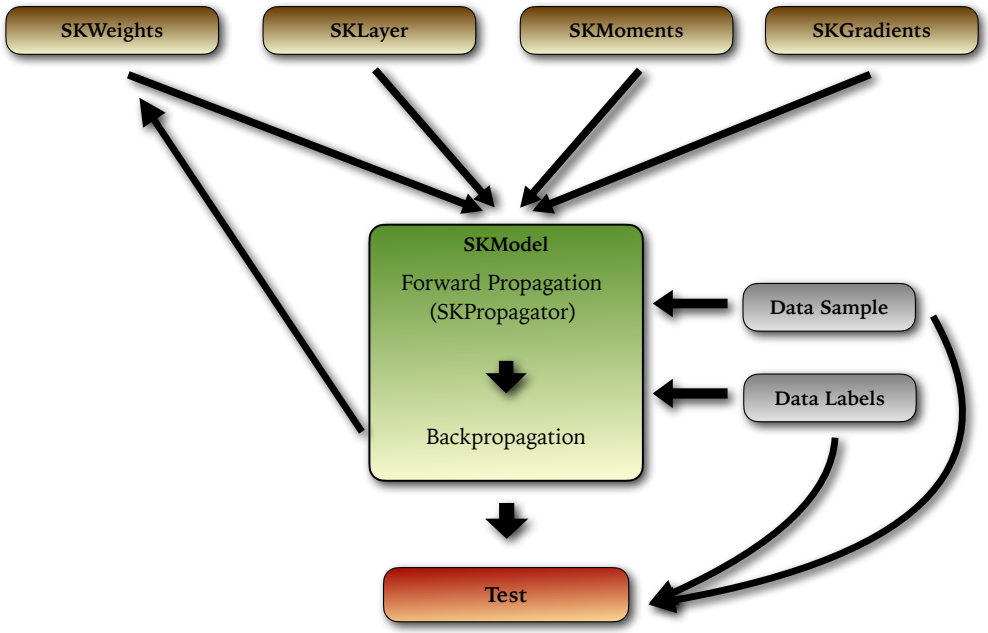

Figure 3.24: Basic structure of the code. Neurons are included inside SKLayer objects and are subject to operations inside SKModel, where data is transformed and propagated through the model.

3.2.5 Models

The basic structure of a model is depicted in Fig. 3.24. The structure objects (neurons, layers, weights, moments, and gradients) are initialized and passed to the SKModel class. This class performs the data processing by calling the SKPropagator class, which moves data from the input layer to the output layer, using matrix operations with the weights stored in the SKWeight objects. The SKModel class includes a Backpropagation algorithm, that performs the gradient calculation and updates every weight according to some algorithm that

has to be chosen by the user (Adam or stochastic gradient descent). Once the training is finished, the calculated weights are stored in .txt files with an appropriate naming scheme that allows the tracing of each model training result. This text file can be loaded by a model to be used for later calculations. A detailed explanation of the code, with the different configuration options, compilation procedure, and other technical details can be found in Appendix C.

3.3 Simulations

In this section, the procedures utilized to simulate the reaction channels under investigation in this thesis work are outlined. These simulations serve the dual purpose of being compared with the physical results obtained through analysis procedures and facilitating the development of analysis methods that depend on simulated data inputs.

3.3.1 Generation of Incoming Particles

It is clear that for an accurate simulation of a spallation or a knockout process, the generated light-primary particles that are scattered must have the proper kinematical distributions, that can be used to obtain angular correlations and energy distributions or be used to calculate the excitation energy of the fragment and compare with experimental data. Two coupled libraries will be used for this event generation: INCL and ABLA07.

INCL (Liége Intranuclear Cascade) [61, 62, 63, 64], is an intranuclear cascade code developed for the modelization of nuclear collisions with light particles (n,p,π...) at relativistic energies, from dozens of MeV to several GeVs. For every generated event, the nucleon is fired into the target with a random impact parameter, from 0 to the sum of the two radii. Every collision inside the nucleus is modeled then as a consecutive series of binary collisions, that follow straight lines. Every nucleon is under the influence of a central potential. Some additions to this classical picture were added to account for the quantum nature of the nucleus, for example, realistic density profiles, Fermi motion of the nucleons inside the target or Pauli blocking that is applied after a collision. When the cascade stops, the ion is left with a certain excitation energy, that is taken as an input by the coupled de-excitation model. For the present case, protons and neutrons resulting from the knockout process are generated at this stage. INCL can be also included as a Geant4 library, for modeling the nuclear reactions that can occur inside active materials.

ABLA07 [65] is a statistical de-excitation code that models the decay of a nuclear system, with predefined angular momentum and excitation energy. This de-excitation process can follow two paths: the emission (evaporation) of particles, such as nucleons, γ-rays, intermediate-mass fragments, and fission decay. This final part of the reaction modelization provides the final fragment masses and charges that are used in this work to calculate cross-sections for the knockout-fission and knockout-evaporation case.

After this two-stage calculation of the different reaction channels, the output of these two frameworks is stored in a ROOT file that serves as an input for the simulation.

3.3.2 Detector Layout

The simulation of the different reaction channels consisted of two key components: the input containing the primary particle information and the realistic simulation of the different detectors and passive materials that were relevant to the experimental analysis performed in this work. Input particles and ions were generated by INCL and ABLA07, and these primary tracks were propagated through the simulated setup. At this point, the realistic simulation of the detector's response allowed for an accurate comparison with the real experimental setup. Every one of these detector subsystems (the reaction chamber, AMS, and CALIFA) included not only the active parts but also all passive parts (wrappings or holders, for instance) that were relevant to reproduce the data obtained in the experiment.

The reaction chamber geometry, based on CAD designs, was placed surrounding the reaction target. The AMS-target system was added inside this reaction chamber, and properly aligned. Finally, the CALIFA detector enclosed these two systems. Every detector was aligned in a precise way, with the AMS measurements taken at Cave C as a reference.

The reaction vertex of particles generated for each simulated event was randomized inside the target region, following a 2D-Gaussian distribution in the XY plane, with a 21 mm width (FWHM). This was the observed beam spot size during the experiment. For the Z axis, the reaction point was uniformly randomized in the interval $Z \in (-7{,}5, 7{,}5)$ mm (the target width), choosing the center of the target as the reference point.

3.3.2.1 CALIFA

The experimental geometry of CALIFA was used for this simulation, with the proper alignment and aperture between halves, as measured after the experiment. This geometry included

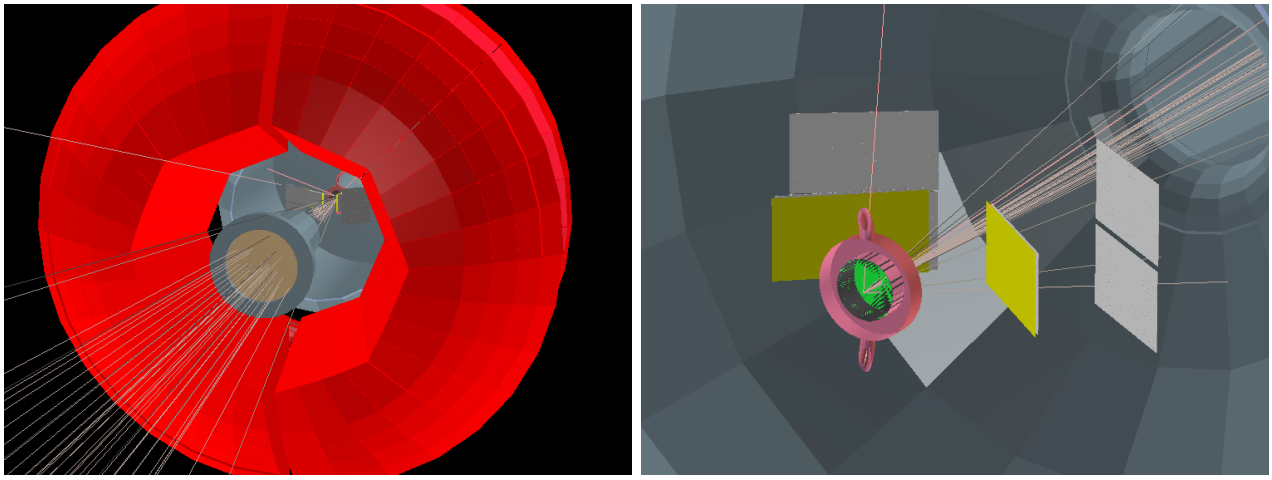

(a) Overview of the simulation. Straight lines correspond to the different generated particles.

(b) Close view of the target, the AMS system, and the gold foils. The target holder was removed for better visibility.

Figure 3.25: Simulated setup.

the full iPhos and half of the barrel, up to 88° in polar angle. Every non-working crystal was included in the geometry, but they were removed from the digitizer, so the active material was present but no hit could be reconstructed from that detection unit.

Regarding the detector response, experimental resolution and thresholds for every crystal were applied as obtained in the calibration procedure (see Chapter 5). The clustering task was configured with the same parameters as in the experimental analysis discussed in the next chapter.

3.3.2.2 AMS

This detector geometry was modified from the nominal one by using the alignment obtained with the laser scan procedure explained in Chapter 5. This method allowed to place every detector in the right place with respect to the others and also with respect to the target position. The gold foil was added with the same width as in the experimental case.

Data Analysis

In this chapter, the procedures for transforming the raw data coming out from detectors into physical observables are described. Given the complexity of the analysis, the calibration of the different detectors was divided between the students analyzing the experiment. The results of the calibration procedure were then shared at a later stage, ensuring a better debugging and quality assessment of the parameters. A. Graña-González performed the tracking, TWIN MUSIC, and NeuLAND detector calibration, while the pedestal subtraction for AMS detectors, the CALIFA calibration, and the TWIN MUSIC calibration for heavy residues were part of this work. The procedures explained within this section go from calibrations and alignments to reconstruction procedures for the different detectors around the reaction target.

4.1 AMS Alignment

Once installed on their holder, the AMS detectors were placed inside the vacuum chamber along with the LH_2 target, which was mounted together with its cooling system. This target-tracker system was carefully installed. However, for a proper reaction vertex reconstruction, precise measurements of the real detector positions were carried out after the experiment, when the vacuum chamber was opened again. These measurements were performed by an external company, Sigma 3D [66].

The procedure consisted of a laser scan of the target region, as displayed in Fig. 4.1. This scanned map was saved as a STEP file, that could be opened at the same time as the reference model of the target area. By matching the scanned model with the reference model, the latter was used to get the real positions of the AMS detectors in a precise way.

After rotating and translating every single AMS reference detector until they matched the

AMS	Distance (S)	Distance (R)	Offset (S)	Offset (R)	Angle (S)	Angle (R)
1	67,91	55,76	0,45	0	-42,27	-45,0
2	129,85	106,3	21,59	21,18	-36,67	-45,0
3	129,28	106,3	-20,73	-21,18	-36,78	-45,0
4	71,28	55,76	-0,04	0	40,08	45,0
5	122,48	106,3	21,93	21,18	34,52	45,0
6	124,66	106,3	-19,40	-21,18	34,30	45,0

Table 4.1: AMS measurements obtained with the STEP models. The units are degrees and mm. The enclosed letter indicates the measured value with the scan procedure (S) and the nominal, reference value before the experiment (R).

measured experimental disposition, the required geometrical parameters for the AMS target reconstruction procedure were obtained. Those parameters are the distance of each AMS detector face with respect to the target center, located at (0, 0, 7,5) (mm, cave coordinates), the Y offset, and the polar angle of each detection unit with respect to the beam line. The result of these calculations, together with the nominal positions are shown in Table 4.1.

These values were used by the reconstruction software to provide angular information on the detected particles. The clustering method groups several adjacent strips with signal into a cluster, and transforms the local coordinates of this cluster into LAB coordinates. This procedure will be explained in more detail in Section 4.6.

4.2 Calibrations

The performed calibrations for the CALIFA detector, the AMS detectors and the TWIN MUSIC calibration for heavy fragments are presented here.

4.2.1 CALIFA Calibration

Several gamma source measurements were taken before and after the experiment. In this section, the automated energy calibration procedure for the CALIFA crystals is explained, which will allow to obtain the energy of the scattered nucleons after the reaction.

CALIFA crystals are suited for both proton and gamma-ray detection, as described in Chapter 3. The proton energies coming out from a typical R3B experiment can vary from

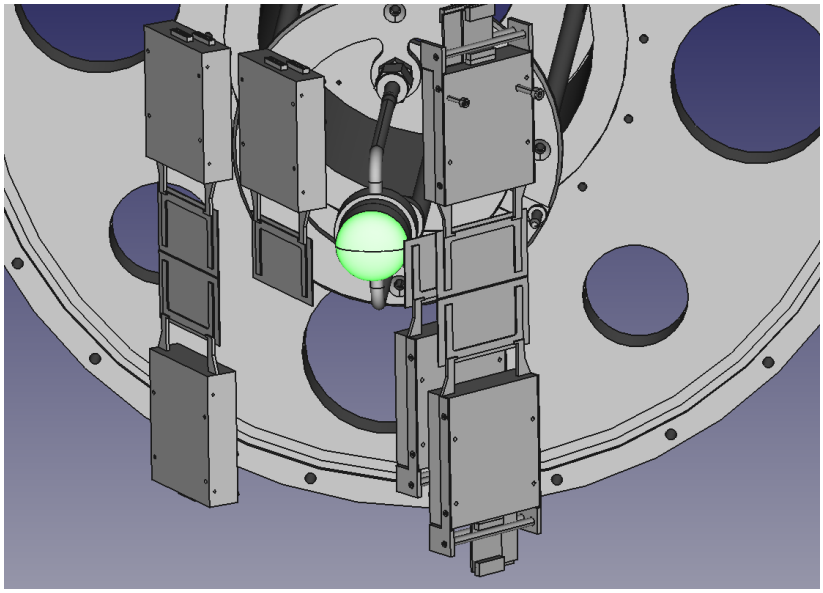

(a)

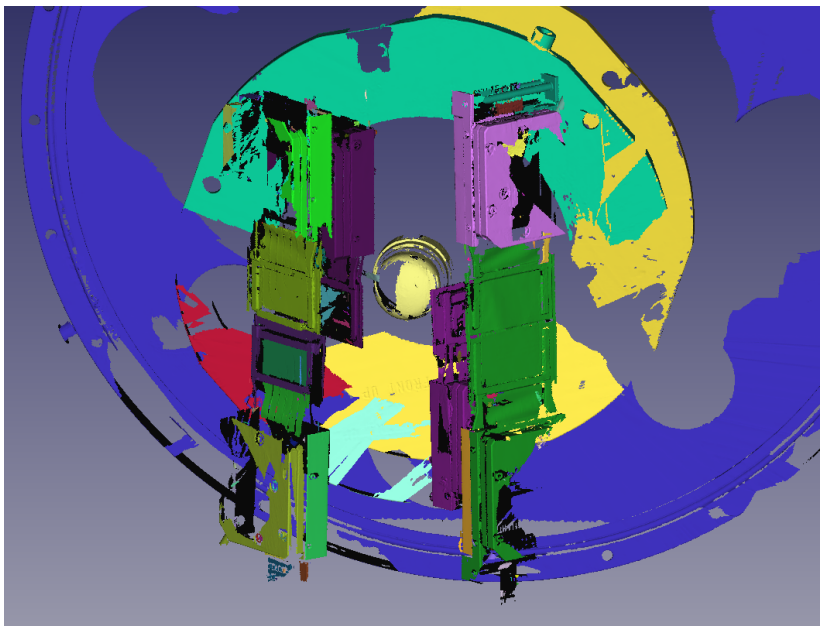

(b)

Figure 4.1: a) Reference STEP model for the target area region. The target itself is highlighted in green. b) Scanned model provided by the company. Missing parts of the setup correspond to those regions that were difficult to scan in a proper way, for example, corners and reflective surfaces.

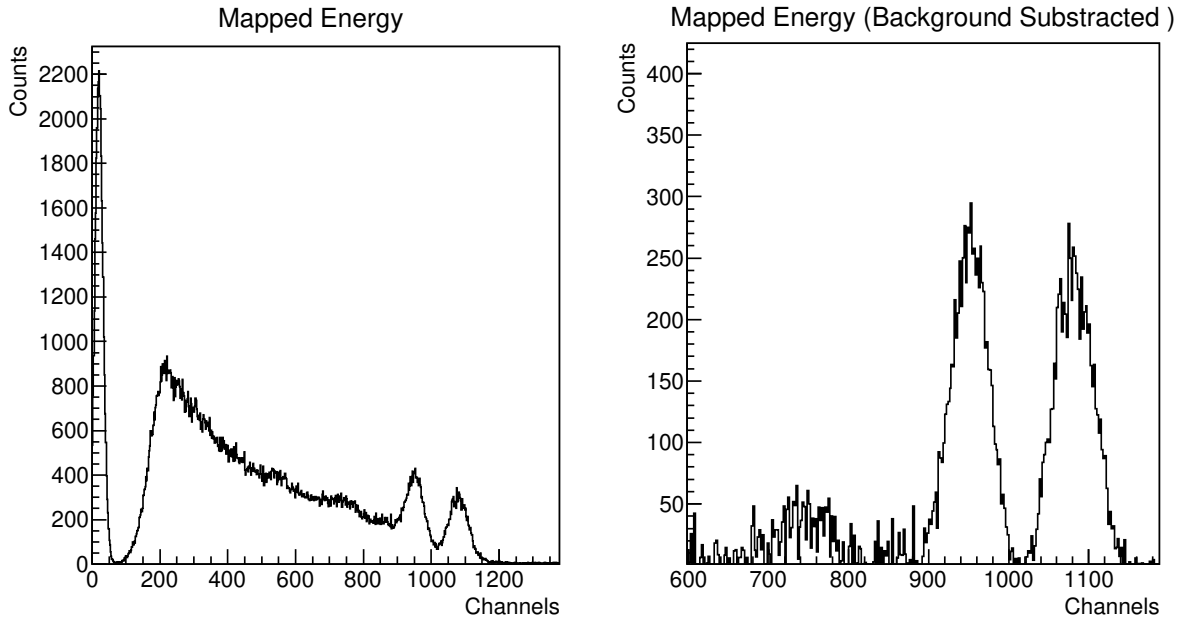

Figure 4.2: Gamma spectrum before calibration for a high-gain set crystal. Displayed units are preamplifier channels. ***Left:*** *Before background subtraction.* ***Right:*** *After background subtraction. See the text for an explanation.*

a few tens of MeV to 1 GeV (although the longest crystals in CALIFA can only stop up to 320 MeV). These high-energetic particles have to be detected in coincidence with gamma rays, so the extrapolation of gamma source calibration was the applied method. The validity of this approach was addressed in [67] by B. Pietras et al, where they demonstrated the linear behavior of the light output for CALIFA crystals and the validity of the gamma-ray calibration by the irradiation of CALIFA crystals with protons up to 200 MeV. As a result, they concluded that the gamma-ray calibration was still valid for high-energy particles, as the residuals for 200 MeV protons were always smaller than 3 MeV and centered at zero. So for this experiment analysis, a careful gamma-ray calibration was performed and used for reconstructing the energies of the scattered protons.

The ^{60}Co source was mounted on one side of the reaction chamber and moved from one side to the other periodically, so both halves were sufficiently irradiated.

The resulting files from calibration runs are LMD (list mode data) files containing raw data. This data is then processed using the unpackers and the calibration class, which performs a three-step parameter finding: First, a histogram is defined for each CALIFA crystal.

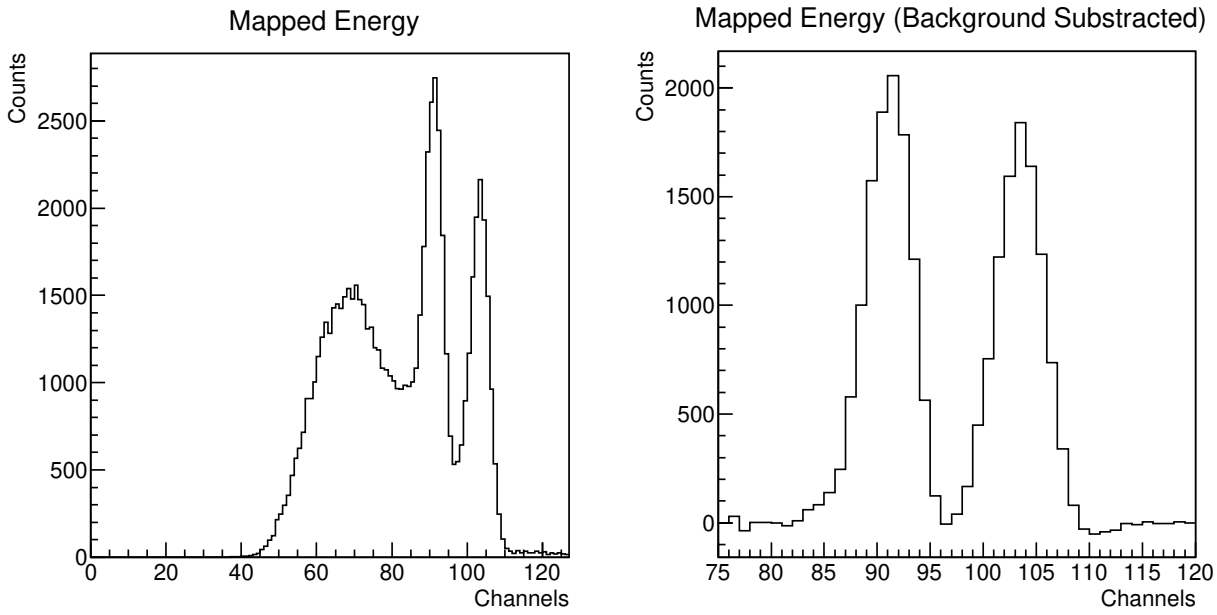

Figure 4.3: Gamma spectrum before calibration for a low-gain set crystal. Displayed units are preamplifier channels. ***Left:*** *Before background subtraction.* ***Right:*** *After background subtraction. See the text for an explanation.*

These histograms have different ranges depending on the gain setting (iPhos part was double read, while the barrel part operated with a mixed configuration, as explained earlier). Once all data are recorded and the histograms are filled, the background is characterized and removed using the TSpectrum method from ROOT. The result of this subtraction is displayed in Figs 4.2 and 4.3 for both ranges. The peaks are then fitted to two Gaussian distributions in a two-step process: first a rough fit is done by searching for peaks in the histograms, and then a second Gaussian fit is performed using a fit window of $\pm 2\sigma$ obtained from the first fit. The channel window for the peak search and the relative amplitude for each peak can be adjusted by the user before the calibration starts. The mean of the Gaussian distributions is obtained and used, together with the nominal energies of the gamma source, for obtaining the calibration parameters.

Two parameters are obtained from this fit, so a linear calibration can be performed as

$$E_{Calibrated} = m\ E_{Raw} + n. \tag{4.1}$$

The obtained energy resolution can be characterized as a Full Width at Half Maximum

(FWHM) measurement:

$$R = \frac{\sqrt{2\ln 2}\sigma}{\mu} = \frac{\text{FWHM}}{\mu}, \tag{4.2}$$

with σ and μ obtained from a Gaussian fit of the photopeak. This resolution can be escalated as stated in [68], if the broadening of the peak is considered to be proportional only to the square root of the photon energy:

$$R(E) = \frac{\text{FWHM}}{E} = \frac{A}{\sqrt{E}}. \tag{4.3}$$

This procedure is used as explained in Sec. 3.2.2.2 for computing each CALIFA crystal's expected resolution at 1 MeV and then using it for realistic simulations.

The obtained energy resolution for the calorimeter is shown in Fig. 4.4. The mean value of this resolution is 5,09 % at 1 MeV (5,03 % for gamma range crystals and 5,25 % for proton range crystals), very close to what was expected in the CALIFA Technical Report [41]. However, the detectors placed at the very end of the calorimeter showed poor performance in terms of resolution. The preamps and APDs attached to those crystals were checked carefully in the summer of 2023, and their performance was improved by checking the APD connections and adding some extra grounding.

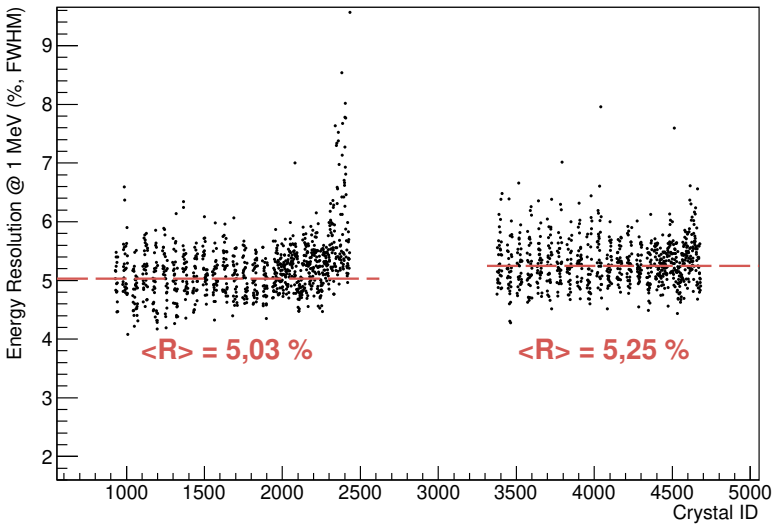

Figure 4.4: Overall resolution after calibration. Crystal ID numbers separate proton ranges (ID > 2432) from gamma ranged (ID <= 2432) crystals.

The energy residuals for the high energy peak of the ^{60}Co calibration, defined as μ − 1332,492 keV, being μ the mean of the Gaussian fit for each crystal, for the second peak,

are represented in Fig. 4.5. For the gamma-ranged crystals, the offset is placed at -1,19

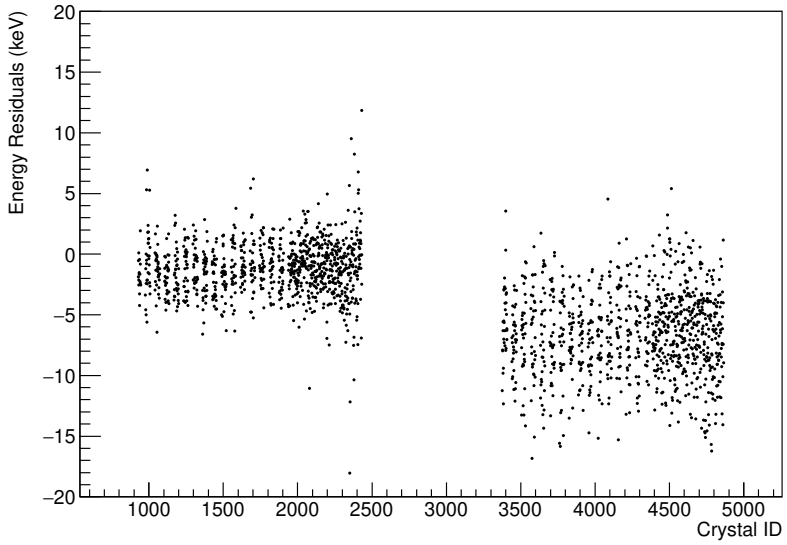

Figure 4.5: Energy residuals after calibration for the second peak of ^{60}Co. The plot is divided into two regions, high-gain crystals having a Crystal ID bigger than 2432, and low-gain crystals having a Crystal ID lower than 2432.

keV, while the standard deviation of the distribution is 2,3 keV. As it can be noted, the proton-ranged crystals have more spread in energy with a standard deviation of 3,46 keV and an offset of -6,55 keV with respect to the 0 line. The linear calibration was performed by fitting the two peaks of ^{60}Co, so it makes no sense that the offset is displaced from the 0 line. An explanation is that the files that were used for calibration were not exactly the same as the ones used for these resolution studies, so little changes in gain due to temperature flow could affect the position of the peaks. However, CALIFA crystals are monitored and a temperature correction is continuously applied. So this difference could come from different natural background or electronic noise, that causes a change of the background distribution to be removed from the spectrum.

4.2.2 AMS Pedestal Substraction

With a silicon thickness of 0,3 mm, the energy deposited in an AMS detector by a proton of 100 MeV calculated with ATIMA [69] is $\sim$ 400 keV, which decreases to $\sim$ 200 keV for 300 MeV protons. These small differences in the deposited energy, despite the wide energy range of the impinging particles and the fact that there are no calibration sources that can emit energies

as high as hundreds of MeVs, do not allow energy spectroscopy measurements with these AMS detectors. However, the goal of the silicon tracker was not to reconstruct the energy of the protons but to accurately determine the angles of each scattered particle. In this case, only the pedestals of each strip have to be removed, in order to have a valid signal, compatible with a detected reaction product valid to generate a cluster in the detector. Pedestal data acquired at the beginning of the experience was used. For each strip, the measured energy follows a Gaussian distribution that is fitted by the calibration class, which generates at the end of the run a calibration parameter container with the mean and the standard deviation of each pedestal distribution for each strip.

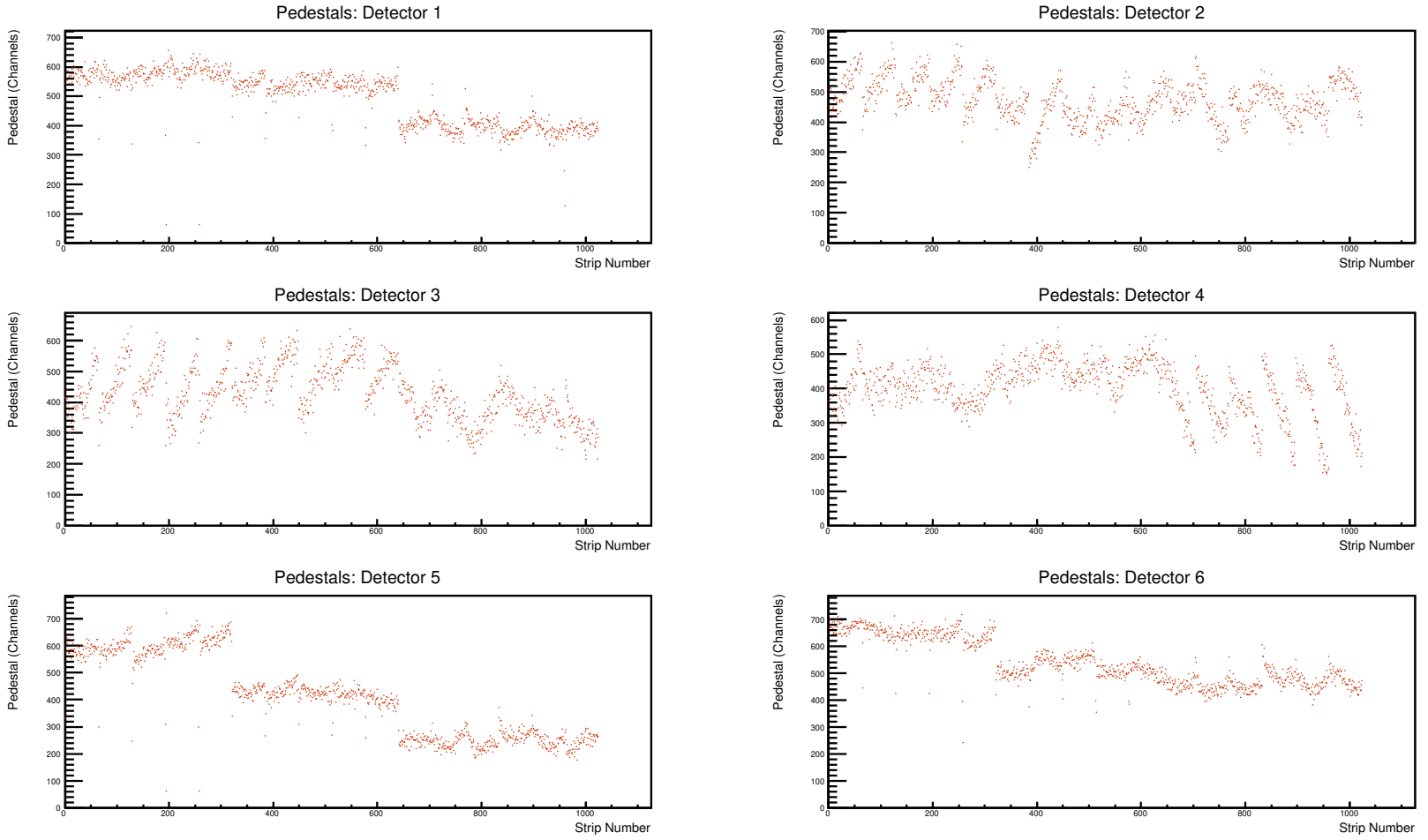

Figure 4.6: Obtained pedestals for the six AMS detectors. Strips from the K and S sides are shown at the same time, with the S side going from strips 1 to 640 and the K side going from strips 641 to 1024.

The obtained pedestals, defined as the mean of the distributions, are shown in Fig. 4.6. The strips for the S and K faces are presented in the same histograms. The saw-like spectrum corresponds to groups of 64 strips being read by different ASIC chips and jumps between S and K faces can be associated with each face being connected to different ADC units.

For obtaining the correct signal on each strip, the task that converts AMS-mapped data into calibrated data subtracts the pedestal value for each strip signal:

$$E = E_{Raw} - E_{Ped} - n\sigma_{Ped}, \tag{4.4}$$

where E_{Raw} is the raw signal stored in the map level, E_{Ped} and σ_{Ped} are the mean and sigma of the strip pedestal distribution, and n is a value set by the user. If this energy value is negative, a zero value is stored instead. For this work, a value of 3σ was used.

4.2.3 TWIN MUSIC Calibration for Heavy Fragments

The charge of the outgoing heavy-spallation residues has to be determined after the reaction occurs. Although the TWIN MUSIC detector was set up and calibrated for medium-charge fragments produced after a fission reaction, it will be shown that a heavy charge could be still reconstructed with less resolution using the calibration procedure presented here. The first step in this reconstruction procedure was to select heavy nuclei travelling through the detector, by choosing only beam events. The energy lost by the incoming heavy ion was collected at the 16 channels of each section of the detector and then aligned. Then, the mean energy of each section was evaluated as the sum of all anode's energies, these energies being the total charge collected by each anode after the electron drift process. This quantity is read at calibrated level, where the pedestals are already subtracted from the mapped level energy. This energy sum was then divided by the number of anodes with signal in the same section. The obtained distribution for each section is displayed in Fig. 4.7.

The next step was to reconstruct the path of the heavy fragment crossing through the gaseous volume. If the fragment was close to the central cathode then the ionized electrons would take longer to drift into the frish grids. Therefore, a correlation between drift time and position at each anode location in the horizontal plane (x-axis in the Cave reference frame) is expected and a calibration can be obtained.

Only events where both the MWPC1 and MWPC2 recorded a single hit in coincidence with a heavy fragment crossing the TWIN MUSIC were chosen. From the MWPCs installed

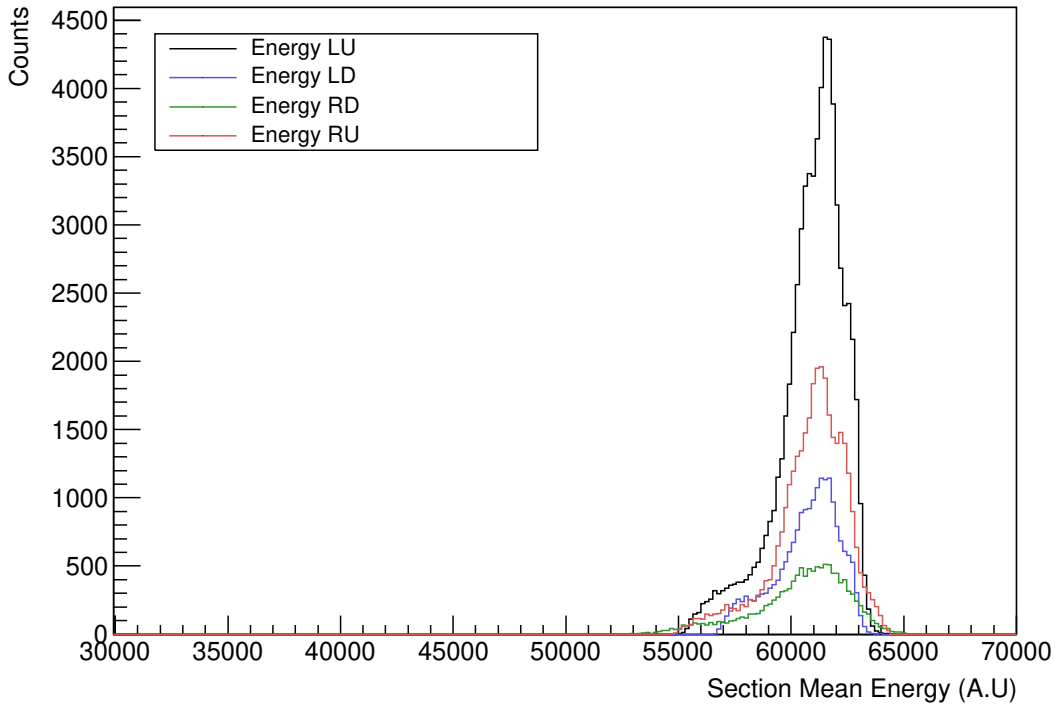

Figure 4.7: Energy reconstructed on each section, calculated as the mean, aligned energy of the 16 anodes of each section. LU, LD, RD, and RU stand for Left Up, Left Down, Right Down, and Right Up sections. The beam spot in this run was slightly shifted to the left and upper part of the detector, so more events are registered in the LU part.

in the beamline, a 3D position could be obtained, so the drift time for each anode could be correlated with the reconstructed position from the MWPCs.

For each anode, the correlation of drift time and reconstructed position can be fitted to a first-order polynomial. The resulting parameters were then used for reconstructing the path of the heavy fragments. Fig. 4.8 shows the result of this procedure.

For a better separation of the different charges, a correlation of the aligned energy versus the mean position with respect to the central cathode was carried out. By fitting the central branches of this distribution (Fig. 4.9) using a 4th-order polynomial function, the corrected energy can be obtained as:

$$E_c = \frac{a_0 E}{f(E)}, \quad \text{with} \quad f = a_0 + a_1 x + a_2 x^2 + a_3 x^3 + a_4 x^4. \tag{4.5}$$

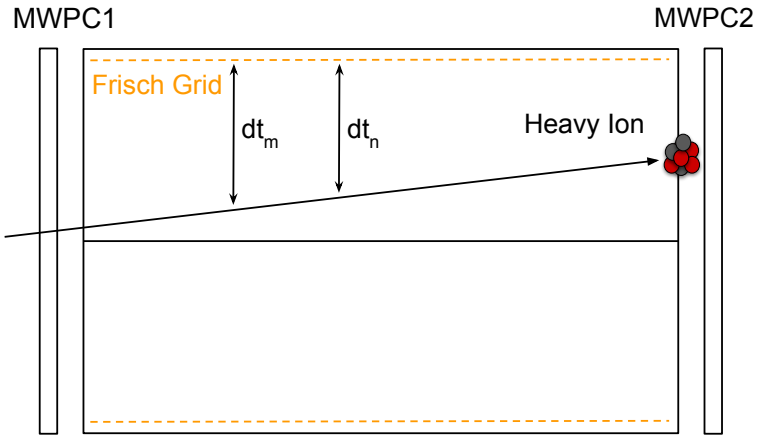

(a) Reconstruction scheme of the heavy ion trajectory. Drift times on different anodes are used to build the path of the particle.

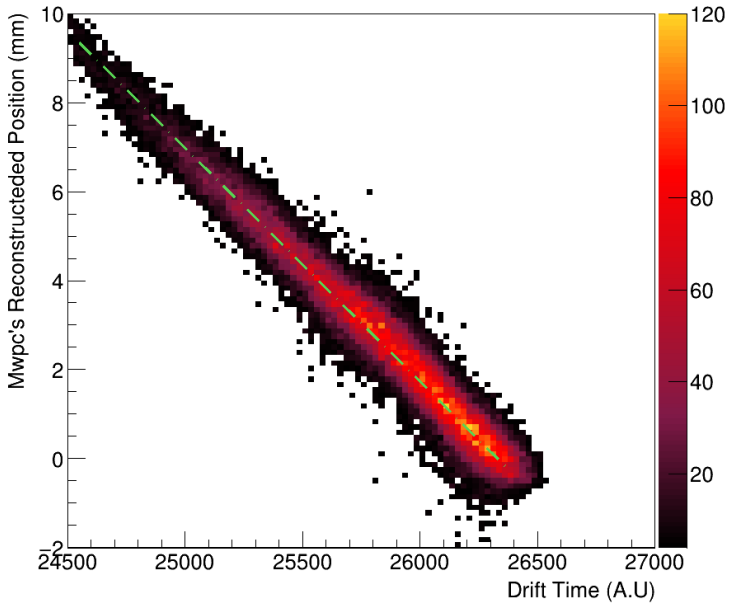

(b) Drift time correlation with position.

Figure 4.8: ***a:*** *Scheme of the position calibration procedure. The angle of the heavy fragment was exaggerated for better visualization.* ***b:*** *Correlation between the reconstructed position by the MWPCs vs drift time for anode 5, section 1. The distribution was fitted to a first-order polynomial.*

The result of this correction is represented in the right part of Fig. 4.9. A simple projection allows to determine the charge distribution of the incoming beam. Three peaks, instead of the expected Z=92 distribution were found. The guess was that this corresponded to different

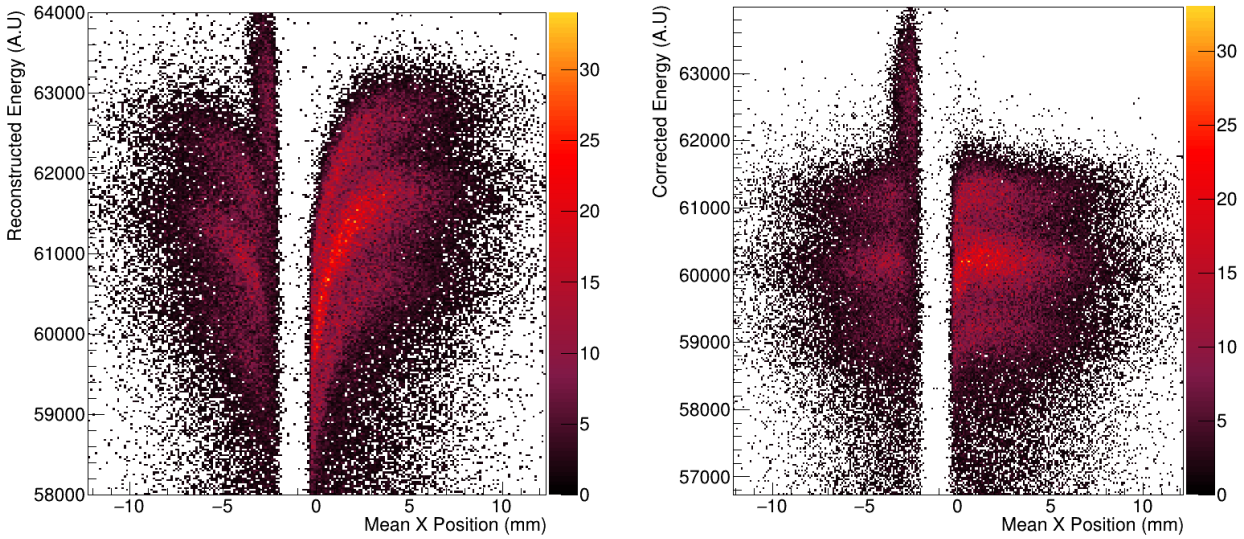

Figure 4.9: Aligned energy of the TWIN anodes vs mean X position with respect to the central cathode. ***Left****: before correction.* ***Right****: after applying the correction. The small distribution at energies around 62000 units on the negative x side corresponds to reactions in the central cathode. The gap corresponding to the central cathode is not centered at 0 due to some misalignments between the TWIN MUSIC and the MWPCs.*

charge states of the incoming beam, as it traveled through the different materials and picked up some electrons. Appendix D gathers the list of the present materials from the Cave C entrance up to the detector. To cross-check this hypothesis, a thorough study was performed by using CHARGE software [70]. A Z=92^{0+} charge was propagated through the different layers of material that were present at Cave C. At the exit of each material, the probability of having different charge states was evaluated, and this was repeated up to the middle point of the TWIN MUSIC detector. A proportion of 34 %, 48,49 %, and 17,15 % was obtained for the 0^+, 1^+ and 2^+ states, respectively. From the experimental data, displayed in Fig. 4.10, these ratios can be calculated by fitting the three distributions and the background, obtaining values of 30,59 %, 46,27 %, and 23,14 % for the 0^+, 1^+, and 2^+ states. As the proportions of the three distributions are well described assuming charge states, the spallation-evaporation residues will be corrected using the same prescription in order to calculate experimental cross-sections. The difference between the experimental distribution shown here and the model calculation will be used later to estimate the uncertainty coming from this correction.

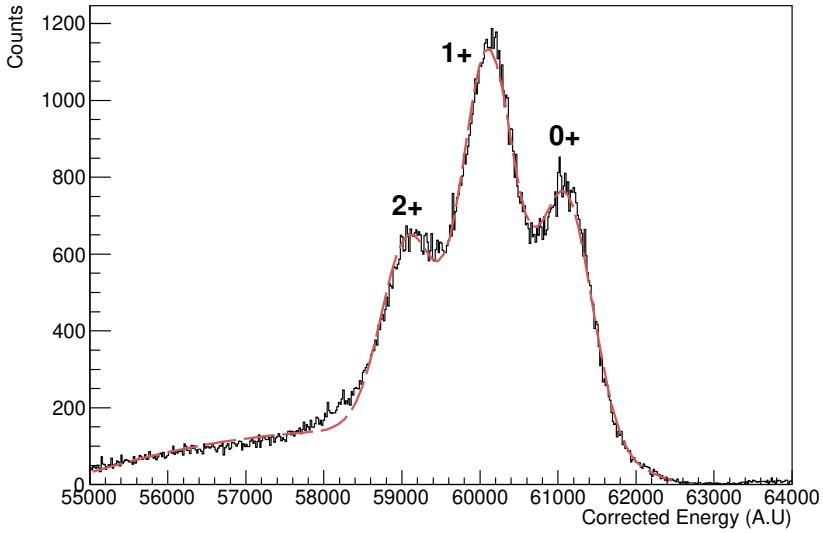

Figure 4.10: Beam charge states for the incoming beam. The nomenclature in this figure follows the convention of 0^+ for naked ions, 1^+ for one-electron pickup and 2^+ for two-electron pickup.

4.3 Event Selection: Spallation-Evaporation Channel

In the present section, the event selection for the spallation-evaporation channel is presented. For this reaction, an incoming nucleus is detected in coincidence with two or more nucleons at the CALIFA calorimeter. Those nucleons come from knockout reactions that remove a variable number of nucleons from ^{238}U, which results in different charges measured at the TWIN MUSIC. After the knockout processes, a heavy fragment is expected to hit the TofWall detector together with some evaporation neutrons that may produce signals in NeuLAND, if the excitation energy of the remnant after the nucleon removal is larger than the separation energy for neutrons.

4.3.1 Trigger Pattern Matrix and TPat Selection

The Trigger Pattern (TPat from now on) value is a binary number associated with every single event recorded by the R3B DAQ that was correctly time-correlated and stored.
A trigger is defined as a good set of detector signals that conforms a suitable physics-like event of interest for the experiment. When the central trigger logic (TRLOII) receives good detector information, the master start signal is sent and the detector data is recorded. Those

different events are then marked with the TPat number, which is different depending on which detectors are fired. The different conditions that a TPat must fulfill are summarized in Table 4.2. The meaning of each condition is:

TPat \ Required Signals	START	FISSION	CALIFA AND	CALIFA OR	AMS Alive	AMS Dead	NeuLAND
1	✓				✓		
2	✓	✓			✓		
3	✓		✓		✓		
4	✓	✓	✓		✓		
5	✓			✓	✓		
6	✓	✓		✓	✓		
7	✓					✓	
8	✓	✓				✓	
9	✓		✓			✓	
10	✓	✓	✓			✓	
11	✓			✓		✓	
12	✓	✓		✓		✓	
13				✓			
14							✓

Table 4.2: TPat matrix for experiment s455. TPats from 1 to 12 corresponded to onspill events and therefore required a valid start signal. This values are divided into two blocks due to the high deadtime of AMS. TPats 13 and 14 were set for offspill data taking, mainly aimed for cosmic calibrations.

- **START:** A signal in the plastic scintillator located before the target. This signal is associated with an incoming nucleus.
- **FISSION:** Two signals in two plastics of the TofWall detector. Those signals are a clear feature of a fission-like event.
- **CALIFA AND:** Two high-energy hits on each CALIFA half. The definition of a high-energy hit was implemented in the CALIFA DAQ as 2000 Ch, corresponding to 20 MeV for crystals in proton range behind AMS coverage.

- **CALIFA OR:** One high-energy hit on one CALIFA half.
- **AMS Alive:** When AMS is ready to take data.
- **AMS Dead:** When AMS is not ready to take data and is on deadtime.
- **NeuLAND:** A signal on a NeuLAND plastic.

Some of these signals are exclusive: for example, an event can not be marked at the same time with AMS alive and AMS dead, although a CALIFA AND can be measured as two CALIFA OR signals.

For the present reaction channel, a selection of TPat 3 or TPat 9 was required to reconstruct the reaction observables, for an incoming nucleus and at least two nucleons detected in CALIFA. However, due to the low CALIFA detection efficiency for measuring two simultaneous nucleons, TPats 5 and 11 were used for event counting and cross-section calculation. This will be discussed in depth in Section 4.5.4.2.

4.3.2 Cluster Selection in CALIFA

The energy deposition of a high-energy particle in CALIFA is normally spread to several detection units. It is then necessary to gather the information in a cluster object. After a proper calibration of the detector, the single-crystal calibrated energy was transformed into cluster information by using the clustering task explained in Section 3.2.2.3. Taking into account the simulations performed using INCL and a realistic configuration of CALIFA, the minimum energy deposited in the detector by a nucleon after a knockout from ^{238}U should be at least 50 MeV [1]. This minimum required energy includes the possibility of fully-stopped protons, punch-through protons, or neutrons. This previous cut was coherently used in the efficiency calculation of CALIFA for the different reaction channels.

With these considerations, the clustering task was configurated as follows:

- Proton cluster threshold: 40 MeV (every particle exceeding this energy is considered to be a proton)
- Gamma cluster threshold: 2 MeV (every particle exceeding this energy is considered to be a gamma ray)

[1] Except for the rare cases where a proton hits just one edge of the most forward crystals and leaves only a small amount of energy.

- Crystal threshold: 800 keV (the minimum energy of a crystal to be included in a cluster)
- Angular window for the acceptance of crystals inside a cluster: 0,25 rad (14,32 °)

In this work, the gamma reconstruction was not considered. Therefore, high values for gamma cluster generation threshold and single crystal thresholds were used for those clustering parameters, to avoid processing all the reaction background. Regarding the angular window, several studies were carried out using different window types and sizes. While the use of a squared or rounded window did not affect sensibly the number of reconstructed clusters or the energy reconstructed, the use of a larger angular window caused more background to be included inside the cluster. Therefore, the 0.25 rad window was chosen.

The number of reconstructed clusters that met the previous conditions, for at least two nucleons detected the two CALIFA halves (TPats 4 and 10), was computed on an event-by-event basis, as displayed in Fig. 4.11. The most probable situation corresponds to the detection of two high-energy clusters, while the detection of 3 and 4 cluster events was much less probable. Those clusters could come from multi-nucleon knockout events, two nucleons that created more than two clusters, or any random hit, mainly cosmic rays, in coincidence with the reaction. It is also noticed that the distribution does not drop to zero (and even 10 high-energy clusters were detected for some events). This is caused by the presence of the START plastic scintillator located -98,75 cm before CALIFA. If a high-energy nucleon is emitted from that position after a reaction in the material, then the propagated trajectory could cross almost the entire detector, and since each cluster can only contain a limited amount of crystals inside the angular limits, more clusters are created in that case.

4.3.3 Heavy Fragment Charge Reconstruction

The TWIN calibration for heavy fragments explained before was used for the heavy fragment charge reconstruction. Since those events with pileups in the START scintillator were removed, only events with a single high-energy fragment travelling through the TWIN MUSIC were considered for this reaction channel. Those events were distinguished from the fission fragment range by their reconstructed energy, which was almost two times the deposited energy by fission fragments.

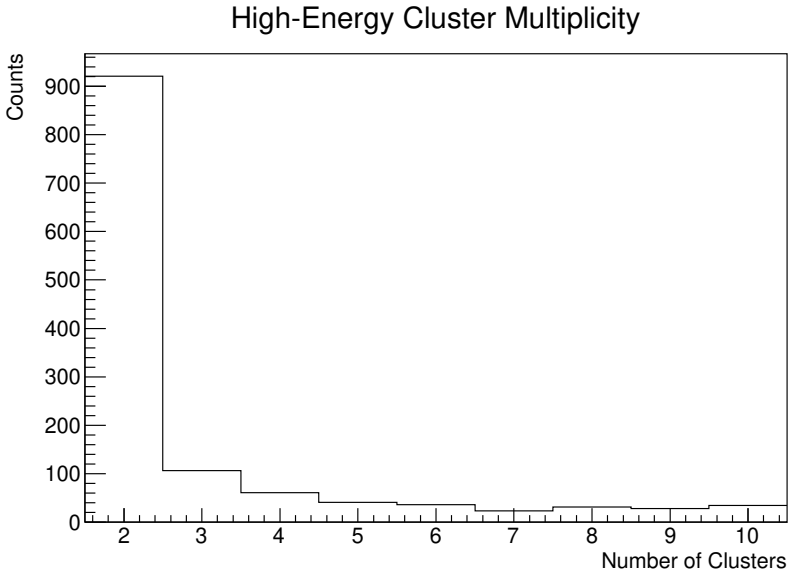

Figure 4.11: Cluster multiplicity per event in CALIFA, selecting a spallation channel together with a heavy fragment detected in the TWIN MUSIC.

4.4 Event Selection: Spallation-Fission Channel

The event selection for this reaction channel was quite similar to the previously explained method for spallation reactions. The signal signature of this reaction is the detection of two or more nucleons in CALIFA in coincidence with two fission fragments reconstructed by the TWIN MUSIC and at least two plastic signals in the ToF Wall at the end of the setup. The TPat values were therefore set to TPat=4 or TPat=10 for the reaction reconstruction. In this case, CALIFA efficiency was even lower than in the spallation-evaporation channel (See Section 4.5.5.1), so single nucleons were required in CALIFA for cross-section calculations (TPat 6 and 12). The cluster selection used for the fission case was the same as in the spallation channel, and the obtained multiplicity distribution is displayed in Fig. 4.12.

When the knockout process happens, the excitation energy given to the residual decides the survival probability of the heavy remnant. If this excitation energy is large enough, fission reactions are more probable than spallation-evaporation processes. This is reflected in the multiplicity distribution of high-energy clusters in CALIFA, where in this case the chances of having more than two detected nucleons are higher. Although the 3, 4 and 5 cluster events are more probable than in the spallation-evaporation case, the distribution quickly drops for multiplicities larger than 6, reflecting the fact that the nucleons are emitted from the target

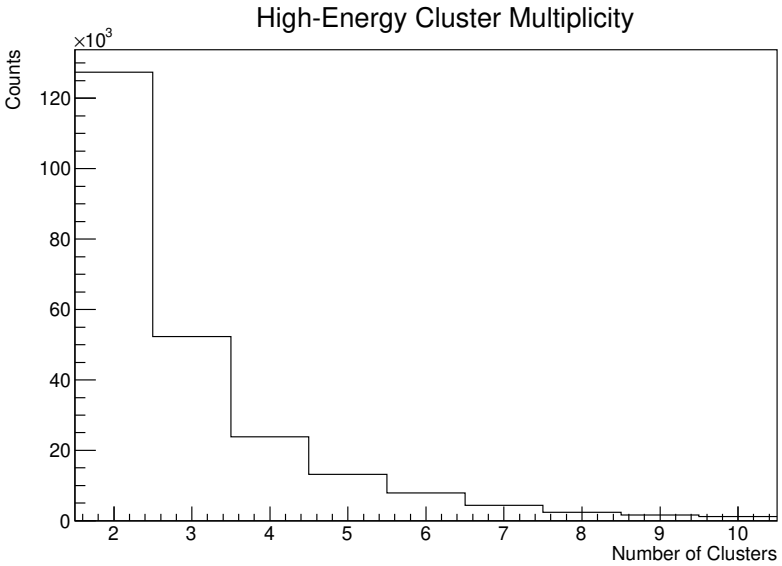

Figure 4.12: CALIFA high-energy cluster multiplicity for spallation-fission reactions, selecting two fission fragments in the TWIN MUSIC.

position.

4.4.1 Fission Fragment Charge Reconstruction

The specificity of the setup for fission studies made possible a high-resolution reconstruction of the fission fragment charges. This high resolution allowed to select univocally the charge of the fission system by adding the charges of the two fission fragments.

Although most fission reactions took place within the target volume, the presence of some materials before and after the LH_2 target resulted in some fission reactions that came from other locations of the setup. The TPat selection is not restrictive enough to isolate those reactions, and fission fragments produced in the scintillator created the valid signals for a fission-like event in the ToFWall detector. However, the high segmentation of the TWIN MUSIC detector allowed to perform a vertex reconstruction by propagating the trajectories of the two fission fragments. This procedure was used to disentangle fission events coming from different parts of the setup, as displayed in Fig. 4.13. This calculation shows that although the resolution was not very good, i.e. the 15 mm target is reconstructed as a 250 mm 2σ-width peak, the most prominent peak comes from target reactions and can be used for a correct event selection. This target peak is located at -1309 mm from the TWIN MUSIC entrance window. The second peak on the left corresponds to fission reactions in the

scintillator, located at -2367 mm. For selecting reactions in the target, a window of 480 mm around the centroid of the Gaussian fit to the target region (3σ) was used.

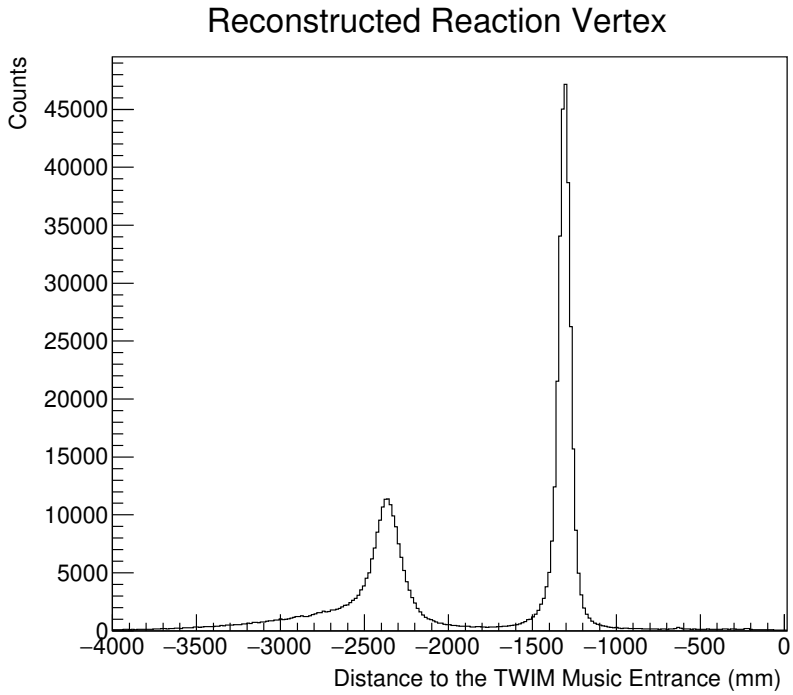

Figure 4.13: Reconstructed vertex for fission reactions. Each fragment trajectory was propagated as a straight line using every anode position and drift time information. The origin was set at the entrance of the detector, being the left part of the x-axis the one closest to the accelerator window, opposite to the beam direction.

4.5 Cross Sections

The number of recorded events belonging to a given nuclear reaction channel (N_r)depends on the number of incoming particles (N_i) that impinged onto the target, the number of dispersive centers (N_c) that the target contains, and the probability of having such a reaction (σ):

$$N_r = N_i \; \sigma \; N_c \; , \tag{4.6}$$

where this σ value is called *cross section* and is usually expressed in terms of multiples of a surface unit called *barn* ($1b = 10^{-28}$ m^2).

The number of dispersive centers for the LH_2 target was calculated as

$$N_c = 2\ \frac{\rho\ w\ N_A}{M} = 6{,}3490878 \cdot 10^{22}\ cm^{-2}, \tag{4.7}$$

with $\rho = 0{,}07085\ g/cm^3$ extracted from tabulated values [69], $w = 1{,}5\ cm$ the nominal width of the liquid hydrogen target, $M = 2{,}01568\ g/mol$ the molar mass of the LH_2 and N_A is Avogadro's number. The 2 factor comes from the fact that these values are tabulated for the molecular form of liquid hydrogen, composed of two H atoms.

Cross-section uncertainties were obtained by using a Monte Carlo approach. A variational analysis of the different observables and correction factors was performed, either by using experimental data or simulations. The obtained probability distributions for each term in the cross-section formula were used later to perform simulations of the measured cross-section, by getting random values of those probability distributions, and in this way taking into account the different correlations between observables and correction factors. The resulting mean and width of each cross-section distribution were used then to assign a final value and its associated uncertainty. This process is described in Appendix C.

4.5.1 Downscaling and Deadtime

There are some TPats that are more frequent than others: for example, a TPat 1 (START) was recorded more frequently than a TPat 4 (START + FISSION + CALIFA AND). In order to avoid the deadtime that those less interesting signals induced in the data taking, a reduction factor called *downscale* was set, so those signals were not always processed. For instance, if TPat 1 had a downscale factor of 10, then only 1 out of $2^{10} = 1024$ start signals (without any other required signal that would be included in other TPats) were processed. The downscaling factors, together with the deadtime information for the different triggers were calculated using the *scalers*. These scalers were recorded after each spill and 4 values were recorded for each TPat:

- Channel ID: From 1 to 16 for the different possible TPat values.
- Before DT: Number of counts for each channel at the end of the spill if deadtime was not considered.
- After DT: Number of counts for each channel at the end of the spill once the deadtime was applied.
- After DS: Reduced counts for each channel after the reduction factor was applied.

TPat	Downscale	Deadtime
1	1023,13 (1024)	0,27 %
2	127,98 (128)	0,23 %
3	31,99 (32)	0,68 %
4	1 (1)	2,91 %
5	127,99 (128)	0,45 %
6	31,99 (32)	0,49 %
7	1022,83 (1024)	39,07 %
8	32,00 (32)	43,16 %
9	15,99 (16)	46,89 %
10	1 (1)	55,59 %
11	31,98 (32)	44,80 %
12	7,99 (8)	45,90 %

Table 4.3: Downscaling factors and deadtime for each onspill TPat. The downscaling factor was rounded to the next power of two. Deadtime uncertainty was considered to be only statistical and was not included in this table.

In this way, the deadtime and dowscale factors were calculated as

$$\text{Deadtime (DT)} = \frac{\text{After DT}}{\text{Before DT}} \tag{4.8}$$

and

$$\text{Dowscale (DS)} = \frac{\text{After DS}}{\text{After DT}} \tag{4.9}$$

The obtained values for these two factors are summarized in Table 4.3. From the calculated factors it can be noted that the second TPat block (7-12) has a much higher dead time than the first one. This is a consequence of the artificially set condition of **AMS ALIVE** that forced every event with a busy AMS onto the second block.

4.5.2 Counting Incoming Particles

The TPat value is represented by a 16-bit number, each position denoting a different detector signal. For example,

$$\text{TPat } 4 = 0b1111 \ (0b0000000000001111). \tag{4.10}$$

If any of the signals that took part in the TPat was downscaled, the bit corresponding to that signal could appear as 0 and therefore these expressions for TPat 4, for example, would be still valid:

$$\text{TPat } 4 = 0b1000, 0b1010, 0b1001, 0b1100... \tag{4.11}$$

As a consequence, the number of starts had to be counted only if the first bit of the TPat value was set to 1. If that value appeared as 0, then the correction by the downscale factor of the corresponding TPat took this into account.

For a correct determination of a cross-section, only the number of incoming particles that truly arrive at the target must be counted. The presence of matter before the target produces a non-negligible number of reactions, mainly in the plastic scintillator, that have to be removed from the incoming count. The main reaction mechanism in this material is fission, as it was shown in Fig. 4.13. So for every incoming event with the first bit on, the reaction vertex was reconstructed, and reactions within the plastic scintillator were therefore not considered as incoming particles. The criteria for considering an event as scintillator fission is to have the reconstructed vertex inside a 3σ region around the mean of the peak.

Not only the fission events at the scintillator were removed from the count. Any other process that transformed the incoming particle in anything different than ^{238}U was taken into account using ATIMA[69] and the list of materials placed before the target. The obtained reaction probability of 7,5% allowed the correction of the number of incoming particles.

The presence of the so-called microspill structure caused that two or more incoming particles could arrive at the same time at the START scintillator. Those events were removed from the incoming count by selecting a unique signal in each one of the three scintillator photomultipliers (two physical signals plus one reference).

Considering these factors, the overall number of incoming particles was determined as:

$$N_i = (1 - 0{,}075) \sum_{j=1}^{12} \frac{n_j \; ds_j}{1 - dt_j}, \tag{4.12}$$

with n_j the number of valid starts inside TPat j and ds_j, dt_j the calculated downscaling and deadtime factors for that TPat.

4.5.3 CALIFA DAQ Efficiency Correction

During the experience, some DAQ issues were present for CALIFA. The cause of these problems is still unclear, but they can be sorted into two different categories:

- From time to time the acquisition of an entire CALIFA half was down. The shift crew had to restart the acquisition and the entire half took some minutes to recover. This failure can be easily observed and evaluated by just plotting some CALIFA observable evolution over time.
- For some events the timestamp was not correctly assigned and those events were discarded. This happened especially at the beginning of each spill, and more frequently with high beam intensities. The DAQ recovered itself without any action taken by the people on shift.

While the first case impact can be straightforward to quantify, the second one is not, and some fine analysis of data is required. For this purpose, a Poisson-based method for CALIFA was developed.

The basic assumption here is that if the beam has an approximated Poisson structure during the spill duration, then CALIFA should see high-energy hits that are correlated with the beam also following Poisson statistics. Restricting the measuring time to the onspill case, the time difference between beam events and CALIFA high-energy events can be studied, as shown in Figure 4.14.

The left part of the spectrum shown in this figure displays the expected exponential behavior for the beam events and the CALIFA events. However, some counts appear at the right part of the spectrum for CALIFA (Figure 4.15), far away from the Poisson-like time differences. This stretch in time can be caused for two reasons:

- The beam events did not come following a Poisson structure.
- The CALIFA DAQ was not properly working.

To account for these two possibilities, a properly working probability can be defined for each CALIFA half as

$$P(Alive) = \frac{t_{PC} - t_{NPC}}{t_{PB} - t_{NPB}} \tag{4.13}$$

where t_{PC} stands for the time where CALIFA measured events with a time difference compatible with the expected Poisson distribution, t_{NPC} stands for non-Poisson CALIFA time located at the right part of the plot, t_{PB} stands for Poisson beam time and t_{NPB} stands for

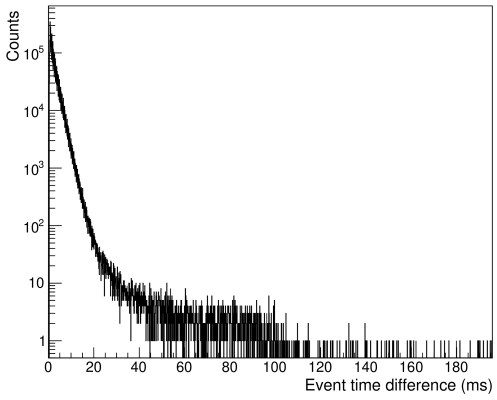

(a) Time difference for beam events.

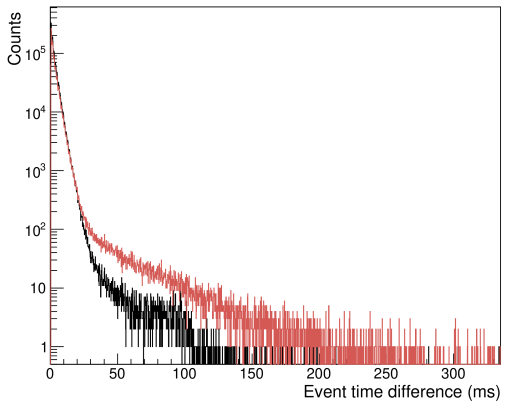

(b) Time difference for high-energy events recorded in the Messel half (red) and in the Wixhausen half (black).

Figure 4.14: Study of time differences for beam events (left) and CALIFA high-energy events (right). The Poisson mean of $\sim$ 10 *ms for the beam case is similar to the CALIFA case due to the downscaling factor applied to the only-beam events. The scale is zoomed near the Poisson region on the x-axis.*

non-Poisson beam time.

Each contribution (both inside and outside the Poisson region) can be computed by fitting the Poisson-time difference distribution to an exponential function on a logarithmic scale. The intersection point, where the counts on the y-axis reach the minimum integer, is marked by this extrapolated function intersecting the time axis. Each count at the left part of this intersection point adds its mean to the Poisson time, but each count on the right side adds its time difference with respect to the Poisson mean of the good events located at the left part of the distribution. Computing times in this way, the alive-half probability can be defined for each system:

- P(Poisson Beam): 97,59 ± 0,00001 %
- P(Alive Messel): 77,8163 ± 0,0006 %
- P(Alive Wixhausen): 90,4503 ± 0,0002 %

For recording a CALIFA AND trigger, the joint probability of having a properly working CALIFA, considering non-correlated DAQ failures, is

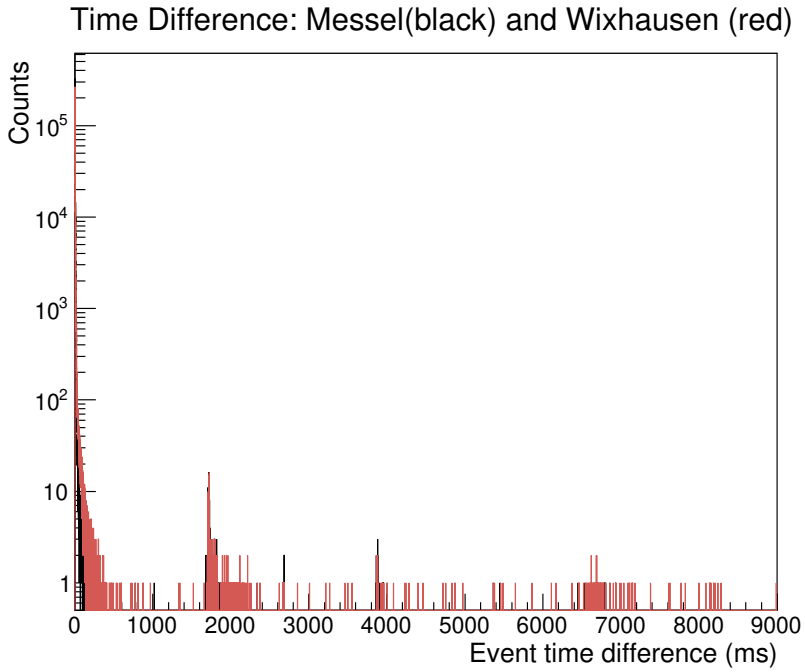

Figure 4.15: Non-Poisson distributed events for CALIFA.

- P(Working CALIFA) = P(Alive Messel) · P(Alive Wixhausen)

In the case of OR triggers, the total number of OR counts must be counted by using the mean probability of failure, assuming that both halves received the same number of projectiles for sufficiently large statistics:

$$N_{\text{OR (Corrected)}} = \frac{2N_{\text{OR (Measured)}}}{P(\text{Alive Messel}) + P(\text{Alive Wixhausen})} \tag{4.14}$$

4.5.4 Counting Reactions: Spallation-Evaporation Channel

4.5.4.1 Heavy Fragment Charge Fitting

For counting the number of isotopes that were produced for each final Z after a spallation process, the charge spectrum obtained using the TWIN MUSIC was fitted to several Gaussian distributions, as shown in Fig 4.16. The integral of each Gaussian distribution was computed as

$$I = \sqrt{2\pi}\ A\ \sigma, \tag{4.15}$$

with A and σ the amplitude and the standard deviation of each peak, respectively. This integral gives the total number of counts for each reconstructed charge peak, including all

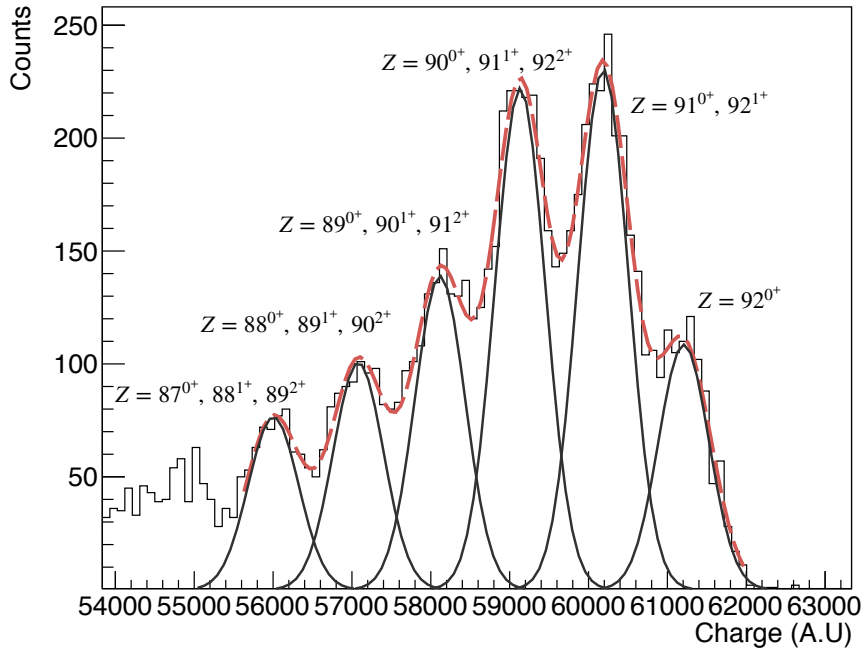

Figure 4.16: Charge reconstruction of the heavy fragments, as explained in Section 4.2.3. Charge states above 2+ are not probable and not labeled here, but are taken into account in further calculations. The reduced chi-square value for this fit is $\chi^2/\nu = 0{,}6358$.

the final masses and charge states. For calculating the amount of each isotope from this distribution, a coupled set of equations can be defined using probabilities obtained from CHARGE [70], propagating naked ions for each reaction product from the target position up to the TWIN MUSIC. The notation 0^+, 1^+ and 2^+ will be used to name ions with 0,1 and 2 captured electrons, respectively.

$$\begin{aligned} I_{92} &= N_{92}P_{92^{0+}} \\ I_{91} &= N_{91}P_{91^{0+}} + N_{92}P_{92^{1+}} \\ I_{90} &= N_{90}P_{90^{0+}} + N_{91}P_{91^{1+}} + N_{92}P_{92^{2+}} \\ I_{89} &= N_{89}P_{89^{0+}} + N_{90}P_{90^{1+}} + N_{91}P_{91^{2+}} + N_{92}P_{92^{3+}} \end{aligned} \tag{4.16}$$

where I_{92} denotes the integral at each charge position, N_{92} the number of residues with 92 protons, and $P_{92^{0+}}$ the calculated probability of having a uranium residue that picks zero electrons on its path up to the TWIN MUSIC from the target position.

4.5.4.2 CALIFA Efficiency

For detecting two high-energy protons in CALIFA, both particles must hit the part of the detector that was set to proton range. In addition, every loss in the detection efficiency due to non-working crystals, straggling, and energy loss in the materials surrounding the target area or losses in the reconstruction method have to be characterized.

The INCL simulation previously described in Chapter 3 was used to evaluate the detector efficiency for these spallation reactions. In this simulation, first the trigger condition was simulated: two single crystal hits above 20 MeV must be detected in the region of CALIFA covered by the AMS detectors and set to proton range. This condition corresponds to the AND requirement in CALIFA used in TPat 4 and 10. Then any other cluster could be recorded if this condition was first met. The two cluster condition was required with the same conditions as in the experimental configuration:

- Cluster energies must be above 50 MeV.
- Clusters must be detected in the CALIFA proton range region.

For every final fragment, from Z=89 to Z=92, the number of good CALIFA events was simply divided by the generated events, for each final system. Calculated efficiencies for this case are summarized in Table 4.4.

Final Fragment Z	CALIFA Efficiency
92	3,18 %
91	9,47 %
90	4,15 %
89	2,83 %

Table 4.4: Calculated CALIFA efficiencies for the spallation-evaporation channels, for the two nucleon detection case.

These low calculated efficiencies are translated into a large correction factor to the cross-section calculation. A small misalignment of the calorimeter, the inclusion of a crystal in the IPhos part that was not correctly working in the experiment, or a change in the angular limits of the proton or the AMS acceptance made the calculated value of efficiency change considerably, resulting in high uncertainty. This effect was even more pronounced for the spallation-fission efficiencies, as those values are smaller. Therefore, the condition of two

nucleons detected in CALIFA was substituted for one nucleon detected at CALIFA in coincidence with a heavy fragment in the TWIN MUSIC for cross-section calculations. In this way, the much larger efficiencies carry less uncertainty. Calculated values of these efficiencies are presented in Table 4.5.

Final Fragment Z	CALIFA Efficiency (BERT)	CALIFA Efficiency (INCL)
92	17,54 ± 0,13 %	16,00 ± 0,11 %
91	24,68 ± 0,18 %	23,86 ± 0,17 %
90	31,14 ± 0,36 %	30,37 ± 0,37 %
89	29,75 ± 0,43 %	28,87 ± 0,43 %

Table 4.5: Calculated CALIFA efficiencies for the spallation case, for the one nucleon detection condition.

Two different GEANT4 particle transport libraries were used: the Bertini cascade model (QGSP_BERT _EMV) and INCL (QGSP_INCLXX_EMV). As it can be noted, INCL systematically gives lower efficiency values than the Bertini model. This can be understood as a better treatment of nuclear reactions by INCL inside the crystal material, which results in more secondary neutrons emitted and therefore less number of recorded events surpassing the energy threshold. The difference in the two values given by the two libraries will be taken into account when calculating systematic uncertainties in the cross-section error estimation.

As expected, the Z=90 channel has the larger efficiency. Three nucleons are emitted from the target position in this case, which makes more probable the single detection condition. The Z=89 fragment is produced after the emission of 4 nucleons, but the shared angle between them is smaller than in the Z=90 case, and many of them escape through the most forward part of the detector. This situation is shown in Fig. 4.17, where an INCL simulation of the different channels clarifies the underlying kinematics. The Z=92 channel is the less probable case to detect in CALIFA, as it requires the detection of one neutron for half the cases.

4.5.4.3 TWIN MUSIC Efficiency

The study of spallation reactions was not optimized in this experiment, since every part of the setup was adjusted and optimized for fission fragment detection. The alignment of the TWIN MUSIC detector for fission products was performed in a way that the central cathode was aligned with the beam position. This maximized the detector efficiency in the fission case

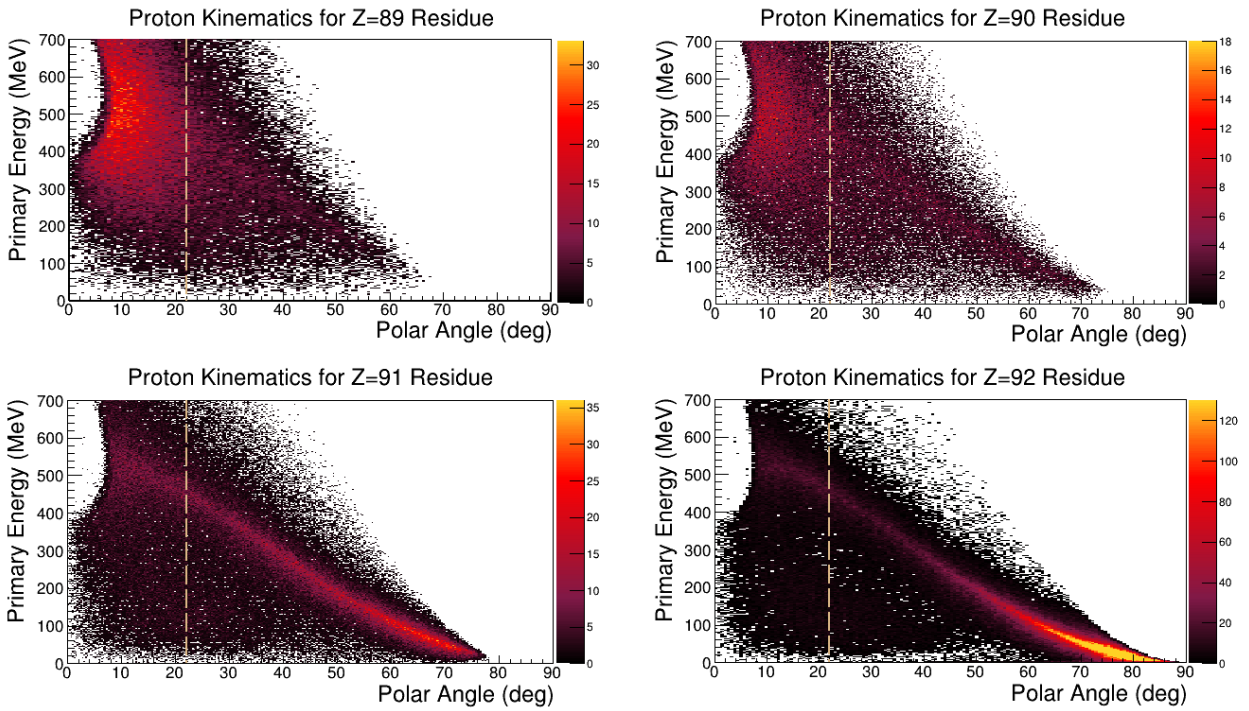

Figure 4.17: Proton kinematics obtained from the simulation of the different spallation-evaporation channels. The brown line at $\theta = 22°$ shows the polar angle of the first CALIFA crystal. The quasi-free-like behavior of the Z=92 and Z=91 channels can be observed in the clear kinematic distribution for both cases. This kinematic distribution is almost not observable in the Z=90 and Z=89 channels and comes from the excited remnant that can also evaporate protons and alphas after the quasi-free process. The rest of the distribution corresponds to non-correlated nucleons emitted at lower polar angles after the knockout processes.

but put a chunk of matter in the middle of the path of heavy-spallation fragments. When a heavy fragment hit the central cathode, the event was lost and therefore this inefficiency had to be evaluated for cross-section corrections. The position distribution (right part of Fig 4.18) shows the shadow that is produced.

By considering only events where the ToFWall detector registered a single hit with a proper time of flight, as illustrated in the left portion of Fig. 4.18, it was possible to determine the number of reconstructed heavy-fragment charges in the TWIN MUSIC and calculate the efficiency. This computation yields a value of

$$\varepsilon_{TWIM} = 46{,}97 \pm 1{,}52\ \%. \tag{4.17}$$

This efficiency is lower than the one calculated only by completing the missing cathode gap

in the fragment X distribution in the detector. This may be caused by the high rate of the incoming beam, which cause a deadtime in the detector that is not accounted in the TPat deadtime, as the TWIN MUSIC does not enter into the trigger logic.

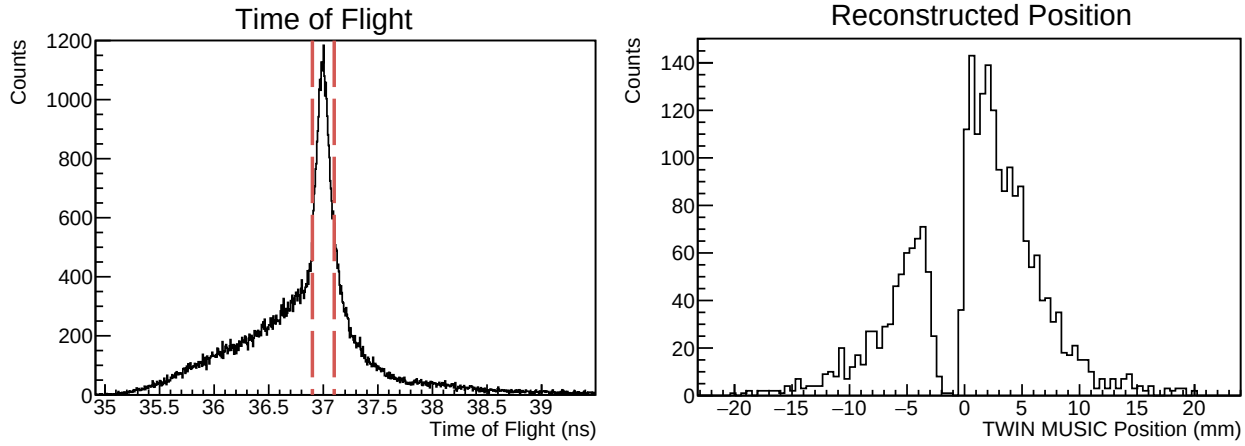

Figure 4.18: ***Left:*** *Selected region of the ToF spectra from single hits in the ToFWall detector.* ***Right:*** *Reconstructed position using drift times at the TWIN MUSIC. The central gap corresponds to the cathode region.*

4.5.4.4 TPat Efficiency

The current selection for cross-section calculations required a TPat value of 5 or 11. This translates, as mentioned before, as a detected START signal together with a CALIFA OR. The only difference between this TPat and the fission ones is that for the latter two plastics with signals were required in the ToFWall detector. This means that if a heavy residue hit the ToFWall and two plastics were fired (because the fragment hit in between two plastics, or a single hit was recorded in coincidence with cosmics, for example) then this TPat was no longer 5 or 11, but 6 or 12. For calculating this TPat efficiency, the probability of two plastics with signal recorded after a non-fission channel was computed using experimental data.

The condition for a heavy nucleus was that the TWIN MUSIC detects a heavy-like signal traveling through one of its sections in coincidence with a START signal. Then the number of events with two or more plastics with signal (2+) and one (1) or zero plastic (0) events were counted for all TPats and corrected by their deadtime and downscale. This efficiency

was then calculated as

$$\varepsilon_{TPat} = 1 - P(\text{Bad TPat}) = 1 - \frac{N_{2+}}{N_0 + N_1 + N_{2+}} = 91{,}542 \pm 0{,}003\ \%. \tag{4.18}$$

4.5.4.5 Scintillator Reaction Correction

As it was shown in previous sections when the fission vertex was reconstructed, a non-negligible number of reactions were produced at the plastic scintillator. While avoiding this contribution in the case of the fission channels can be easily achieved by selecting an appropriate vertex window around the target position, the absence of a reconstructed vertex for spallation reactions makes this correction more difficult. If an incoming nucleus reacts in the plastic scintillator, a final charge Z can be detected in coincidence with two nucleons in CALIFA, even if the reaction takes place at the scintillator location, at -98.75 cm behind the LH2 target.

This contribution has to be calculated using a simulation of the reaction for the different components of the scintillator plastic. This plastic, called BC400, has an empirical formula of C_9H_{10}, so reactions of ^{238}U with carbon and hydrogen were simulated. The number of detected nucleons after a reaction in the plastic (N_{Sci}) that arrive at CALIFA can be calculated as:

$$N_{Sci} = N_i\ \sigma\ \varepsilon_{Sci}\ C, \tag{4.19}$$

where N_i is the number of incoming particles, C is the number of dispersive centers contained in the material, σ is the cross section for a given reaction channel in the scintillator materials and ε_{Sci} is the CALIFA efficiency for reactions coming from the scintillator position. This efficiency is calculated in the same way as explained in the previous section with reactions coming from the target position. A correction factor can then be defined as

$$F = \frac{\sigma_H\ C_{1H,Target}\ \varepsilon_{1H,Target}}{\sigma_H\ C_{1H,Target}\ \varepsilon_{1H,Target} + \sigma_{12C}\ C_{12C,Sci}\ \varepsilon_{12C,Sci} + \sigma_H\ C_{1H,Sci}\ \varepsilon_{1H,Sci}}. \tag{4.20}$$

The obtained correction factors are summarized in Table 4.6.

The largest uncertainty on these calculated values comes from the neutron knockout channel. It was observed [50] that substantial discrepancies between the two libraries were found when the detection of one neutron was required.

Final Fragment Z	CS (1H, mb)	CS (12C, mb)	Correction Factor
92	145,95	1734,56	0,525 ± 0,014
91	122,42	1064,17	0,545 ± 0,006
90	57,57	170,134	0,674 ± 0,004
89	31,14	81,23	0,648 ± 0,005

Table 4.6: Theoretical cross-sections and correction factors obtained from simulations for each reaction channel, using the Bertini and INCL Geant4 libraries. The correction factors in this table are an average from the simulations using the two GEANT4 libraries.

As a summary, the final expression for the spallation cross-section is:

$$\sigma = \frac{1}{2}\frac{F\ N_r\ D\ M}{N_i\ \rho\ w\ N_A\ C_{\mathrm{OR}}\ \varepsilon_{Califa}\ (1-dt)\ \varepsilon_{Twim}\ \varepsilon_{TPat}} \tag{4.21}$$

where F is the calculated correction factor, N_r is the number of reactions, D is the downscale, dt is the measured deadtime for the reaction trigger, and C_{OR} is the correction to the OR case using the DAQ failure probabilities. As before, N_i stands for the number of incoming ions, ρ is the target density, w is the target width, M is the LH_2 molar mass and N_A is Avogadro's number.

4.5.5 Counting Reactions: Spallation-Fission Channel

For the case of the spallation-fission channel, the charge of the fissioning system is fitted to several Gaussians, in the same way as in the spallation-evaporation channel. The higher statistics combined with a greater resolution for the detected fragment charges results in a robust fit of this observable, as shown in Fig. 4.19. The total amount of counts for each fissioning system was obtained by integrating each Gaussian distribution.

4.5.5.1 CALIFA Efficiency

Unlike the spallation-evaporation channel, the fission process is more likely to happen after a rescattering process, where the remnant nucleus has more excitation energy. This rescattering translates into the nucleons being dispersed at lower polar angles, not covered by the CALIFA configuration in this experiment (22°). This results in lower efficiencies for these reaction channels.

The efficiencies for each fission channel are calculated in a very similar way to the ones for spallation-evaporation reactions. Two fission fragments are required in the simulation.

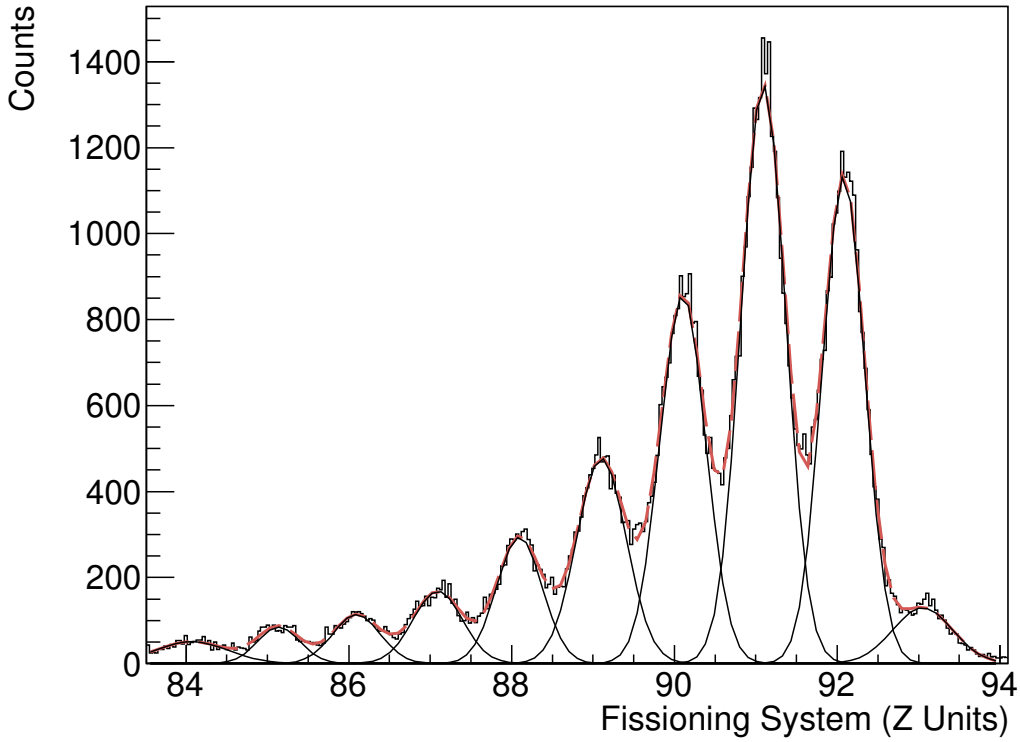

Figure 4.19: Fission system charge distribution. The plot was obtained by adding the charge of the two fission fragments detected by the TWIN MUSIC. The reduced chi-square value for the charge fit is $\chi^2/\nu = 0{,}8389$.

The charge sum defines the fissioning system in Z. For every fissioning system, two nucleons are required, a condition that matches the experimental TPat 4 or TPat 10. The obtained values are summarized in Table 4.7.

The low values of these efficiencies result in a huge uncertainty for every calculated value. A change in the simulated conditions, for example, the usage of a different particle transport library, may cause a change of $\sim 25\%$ in the obtained values. For that reason, and following the same procedure as in the spallation-evaporation case, event selection was performed by choosing events with one nucleon at CALIFA, in TPats 6 and 12. In this case, the detection condition is relaxed and the calculated efficiencies are larger, resulting in less uncertainty regarding the detection conditions. Table 4.8 collects the obtained values.

In this case, switching between libraries leads to variations in the efficiency calculations, with an uncertainty of around 3% of the total value. While different GEANT4 libraries in-

Fissioning System Z	Efficiency (BERT)	Efficiency (INCL)
92	2,32 %	1,72 %
91	2,73 %	3,18 %
90	2,12 %	2,51 %
89	1,65 %	2,39 %
88	1,48 %	2,64 %

Table 4.7: Calculated CALIFA efficiencies for the fission case, for the two nucleon detection condition. Uncertainties are not presented as these efficiency values will not be used for cross-section calculations.

Fissioning System Z	Efficiency (BERT)	Efficiency (INCL)
92	23.15 ± 0,16 %	22,37 ± 0,18 %
91	25,89 ± 0,20 %	24,65 ± 0,25 %
90	23,66 ± 0,23 %	21,93 ± 0,26 %
89	18,69 ± 0,23 %	16,88 ± 0,23 %
88	15,23 ± 0,19 %	12,79 ± 0,18 %

Table 4.8: Calculated CALIFA efficiencies for the fission case, for the one nucleon detection condition.

troduce some discrepancies in the calculated efficiencies, these differences remain below 1%. These variations will be utilized to determine the uncertainty in the measured cross-sections when employing the combined values.

In conclusion, for both evaporation and fission channels, the event selection will be done by asking for one nucleon at CALIFA and using the calculated efficiencies for this case.

4.5.5.2 TWIN MUSIC Efficiency

Similar to what happened with the spallation-evaporation reaction, the presence of the central cathode makes no possible the detection of a reaction product that hits the metal plane. However, the fission fragments are emitted in an open cone, so the probability of having one of them hitting the cathode is lower. To take this into account, together with the possible deadtime induced in the detector by the high rate, this efficiency is calculated by choosing events inside the required TPat where two non-consecutive plastics at the ToFWALL detector were fired. In that case, the amount of events where the TWIN MUSIC saw hits was recorded,

and the efficiency was calculated as

$$\varepsilon_{TWIN} = \frac{n_{TWIN}}{n_{ToFWALL}} = 84{,}38 \pm 0{,}24\ \% \tag{4.22}$$

4.5.5.3 TPat Efficiency

While the spallation-evaporation trigger could be faked into a fission trigger when the heavy residue created two signals at the ToFWall detector, the fission trigger can be confused with a non-fission trigger if the two fission fragments generated less than two signals in the plastics. This can happen if both of them are emitted in a parallel plane with respect to the TofWall detection units, or if one fragment is lost in its path to the end of the setup. This probability can be extracted from experimental data in the same way as in the spallation case:

$$\varepsilon_{TPat} = 1 - P(\text{Bad TPat}) = 1 - \frac{N_0 + N_1}{N_0 + N_1 + N_2} = 93{,}191 \pm 0{,}004\ \% \tag{4.23}$$

As a summary, the final expression for cross-section calculation is:

$$\sigma = \frac{1}{2}\ \frac{N_r\ D\ M}{N_i\ \rho\ w\ N_A\ C_{\text{OR}}\ \varepsilon_{Califa}\ (1 - dt)\ \varepsilon_{Twin}\ \varepsilon_{TPat}}, \tag{4.24}$$

where N_r is the number of reactions, D is the downscale factor, M is the molar mass of the target, N_i is the number of incoming particles, ρ is the target density, w is the target width, N_A is Avogradro's number, C_{OR} is the correction to the OR case, ε_{Califa} is the CALIFA efficiency for each channel and dt is the deadtime of the corresponding TPat.

4.6 Target Reconstruction

For a proper reconstruction of the excitation energy, the reaction vertex has to be determined as accurately as possible in order to achieve a good angular resolution for the scattered protons. In this section, the procedures for reconstructing this reaction vertex using AMS data are described. The detector layout and naming for this reconstruction are depicted in Fig. 4.20. For now on, only the case of a (p,2p) induced fission will be considered, since this is the physical case of interest. Therefore, the reconstruction using AMS only will be carried out for this reaction channel, selecting TPats 4 and 10, two clusters in CALIFA, and two fission fragments with $Z_1 + Z_2 = 91$.

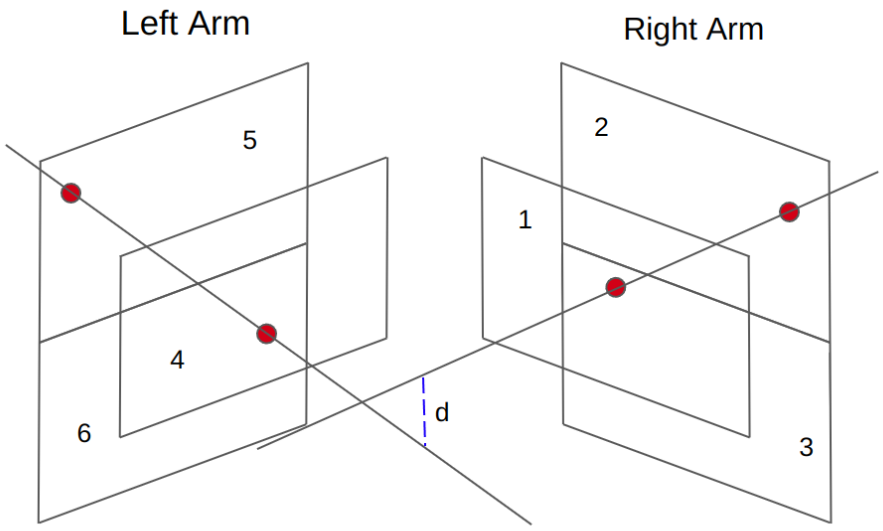

Figure 4.20: Scheme of the reconstruction method for vertex calculations. Each AMS plane is associated with a number, that will be used to refer to each subdetector.

4.6.1 The δ-electron problem

One of the critical points identified during the experiment preparation was the possible presence of a high number of δ-electrons, produced when the incoming beam hit the LH_2 and the surrounding mylar windows. The production of these δ-electrons is proportional to the charge of the particle and inversely proportional to its velocity, i.e, $N_\delta \propto Z^2/\beta^2$ as stated in [71]. This behavior is especially critical for this experiment due to the high Z charge of ^{238}U. The problem arises when a lot of electrons arrive at the silicon strips at the same time as the protons coming out from the reaction. The induced signal by both particles is mostly the same, with overlapping energy deposition spectra. That means that if a particle is detected in AMS, there is no way of disentangling the electron hits from the proton hits. The proposed solution was to install a gold foil before each front detector. The assumption here was that this gold layer would absorb or deflect the incoming electrons while inducing a minimum straggling on the protons. Simulations were performed before the experiment as a part of a thesis dissertation [49], resulting in an optimum gold thickness of 10 μm.

In Fig. 4.21 the strip multiplicity per event is shown. These spectra were obtained by imposing a knockout-fission event and restricted to those events at which a high-energy proton impinged into a CALIFA crystal behind the AMS coverage. As can be observed, the

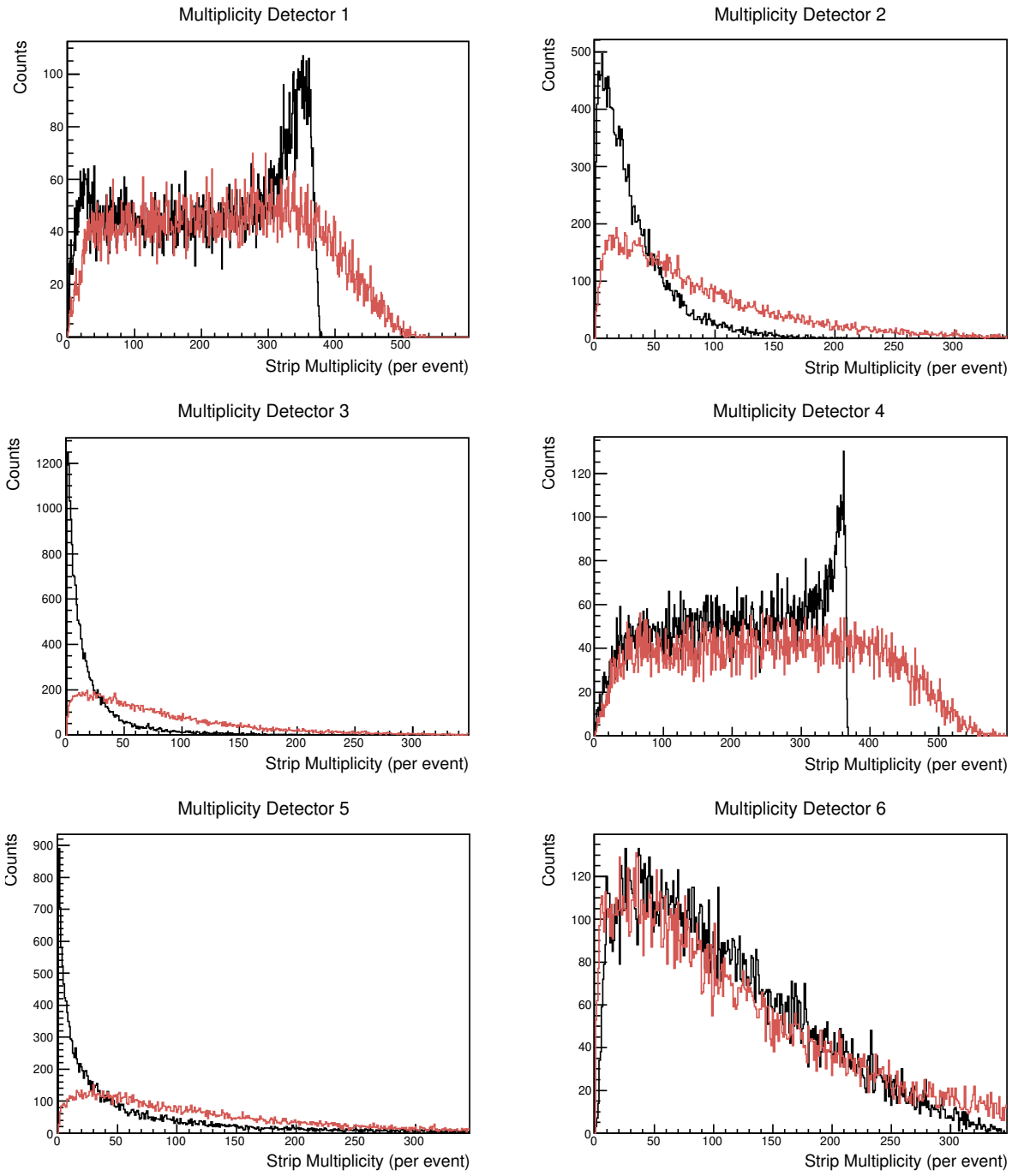

Figure 4.21: Strip Multiplicity per event, measured at CAL level. The black and red lines correspond to the K and S faces, respectively. The scale is zoomed for rear detectors (2,3,5 and 6). The naming scheme is the same as in Fig.4.20.

two front detectors, 1 and 4, have an enormous amount of fired strips on each event. By taking for example the left arm of AMS, where the beam was hitting more frequently, the observed mean multiplicities for front (4) and rear (5) detectors in the S face are 260 and 110. Obviously, these high multiplicities are a drawback, as single-strip hits can produce an enormous amount of possible trajectories.

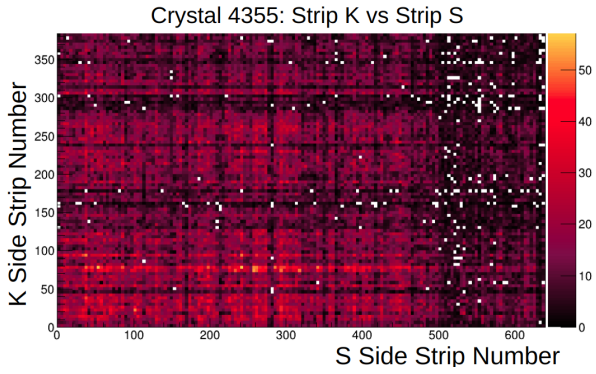

(a) Strip correlation for detector 2.

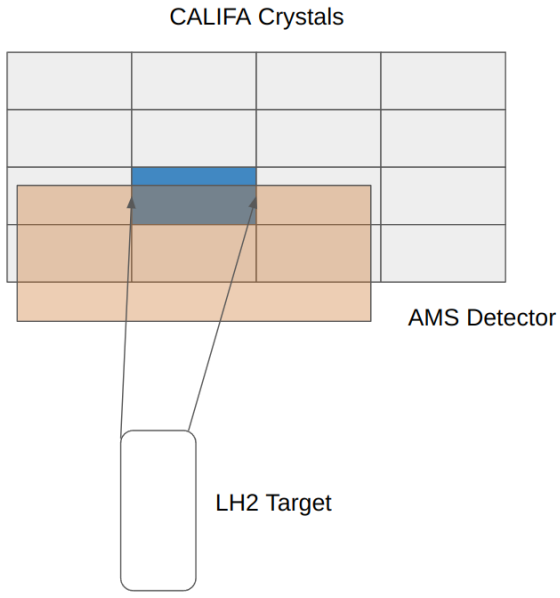

(b) Scheme of the CALIFA-AMS correlation.

Figure 4.22: ***a):*** *Correlation between S and K side for a proton impinging into crystal 4355. This detector is placed in the rear part of the tracker, where the number of detected δ-electrons should be smaller.* ***b):*** *Scheme of the correlation between CALIFA crystals and AMS.*

Before trying to reconstruct any trajectory, a simple check was performed: proton events

in CALIFA crystals behind AMS (detector 2) were selected, and all combinations of S and K strips for rear detectors were performed, in order to check if any correlation could be seen. If a proton travels through an AMS detector and deposits some energy in the crystals behind, a moving shadow, corresponding to proton signals in S and K faces, should be seen depending on which crystal is selected. The result of this procedure is displayed in Fig. 4.22. As expected, no correlation can be found between S and K faces, which should appear as the shadow of the crystal that is placed behind that AMS plane.

In an attempt to reduce the number of combinations, only events at which this detector sees a few strips on both sides were chosen. In this unusual scenario, the selected crystal positioned behind AMS began to reveal its surface, and a correlation could be observed, as displayed in Fig. 4.23. This correlation corresponds to a proton being emitted from the reaction target, passing through two AMS detectors, and eventually detected by the specific CALIFA crystal that had been chosen. Although this method is able to extract some information in a global way, it is worth noticing that this was obtained under very restricted circumstances: the multiplicity was reduced to the very rare cases of less than 10 strips with signals on both sides and only for a rear detector. If the same condition is imposed on all AMS planes at the same time the number of events that accomplish this condition at the same time is basically 0. However, this assures that CALIFA and AMS are properly correlated on an event-by-event basis and that the proton information is correctly stored.

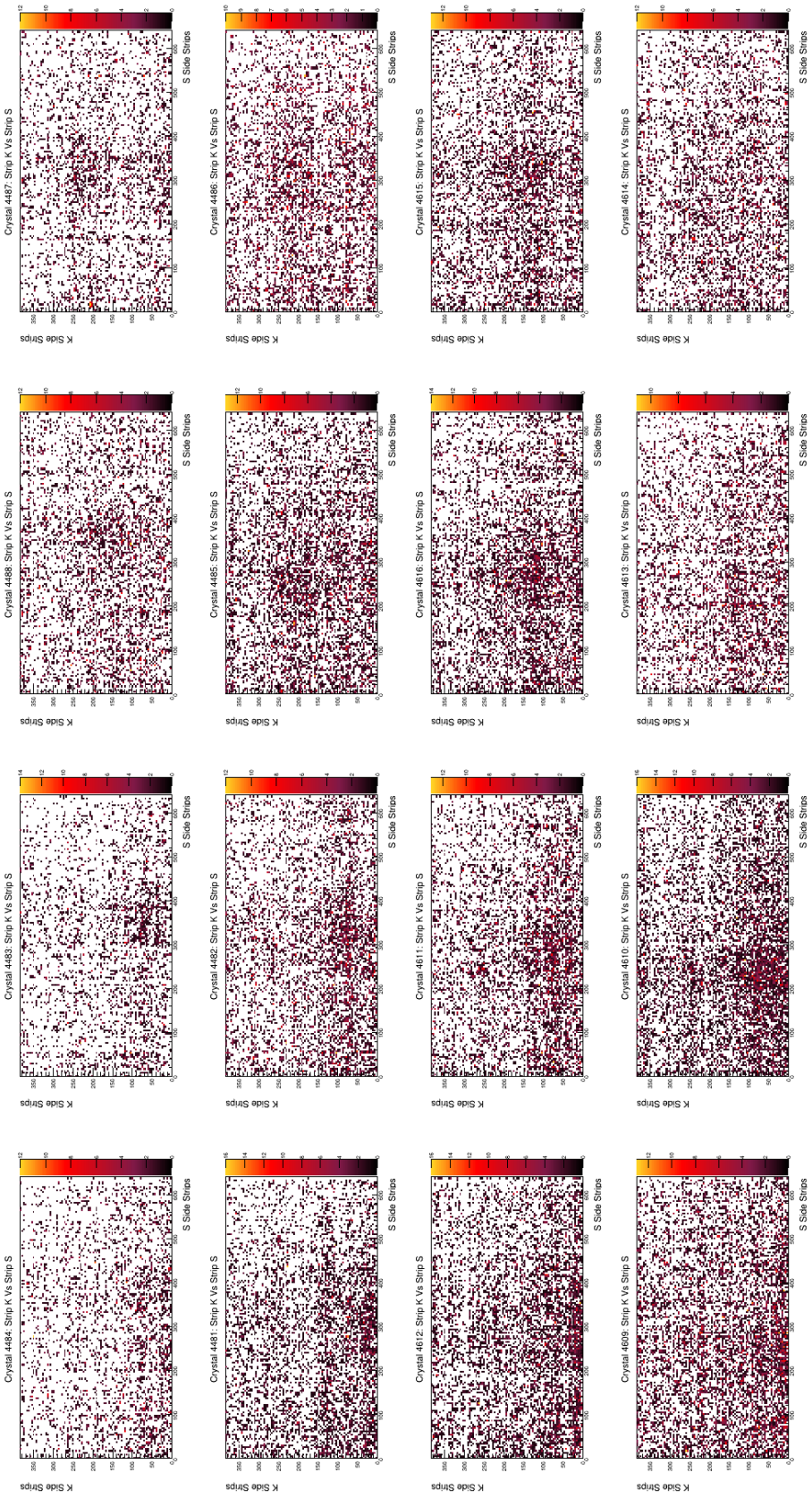

Figure 4.23: Strip correlation for several crystals under AMS coverage.

4.6.2 The Algorithm

Even if the electron multiplicity is high, there are some tracks that once reconstructed and correlated with others can result in a reconstructed vertex which can be directly discarded, for example, if the calculated reaction point is outside the target region. The next step was then to process the information provided by single-strips and transform those hits into clusters, that can retrieve LAB positions and angles. This work is performed by the AMS clustering class. The algorithm works as follows:

1. Once every pedestal is subtracted and the CAL level of the detector is filled, this task reads the CAL container and two histograms are defined and filled for each AMS detector side. Every bin content in those histograms is set to the recorded strip energy.

2. The ROOT peak finder method is run over the histograms, and the number of found peaks and their position are stored.

3. For each AMS detector side several clusters are defined. These clusters are formed by grouping consecutive strips around the peaks found in the previous step. The energy of the cluster is calculated as the sum of each strip's energy inside the cluster. The position of the cluster is defined as a center of gravity:

$$\mathrm{CoG} = \sum_i \frac{s_i \; e_i}{e_i}, \tag{4.25}$$

   being e_i the strip energy and s_i the strip number. This value is multiplied by the pitch size of the corresponding face, in order to get a position over the detector face.

4. The reconstructed cluster information (position and energy) is stored for each detector side.

5. Final clusters are made by combining side clusters (those formed on thee S and K sides, corresponding to X and Y coordinates over the detector face). Those side clusters are ordered by energy, so the combinations of S and K clusters are made in descending order of energy. The (X,Y,Z) LAB positions are calculated using the position information of S(X coordinate) and K (Y coordinate) clusters and the calculated geometry parameters in the alignment procedure (Sec. 4.1). For example, the transformations for detector 1 are

$$\begin{aligned} x &= d \;\sin\theta - (S_{Pos} - S_C) \;\cos\theta \\ y &= K_{Pos} - K_C + \mathrm{Offset} \\ z &= d \;\cos\theta + (S_{Pos} - S_C) \;\sin\theta \end{aligned} \tag{4.26}$$

where d is the distance from the detector face center to the target center, θ is the angle between the face center and the Z axis, $S_C(K_C)$ and $S_{Pos}(K_{Pos})$ are the positions of the detector face center and the position of a given cluster, and Offset is the displacement of each face center respect to the y=0 line.

This procedure was repeated on an event-by-event basis until all strips were included on a cluster or the maximum number of clusters per event was reached. This value was set to 40 clusters.

After a proper selection of the reaction channel, if the two protons coming out from the reaction impinged into CALIFA regions covered by AMS, the vertex reconstruction was carried out. Two arms were defined as the set of detectors 1, 2, and 3 (right arm) and the detectors 4, 5, and 6 (left arm). For every couple of 3D points defined on each arm, a straight line in space was constructed. Then every trajectory on the left arm was correlated with every trajectory on the right arm. The minimum distance in space between the two lines was calculated, and the reaction vertex was defined as the middle point of the perpendicular line that joins the two trajectories at the point of minimum distance. A sketch of this reconstruction is depicted in Fig. 4.20.

In order to check that both the algorithm and the aligned geometries are correct, the procedure was checked by using the simulation. In this case, the propagation of delta electrons was suppressed so the ideal scenario could be reconstructed. The result of this reconstruction is sketched in Fig.4.24. As expected, the algorithm is able to reconstruct the target position for the case that only two protons come out from the reaction. The target region is well reproduced according to the expected beam spot size of $\sigma \sim 10$ mm and the target length of 15 mm. The obtained correlations between the reconstructed angle of CALIFA and AMS, presented in Fig. 4.25 also show that the procedure correctly works.

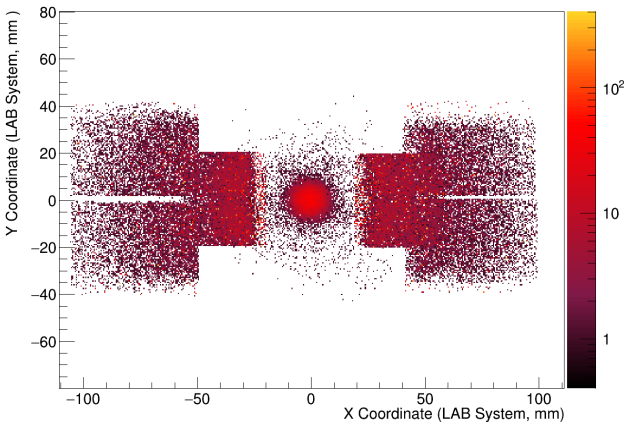

(a) Reconstructed XY Position of the Target + Tracker system.

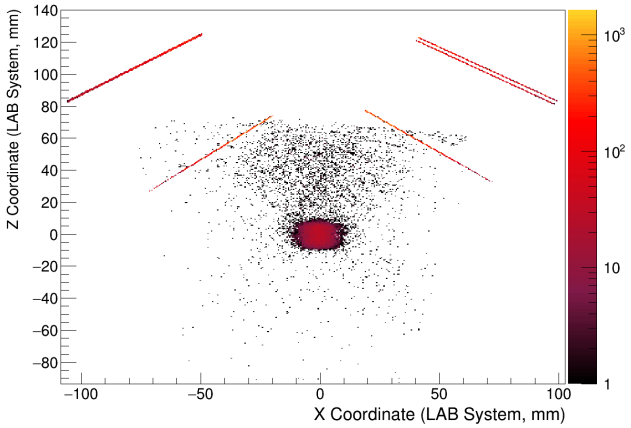

(b) Reconstructed XZ Position of the Target + Tracker system.

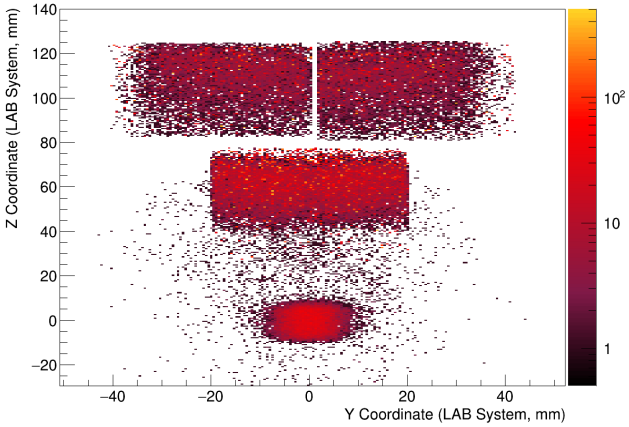

(c) Reconstructed ZY Position of the Target + Tracker system.

Figure 4.24: Reconstructed reaction vertex and tracker positions for the simulated data. All units are expressed in mm.

4.6.3 Real Case Application

Following the same procedure as explained before with the simulation data, experimental data was reconstructed. In an attempt to reduce the number of reconstructed tracks due to the high δ-electron multiplicity, the following cuts were applied:

1. Only events at which CALIFA detected both protons inside AMS coverage were considered.

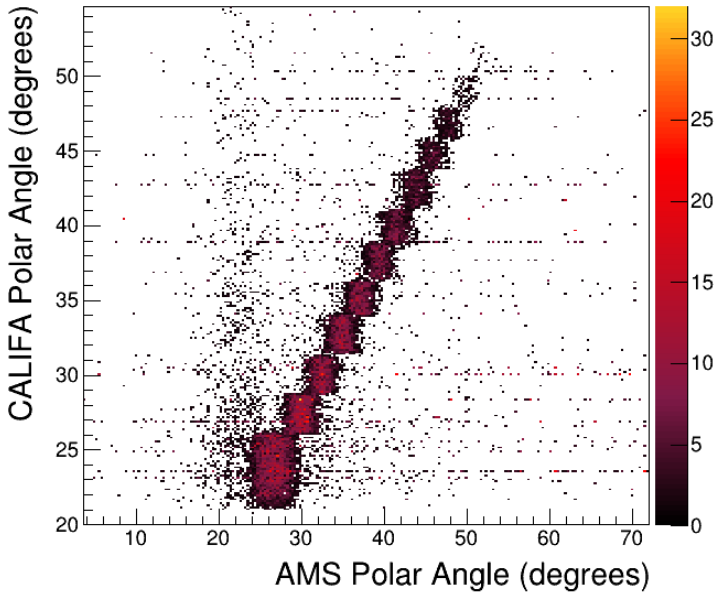

Figure 4.25: Correlation between CALIFA and AMS polar angles, for the simulated case.

2. The maximum distance at the minimum separation point between tracks was set to 5 mm.

3. The reconstructed track polar and azimuthal angles were conditioned to AMS angular coverage.

The first thing to notice in Fig 4.26 is that detectors 3 and 5 have almost no reconstructed data. This situation is also reflected in Fig. 4.27, where the recorded number of clusters per detector is shown. The same plot was calculated using 2σ, 3σ, and 5σ pedestal cuts, but a similar distribution was obtained.

Regarding the vertex reconstruction, even with the previous restrictions, no correlation or vertex could be found. Fig. 4.28 shows that the polar correlation between angles is not present like in the simulated case. The high number of reconstructed tracks, that are compatible with the applied restrictions, makes it impossible to correlate any information coming out from the AMS detectors, that is mostly filled with δ-electron signals.

Fig. 4.26 shows the result of the vertex reconstruction. Although the XY case can be in principle compatible with the target position, this is only an effect of the tracker geometry. If random particles are generated in all directions, the reconstructed XY plane should be a circle centered at (0,0), as the detector is completely symmetric. In addition, the beam

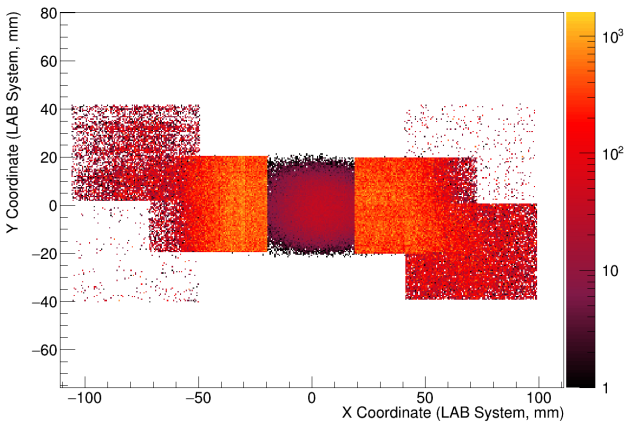

(a) Reconstructed XY Position of the Target + Tracker system. The less populated regions on opposite corners correspond to detectors 3 and 5.

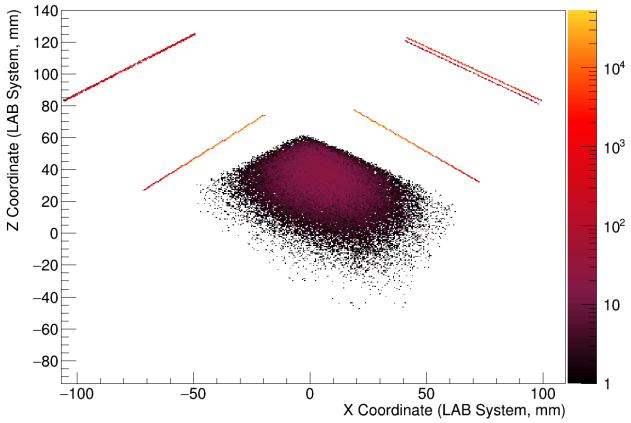

(b) Reconstructed XZ Position of the Target + Tracker system.

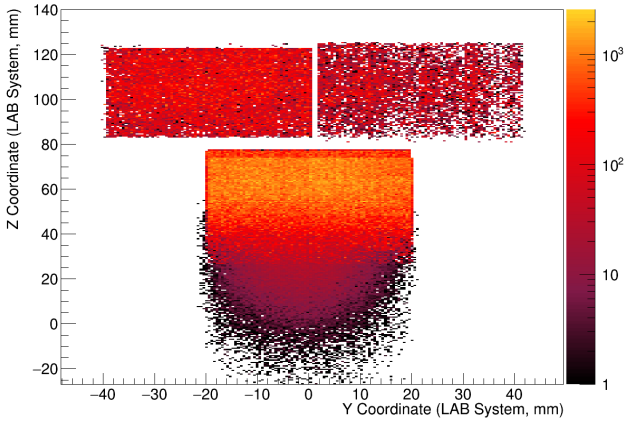

(c) Reconstructed ZY Position of the Target + Tracker system.

Figure 4.26: Reconstructed reaction vertex and tracker positions for the reaction under study. All units are expressed in mm.

spot was known to have a diameter of ~ 2 cm, much narrower than the reconstructed circle. These random points are then a product of all the combinations that the $\delta-$electrons can produce, especially at the target surface where is more probable that an electron can escape.

For the case of the YZ and XZ planes, the distribution is clearly upstream-centered, far away from the expected target center at Z = 0. Since almost all measured particles are δ-

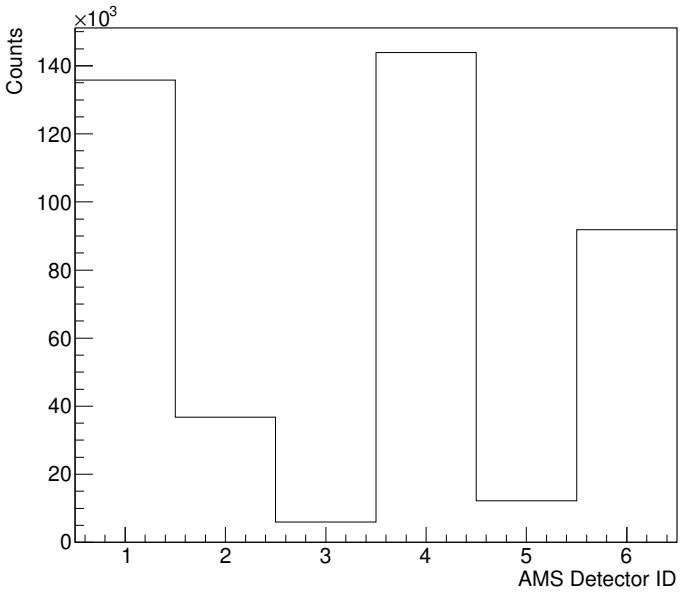

Figure 4.27: Processed number of clusters per detector ID.

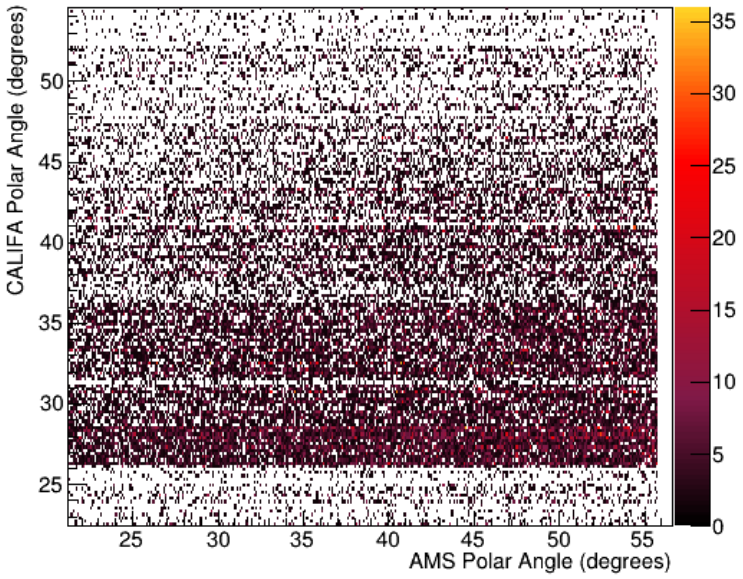

Figure 4.28: Correlation between reconstructed polar angles in CALIFA and AMS.

electrons, the gold layer and the silicon planes cause much more angular straggling for these particles than for protons. If the delta electron production is distributed in a forward cone, the parts of the detectors located at higher Z positions are more irradiated. Although those electrons can be deflected at any possible polar angle, only those deflected towards lower

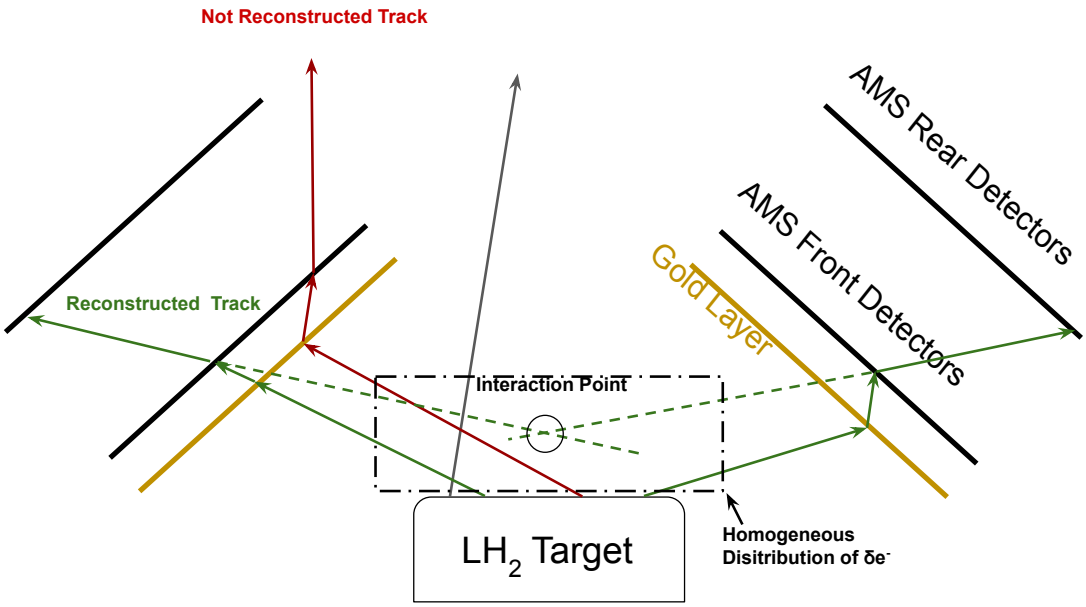

Figure 4.29: Scheme of the δ-electron straggling in gold and silicon layers. The red tracks correspond to non-detected trajectories, that can not generate a valid reconstructed vertex. These non-reconstructed tracks generate a bias in the obtained vertex distribution, which is shifted towards larger values of the Z coordinate.

angles are detected in the second AMS plane. This causes a bias in the reconstructed vertex positions in the upstream direction. A scheme of this explanation is displayed in Fig. 4.29.

More correlations were made using the minimum distance between lines, different pedestal cuts, restrictions in the multiplicity of the different AMS detectors, or even correlations with the MWPC 0. None of these studies ended in a better identification of the vertex or in a reasonable correlation with other detection systems, in particular with CALIFA.

As a result of this study with the detector, some conclusions were extracted.

1. The angular information of protons coming out from the reaction target and arriving at CALIFA could not be extracted by AMS on an event-by-event basis. The thousands of reconstructed trajectories made no possible the reconstruction of the reaction point.

2. CALIFA angles had to be used for the momenta reconstruction of the scattered particles. The poor angular resolution of CALIFA for this case resulted in a resolution worse than the one expected for the obtained excitation energy. This effect will be quantified

in Sec. 4.8.

3. Stripped-tracking detectors are not well suited for experiments with heavy ions. Some studies with pixel-based detectors are been carried out at the moment with ALPIDE (ALice PIxel DEtectors) as the preferred future solution for the vertex detector at R3B, providing a better δ-electron rejection together with a great angular resolution.

4.7 Punch Through Reconstruction

When a light-charged particle is emitted from the reaction point and hits the calorimeter, the maximum amount of scintillator material that this particle can encounter is 22 cm of CsI(Tl) located in the most forward crystals of the IPhos part. In the case of protons, the maximum energy that these long crystals can collect is 317 MeV. The more energetic protons that escape from the active material are called punch-through protons, and their reconstruction is crucial since the four-momentum of the scattered protons is used for excitation energy calculations.
Some studies [72] were performed at IJF PAN in Krakow, Poland, with the prototype crystals that would be used later in the detector. As described in this work, different proton energies of 90, 100, 105, 110, 120, 130, 155, and 180 MeV were emitted in a perpendicular direction to the main crystal's axis. The effective length of the active material in this experiment was 15,3 mm, which corresponds to a stopping power of 65 MeV, so all of those particles were punch-through cases. The original energy can be reconstructed by evaluating the deposited energy and using some energy loss databases like ATIMA[69]. The obtained energy resolutions ranged from 4,9% (FWHM) for the lowest energy to 13% for the biggest one. This method is the common way to proceed in nuclear physics experiments and was the first one to be studied for the present case.

4.7.1 Energy Loss Method

This method was first examined by using simulations. For every simulated fission, events at which the outgoing protons were detected by CALIFA after a $Z_1 + Z_2 = 91$ fission were selected. By getting the primary angles of the protons, every proton pair was associated with events at CALIFA in which only two clusters were recorded. Each cluster was then matched with the particle that generated the hit and a 2D plot of primary energy vs deposited energy was filled. Since CALIFA crystals have different capabilities (due to the different geometries and sizes) to stop different energies, 26 different cases were studied, for the 26 different crys-

tal geometries in CALIFA. To complete the study, every case was separated into two plots, one using the total deposited energy on each cluster and another for the deposited energy in the crystal that generated the cluster. For the cluster case, each plot corresponds to the geometry of the cluster's mother crystal.

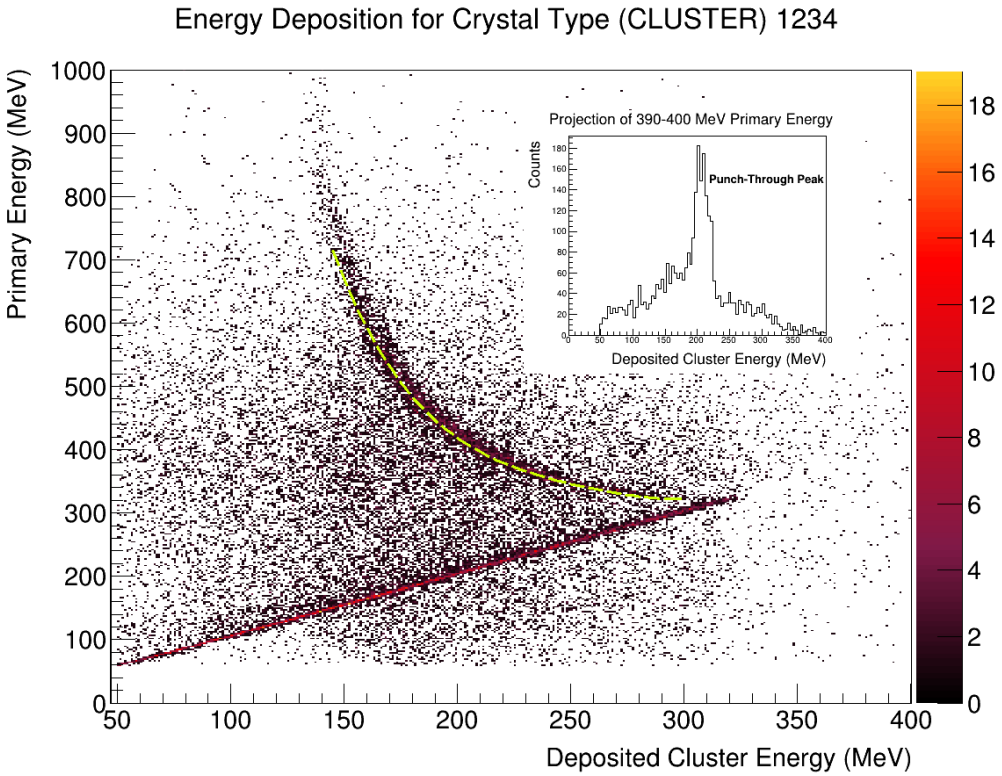

Figure 4.30: Correlation between the deposited energy in a CALIFA cluster and the primary energy of the proton. The fitted curve for punch-through protons is displayed in green. The inset figure shows the projection of this primary energy for the E=395 MeV vicinity.

Figure 4.30 shows the obtained correlation for a given geometry (22 cm long crystal). As expected, primary energies below $\sim$ 320 MeV are reconstructed by both cluster and single crystals as a narrow-straight line corresponding to $\Delta E/E$ resolution $< 1\%$. From 320 MeV and above, the deposited punch-through energy follows a curved line from this energy up to an energy of 150 MeV for the most energetic protons. If the proton energies are large enough, the deposited energy begins to be the same for all the spectrum, as they are far away from the Bragg peak. When projecting onto the energy deposition axis at 150 MeV, a broad distribution of primary energies emerges, contributing to the method's resolution deteriorating as the energy of the primary particle increases. The energy ranges and limits

for the different parts of the distribution that is shown in Fig. 4.30 depend on the crystal's length, of course.

In addition, there are a lot of events at which a proton can knock out a nucleon from the scintillation material. If the knocked-out particle is a proton, then the energy can be still recovered, as this secondary proton can be stopped and detected by the same crystal or the neighboring ones. If the knocked particle is a neutron (and this is probable since Thallium and Cesium have many more neutrons than protons) the total deposited energy is less than the original energy, as the neutron is way more difficult to completely stop and detect. The probability of having such a nuclear reaction rises with higher reaction energies. This situation is translated into the middle region of the plot, between the fully-deposited line and the punch-through curve.

The energy reconstruction algorithm consisted of the following steps:

1. The reaction was simulated with the experimental conditions described in Chapter 5.
2. The punch-through curve was fitted to a 4th-order polynomial for the different 26 geometries of CALIFA. The cluster reconstruction was chosen over the single crystal one, as the punch-through line is more clear in this case. Fit parameters were calculated and stored.
3. Every time a punch-through case is identified, the deposited energy in the cluster is collected, the corresponding function is evaluated, and the reconstructed energy is obtained.

The resolution of this method can be evaluated if the residual of this reconstruction is calculated for several energy ranges of the scattered particle. This result is shown in Fig. 4.31. The prominent peak centered at 0 is the result of the reconstruction for the events at which the deposited energy follows the punch-through line trend. The width of this peak starts to grow for increasing energy. So the resolution does, as the projection of the curve for a narrow region in the deposited energy axis includes a larger region in the primary energies domain. The distribution on the right and on the left of this peak corresponds to the regions in Fig. 4.30 below and above the punch-through fit line, respectively. The contribution on the right is more pronounced at higher energies and starts at 320 MeV, where the fit curve flattens. If this deposited energy region is evaluated, the reconstruction gives a smaller value than expected, as the deposited energy is bigger.

The algorithm's suboptimal performance, particularly evident at higher energies where the second distribution on the right side of the spectrum emerges, together with its limited application for reconstructing only energy losses attributed to a punch-through process, prompted the exploration of alternative approaches for this reconstruction.

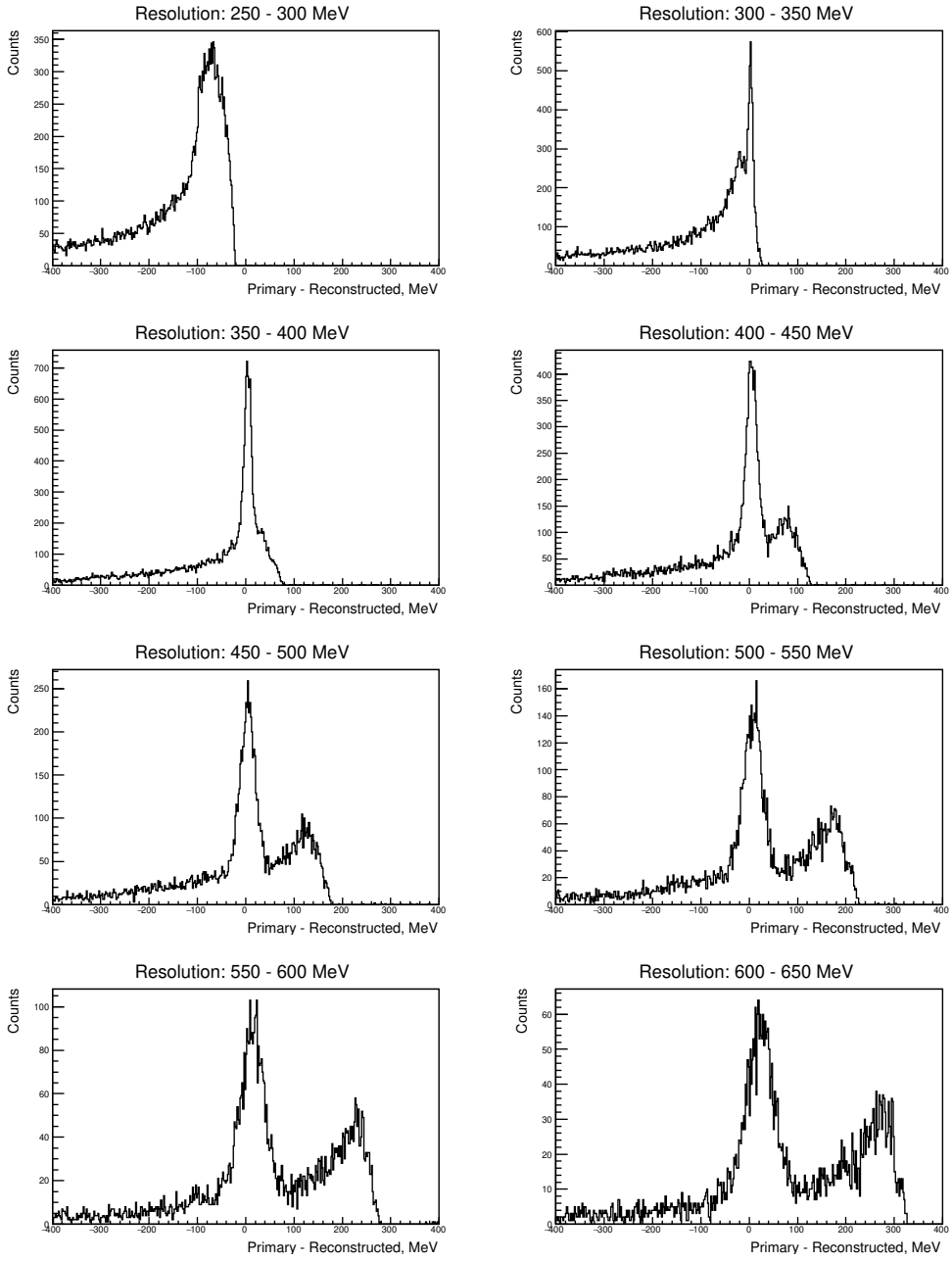

Figure 4.31: Obtained energy residuals for the energy loss method reconstruction. The title on top of each plot corresponds to the considered energy range of the primary particle.

4.7.2 Neural Network Approach

A basic plot showing the difference between the reconstructed cluster energy and the energy of the simulated proton emerging from the INCL reaction simulation striking CALIFA can be created, so it becomes apparent that hardly any particles are completely reconstructed by the clustering procedure, for the spallation-fission reactions.

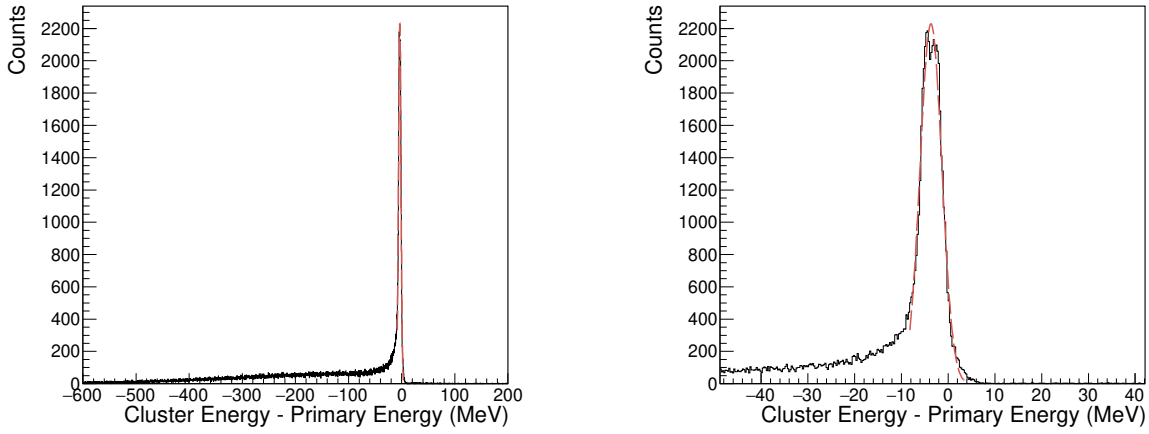

(a) *(b)*

Figure 4.32: Simulated reconstruction differences for the cluster method. ***a):*** *Full distribution.* ***b):*** *Zoomed region around the fitted peak, corresponding to fully reconstructed energies.*

The displayed peak in Fig. 4.32, with $\sigma = 2{,}32$ MeV and centered at $\mu = -3.68$ MeV represents only the $\sim 30\%$ of the total cases. This difference is the sum of the punch-through processes, losses in the cluster reconstruction, and losses in the material, mainly in the alveoli carbon fiber structure and the interface between crystals. Taking this into account, a method for reconstructing all the particles at the same time, without sorting first into the different punch/stopped cases was developed.

The chosen method was a neural network approach. The input data was obtained from a realistic simulation, so the same observables as in the experimental case serve as the input for the first model layer. The labels, corresponding to the true proton energies that have to be reconstructed, were obtained from the energy values stored in the MCTrack class.

4.7.2.1 Principal Component Analysis

There are a lot of observables in CALIFA that can be used for neural network training. Some of them are direct measurements (crystal energies, multiplicities...) and others can be

built from other observables (cluster information, weighted angles, dispersion inside a cluster, calorimetric energy per event...). In order to choose the most convenient set of input variables for the neural network model, a Principal Component Analysis (PCA) of the different variables was performed.

The first step was to collect the different variables. From a typical knockout reaction, this set of quantities constitutes a set of a priori interesting variables for the analysis:

1. Cluster energies (E_1,E_2).
2. Cluster angles (θ_1,θ_2,φ_1,φ_2).
3. Mother crystal energies (the crystal with higher energy inside a cluster) (e_1,e_2).
4. Fast and slow components of light (Nf, Ns).
5. Angular dispersion inside a cluster (η_1,η_2).

This angular dispersion, defined as

$$\eta = \sum_i \frac{e_i \ [(\varphi_i - \varphi)^2 + (\theta_i - \theta)^2]}{E}, \tag{4.27}$$

is a weighted sum of the angular difference between single crystals (θ_i,φ_i) and the cluster's mother crystal center (θ,φ).

The Nf and Ns components could potentially serve as interesting observables, as combinations of these variables are commonly used to separate punch-through processes from fully stopped cases [72]. However, it was decided to use a combination of these two observables,

$$\mathrm{PID} = \frac{N_f}{N_f + N_s}, \tag{4.28}$$

to characterize the ΔE from the fully stopped processes. Fig. 4.33 shows this PID for both simulated and real data, which can separate both processes inside the crystals. These PID distributions were normalized before being used as input for the Neural Network (NN) model, so both had the same maximum and minimum values and the same separation for the two branches at low crystal energies.

The next step involved the calculation of the covariance matrix. If the variables are standardized first,

$$\hat{x} = \frac{x - \bar{x}}{\sigma_x} \tag{4.29}$$

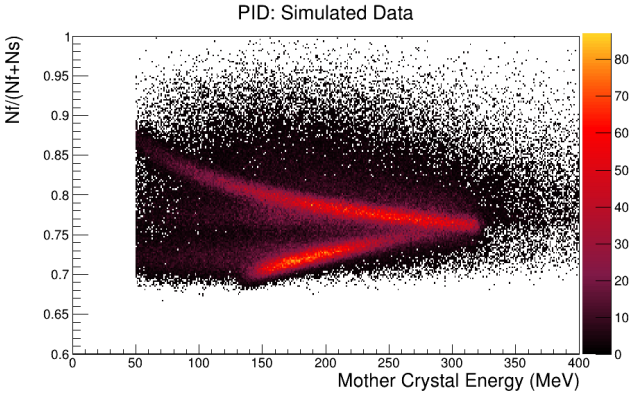

(a) PID vs mother crystal energy for the simulated case.

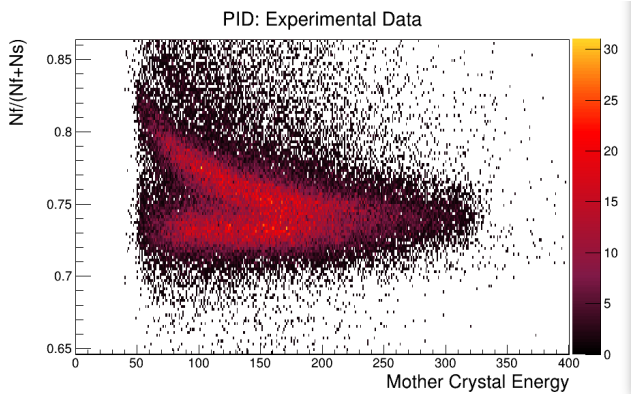

(b) PID vs mother crystal energy for the experimental case.

Figure 4.33: PID plot for the simulated and the real case. In both cases, the defined PID was represented as a function of the highest energy inside a cluster. A selection on $Z_1+Z_2 = 91$ for the fissioning system was performed for both simulated and real data. These plots should come then from proton signals after the knockout process. The upper region on each plot corresponds to fully stopped particles in the active material, while the lower branch of the correlation is produced by non-stopped particles, either by punch-trough processes or by nuclear reactions.

where $\bar{x}$ and σ_x are the mean value and the standard deviation for variable x. The covariance between two variables is defined as

$$Cov(x,y) = \frac{1}{N}\sum_i \hat{x}\ \hat{y} = Corr(x,y), \tag{4.30}$$

with the correlation being the normalized covariance between (-1,1). The correlation matrix for the considered variables in CALIFA and the primary information of the two protons is

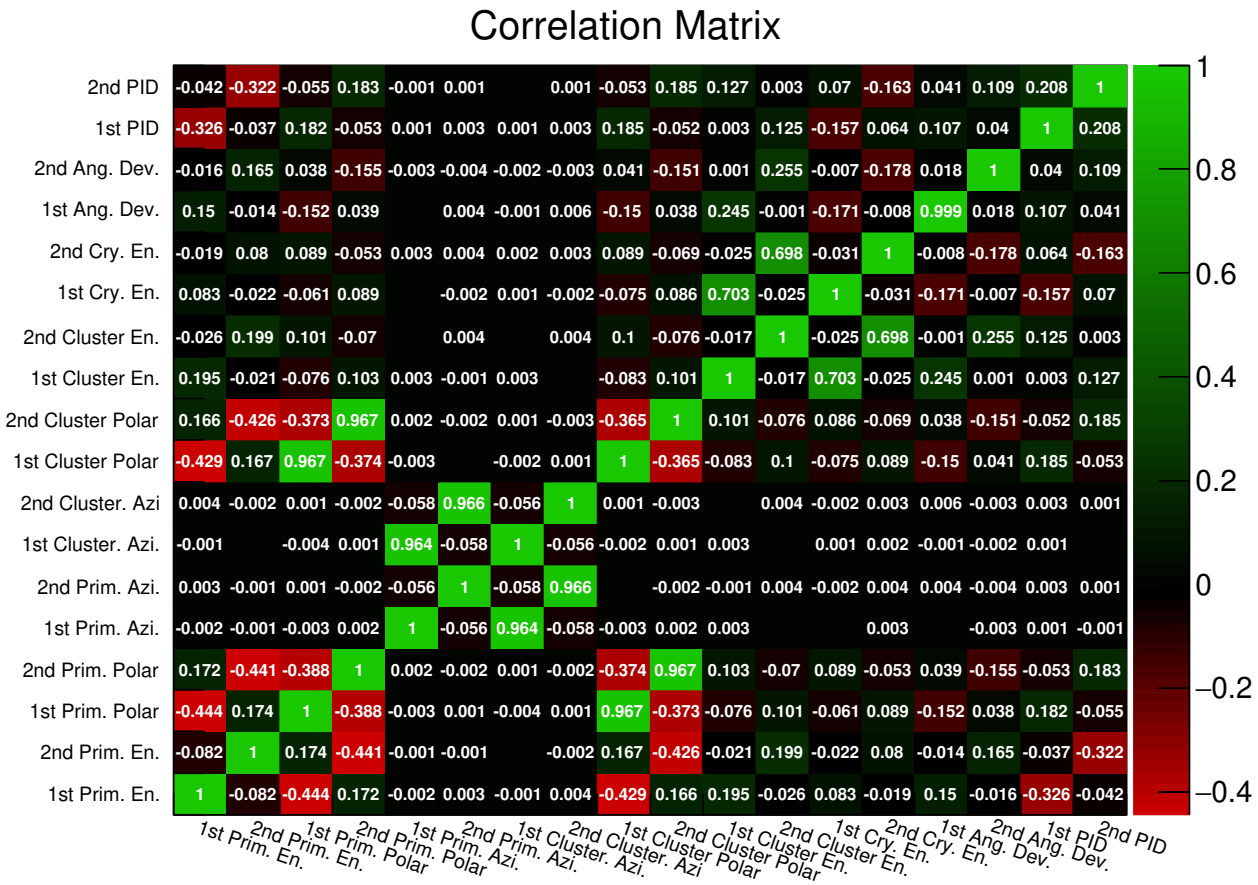

Figure 4.34: Correlation matrix for the different reaction variables obtained from the simulation. Empty elements correspond to correlation values smaller than 0.001.

depicted in Fig. 4.34. The labels *1st* and *2nd* correspond to the information of the two clusters detected in CALIFA for reactions where only two clusters were recorded. Angular coordinates and energies for simulated protons are labeled as *Prim. Azi, Prim. Polar, and Prim. En.* Signals in CALIFA are named *Cluster En, Cluster Polar, and Cluster Azi* for energy and angular information about the reconstructed clusters. Angular deviations inside each cluster and the largest energy are shown as *Ang. Dev and Cry. En.*

Some interesting information can be extracted from the matrix. The correlation value for the proton energy and the respective formed cluster is positive but rather small. This reflects that the proton energy is rarely fully reconstructed due to punch-through processes, as discussed before. Cluster energies and mother crystal energies are highly correlated ($\sim 70\%$), but the non-full correlation shows that the collected energy in a cluster is typically spread

across several crystals.

Polar angles are highly correlated for clusters and primary particles, as expected. The correlation between polar angles and energies follows the kinematical distribution, where more energetic particles are scattered at lower polar angles. From this representation of data, it can also be noted that azimuthal coordinates have no relevance in the reconstruction, as they are not correlated with any other observable. For this reason, this information was removed from the neural network input.

The eigenvalues of the submatrix containing the considered ten observables (two cluster energies, two mother crystal energies, two PIDs, two cluster polar angles, and two angular dispersions) were computed with the following result (not ordered)

$$\vec{\lambda} = (1{,}972\ ,\ 0{,}177\ ,\ 0{,}185\ ,\ 0{,}566\ ,\ 0{,}635\ ,\ 1{,}661\ ,\ 1{,}327\ ,\ 1{,}365\ ,\ 1{,}042\ ,\ 1{,}068) \quad (4.31)$$

where each eigenvalue has a weight:

$$\vec{w} = (0{,}197\ ,\ 0{,}018\ ,\ 0{,}019\ ,\ 0{,}057\ ,\ 0{,}064\ ,\ 0{,}166\ ,\ 0{,}133\ ,\ 0{,}137\ ,\ 0{,}104\ ,\ 0{,}107) \quad (4.32)$$

since there is no subset of the eigenvalue vector that represents a substantial part of the information, it was decided to use the normalized variables as they are, without reducing the input space according to the linear combinations dictated by the associated eigenvectors.

4.7.3 Models

For each event, the two protons are reconstructed using the model shown in Fig. 4.35. The information of the full reaction detected in CALIFA is given as input for the network. The first proton observables are given together with the second proton observables, so the underlying kinematic is contained inside the model. As a simple example, if the reaction was a quasi-free knockout process and one of the protons is fully detected, the other one should have deposited energy correlated with its polar angle and also with the energy and polar angle deposited by the other particle. For each simulation event, two neural network inputs are created, one to reconstruct the first proton and another to reconstruct the second proton.

The trained models were then fully connected forward networks, with 1, 2, and 3 hidden layers. Absolute and quadratic functions were used as metrics and loss functions. Although Leaky-ReLU functions are the standard now in regression and classification models, it was

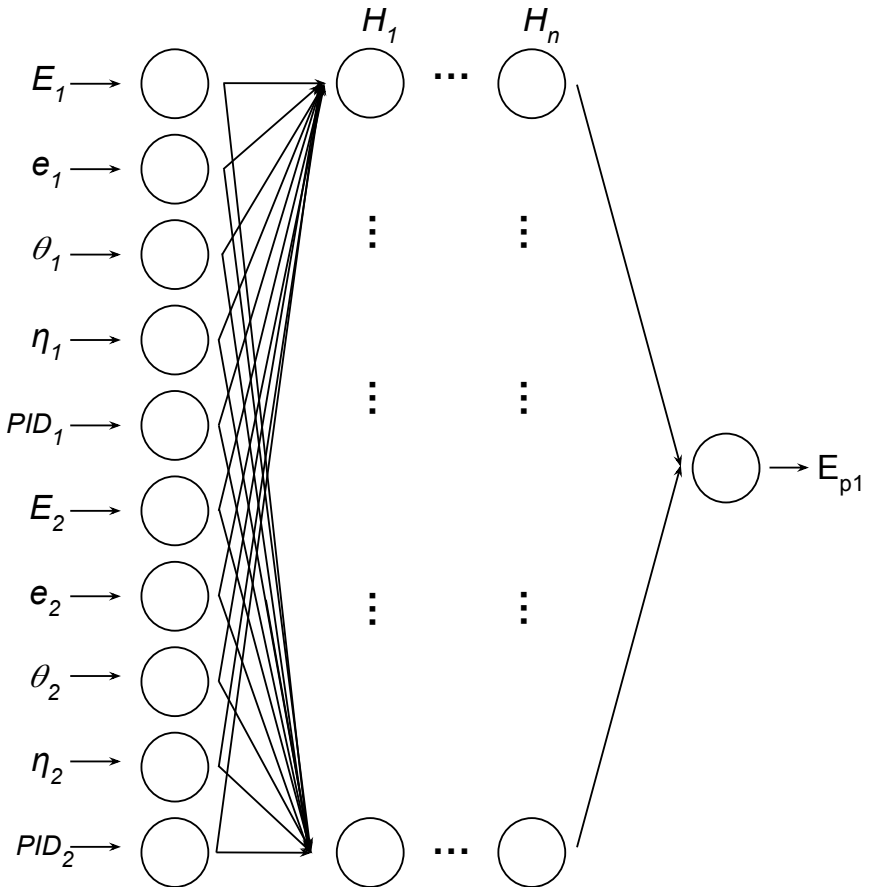

Figure 4.35: Model diagram for the punch-through reconstruction network. The corresponding diagram for the second proton can be obtained by swapping 1 and 2 indices. $E_{1(2)}$, $e_{1(2)}$, $\theta_{1(2)}$, $\eta_{1(2)}$, $PID_{1(2)}$ stand for cluster energy, mother crystal energy, cluster polar angle, angular deviation and PID value for first (1) and second (2) cluster. $H_1 ... H_n$ denote a variable number of hidden layers. The output of the network is the reconstructed energy of the first proton.

observed that the non-linearity induced by the use of Sigmoid functions helped in the reconstruction process, so these functions were considered for the model architecture, using them in the hidden layers. A variable number of neurons was used for the hidden layers and several batch sizes were studied. Tables 4.9, 4.10, 4.11 contain a summary of the hyperparameter configuration for the three configurations.

Each one of the 336 models was trained using 65000 samples and 800 epochs, where each epoch is defined as a complete iteration of the dataset. The data sample was divided into a training sample containing 7/10 of data and a test sample containing 3/10 of data, aimed at

Three Layer Model						
Batch Size	H_1	f_1	f_2	f_3	**Loss**	**Combinations**
8,16	8,16	L	L,S	L	Q, A	16

Table 4.9: Three-layer model hyperparameters. Each possible value for every hyperparameter is separated by commas. L and S stand for LeakyReLU and Sigmoid activation functions. Q and A stand for Quadratic and Absolute loss functions. f_1...f_n denote the different activation functions of each model layer, and H_n denotes the number of neurons on each hidden layer (in this case, H_1 corresponds to f_2)

Four Layer Model								
Batch Size	H_1	H_2	f_1	f_2	f_3	f_4	**Loss**	**Combinations**
8,16	8,16	8,16	L	L,S	L,S	L	Q, A	64

Table 4.10: Four-layer model hyperparameters.

Five Layer Model										
Batch Size	H_1	H_2	H_3	f_1	f_2	f_3	f_4	f_5	**Loss**	**Combinations**
8,16	8,16	8,16	8,16	L	L,S	L,S	L,S	L	Q, A	256

Table 4.11: Five-layer model hyperparameters.

checking the model performance after the training was finished.

4.7.4 Results

The global information about the models' performance is presented in Appendix B. The trained models were evaluated by their residues, defined as the difference between the energy reconstructed by the model and the simulated energy. These residues were studied for eight different cases, for energies of the primary particle ranging from 250 to 650 MeV. Each one of these primary energy ranges is represented by a color in the performance plot (Fig. B.1). The spread around the mean value of the residue was used for a resolution characterization, defined as a FWHM measurement:

$$R(\bar{E}) = \frac{100\ \sqrt{2\ \ln 2}\sigma}{\bar{E}}, \tag{4.33}$$

where σ is the standard deviation of the residue, non-necessarily Gaussian distributed, and $\bar{E}$ is the mean value of the energy region. A gross model performance measurement was obtained using this value, along with the mean and standard deviation of the residue means for

each energy range. Models exhibiting reasonable performance underwent in-depth analysis, including proper fits and correlations.

4.7.4.1 Training Results

Each three-layer model (an input layer, one hidden layer, and an output layer) number was codified by a number starting with a three followed by the combination number for each hyperparameter configuration, from 3001 to 3016. In the same way, the four-layer models (an input layer, two hidden layers, and an output layer) numbers started from 4000 up to 4064, and five-layer models (an input layer, three hidden layers, and an output layer) were marked with numbers ranging from 5000 to 5256. Appendix B gathers the obtained results for the three different NN architectures.

The most precise models were the 5-layer models. All of them were tested by propagating simulated data through them and studying their performance in terms of residues and correlations. This data was different from the one used for training. The best performance was achieved by models 5025, 5121, 5187 and 5239, all of them corresponding to configurations with LeakyReLU, Sigmoid, Sigmoid, LeakyReLU, and LeakyReLU functions and an absolute loss function. The presence of sigmoid functions in the best models means that the non-linearity induced by those functions is needed to achieve a proper reconstruction. It is also noted that models with absolute losses performed better. The reconstructed energy is shown correlated with the simulated energy in Fig. 4.36.

As it can be seen, primary energies below the punch-through limit are well reconstructed, except for a branch that appears on the right-lower part of the plot. That branch corresponds to primary particles with energies below 300 MeV, that are wrongly identified by the network as punch-through cases, as the energy deposition on those clusters is similar to fully-stopped particles at low energies. This branch is way more prominent for some previous models that were trained without the Nf, Ns information, showing that in this case, the PID helps to identify those cases. For model 5187, the one that will be used in the subsequent analysis, the number of events going in that branch accounts for 4,89 % of the cases.

The obtained residues, presented in Fig. 4.37, show the difference between the reconstructed particle energy and the primary energy at different energy regions. This residue is defined as $E_{Prim} - E_{NN}$. The most probable case, between 250 and 500 MeV shows that this region is well reconstructed, with narrow distributions around 0. The high energy cases, for

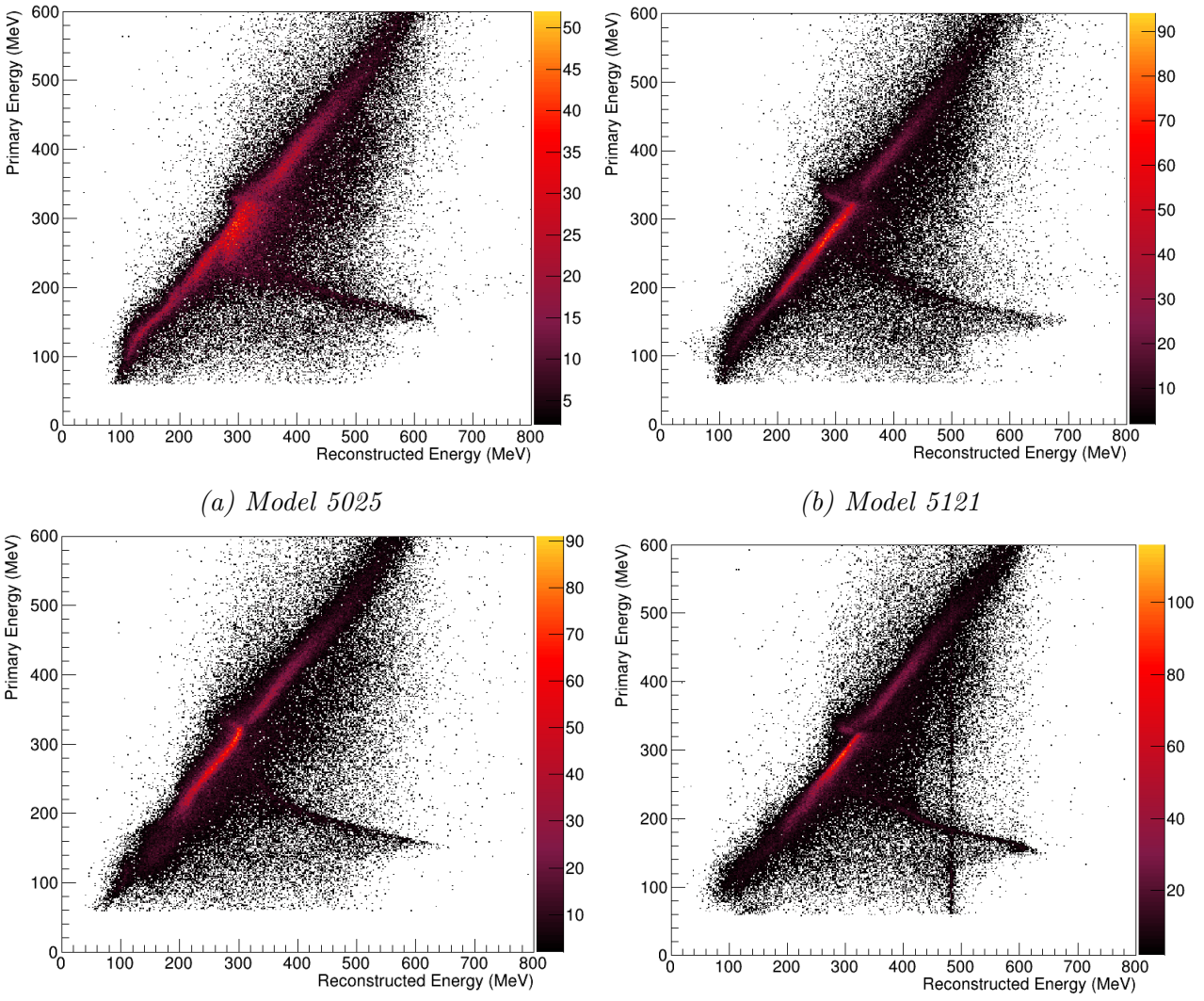

(a) Model 5025

(b) Model 5121

(c) Model 5187

(d) Model 5249

Figure 4.36: Reconstructed proton energies compared with the simulated energies.

protons above 550 MeV are not as precise, but as those cases are really a few, the overall performance is suitable for a proper reconstruction. If the residue distributions are fitted to two Gaussian functions, as displayed in Fig. 4.38b, the most prominent distribution can be used to estimate the resolution of the method as an FWHM measurement (Fig. 4.38).

The best performance, with resolutions lower than $\sim 9\%$, is achieved for energies in the range of 350 to 500 MeV, which is the center of the proton energy distribution generated by INCL. The network presumably tries to perform a proper reconstruction for all energies at the same time, resulting in a worse performance of the method for values on the edges. This effect is convoluted with the intrinsic problem of reconstructing high-energy particles

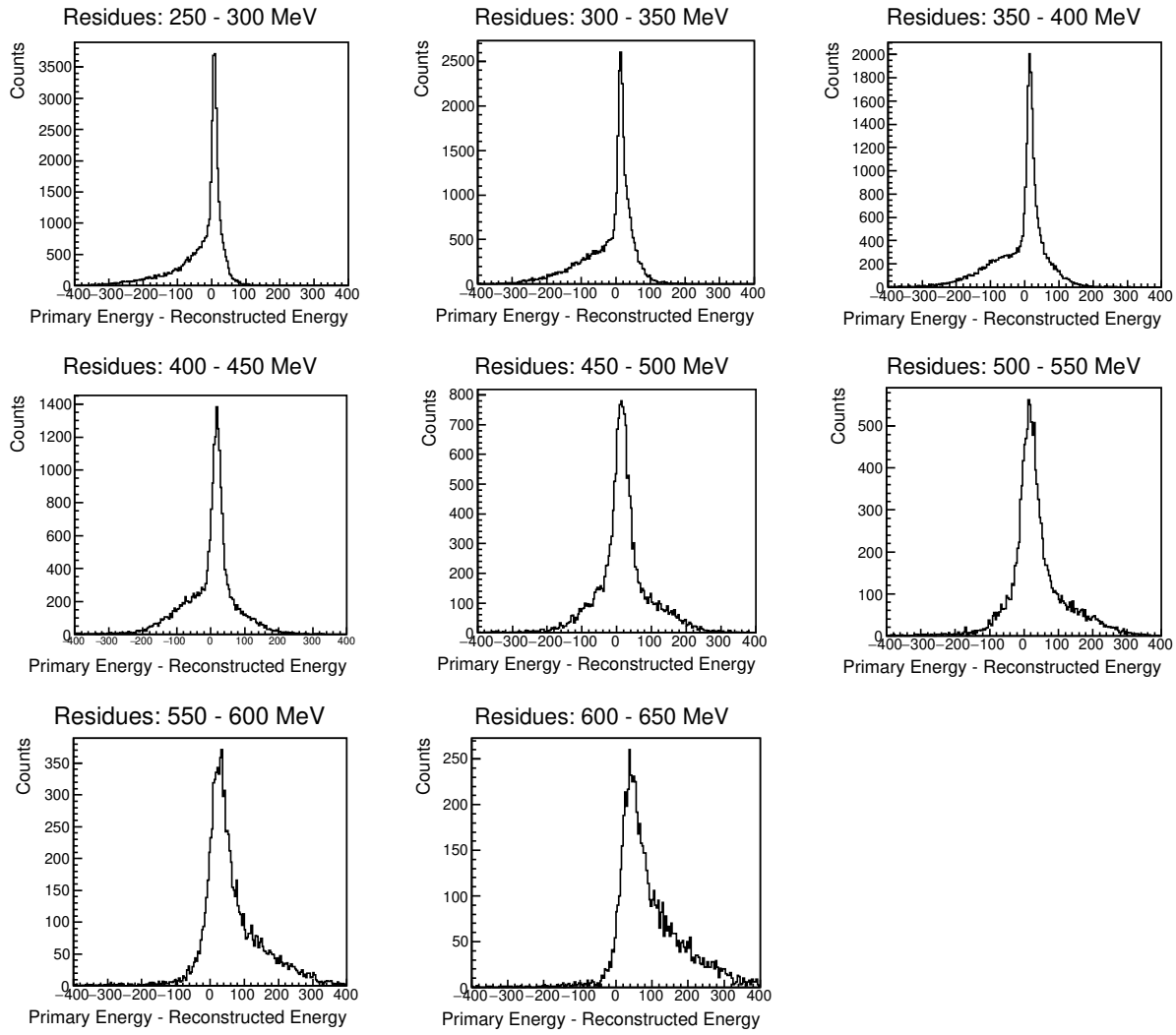

Figure 4.37: Obtained residues for model 5187. X-axis units are MeV.

far away from the punch-through limit.

The kinematic distribution for raw energies in CALIFA, NN reconstruction, and the generated distribution from INCL is presented in Fig. 4.39. From this distribution, it can be noted that the wrongly reconstructed punch-through branch at low energies is reflected here in the difference between NN kinematics and INCL kinematics in the region around $\theta \sim 35°$ and $E \sim 150$ MeV.

It may be interesting to study the NN performance under different knockout processes. The huge amount of rescattering events and the large fraction of lost energy that those events

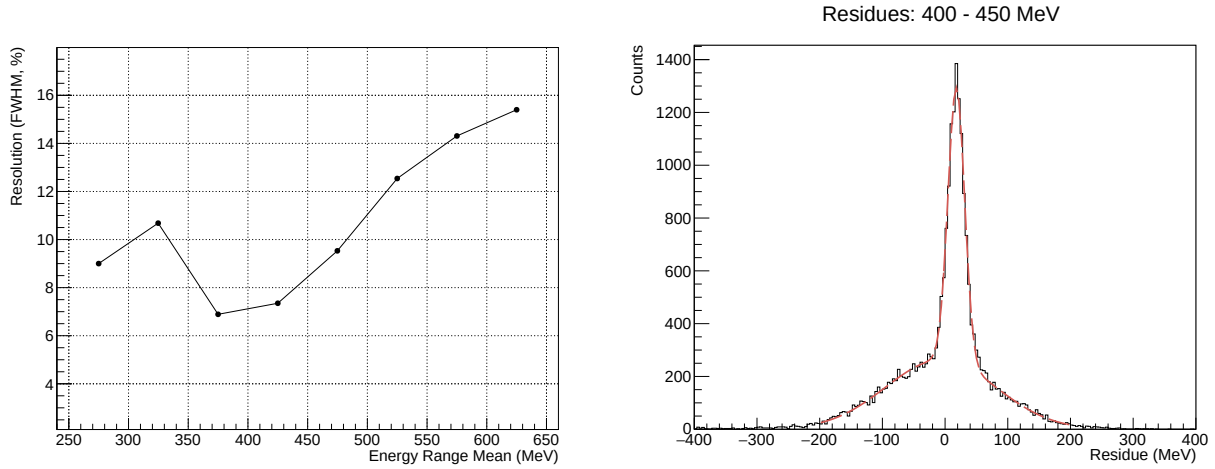

(a) Calculated resolution for the different energy ranges.

(b) Two-Gaussian fit.

Figure 4.38: Results from the proton energy reconstruction.

cause may be a challenging case for a reconstruction procedure. If the opening angle between protons is gated for values larger than $\hat{\alpha} > 70°$, then the amount of quasi-free events will be enough to have both fully stopped and punch-tough cases in a similar amount. Fig. 4.41 shows the more clear correlation between primary energies and reconstructed energies by the same model. The mistaken branch at the low-right part of the correlation is now less pronounced with only 3,07% of the events inside. This can be understood as a more clear kinematic distribution, that can be used by the NN to infer the true energy of the primary particle. Residues show that in this case the energy is similarly reconstructed, but the kinematic distribution is more accurately replicated by the NN, as displayed in Fig. 4.40

This algorithm outperforms the energy loss method discussed earlier, and it efficiently reconstructs both protons without requiring prior sorting into punch-through, nuclear reaction, and fully stopped cases. From the energy residuals that are shown in Fig. 4.37 and Fig. 4.31, it can be noted that the neural network surpasses the energy loss method discussed earlier, as the central peak is narrower for the network, and no further structures appear on both sides as in the previous procedure. Therefore, this approach will be employed to extract the excitation energy for knockout-fission cases using the proton energy provided by the neural network.

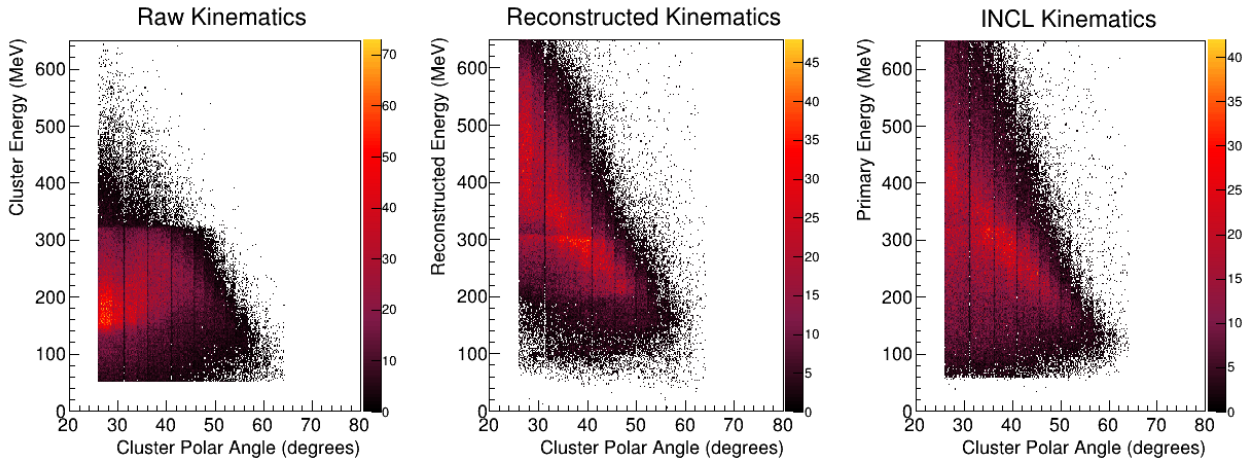

Figure 4.39: Kinematic distribution obtained with model 5187.

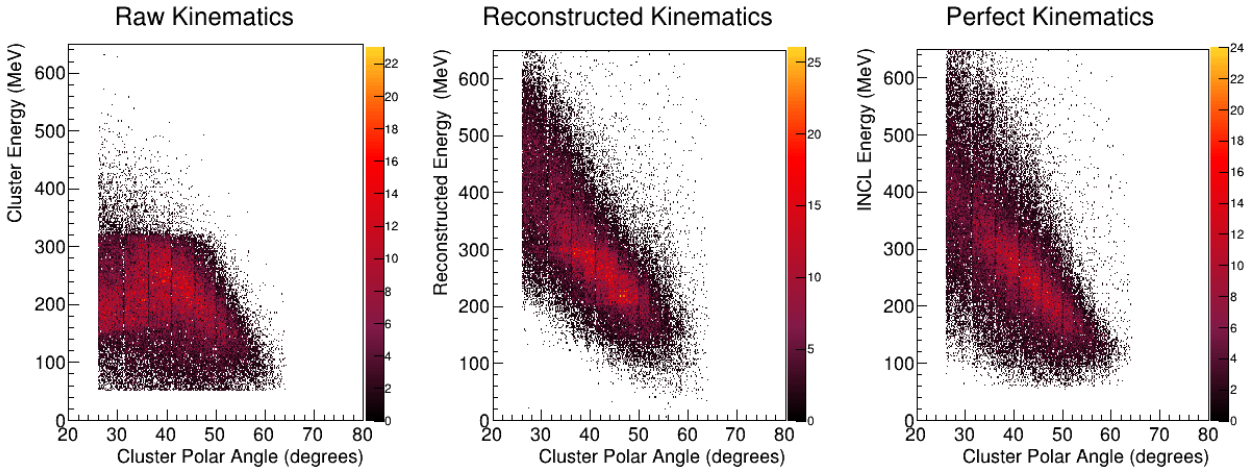

Figure 4.40: Kinematic distribution reconstructed with model 5187 and the opening angle cut applied.

4.8 Excitation Energy Reconstruction

Since the proton vertex reconstruction was not possible for this experiment using the AMS detectors, as shown in previous sections, the angular information of the scattered proton pair was obtained using CALIFA cluster information.

By simulating the reaction in a realistic way, using an INCL event generator and a precise simulated setup, the expected resolutions using AMS and CALIFA can be calculated, as presented in Table 4.12. For the first two cases, the nominal energy resolution of 1% was calculated by smearing the primary proton energy generated in the simulation, using

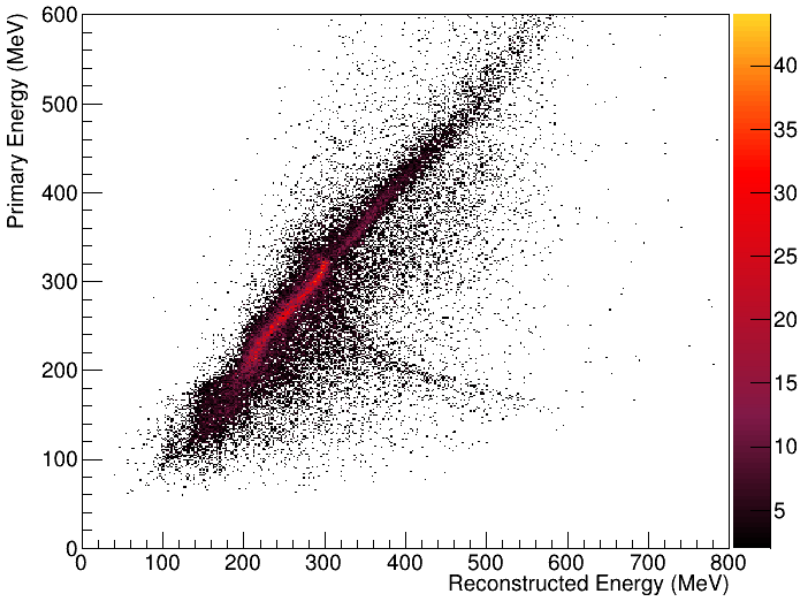

Figure 4.41: Correlation between the reconstructed energy by the NN and the INCL primary energy, with the opening angle of $\hat{\alpha} > 70$ cut applied.

Detection Conditions	**Residue**
AMS + Energy 1%	6,37 MeV
CALIFA Angles + Energy 1%	13,94 MeV
CALIFA Angles + Cluster Energies	39,49 MeV

Table 4.12: Calculated energy differences between simulated excitation energies and reconstructed ones.

a Gaussian distribution. The obtained distributions are Gaussian-shaped and were fitted to obtain the residue. For the case of reconstructing the excitation energy just by taking CALIFA cluster energies, the distribution is asymmetric and not centered in 0, as displayed in Fig 4.42 (left). In that case, the standard deviation of the distribution was given. Clearly, the use of CALIFA angular information degrades the resolution, as the obtained residues are twice the ones obtained using the AMS reconstruction. When the cluster energy is used as the total energy assigned to the protons, the resolution degrades with a standard deviation of 39,49 MeV (92,80 FWHM) in the excitation energy residue.

The same study can be carried out using the NN output, with the two proton energies calculated by the network. Residues can be calculated for several E^* ranges, and fitted to

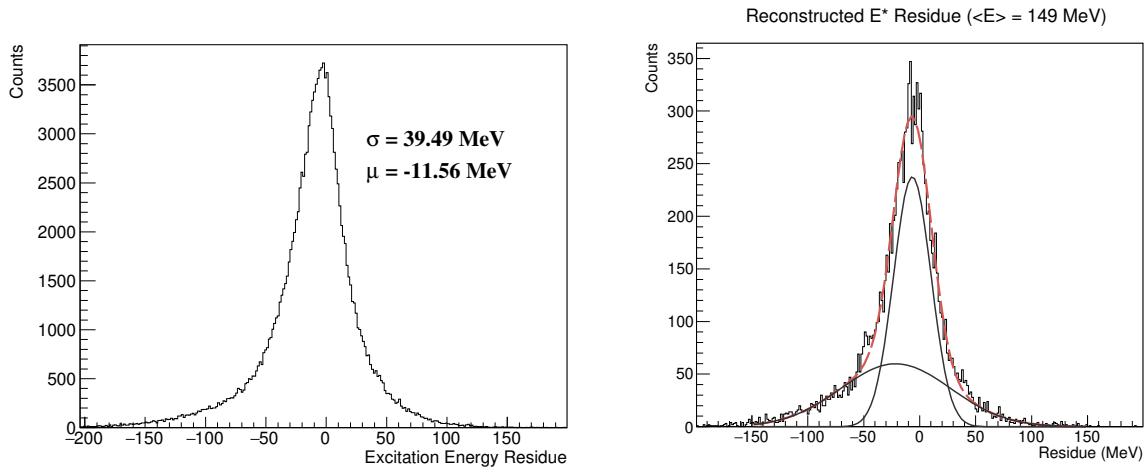

(a) Calculated resolution for cluster case.

(b) Two-Gaussian fit of the NN output at $< E^* >= 149$ *MeV.*

Figure 4.42: Results from the proton energy reconstruction, using raw, cluster energy (left) and the neural network output (right).

two Gaussian distributions (Fig. 4.42, right). These resolutions are obtained as a weighted mean of the two fitted distributions:

$$\begin{aligned} \sigma =& \frac{\sigma_1 A_1}{\sigma_1 A_1 + \sigma_2 A_2}\sigma_1 + \frac{\sigma_2 A_2}{\sigma_1 A_1 + \sigma_2 A_2}\sigma_2 \\ \mu =& \frac{\sigma_1 A_1}{\sigma_1 A_1 + \sigma_2 A_2}\mu_1 + \frac{\sigma_2 A_2}{\sigma_1 A_1 + \sigma_2 A_2}\mu_2 \end{aligned} \tag{4.34}$$

with $\sigma_{1(2)}$ and $\mu_{1(2)}$ the standard deviation and the amplitude of each fitted distribution. The obtained residue width, which characterizes the resolution, is presented in Fig. 4.43. One conclusion that can be extracted from this result is that the resolution does not degrade in a sensible way with the rising excitation energy. This residue width ranges from 26 to 34 MeV and is similar to FWHM characterization. Since the obtained resolution with CALIFA angles and cluster energies was 92 MeV (FWHM), this reconstruction represents a huge improvement over the standard reconstruction method. The correlation curve between the reconstructed and the simulated excitation energy, also presented in the same figure, can be used to correct dependencies.

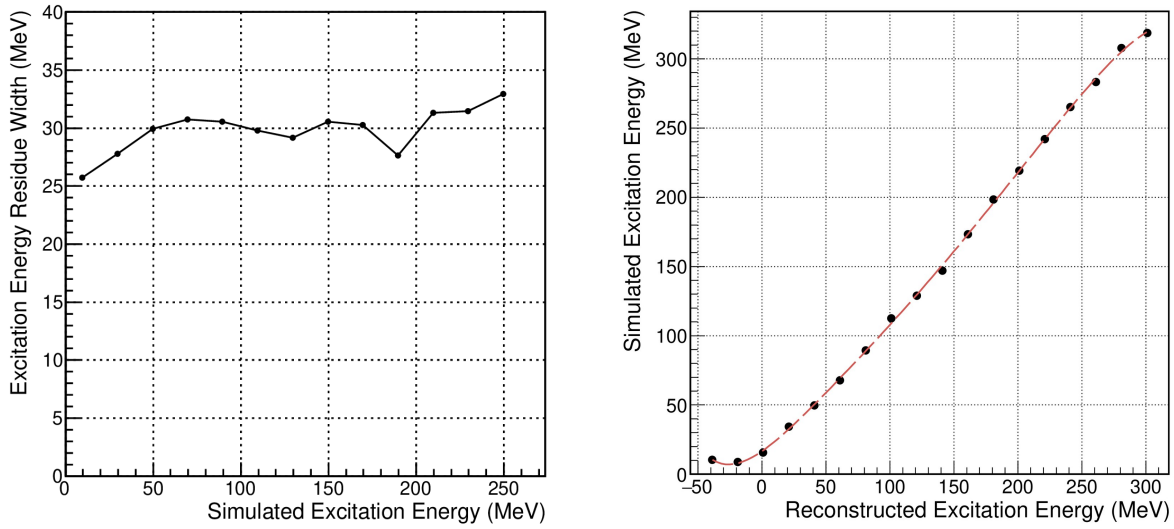

Figure 4.43: ***Left:*** *Obtained excitation energy resolution for each considered range.* ***Right:*** *Simulated excitation energy as a function of the reconstructed value.*

Results and Interpretation

In this chapter, the results obtained by means of the explained analysis tasks and procedures are presented. These results are divided into two parts: the ones corresponding to the spallation-fission case, and the ones corresponding to the spallation-evaporation case. For the spallation-fission reactions, at least two nucleons are scattered, and a charge sum of Z=91 is needed to reconstruct the excitation energy of the protactinium system, although the direct knockout of neutrons in the cascade process is also expected and discussed. This multi-nucleon knockout process results in different remnants and fissioning systems at the end of the intra-nuclear collisions.

In the spallation-evaporation scenario, observable phenomena, such as high-energy clusters detected at CALIFA, stem from reactions dispersed throughout the experimental setup. These reactions primarily take place within the plastic scintillator and the liquid hydrogen target. To accurately quantify the effects of interaction with only the liquid hydrogen target, models are necessary for corrections.

In a general way, fission channels will be referred to as spallation-fission channels, while channels with one heavy ion at the end will be named spallation-evaporation channels. Multi-nucleon knockout naming will be used to characterize a specific reaction channel, where information from outgoing nucleons is measured, studied, and compared with models. Unless otherwise stated, the experimental results are compared with simulated physical cases using INCL + ABLA07, and these simulated observables (angles, particle energies, excitation energies) are obtained from the primary tracks generated by these theoretical models.

5.1 Spallation-Fission Channels

5.1.1 Angular Correlations and Kinematics

For a proper selection of the reaction of interest, first, a fission fragment charge sum of $Z_1 + Z_2 = 91$ was required at the TWIN MUSIC. This corresponds to the Z=91 peak in Fig. 5.1. With this selection, if two clusters are detected in CALIFA, the opening angle between the scattered pair can be calculated as presented in Eq. 2.9.

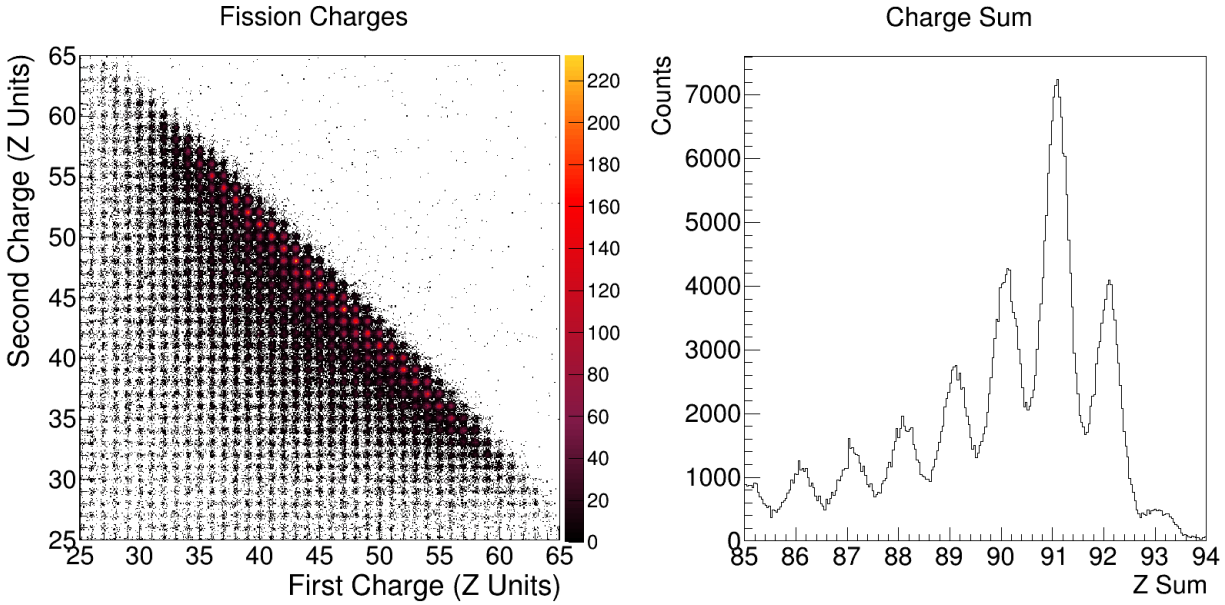

Figure 5.1: Fission charges spectrum for TPat 4 and 10. ***Left:*** *Charge correlation between the two fission fragments.* ***Right:*** *Charge sum of the fission fragments. The peak at $Z_1 + Z_2$=91 corresponds to the two-proton knockout process. The fitted $Z_{Sum} = 91$ peak has a width of $\sigma = 0{,}26$ (0,61 FWHM) charge units.*

The obtained distribution in the left part of Fig. 5.2 shows the experimental opening angle reconstructed with CALIFA angular information. In the same figure, right plot, three simulated cases are displayed: the black distribution corresponds to the reconstructed CALIFA opening angle distribution, with a two-nucleon condition imposed (two high-energy clusters) and the charge sum selection for the two-proton knockout process. The red distribution shows the same observable but obtained with the angular information of the generated tracks by INCL. This distribution is restricted to CALIFA detection conditions (two high-energy clusters inside the AMS acceptance, as in the experimental case). Finally, the green line shows the full opening angle distribution, with no conditions on CALIFA detection, and is also

reconstructed by using primary track coordinates. These three distributions are scaled so a comparison can be made.

This opening angle distribution should reach a maximum value of $\sim 81°$, corresponding to the case where two protons were scattered in a quasi-free regime. This behavior is represented in the right part of the figure by the narrow peak around the expected value of $\sim 81°$, but the lack of angular resolution in the experimental case due to the non-usable silicon tracker makes no possible the direct observation of this reaction process, isolated from the rescattering part on the left side.

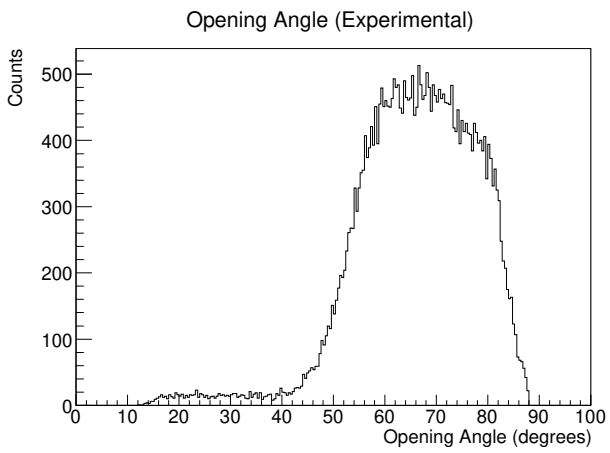

(a) Experimental opening angle.

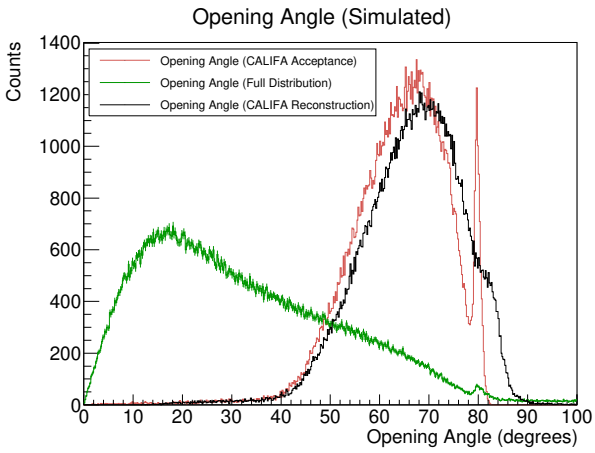

(b) Simulated opening angle.

Figure 5.2: ***a)*** *Experimental opening angle reconstructed with CALIFA.* ***b)*** *Simulated opening angle, for different detection conditions. The green distribution corresponds to the full process. The red and black distributions are conditioned for a two-cluster detection in CALIFA, and represent the primary-track distribution and the reconstructed distribution by CALIFA in simulations. The green distribution for the full process is scaled for better comparison. This scaling factor, defined as the integral of the full distribution divided by the CALIFA reconstructed distribution is about* ~ 0.03 *(CALIFA efficiency for this reaction, with two-proton detection condition under the AMS acceptance).*

For the non-restricted case (green distribution), the quasi-free peak is only a small contribution, as the complete distribution is dominated by the rescattering process, which results on smaller opening angles due to the sequential collisions of the scattered protons inside the nucleus. As the two quasi-free protons share a bigger opening angle, the calorimeter efficiency for this case is much larger than for the general case, resulting in more quasi-free events col-

lected by CALIFA. It can be also observed that for the experimental case, more events appear at the lower part of the distribution, corresponding to angles between 10° and 40°. These low opening-angle values are caused by a single proton detected in CALIFA that formed two adjacent clusters, being this minimum value in opening angle the one corresponding to the chosen angular window for the clustering method (14°).

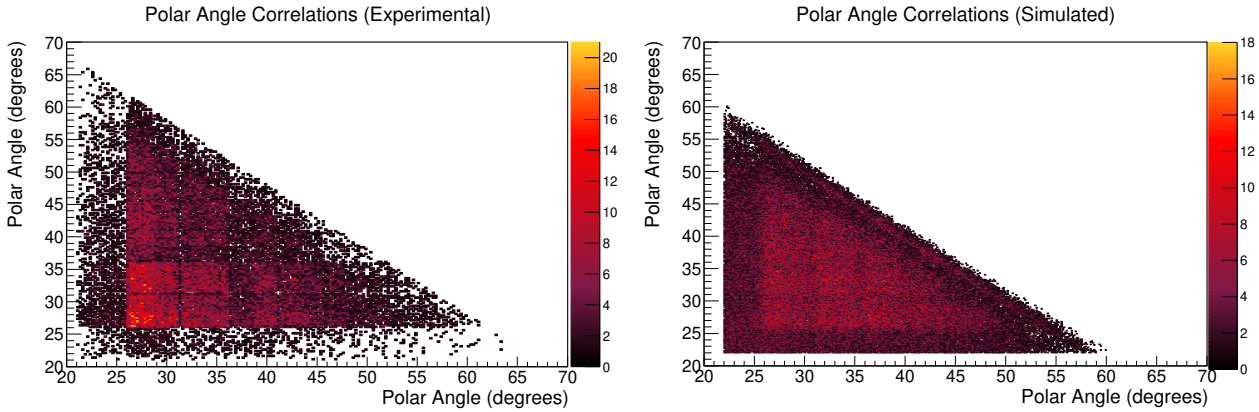

(a) Experimental polar angle correlation. *(b) Simulated polar angle correlation.*

Figure 5.3: Polar correlation of the detected nucleons at CALIFA.

The polar angles of the two clusters detected at CALIFA can be correlated as shown in Fig. 5.3, where the left plot shows the experimental data and the right plot is the simulated one. The simulated case is also conditioned for the detection of two nucleons in CALIFA, resulting in the less populated regions at $\theta < 26°$, corresponding to the AMS detectors acceptance. The quasi-free line appears in the simulated case as a diagonal at $\theta_1 + \theta_2 \sim 81°$.

Regarding the kinematics, the measured distribution is presented in the left plot in Fig. 5.4. This correlation plot displays polar angles of the reconstructed clusters vs cluster energies and shows a sudden cut around 320 MeV, the maximum energy that a CALIFA crystal can stop. If the particle travels through several crystals, then the collected energy in a cluster can be bigger than the single crystal energy, as collected in the experimental case. These energies above the 320 MeV value can also be caused by some background in coincidence with the proton signal grouped in a single cluster.

For a quasi-free like event, the incoming energy per nucleon of 540 MeV would be split between the two scattered protons resulting in, for example and as a simplification (not taking into account fermi momentum inside the nucleus), 270 MeV per particle, a value that could

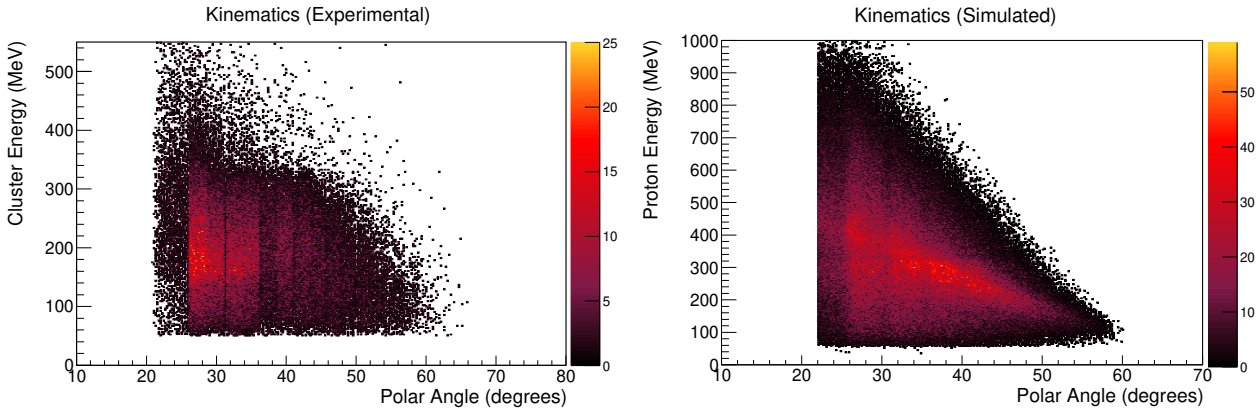

(a) Experimental correlation between cluster polar angles and cluster energies, for the two-proton knockout reaction in coincidence with a fission fragment charge sum of $Z_1 + Z_2 = 91$.

(b) Simulated energy-angle correlation, using information from simulated tracks inside CALIFA acceptance, for the same reaction channel.

Figure 5.4: Experimental and simulated kinematic distributions.

be fully reconstructed by the CALIFA clustering procedure. However, the many intranuclear collisions result in more momentum transferred to the outgoing particles, which can reach energies up to 1 GeV. This case is presented in the right plot of Fig. 5.4. If the distribution is not cut for protons reaching CALIFA (as in the case of having an ideal calorimeter, with perfect energy reconstruction and complete angular coverage), then the full rescattering simulated spectrum can be studied, as shown in Fig. 5.5. From this distribution, it is clear that the majority of the emitted protons after the spallation process are emitted almost collinearly with the beam, escaping through the CALIFA low-angle aperture at high energy.

To overcome the limitations of the energy reconstruction by the CALIFA clustering method, experimental kinematics were obtained using the neural network approach explained in the previous sections. By normalizing the input variables in the same way as in the training procedure, the trained network can be used to obtain the reconstructed proton energies. Fig. 5.6 shows the reconstructed kinematic distribution. Although the resolution is far from the expected 1% for the fully stopped case, the obtained distribution shows that the correction applied by the neural network results in a distribution closer to the real one, with single proton energies up to 600 MeV for the most probable case at $\theta \sim 26°$.

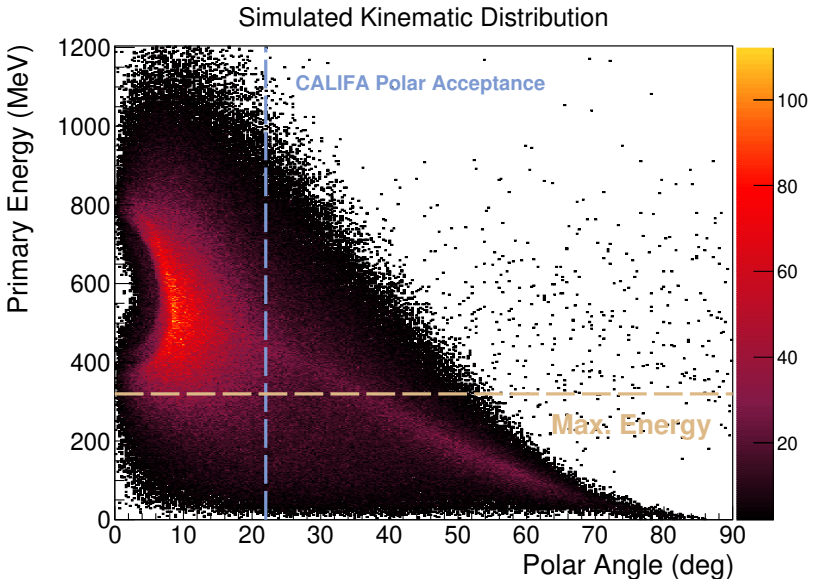

Figure 5.5: Simulated proton energy-angle correlation with no restrictions on CALIFA detection, using primary tracks. The blue and yellow lines show the calorimeter acceptance and the maximum energy that can be stopped by the amount of scintillator material at the iPhos region.

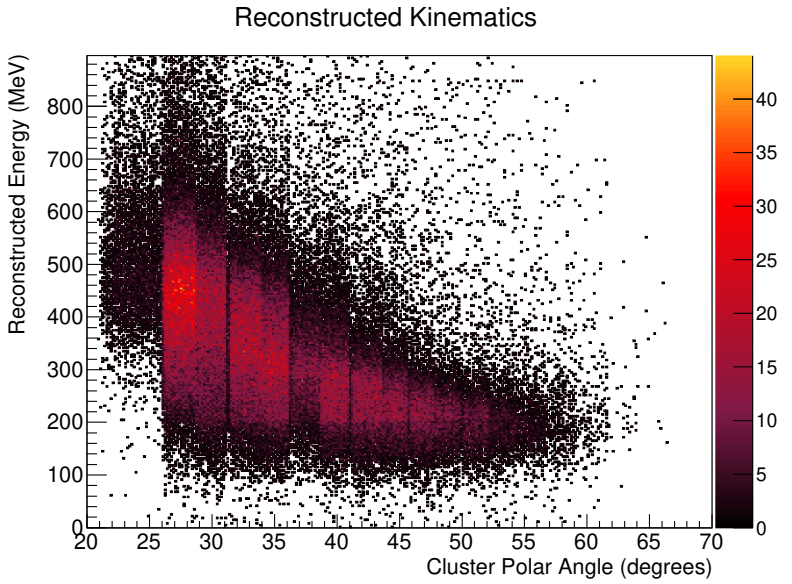

Figure 5.6: Reconstructed experimental kinematics using neural network model 5187. This model is a five-layer model as explained in Chapter 4.

5.1.2 Evolution of the Fission Fragment Charges

5.1.3 Opening Angle

The most direct observable that can be correlated with the evolution of the fission charges is the angle between the two scattered protons. If one (or both) particles suffer from rescattering processes inside the nucleus, then the remnant is left with more excitation energy. In addition, the shared opening angle for the two protons is smaller if one or several neutrons are also knocked out prior to fission. This correlation is presented in Fig. 5.7, and shows the contribution of these two cases.

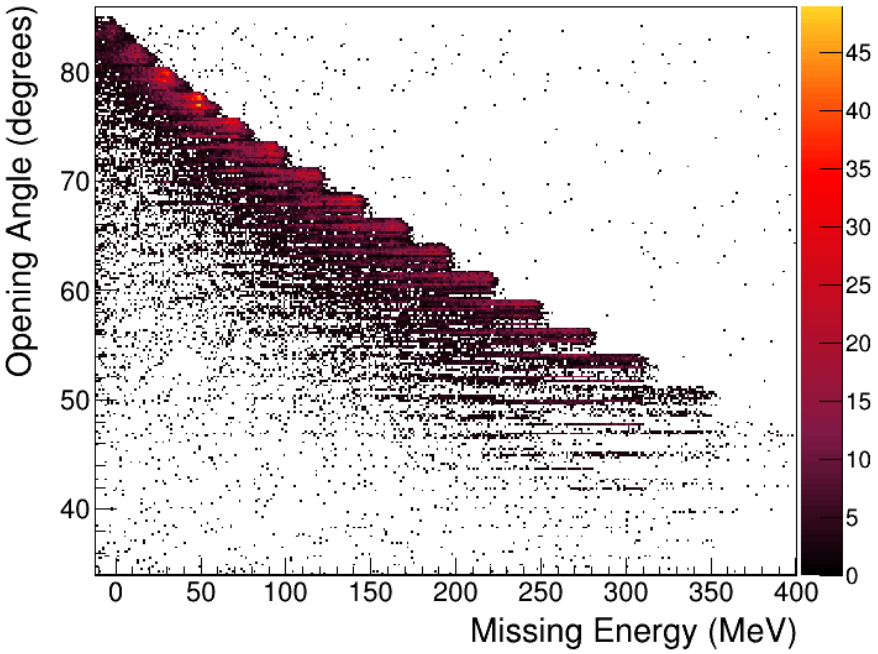

Figure 5.7: Correlation between the reconstructed opening angle and the obtained missing energy, using the neural network approach for proton energy reconstruction.

As shown in this figure, quasi-free-like opening angles, near the 80° region, are associated with lower values of the measured excitation energies, that come from single particle-hole excitations of the ^{237}Pa remnant. If the scattered nucleon collides with more particles inside the nucleus, then these successive collisions result in a momentum addition between the initial scattered proton and the incoming nucleon inside the ion. This translates into smaller polar angles after successive interactions, i.e., smaller opening angles. At the same time,

these interactions leave more excitation energy to the remnant, leading to the correlation that is presented in the figure. Details about the obtained excitation energy distribution will be discussed in the next section.

This observable can be correlated with the obtained fission fragment charge yields, as presented in Fig. 5.8. These yields are defined as

$$Y(Z) = \sum_{A} Y(Z,A), \tag{5.1}$$

which is the sum of a given fragment charge for all the fragment masses.

It can be observed that a transition from symmetric to asymmetric fission occurs as the opening angle rises from the pure-rescattering region to the quasi-free-like region at $\hat{\alpha} \in (75°,85°)$. As stated in the text, the angular resolution of CALIFA is not enough to separate the pure quasi-free region from the rescattering part of the spectrum, as shown in Fig. 5.2. Furthermore, selecting a pure quasi-free process does not necessarily ensure a completely asymmetrical charge distribution. Calculations indicate that the average potential well of the knocked-out nucleon is approximately 21 MeV, which significantly differs from the fission barrier of Pa isotopes.

As it was mentioned before, the obtained opening angle distribution can be wrongly assigned to a proton-neutron pair instead of the two-proton combination. This case is highly improbable in CALIFA, as it requires the detection of a neutron with large enough energy to form a cluster, while one of the protons escapes through the CALIFA aperture at low polar angles, in a way that only two clusters are detected in an event-by-event basis.

5.1.3.1 Excitation Energy

Using simulated data, it can be shown that even if a charge sum of 91 is required at the entrance of the TWIN MUSIC in coincidence with two high-energy clusters at CALIFA, the knock-out of several nucleons before fission is still probable, as shown in Fig. 5.9 (a). These theoretical calculations are obtained with the condition of the two outgoing protons being emitted inside CALIFA experimental acceptance.

The most common case is that a neutron is scattered from the nucleus together with a proton, resulting in a ^{236}Pa remnant, as shown in the left part of Fig. 5.9. As presented in Section 2, the excitation energy of the residual after the knockout process can only be

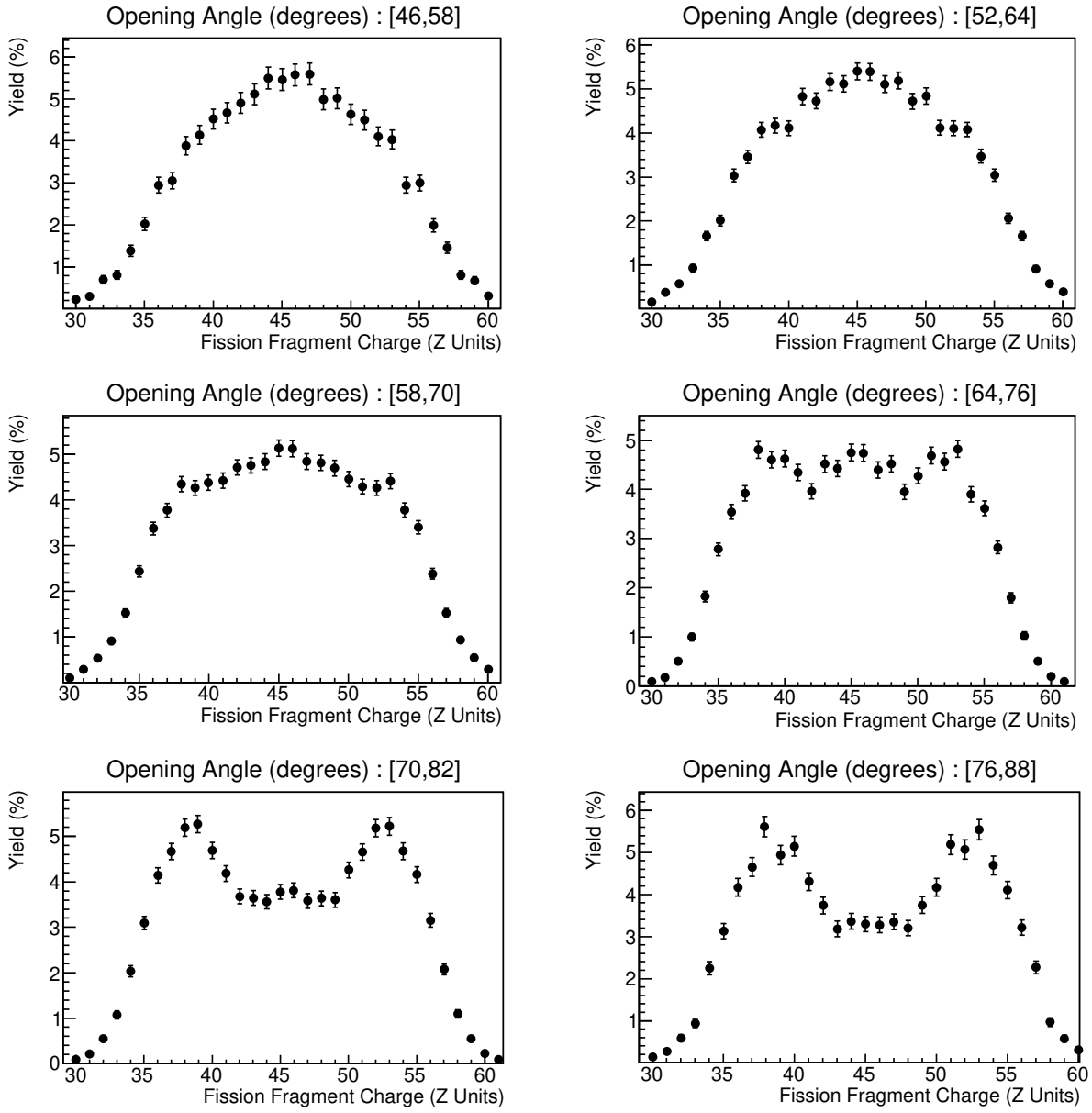

Figure 5.8: Measured fission charge yields as a function of the opening angle between the two nucleons detected in CALIFA. Error bars account for the statistical uncertainty of each fission product. The opening angle region for each case contains the experimental resolution and the chosen window for extracting the fission fragment charges.

measured if only two protons are scattered at the end of the process. In the case of having more nucleons, Eq. 2.17 overestimates the excitation energy attributed to the remnant, as the four-momentum of the scattered neutrons are not considered since these particles are

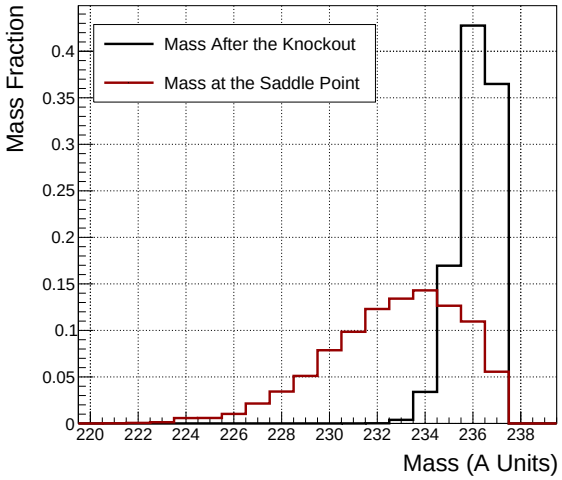

(a) Masses after the two-stage reaction modelization by INCL + ABLA07.

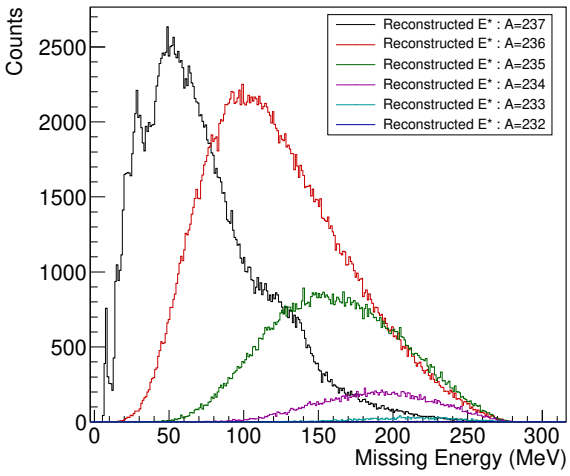

(b) Missing energy reconstruction using the two-proton procedure, for the simulated case and primary tracks energies and angles.

Figure 5.9: ***a)*** *Residue masses after the intranuclear cascade process (black) and masses at the saddle point after neutron evaporation (red).* ***b)*** *Reconstructed missing energy using only the two scattered proton four-momenta. Each distribution corresponds to different masses at the end of the knockout process. These masses and energies are obtained under the coincidence of two high-energy clusters in CALIFA and a charge sum of 91.*

not measured in CALIFA. In this case, the calculated excitation energy is only correct for the ^{237}Pa remnant, being a missing energy for the rest of isotopes, an energy that is shared as kinetic energy of the scattered neutrons and excitation energy of the Pa isotopes. This is presented in Fig. 5.9 (b), where the missing energy is calculated theoretically using only the coordinates of the two outgoing protons, as in the experimental instance. These missing energy distributions overlap when this procedure is used to reconstruct the excitation energy, so no cut is able to separate the different fissioning systems using this observable.

The obtained experimental excitation energy distribution (Fig. 5.10), reconstructed with the two-proton procedure, represents then the missing energy that is associated with the different knockout remnants, that can not be separated experimentally. A cut on the opening angle, with a selection of $\hat{\alpha} \in (70°,83°)$, leads to a decrease in the measured value for this observable, as earlier discussed. The validity of this cut for selecting single isotopes at the end of the cascade will be studied in depth in the upcoming sections.

The peak structure that appear in these two distributions is caused by the gross angular resolution of the califa crystals. As this observable is obtained using discrete angles, the convolution of discrete angles and continuous energies results in those peaks. The use of randomized angles makes this structure disappear, but the resolution in excitation energy is degraded as the reconstructed angles have a bigger error.

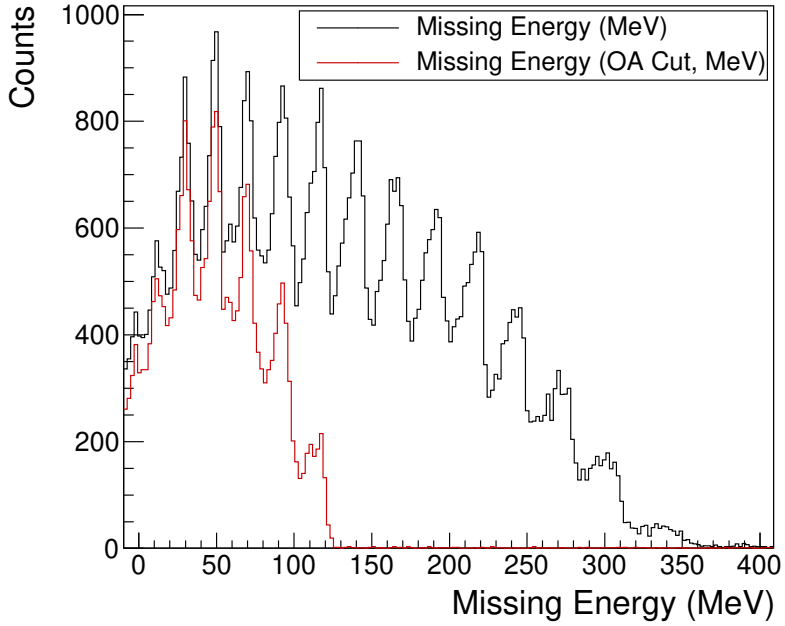

Figure 5.10: Experimental missing energy distribution. The black line corresponds to the full distribution, with no cut on the opening angle (OA). The red line represents the same observable but conditioned for the detection of a reconstructed opening angle in CALIFA in the interval of $\hat{\alpha} \in (70°,83°)$.

Even if different fissioning systems are mixed using this procedure, a study of the yield dependency with this reconstructed missing energy can still be carried out. By reproducing the same experimental conditions with the INCL+ABLA07 models, the damping of the shell effects with increasing energy given to the system can be studied. This comparison involves two steps:

- Reconstruct the theoretical missing energy of the process with only two-proton information, so at the end, several isotopes of Pa are mixed, as in the experimental case.
- The two-proton pair must be within the CALIFA experimental acceptance.

- The missing energy cuts in the simulated case must be applied with a width that corresponds to the expected resolution of the data reconstruction, which can vary for different missing energy ranges.

These calculations can be compared with the obtained fission fragment charge evolution, as is presented in Figures 5.11 and 5.13.

The first comparison involves the standard output from the de-excitation code ABLA07, represented as the blue line in Fig. 5.11. The green line represents a shift of the superfluid phase from 5 MeV to 20 MeV. As stated in [28], based on measured data from [73] and [74], the addition of more excitation energy results in a constant temperature behavior, as this extra energy is used by the system in the creation of more internal degrees of freedom, so this temperature stays constant and follows the relation

$$\rho(E^*) \propto exp(E^*/T), \tag{5.2}$$

where ρ is the level density at a given excitation energy (E^*). This phase shift is coupled then to a fermi-gas model at 20 MeV as measured in [74]. This shifted phase change would be more visible by correlating the final masses of the fission fragments with the excitation energy, as up to 20 MeV, the two fragments in thermal contact would exchange energy from the lighter fragment to the heavier, resulting in a net increase of the system entropy. This theory explained the behavior presented in [75], where the addition of more E^* to the system resulted in more evaporated neutrons only for the heavy fragment. For this reason, the calculated, theoretical yields will be studied using this phase shift.

As shown in Fig. 5.11, the difference between the two calculations is more prominent in the low-energy region, where the shell effects are expected to play a major role. In particular, at low energy, the first plot centered in a missing energy (M.E) of 22 MeV shows a notorious difference for the shifted-phase calculation, that correctly accounts for the SL fission mode contribution centered at charges 45 and 46. These differences are almost non-existent at higher energies, as expected, but only up to the third M.E cut, where these differences are present again. This M.E region is the place where the second system, ^{236}Pa, appears. This energy slice corresponds then to a mixture of ^{236}Pa at low energy and ^{237}Pa at high energy and explains why the two calculations differ at this point, and also explains the asymmetric components of these distributions, as this measured missing energy does not correspond to the excitation energy left to the remnant. The same behavior is repeated at different places, according to where the different distributions presented in Fig. 5.9 (b) start to appear,

weighted by their probability of appearance. Even if the two calculations are consistent,

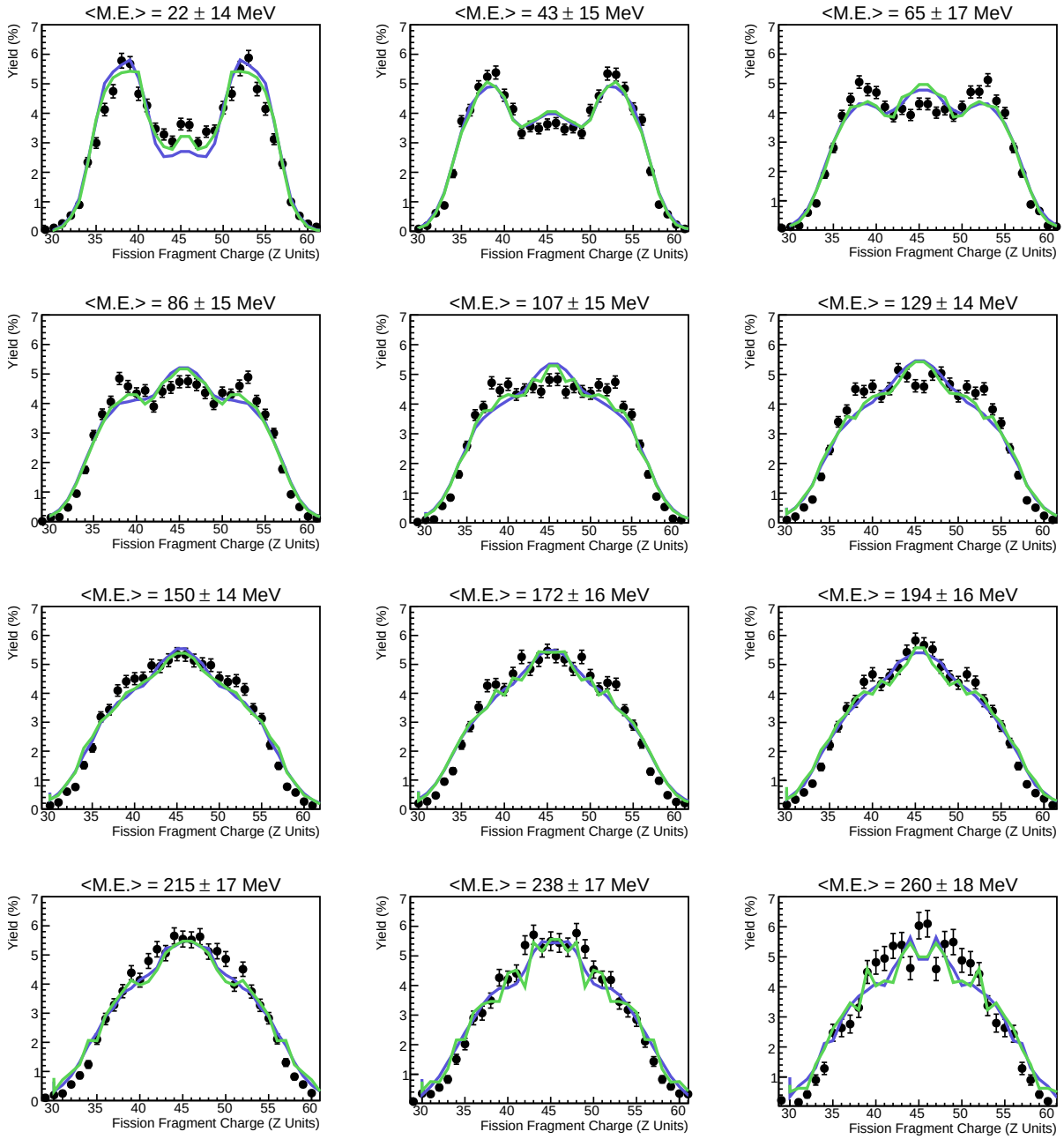

Figure 5.11: Experimental yields compared with ABLA07 calculations, for the standard version of the code (blue-dashed line) and for the shifted superfluid phase (green-dashed line). Missing energy intervals are selected with a width of 4 MeV, with each energy value displayed here as the center of the selection. Theoretical yields are obtained with the same width for comparison. Error bars account for the statistical uncertainty of the charge yields.

there are some discrepancies between the model and the experimental data. It seems that for higher missing energies, the asymmetric component has more weight than expected by the calculations. This can be caused by two reasons:

- The damping function applied to the shell energy correction, or the method that calculates this contribution, is inadequate to reproduce the experimental trend.
- The evaporation of neutrons and gammas before the saddle point is not correctly modeled. In this case, an underestimation of the amount of evaporated particles would lead to a compound system with more excitation energy at the saddle point, which would cause more contribution from the symmetric fission mode.

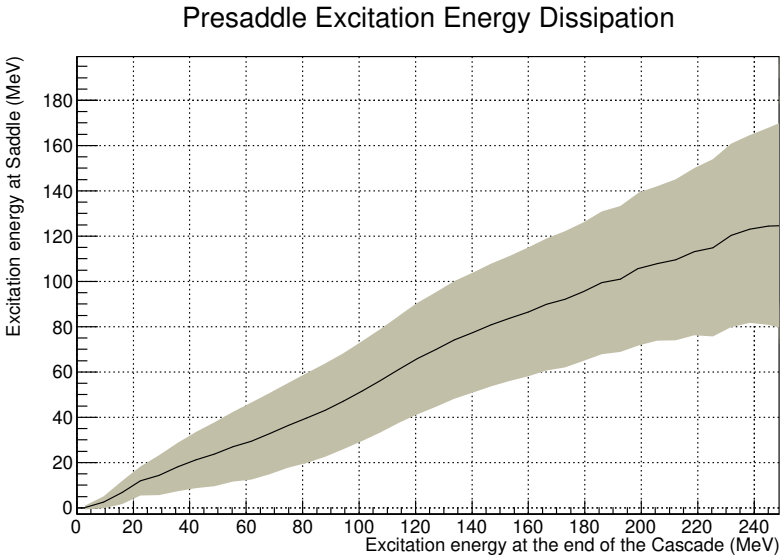

Figure 5.12: Theoretical dissipation curve for ^{237}Pa. The excitation energy at the saddle point is calculated as a function of the remnant excitation energy after the knockout process.

This effect is shown in Fig. 5.12, where the solid-black line represents the mean value of the excitation energy at the saddle point as a function of the energy left to the remnant after the intranuclear cascade. The shadowed region represents the width of the distribution, measured as a standard deviation, for each energy cut. The evaporation of gammas results in different excitation energies at the saddle, but the evaporation of neutrons also results in different fissioning systems, that are calculated theoretically in Fig. 5.9 (a). No experiment in inverse kinematics can measure how many neutrons are emitted before scission on an event-by-event basis, as they are emitted at the same angles as the ones that the fission fragments evaporate. However, the study of the obtained mass distributions, together with

a high-resolution measurement of the excitation energy can be used to compare calculations and experimental yields, as performed in [76] and [77].

The experimental-obtained yields were also compared with the calculations, but this time, a damping function was proposed to study the asymmetric mode's contribution as a function of the excitation energy, instead of the level-density dependent calculations provided in ABLA07, based on the original calculations in [78]:

$$Y(M) = \frac{\int_0^{E-V_f(M)} \rho(U)\ dU}{\sum_{M=0}^{A} \int_0^{E-V_f(M)} \rho(U)\ dU} \cdot 200(\%), \tag{5.3}$$

where each fission mode yield ($Y(M)$) was calculated using the density of excited states $\rho(U)$ at the saddle point. The sum is performed from an energy of 0 up to the energy of the excited nuclei (E), minus the height of the fission barrier ($V_f(M)$) for each fission mode. This barrier height depends on liquid drop model calculations, shell corrections and potential energy surface curvatures for each fission path.

For the modified calculations where the superfluid phase was displaced to 20 MeV, the shell energy correction was weighted instead by an exponential function, dependent on the excitation energy of the system, in the form

$$S(E^*) = \exp\left(-E^*/E_0\right), \tag{5.4}$$

with different values of the damping parameter, E_0. Randrup's parametrization was also used as presented in 2.14, with values $E_0 = 15$ MeV and $E_1 = 20$ MeV, as stated in the published work.

This comparison is depicted in Fig 5.13, where the different curves represent different values of this E_0 constant. As a result of this study, it can be concluded that a damping parameter of 40 MeV and Randrup's damping function are the ones that better reproduce the general trend of the obtained yields. These prescriptions describe well the asymmetry components at high missing energies. However, this result cannot be directly compared with the ideas in [26] and [27], where the damping functions of the shell effects were presented. In these theoretical works, calculations are made for single fissioning systems, that evolve from the saddle point up to the scission point according to the presented theories. In this case, these experimental results gather different fissioning systems, from ^{224}Pa to ^{237}Pa, as a result of different reaction processes and particle evaporation on the way up to the saddle point.

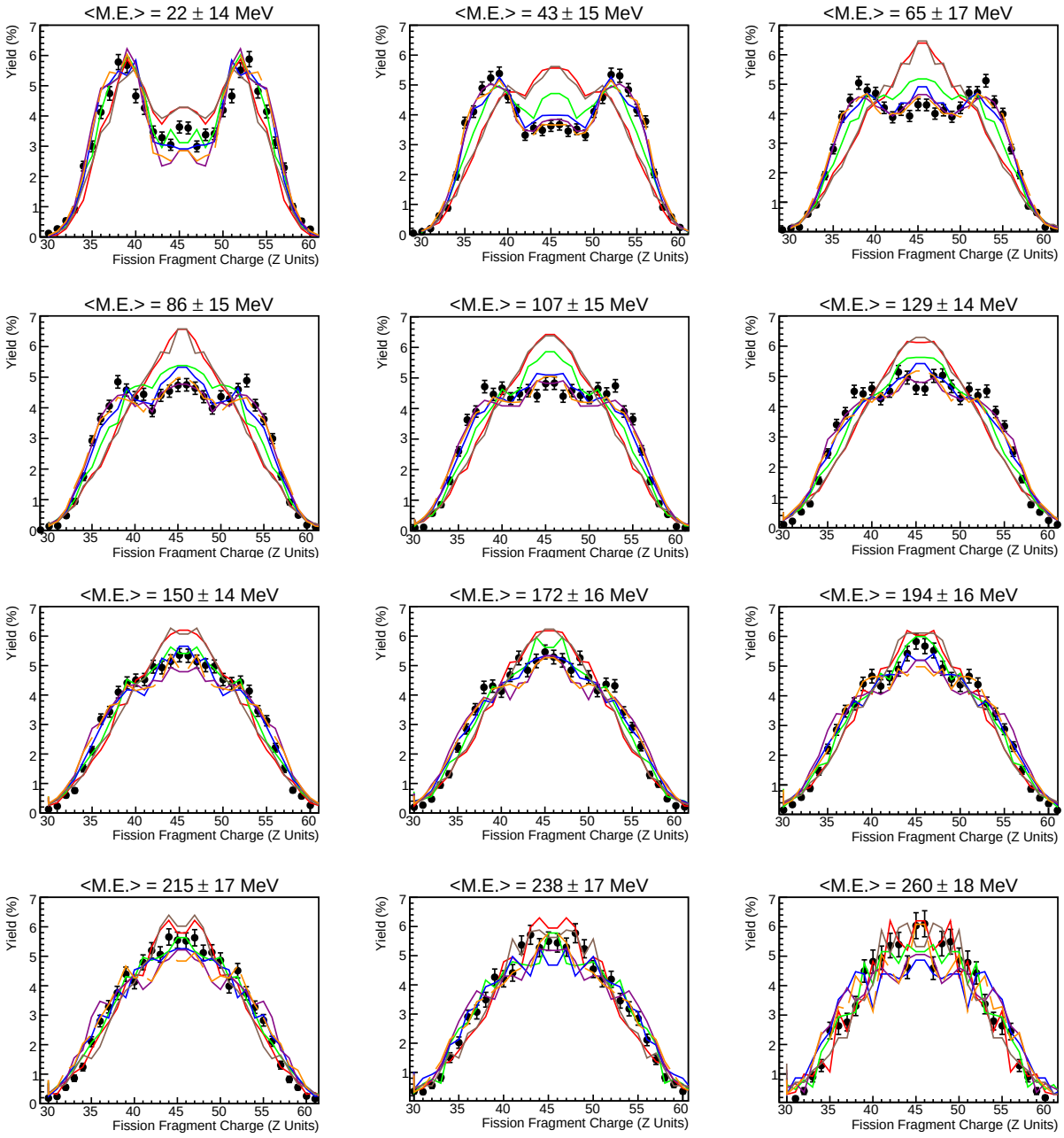

Figure 5.13: Experimental charge yields compared with ABLA07 calculations, with different values of the damping constant: E_0=10 MeV in red, E_0=20 MeV in green, E_0=30 MeV in blue and E_0=40 MeV in purple. Randrup prescription is shown as a dashed-orange line.

In an attempt to select only reactions with two protons at the end of the reaction process, a study of the different opening angle distributions for the different masses at the end of the cascade was carried out using INCL. As presented in Fig. 5.14(a), the opening angle distri-

bution for the A=237 residue can be separated from the rest by setting an appropriate cut around $\hat{\alpha} \sim 75°$. These distributions were convoluted with CALIFA angular resolution by propagating the primary particles generated by INCL in the simulation explained in previous sections. Table 5.1 gathers the obtained contaminations and efficiencies for the different cuts.

Cut	Ratio of A=237	Contamination	Cut Efficiency (A=237)
$\hat{\alpha} > 70°$	84.57 %	15.43 %	40.51 %
$\hat{\alpha} > 75°$	94.12 %	5.87 %	21.53 %

Table 5.1: Obtained contaminations and efficiencies rates for different opening cuts at CALIFA.

As it can be observed, a cut of $\hat{\alpha} > 75°$ could potentially clean the spectrum and therefore leave only events with a remnant mass of A=237. In that case, only a 21.53 % of the original distribution can be studied. While statistics are high enough to apply this condition, by selecting only those events at a high opening angle the associated excitation energy distribution is only reaching 78 MeV. In this case, with a resolution of nearly 30 MeV, only two meaningful cuts could be applied, so it was decided to use a minimum opening angle value of 70°, which allows some of the rescattering processes to occur and the excitation energy of the process can then rise to 120 MeV, as presented in Fig. 5.10 (b).

The theoretical fission probability as a function of the excitation energy given to the ^{237}Pa residue, which would be the most probable isotope after the quasi-free cut is displayed in Fig. 5.14 (b). As this excitation energy is conditioned for later fission, the minimum excitation energy required is directly related to the fission barrier for ^{237}Pa. This energy is represented by the narrow peak around 6 MeV. This barrier was also calculated by using the prescription of GEF [79] (5.43 MeV) and by P. Möller et al [80] (5.99 MeV). It can be also observed that a second larger probability region arises at higher excitation energies, around 12 MeV (second-chance fission), and it is repeated periodically. Those distributions correspond to the sum of the fission barrier plus the required energy to evaporate several neutrons and gamma rays. On its way up to the saddle point, the excited nucleus has enough energy to de-excite via neutron evaporation and gamma-ray emission, a process that competes with the fission process. The amount of evaporated neutrons in this pre-saddle stage depends on the ratio between the fission barrier and the neutron separation energy, S_n. If this separation energy is lower than the fission barrier, then more neutrons are evaporated in the pre-saddle stage. If S_n and the fission barrier are comparable, as this is the case (S_n (^{237}Pa) = 5.87 MeV),

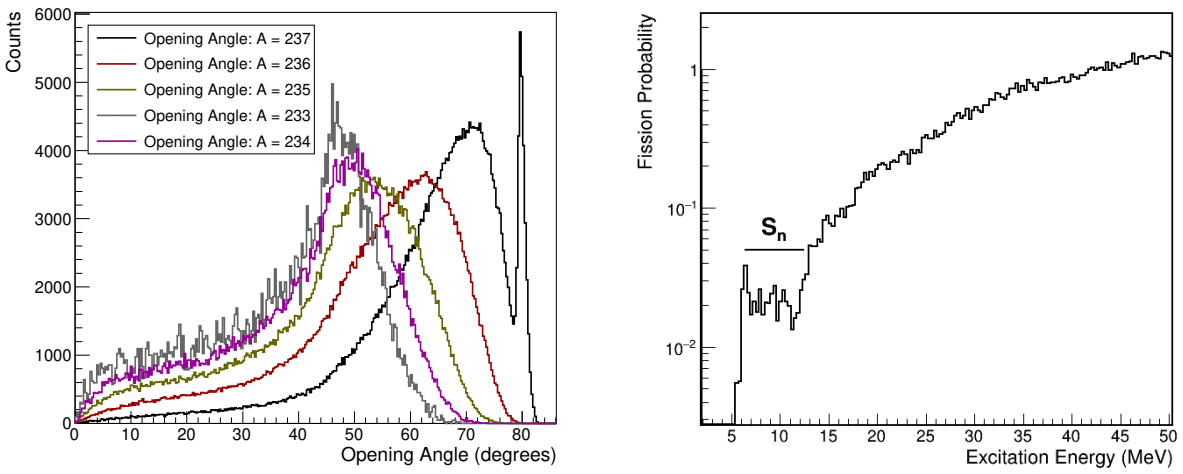

(a) *(b)*

Figure 5.14: Theoretical distributions. ***a):*** *Opening angle distributions for different residues after the knockout process.* ***b):*** *Fission probability for an A=237 residue as a function of the excitation energy.*

fewer neutrons are emitted in this process, but resulting in different fissioning systems at the saddle point, as shown in Fig. 5.9 (a) for the full reaction process.

Yield evolutions are shown in Fig. 5.15, for the applied quasi-free cut. As obtained with the previous case, the best approximation to the obtained experimental yields is achieved by a damping function with an E_0 value of 40 MeV and also using Randrup's formula. These calculations mostly differ in a sensible way from data near $E^* = 65$ MeV, as mentioned before, this point is where the contamination from the ^{236}Pa residue is expected to come, resulting in a more notable contribution from asymmetric fission modes.

5.1.4 Cross Sections

The fission cross-sections, obtained using the analysis methods detailed in the preceding sections, are showcased here. Even when a specific charge sum is chosen for the two fission fragments, the exact mass of the fissioning system remains indeterminate due to neutron knockouts in addition to proton knockouts prior to fission. Hence, the cross-sections are presented as a sum across various isotopic chains following the knockout process (U, Pa, Th, Ac, Ra).

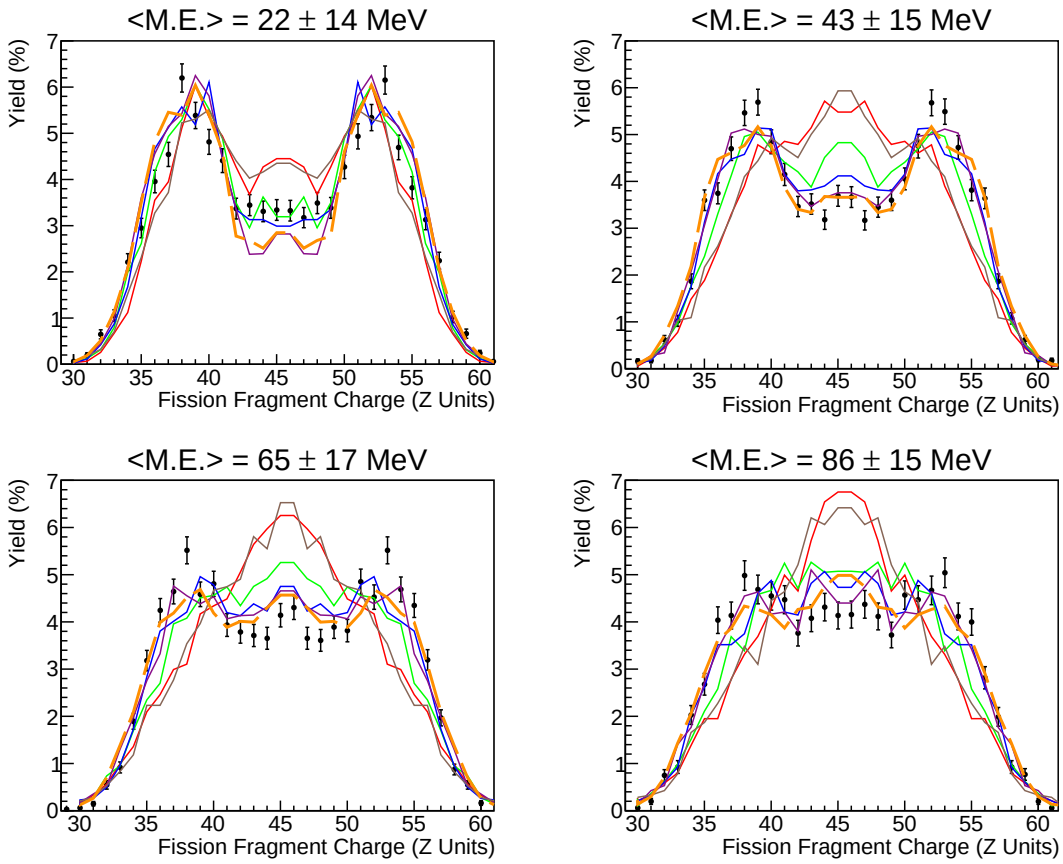

Figure 5.15: Evolution of the fission yields as a function of the excitation energy, with a quasi-free cut applied for $\hat{\alpha} > 70°$. Error bars account for the statistical uncertainty of each charge yield. The damping functions are represented by different line colors: E_0=10 MeV in red, E_0=20 MeV in green, E_0=30 MeV in blue, and E_0=40 MeV in purple. Randrup prescription is showcased as a dashed-orange line.

For each charge sum, the obtained cross-section was obtained using two methods: with CALIFA efficiencies calculated using the INCL libraries for Geant4 and the Bertini cascade model. Systematically, INCL libraries in simulation give lower values for the calculated efficiencies, resulting in higher cross-section values. This behavior is explained by studying the energy deposition in CALIFA using this library, which produces a higher number of nuclear reactions inside the crystals.

This trend is presented in Fig. 5.16, where in addition the obtained values calculated using the Bertini model for the simulations and the combined value are presented. This combined value is obtained by randomly choosing one of the efficiency distributions obtained

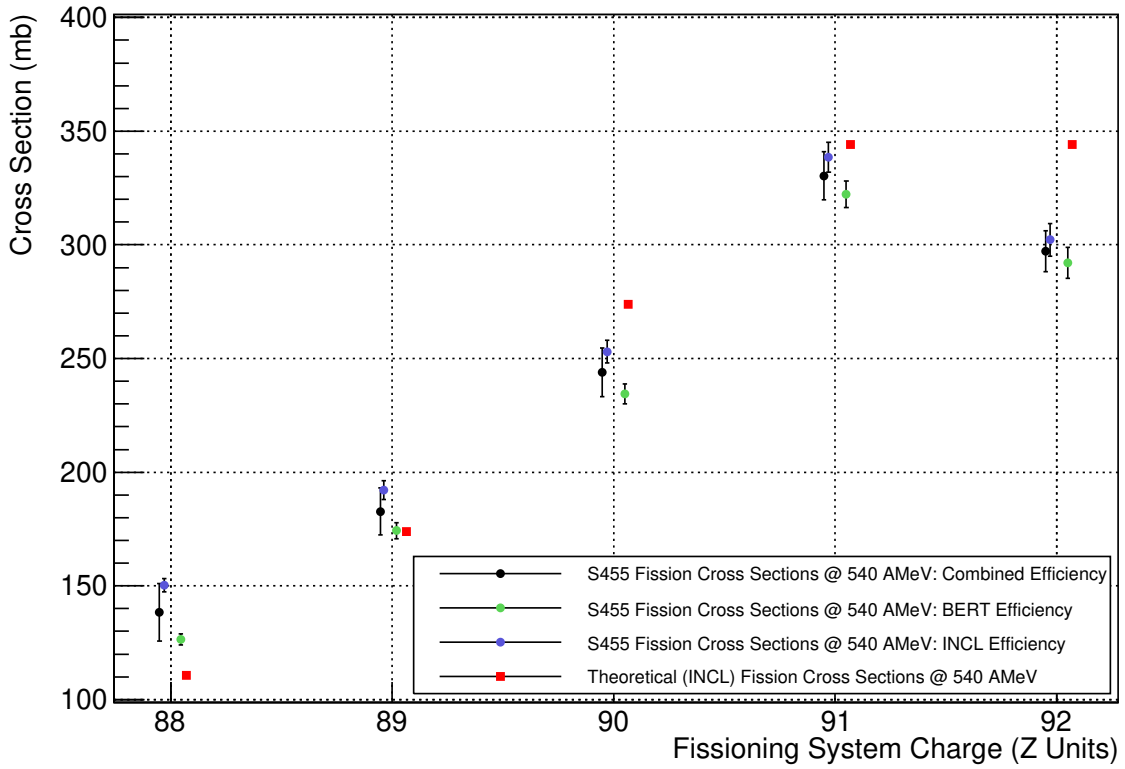

Figure 5.16: Fission cross-sections for the different fissioning system charges. Each experimental point error bar includes systematic and statistical uncertainties.

with the two libraries and simulating the cross-section calculation. The obtained width of the cross-section distribution is then a convolution of the difference between the two calculations and the associated systematic and statistical uncertainties of the different cuts and observables used for the measurements. This width is therefore used for estimating the associated uncertainty of the measured cross-sections. The procedure is depicted in more detail in Appendix C. The obtained numerical values are presented in Table 5.2.

The largest disagreement between theory and the experimental results corresponds to a charge sum of $Z_1 + Z_2$=92, the knockout and evaporation of neutrons without any outgoing proton. This case is especially difficult for CALIFA, as the detector was not designed to be efficient and precise in terms of neutron detection and energy reconstruction. However, the two methods used are consistent, and both differ from the theory calculation in a similar amount. The rest of the cases are well reproduced by theory, with some discrepancies, always

$Z_1 + Z_2$	σ_{INCL}	σ_{BERT}	$\sigma_{\mathrm{Combined}}$	σ_{Theory}
92	302 ± 7 mb	292 ± 7 mb	297 ± 9 mb	344 mb
91	338 ± 7 mb	322 ± 6 mb	330 ± 11 mb	344 mb
90	253 ± 5 mb	234 ± 4 mb	244 ± 11 mb	274 mb
89	192 ± 4 mb	173 ± 4 mb	183 ± 10 mb	173 mb
88	150 ± 3 mb	126 ± 2 mb	138 ± 13 mb	111 mb

Table 5.2: Numerical values for the obtained fission cross-sections.

smaller than 10% of the total value.

For the $Z_1 + Z_2 = 91$ fissioning system, where two protons are scattered before fission, it could be interesting to know how much of the quasi-free processes contribute to this reaction. Since only one nucleon is required to measure these cross-sections, the quasi-free peak cannot be isolated using just experimental data from CALIFA, which in addition does not have the required angular resolution to perform this task. For this reason, only an estimation of this process is given here, relying on INCL simulations. From this simulation, the fraction of quasi-free events arriving to CALIFA using the same experimental configuration can be calculated and used to weight the experimental cross-section.

$Z_1 + Z_2$ (Quasi-free)	σ_{INCL}	σ_{BERT}	$\sigma_{\mathrm{Combined}}$	σ_{Theory}
91	3.12 ± 0.07 mb	2.89 ± 0.05 mb	3 ± 0.10 mb	3.18 mb

Table 5.3: Numerical values for the obtained fission cross-sections, for the quasi-free condition.

Table 5.3 gathers the obtained values for this quasi-free cross-section estimation. As already seen in the simulation where the opening angle between protons was studied (Fig. 5.2), this process is only a small portion of the complete scattering mechanism, resulting in an experimental value of around 3 mb, very close to the calculated theoretical value. However, this estimation completely relies on the fraction of quasi-free events that INCL generates at the end of the intra-nuclear cascade, which is used to calculate this fraction that is applied to experimental, total cross-sections. This result should be then understood as an estimation of the real value, which should fall within this order of magnitude. In addition, the complete quasi-free mechanism is divided into fission and evaporation channels. For the latter, no isolation of charge or vertex can be used to estimate the quasi-free part, which should be added to the one estimated here for fission channels.

5.2 Spallation-Evaporation Channels

5.2.1 Angular Correlations and Kinematics

The angular correlations after a two-nucleon detection in CALIFA are presented in Fig. 5.17. As in the case of a spallation-fission reaction, the assignment of the remnant charge on an event-by-event basis does not guarantee that only two nucleons were scattered in the knockout process. However, contrary to the case of fission channels, multinucleon knockout and rescattering processes are less probable since the excitation energy given to the remnant would be high enough making fission much more probable than only evaporation of particles by the heavy remnant. This is reflected in the reconstructed polar and opening angle

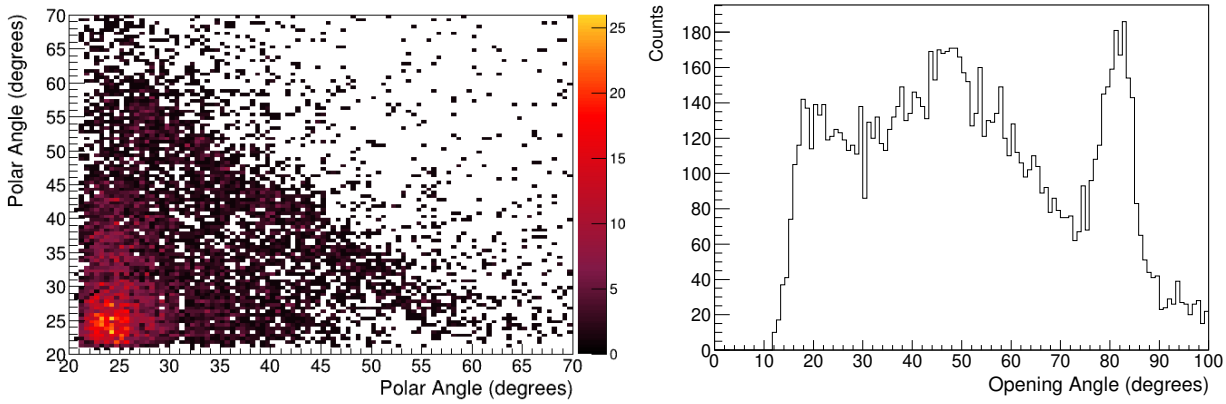

(a) Experimental two-nucleon polar correlation, in coincidence with a heavy fragment travelling through the TWIN MUSIC detector.

(b) Experimental opening angle distribution.

Figure 5.17: Experimental polar correlations and reconstructed opening angle for the spallation-evaporation channel. No specific charge is selected for any of the plots.

distributions of Fig. 5.17. The peak centered in $\sim 80°$ in the right part of the figure and the diagonal distribution on the left side account for quasi-free processes produced in the reaction target, for the reactions ^{238}U(p,2p)^{237}Pa* and ^{238}U(p,pn)^{237}U*. The perfect isolation of the quasi-free distribution, even with CALIFA angular reconstruction, shows that almost no rescattering process is present in this case, as expected. The left part of the opening angle distribution is caused by reaction channels coming from other parts of the setup or by reaction channels with more than two nucleons at the end of the knockout process. A charge selection to isolate these two distributions is not possible for two reasons:

- Charge states mix several heavy residue charges, so a complete isolation of a single reaction process can not be performed.
- The quasi-free-like channels, $^{237}U^{*}$ and $^{237}Pa^{*}$, can be also produced in other parts of the setup, mainly in the start plastic scintillator.

The effect of having reactions coming from other parts of the setup can be also observed if the kinematic distribution of the detected nucleons in CALIFA is obtained. In Fig. 5.18 (a), the kinematic distribution presents a quasi-free-like behavior for polar angles larger than 25 degrees. The high-energy clusters detected at lower angles are coming from reactions before the calorimeter. The maximum energy that a cluster should collect from reactions centered in the target should be around 320 MeV, but if a high-energy nucleon comes from behind the detector transversing several layers of crystals, and on top of that several nucleons are detected, a single cluster with high energies can be formed at low polar angles. For a better understanding of the process, the correlation between the opening angle and the cluster energy is shown in Fig. 5.18 (b). As explained before, quasi-free-like opening angles, around 80° correspond to reasonable cluster energies coming from the reaction target position, being 320 MeV the approximate limit for these cluster energies.

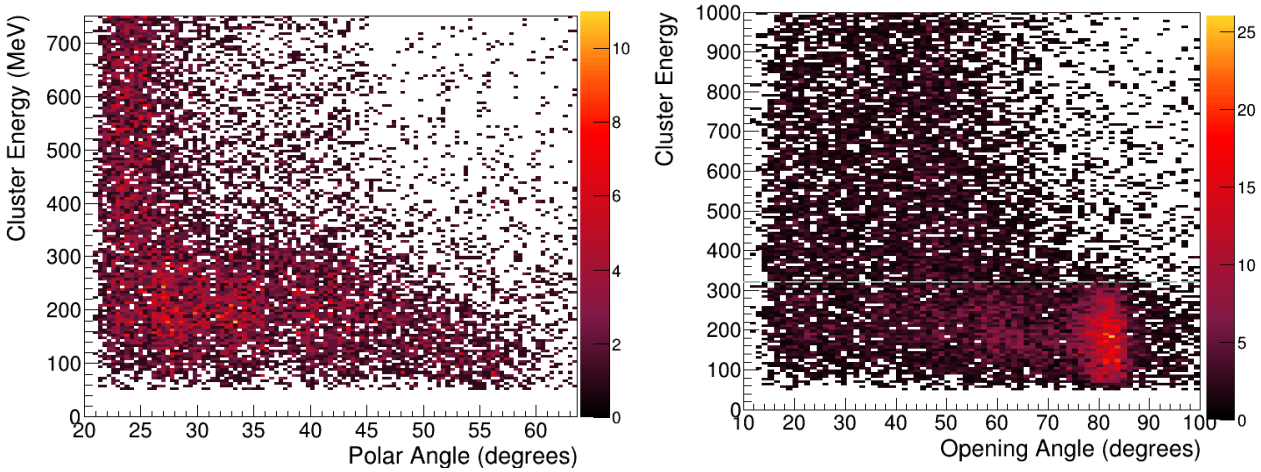

(a) *(b)*

Figure 5.18: ***a):*** *Energy-angle correlation showing kinematic distribution for all spallation reaction channels.* ***b):*** *Correlation between the measured opening angle at CALIFA and the collected cluster energies. The green line represents the 320 MeV energy line, the maximum energy that a crystal in the iPhos region of CALIFA can measure if the particle travels along the main crystal axis (i.e. particles emitted from the target region).*

Examining how the distribution of opening angles is influenced by the selection of cluster energies, particularly when they fall below the anticipated energy threshold, could clean the opening angle distribution. This was done by implementing a restriction on polar angles exceeding 26 degrees, and allows for a cleanup of the opening angle distribution, as presented in Fig. 5.19.

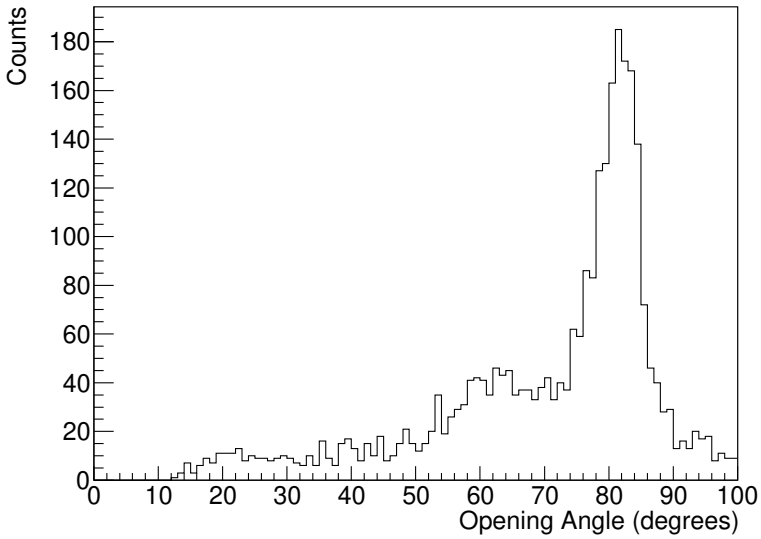

Figure 5.19: Opening angle distribution with cuts on cluster energies and angles.

As discussed before, this cut leaves mostly reactions coming from the reaction target point, with a major contribution of the quasi-free reaction channels. As presented in Chapter 5, model calculations were performed to correct reactions coming from other parts of the setup, as these cuts on cluster energies and angles completely overlap for the two cases, making it difficult to calculate contaminations and efficiencies in this way.

5.2.2 Cross Sections

The obtained spallation-evaporation cross-sections are discussed here. The analysis methods presented in Chapter 4 allowed for the determination of these cross-section values for the different channels, that are compared with theoretical calculations. For these reaction channels, a comparison is made between the obtained values and experimental results from [81], and theoretical calculations for the latter are also presented. Fig. 5.20 represents the trend for different isotopic chains, from actinium to uranium. Experimental data from [81] were used

for comparison, as the expected cross-section for nucleon removal at these energies is similar. The obtained values in this work are presented by using three different CALIFA efficiencies, similar to the case of the spallation-fission cross-sections. Contrary to the previous results, the use of different Geant4 libraries for particle propagation inside the active material does not change the result in a sensible way. The main difference between INCL and the Bertini cascade model was the treatment of nuclear reactions inside CALIFA crystals. In the case of fission, rescattering is more probable as the excitation energy left to the remnant is larger. This leads to increased energies for the scattered nucleons. As previously explained, higher energies are more likely to undergo nuclear reactions within the scintillator material. For the present case, the quasi-free-like behavior of the two main reaction channels results in a similar response by the two models. From the values displayed in Fig. 5.20 and in Table 5.4, it can

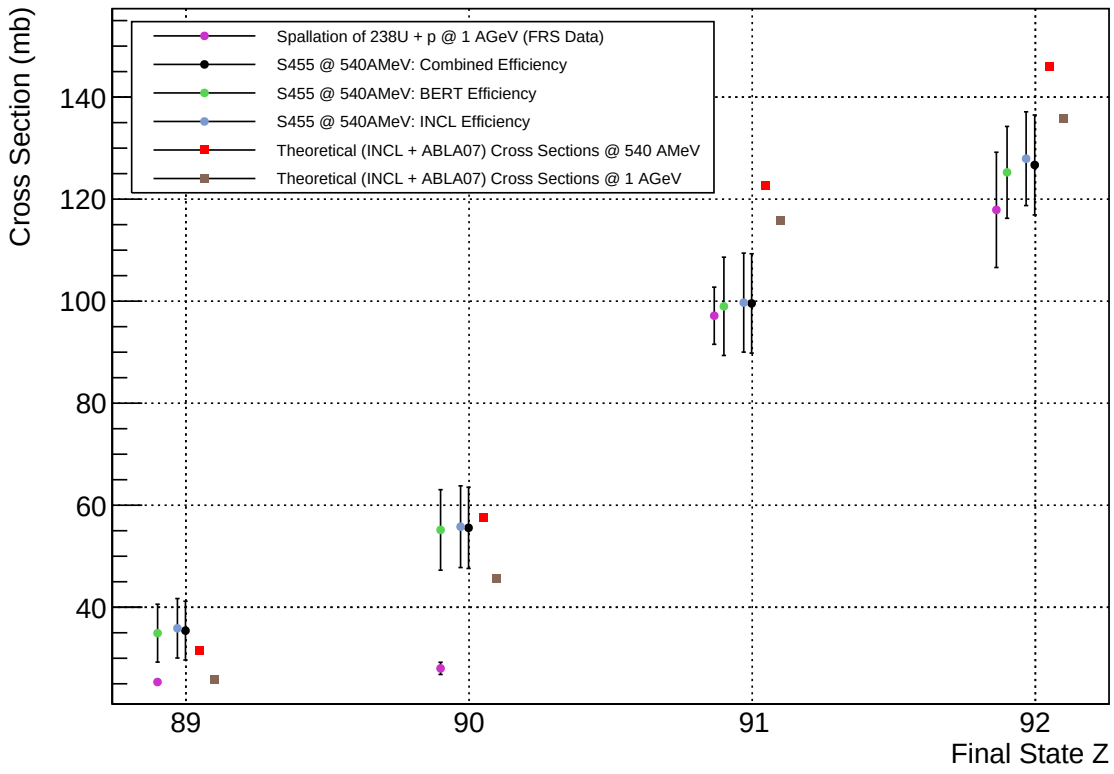

Figure 5.20: Obtained cross-sections for the spallation-evaporation channels. Experimental values using different methods for CALIFA efficiency calculations are showcased. Uncertainties in [81] for single isotopes were propagated for the sum over the isotopic chain of a given element.

be seen that results from both experiments match within a one-sigma interval of the assigned uncertainty for this work, chosen from the cross-section distribution obtained by simulating the different uncertainties in calculations, cuts, and models. The only point of discrepancy is the obtained value for Z=90, where data in [81] do not match the trend with respect to theoretical cross-sections and show a similar value to the Z=89 case. The reaction channels with Z=92 and Z=91 show a reduction with respect to the theory calculations, for both experimental cases. These two channels contain the sum of all final masses, either coming from the evaporation of particles or direct knockout processes. In these channels, single-proton

F. State	$\sigma_{\mathbf{INCL}}$	$\sigma_{\mathbf{BERT}}$	$\sigma_{\mathbf{Combined}}$	$\sigma_{\mathbf{Theory}}$	σ([81])	$\sigma_{\mathbf{Theory}}$([81])
Z=92	128 ± 9 mb	125 ± 9 mb	126 ± 10 mb	146 mb	118 ± 11 mb	136 mb
Z=91	100 ± 10 mb	99 ± 10 mb	99 ± 10 mb	122 mb	97 ± 6 mb	116 mb
Z=90	56 ± 8 mb	55 ± 8 mb	55 ± 8 mb	57 mb	28 ± 1 mb	45 mb
Z=89	36 ± 6 mb	35 ± 6 mb	35 ± 6 mb	31 mb	25 ± 1 mb	26 mb

Table 5.4: Numerical values for the obtained spallation cross-sections.

and single-neutron removal reactions are included, and in principle, one could argue that the already obtained quenching factor of these measured cross-sections for medium mass isotopes [82, 83] and summarized in [84] could account for this difference. For this reason, INCL + ABLA07 calculations for experimental data in [81] were split for different final masses, as shown in Fig. 5.21.

From this calculation it is clear that at least single-proton and single-neutron removal cross-sections are well reproduced by the model, as the obtained results closely resembles the measured data. The major difference comes from the light part of the isotopic chain, a difference that could be understood as an underestimated particle evaporation for those isotopes. This suggests that the differences observed in this work with respect to the calculations have the same origin.

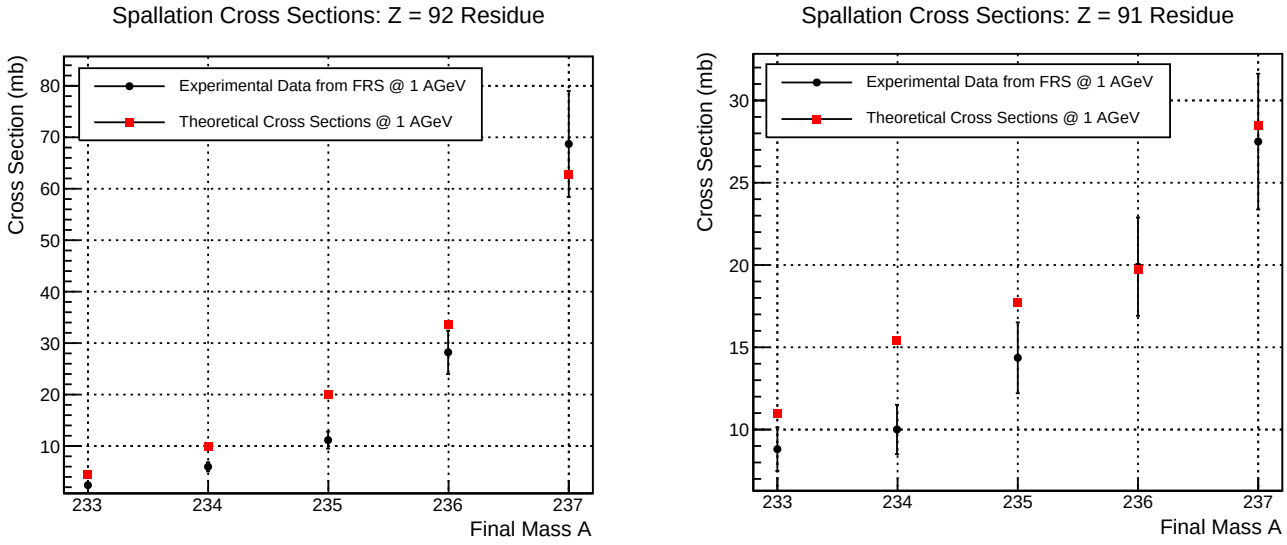

Figure 5.21: Single-isotope cross-sections for [81] data (black dots) and INCL theoretical values (red squares).

Conclusions

The first experiment on knockout-induced fission of ^{238}U has been successfully carried out at GSI, in the context of the R^{3}B collaboration. The obtained data and the posterior analysis have confirmed that the study of fission dynamics and cross-section measurement with this method is a suitable way to study yield dependence with the excitation energy of the process, and can be applied to the study of exotic nuclei. However, some improvements of the current setup would be required to perform a precise measurement of these observables. The large number of delta-electrons generated by the heavy ion traveling through the liquid hydrogen target did not allow a proper reconstruction of the reaction vertex, which translated into a non-optimal resolution for the excitation energy of the remnant and the angular correlations of the scattered proton pair. This affected the precision of the comparisons with theoretical models and the isolation of single fissioning systems by using the opening angle information.

These results encourage the search for a new tracking system for protons within the R^{3}B collaboration. Silicon pixel detectors from ALICE (ALPIDE) were chosen to be the replacement of the stripped AMS detectors. These new system is being developed at the moment, with promising results from simulations and first tests with proton beams. These detectors would allow to improve the delta-electron rejection and the resolution of the excitation energy, which would permit to even measure fission barriers for exotic, neutron rich isotopes.

CALIFA was effectively working during the experiment, with some DAQ-related problems that were solved afterward by means of a carefully study of the temporal correlations. Proton energies were reconstructed using a custom clustering algorithm and a neural network approach that were developed as part of this work. These methods allowed for the reconstruction of the excitation energy of the process, by obtaining the proton energies at the end of the neural network propagation. This reaction was indeed the most difficult case for this kind of reconstruction, due to the rescattering processes inside the heavy nucleus that result

in high-energy protons above the energy that was considered in the CALIFA designs. This ended up with more nuclear reactions inside the crystals but was managed by the neural network approach, from which a reasonable resolution in the proton energy was obtained. Is it expected that for the reconstruction of medium and light mass isotopes this type of algorithm will work close to the expected, nominal resolution of CALIFA for protons, even for the punch-through cases.

The results from the analysis were well understood and matched with the expected behavior of the used theoretical models, INCL and ABLA07.

For the spallation-fission reactions, the reconstructed opening angle using CALIFA showed a clear rescattering distribution. This process dominated over the quasi-free mechanism and was associated with a higher excitation energy left to the remnant after successive nucleon-nucleon collisions inside the nucleus. The reconstructed excitation energy showed a clear correlation with this opening angle.

Despite the wide excitation energy cuts that had to be performed, an study of the fission fragment charge evolution with this observable could be carried out. Different model variations for the ABLA07 code showed that a shifted superfluid phase together with standard exponential function, with a damping value of $E_0 = 40$ MeV and Randrup's formula with values $E_0 = 15$ MeV and $E_1 = 20$ MeV described in a consistent and precise way the observed charge yields.

Cross-section measurements were in good agreement with the theoretical calculations. The largest disparity was observe for the $Z_1 + Z_2 = 92$ fissioning system, were at least one neutron was knocked-out from the incoming ion. The measured value for this cross-section was 297 ± 9 mb, quite different from the theoretical value of 344 mb. This discrepancy could rely in the CALIFA simulated response for neutrons. The rest of the measured cross-sections were in good agreement with theoretical calculations. An estimation of the quasi-free contribution for the $Z_1 + Z_2 = 91$ channel was carried out, obtaining a value of 3 ± 0.1 mb, a small contribution to the total process that is consistent with the observed opening angle for the full opening angle distribution.

The spallation-evaporation channels were also studied. The lack of reaction vertex reconstruction complicated the analysis, and models had to be used for taking into account reactions coming from the plastic scintillator at the entrance of the setup. However, a quasi-

free like distribution could be obtained, that were associated with the $Z = 92$ and $Z = 91$ residues after the evaporation processes. Charge states at the entrance of the TWIN MUSIC were also observed and corrected by using the CHARGE model. Cross-sections were in good agreement with previous measurements at the FRS at GSI. From these calculations, smaller results were obtained for the $Z = 92$ and $Z = 91$ reactions, that could in principle be associated with the already observed single-particle removal quenching factors. However, a theoretical calculation was carried out for the data taken at FRS, and no hints were found related to this quenching.

R3BRoot Description

A.1 Data Structures

There are two ways of extracting information when a particle interacts with a sensitive material from which a detector is made: either only the interaction is registered, as counting detectors do (for example a Geiger, where only the number of pulses is recorded) or also the amount of energy deposited in the material is measured (for example a scintillation crystal, where the integral of the pulse that is generated by secondary particles is proportional to the deposited energy). These interactions can cause a direct ionization of the material (ionizing particles, such as protons, electrons, or any other charged particle) or an indirect one (gammas or neutrons that lose energy after a secondary reaction with the material). The products of these ionization processes are collected in several ways, depending on the type of detector used. This collection of charged particles produces a signal that is measured using electronic modules which can also perform some fast transformations on data before this signal is sent to the data stream.

In the R3B collaboration data unpacking, preprocessing, and time sorting are managed by UCESB (Unpack and Check Every Single Bit), that in combination with an unpacker allows the R3BRoot user to obtain raw root files. The in-depth details of how this data acquisition works can be found in [85], but some general aspects of this process are:

- There are several DAQ groups in the cave (for example SOFIA, NeuLAND, CALIFA, AMS...) that write time-stamped data to the storage or to the data stream.
- The information is stored as LMD[1] files, and then a time sorter is used to allocate each detector signal correctly in time, using the White Rabbit[2] clock and transform

[1] LMD stands for List Mode Data.

[2] The White Rabbit protocol is an ethernet-based network that was developed by GSI, CERN, and others,

unsorted data into sorted LMD files. This process is called *time-stitching* and can be also done in flight for online monitoring purposes.

- Raw files can be processed to obtain ROOT files at different reconstruction levels using an *unpacker*. This unpacker provides the data structure that UCESB uses for writing in ROOT files. This data structure is of course detector and experiment-dependent, so every experiment has its own unpacker. This unpacker is also used by R3BRoot at a first level to transform raw, list mode data into R3BRoot structure data.

After the unpacking stage data structures in R3BRoot are filled and then subsequent tasks can perform other transformations on data, leading to new data levels, calibration parameters or even online plots. The basic structures for data storing inside R3BRoot follow a naming convention in this way (exemplified for a CALIFA data object):

R3B + Det + Data Level + Data → R3BCalifaCrystalCalData

Each data structure contains different information, according to how much is data processed:

- **Mapped Level:** This is the direct output from the unpacker. Contains raw data matched with the detection unit that produced that data (hence the name), as it is recorded from the detector output. Some examples of this data are preamplifier channels, coarse and fine times, or sub-detector ID channels.
- **Cal Level:** Contains data after some calibration, that can be for instance energy calibration or time calibration. This data level is reached by a task that loads calibration parameters and applies them to get this new data level.
- **Hit Level:** Reconstructed data after some kind of algorithm that gives physical information: times of flight, crystal or strip clusters, angles, fragment charges...
- **Point Level:** The output from Geant4 simulations. A simulation in R3BRoot is generally run over Geant4 using Virtual Montecarlo (VMC), so this framework is in charge of transporting particles through the active volume of the detectors.

From a programming point of view, it can be explanatory to define R3BRoot data structures as C++ classes whose data members contain the information that has to be stored. These classes have *setters* methods (so tasks can create new information for the next levels)

aimed for data transfer and clock timing distribution, with high stability and resolution beyond nanosecond.

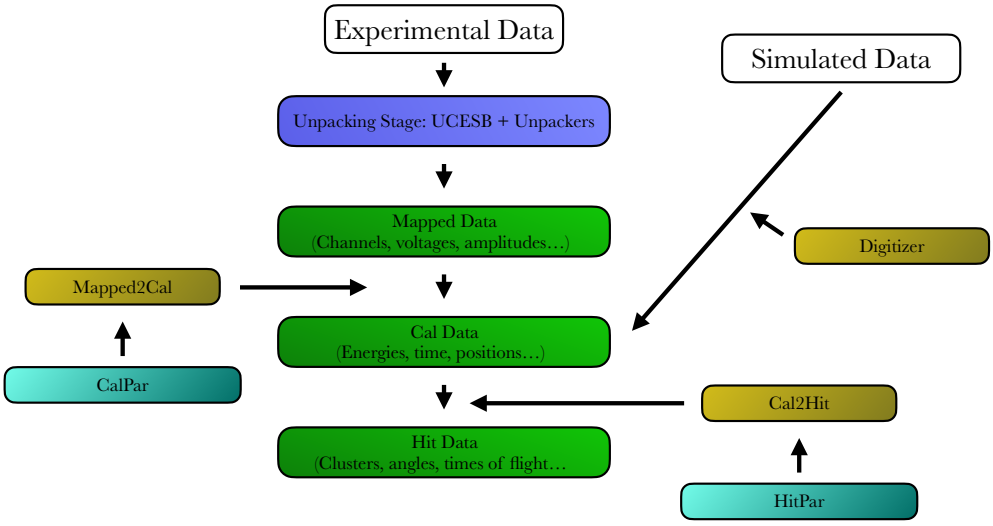

Figure A.1: R3BRoot data flow scheme. Data structures are displayed in green, tasks are in yellow, and parameter containers are in turquoise.

and *getters* methods (so tasks can process data from previous levels and also the user is able to get the information, as it is done in analysis macros or any other task). This data flow is schematized in Fig A.1.

A.2 Tasks

Once the data structure is clear, it is time to dig into how data is transformed inside R3BRoot. The process is entirely based on the use of the so-called R3BRoot *tasks*, that are inherited from FairRoot tasks. These tasks are basically classes in which the methods are the ones that perform operations on data, such as clustering, calibrations, histogram fitting, and online plots... every task inherited from the FairRoot task has at least those methods (besides typical C++ inherent methods for classes, i.e constructors and destructors),

- **Init:** Registers input/output arrays for data, loads parameters, geometries, and positions for detectors...

- **Reset:** Sets everything again. This method is called for example when a runId changes, so correct versions of parameters are loaded again.
- **Exec:** This is the task eventloop. Processes event by event data, applying calibration parameters, performing some kind of algorithm for reconstruction, filling histograms... this method usually reads data from previous levels and write data for the next ones.

and of course, more methods can be added to these tasks if needed. There are five types of them:

1. **Parameter creation tasks.** They are used to obtain parameters for calibration purposes, typically by processing some calibration files (cosmic runs, gamma source files, beam sweep runs, etc...). The output is a parameter container in ASCII or ROOT format. This file is then loaded and used for calibration tasks. A naming example, with and RPC task:

   R3B + Det + Prev. Level + 2 + Next Level + Par → R3BRpcCal2HitPar

2. **Calibration tasks.** These classes perform data calibration, and require a set of parameters, that are loaded in the *Init* method of the class. Previous existing data structures from other data levels are read and processed, so by the end of the algorithm, new data is created. This data can be directly written to some ROOT file or stored in memory for other subsequent tasks to proceed.

   R3B + Det + Prev. Level + 2 + Next Level → R3BAlpideMapped2Cal

3. **Readers.** A *reader* is a class that transforms data structures coming from LMDs or data streams into the first level of R3BRoot data (mapped), by using UCESB data structures. This is usually done by transforming this zero-suppressed data into the members of the mapped data class.

   R3B + Det + Reader → R3BAmsReader

4. **Digitizers.** The purpose of a digitizer is to load point data (step length, ΔE, in-out coordinates...) in a proper way to create a signal in an active volume (for example, the energy loss of a gamma inside a CALIFA crystal) and fill the CAL level of the detector.

   R3B + Det + Digitizer → R3BTofDDigitizer

5. **Onlines.** In R3BRoot an online spectrum is a class in which some data levels are filled and represented in histograms, so a detector can be monitored during beamtime. This online class usually shows per-channel histograms, correlations, temperatures, or rates. More than one online class can be loaded and run in the online macro, so it is also possible to make correlations among different detectors.

   R3B + Det + OnlineSpectra → R3BCalifaOnlineSpectra

A.3 Parameters

Parameters in R3BRoot are a collection of objects with very different applications, from transforming a raw time clock signal from a TDC into calibrated time to placing a detector correctly in the cave for simulation or data unpacking. There are two different formats for parameters: ASCII files and root files.

- **ASCII** files store the numbers of a given parameter associated with a given channel (for example, the two parameters for a linear calibration of energy in a CALIFA crystal). Those parameters are placed one after the other, following the order of the channels in the detector. Those ASCII files can also store geometrical parameters ((x,y,z) position of a detector in the cave, along with rotation angles), thresholds, maps of magnetic fields, mapping parameters...
- **ROOT** files can store every parameter an ASCII file is able to, but with some additions/advantages: they are more compressed than plain text, so usually root files are the only viable candidate for storing large sets of parameters, such as detailed magnetic maps of GLAD. Root files can also store *versions* of the same parameter. On the other hand, root files are not human-readable, so a macro is needed to translate them into something that can be legible.

A parameter version is another set of the same parameter but with different values, that is usually applied in different moments of time. These parameter versions are matched with a *Run Id*, a number that is associated with a given interval of time, so different versions have different run IDs. Every time the run ID changes, the software calls the ReInit() method of the classes and loads the corresponding parameter versions, so the unpacking and calibration procedures are completely automatic.

A.4 Geometries

Detector geometries are often used for simulation purposes, where active volumes are defined in order to register particle interactions within the material. This active volume can be also created along passive volumes, which are pieces of material present on the real configuration of the detector that do not contribute to the detection (but maybe distort it by interacting with the primary particle before is detected or interacting with the secondary particles that are created after the primary particle enters in the active material). Examples of these two types of materials could be for example the CsI(Tl) crystals (active) in CALIFA along with the carbon fiber that conforms the alveoli structure (passive).

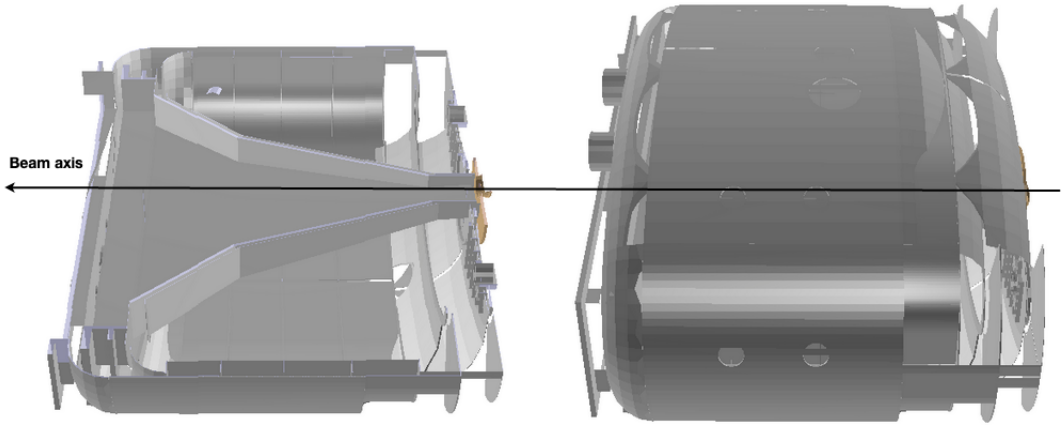

Figure A.2: Right: full GLAD geometry. Left: A cut applied in the geometry, where the acceptance effects for reaction products are clearly seen.

Geometries are not only used for simulation. They can be used for alignment purposes, so they are placed according to the real disposition of a detector during the experiment. Once this is done, this geometry can be used by algorithms to reconstruct trajectories, hits, angles...

Another purpose of including a geometry in R3BRoot is to study the acceptance of the setup, for analysis calculations or simulations before the experiment. An example of this is shown in Figure A.2, where the effect of the inner chamber acceptance of GLAD for reaction products has to be taken into account for calculations.

There can be more than one geometry per detector, according to how the detector was installed during a given experiment analysis. For instance, NeuLAND has several geometries conforming to how many double planes were installed, and CALIFA has different geometries

for different numbers of crystals in place... these geometries are created in a macro that defines the shapes of the active parts, their positions, materials, and every necessary part in order to achieve a realistic simulation of the detector.

A.5 Runs: Online, Analysis and Simulation

As it has been shown, a lot of different software pieces are needed when it is time to unpack, analyze, or simulate data. A *run* in R3BRoot is also a class that comes from FairRoot and is in charge of setting up the environment to perform those jobs. The run loads the tasks in the right order (for example, a Map2Cal transformation has to be performed always before a Cal2Hit), loads as many parameters as needed, sets the input/output files with data, and runs the event loop. There are three types of runs: Simulation runs (**FairRunSim**), unpacking/analysis runs (**FairRunAna**), and online runs (**FairRunOnline**). Some methods of those classes:

- **SetSink.** Sets the output file for data. It is usually stored as a root file.
- **SetSource**. Sets the input file with data to process. It can be an LMD file, so a reader task is needed, or a root file, and then things can start from the mapped level. FairRunSim does not have this method.
- **AddTask.** Adds tasks to the event loop. Tasks are added in order, so they also perform transformations on data in order.
- **Init.** Calls the *Init* method for each added class. This loads parameters for each task, register output TClonesArrays for the next data levels, and loads them for previous ones.
- **Run.** The event loop. This processes as many events as desired on an event-by-event basis. Each task executes its *Exec* method in order for each event and writes the output before starting with the next event.

Model Training Results

B.1 Global Performance

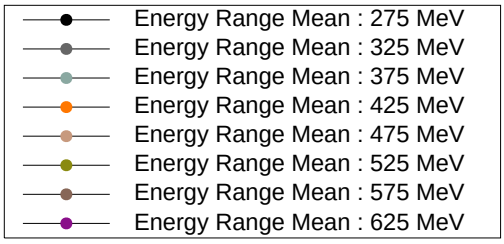

Figure B.1: Color Scheme representing the mean of the different energy ranges of the primary particle.

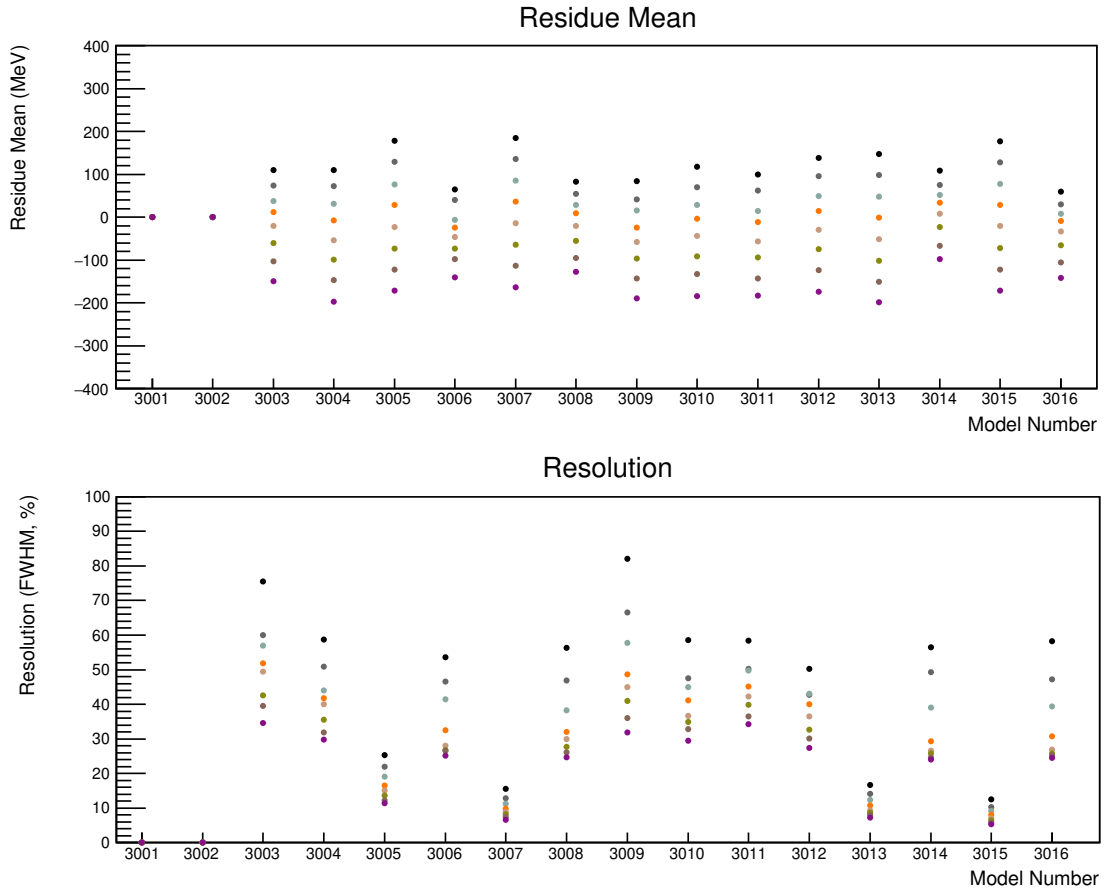

Figure B.2: Overview of the three-layer model performance. The first plot shows the center of the residue distribution for each energy range. The second plot summarizes the obtained resolution measured as 4.33.

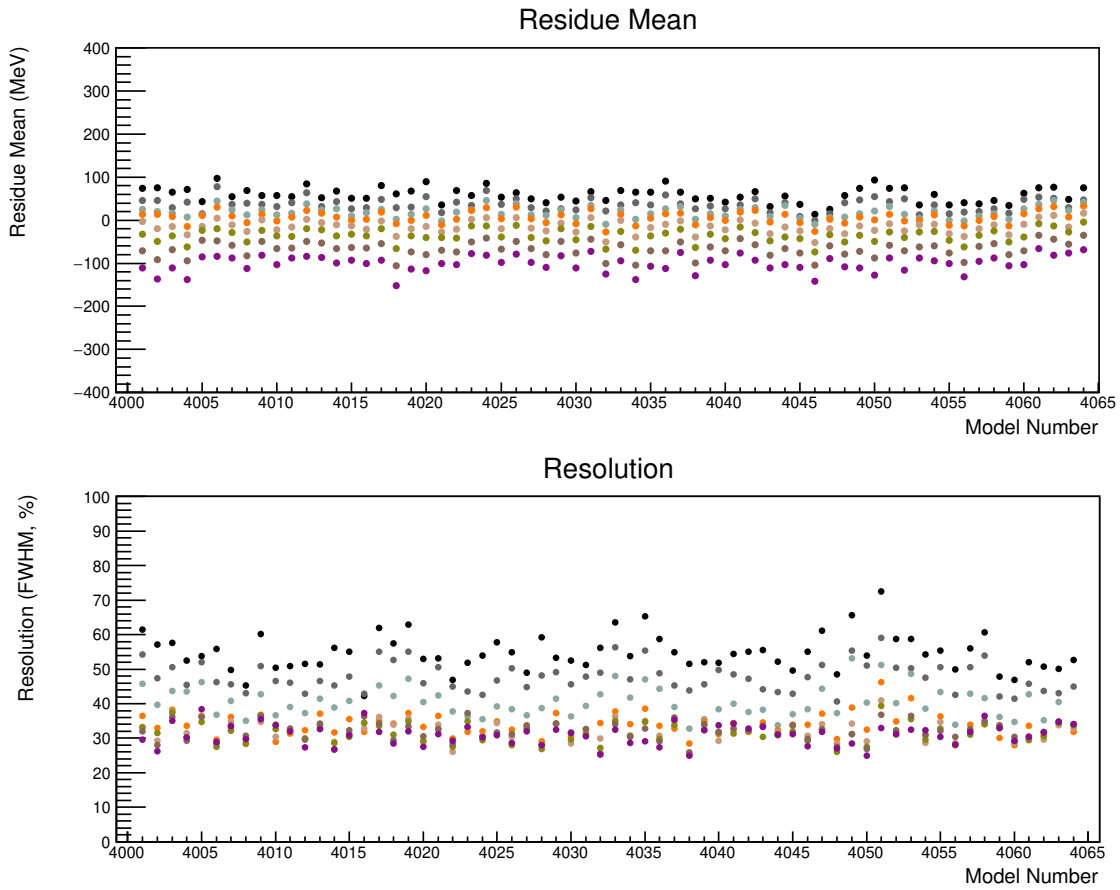

Figure B.3: Overview of the four-layer model performance. The first plot shows the center of the residue distribution for each energy range. The second plot summarizes the obtained resolution measured as 4.33.

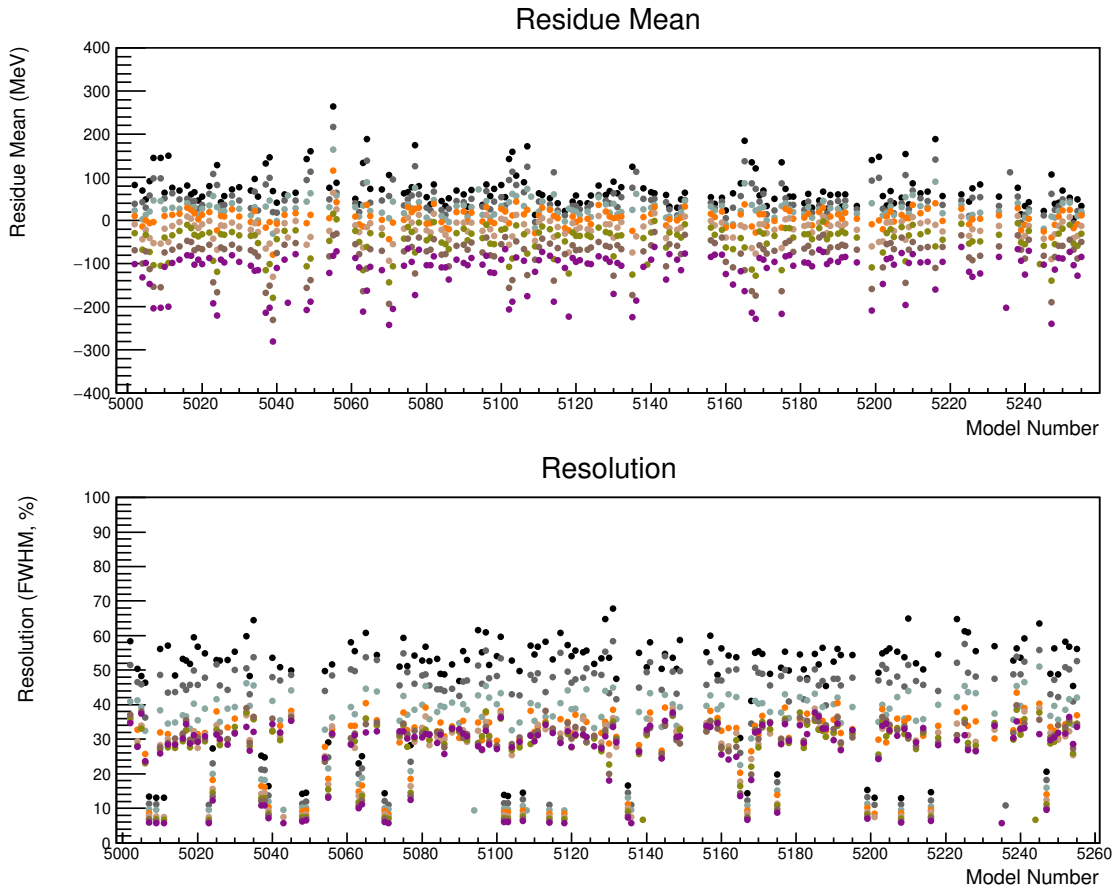

Figure B.4: Overview of the five-layer model performance. The first plot shows the center of the residue distribution for each energy range. The second plot summarizes the obtained resolution measured as 4.33.

Cross Sections Uncertainty Calculation

The uncertainty calculation associated with each cross-section value, for the two types of reaction processes is explained here. The calculation is performed in two steps:

1. First, for each observable or correction factor, a variation over the conditions for obtaining these values is performed, either by using simulations or experimental data.

2. The obtained distributions are used later in cross-section calculation repetitions. From the previously obtained distributions, random values are used to calculate cross-sections. Correlated variables share the same random values when necessary.

C.1 CALIFA Efficiency Uncertainty

CALIFA efficiency was obtained using simulations of the different reaction channels, as explained in Chapter 4. Experimental parameters for resolution and thresholds were used for each crystal in those simulations. For the systematic uncertainties associated with the calculation, repetitions of the simulation procedure were performed, with different conditions:

- The detector was randomly misaligned on purpose, for each repetition. This misalignment accounts for the uncertainty in the position measurement.

- Several crystals were randomly turned off between repetitions. For this calculation, 1% of the crystals (15 crystals) were removed from the simulation. This value was the typical number of non-working crystals during other experiments.

- Angular limits that mimic the real AMS acceptance during the experiment were smeared, accounting for possible angular deviations of the reconstructed cluster.

With these conditions, this calculation was simulated thousands of times, resulting in different efficiency distributions for each spallation-evaporation and spallation-fission channel, as

presented in figure C.1. This procedure was repeated for the two GEANT4 libraries, BERT and INCL.

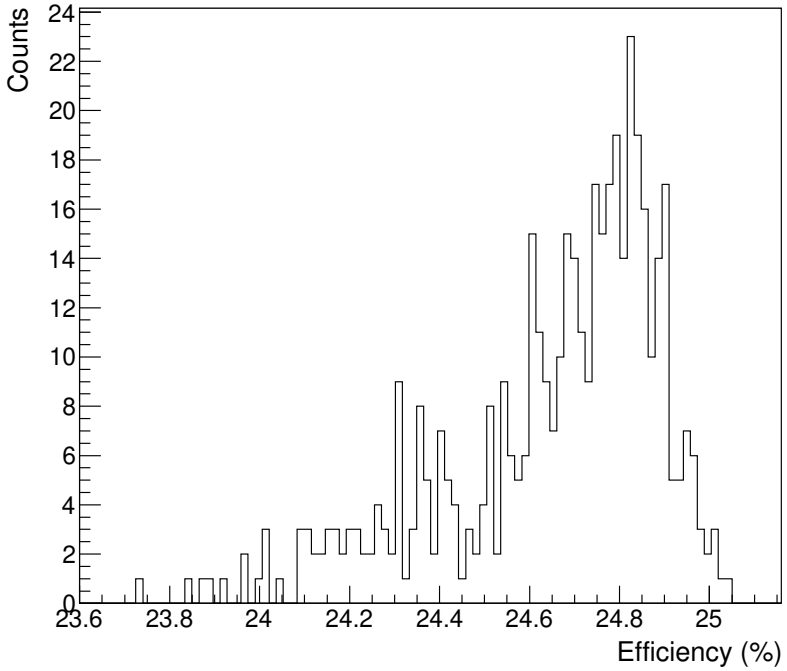

Figure C.1: Probability distribution of CALIFA efficiency for the $Z_1 + Z_2 = 91$ spallation-fission channel, using INCL library.

C.2 Correction Factors for Scintillator Reactions

These correction factors were calculated using random values from the probability distributions of CALIFA efficiencies, for both target reactions and scintillator reactions. For each cross-section calculation repetition, a random efficiency was obtained, that was used to correct the number of counts in CALIFA and to obtain this correction factor. In addition, the reaction point was considered to be located at any random point within the target limits.

C.3 CALIFA DAQ Correction

The calculated non-working times for each CALIFA half were varied using experimental data. The high energy hit condition on the detector was imposed by choosing a random

value from a uniform distribution of 40 to 60 MeV. The defined cut where the events were not Poisson-distributed anymore was also randomized using the fit error as the limit for these cuts.

C.4 Deadtimes and Incoming Ions

These two observables were obtained by choosing some conditions on the data that were not tuneable: deadtimes were calculated by just counting events before and after deadtime on the scalers. The number of incoming ions was obtained by counting hits in the scintillator at the entry of Cave C. For this reason, only statistical uncertainties were associated with these observables, which were assumed to follow a Gaussian distribution.

For the number of incoming particles, each repetition of the cross-section calculation used a random number from a Gaussian distribution of width $\sqrt{N_i}$, with N_i the number of incoming ions.

For the deadtimes (DT), calculated as

$$\text{Deadtime (DT)} = \frac{\text{After DT}}{\text{Before DT}} \tag{C.1}$$

uncertainties were propagated using the usual error propagation formula. The resulting uncertainty was used as the width of a Gaussian distribution.

C.5 TWIN MUSIC Efficiency

C.5.1 Spallation-Evaporation Case

The systematic uncertainty associated with this calculation was estimated by randomly smearing the two cuts applied to this calculation: the time of flight on the ToFWall detector and the minimum charge collected at the TWIN MUSIC that was considered as a heavy fragment. The cut on the time of flight was chosen to be inside the interval (σ, 1,5σ) of the fitted Gaussian peak. The minimum charge required at the TWIN MUSIC for a heavy fragment was obtained from a random, uniform distribution between 50.000 and 55.000 a.u. for the reconstructed heavy fragment. The obtained efficiency distribution was used later for the cross-section calculation procedure.

C.5.2 Spallation-Fission Case

This systematic uncertainty was simpler in its calculation, as the condition of two hits on the ToFWall did not require any cut on time. However, as this calculation had to be performed at CAL level of the TWIN MUSIC, calibrated energies were used instead of charges. This region was chosen from the correlation energy plot between sections, as shown in Fig. C.2. The limits of this region were moved randomly within a ±1000 a.u. range to account for systematic deviations.

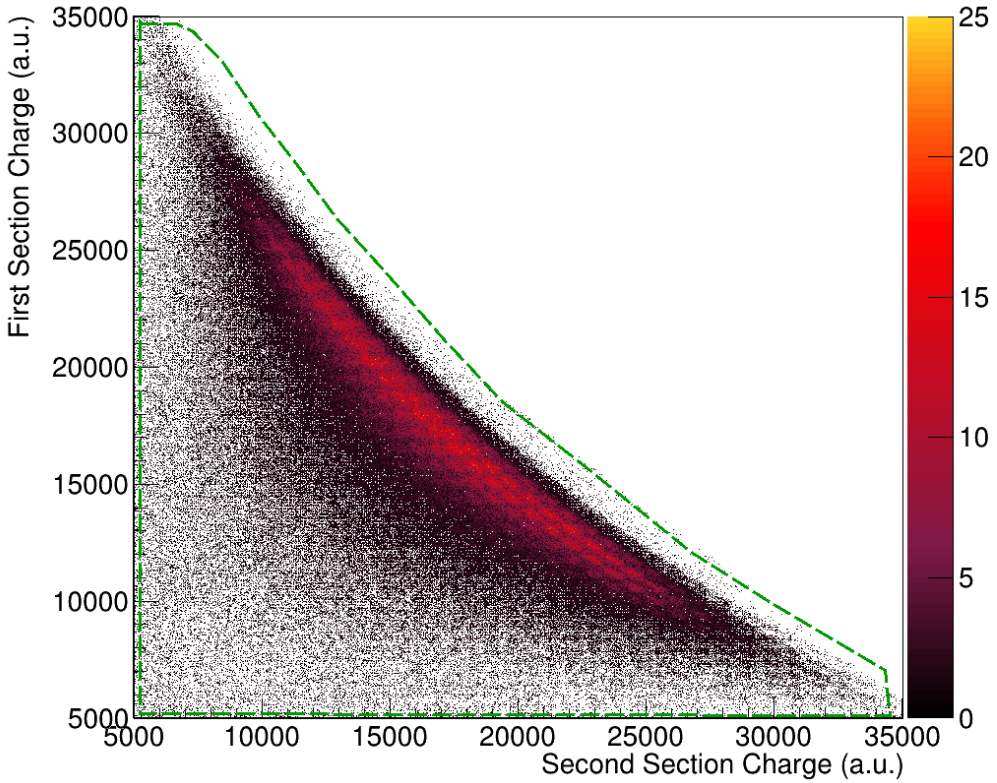

Figure C.2: Fission fragment charge region. The green curve shows the selected limits to consider a fission event.

C.6 Number of Reactions

As CALIFA was used for selecting reaction channels, for both spallation-evaporation and spallation-fission cases, the required minimum energy of the cluster was randomized in the interval $E \in (40,60)$ MeV. For the fission case, the vertex window was chosen to be inside a 3σ window, which was randomized inside a window of $2{,}5\sigma$ to $3{,}5\sigma$. This generated several

charge spectra, that were then fitted. Each reaction channel counts were stored for each variation of the selection parameters. The resulting distribution was then used for cross-section calculations. An example of this distribution is presented in Fig.

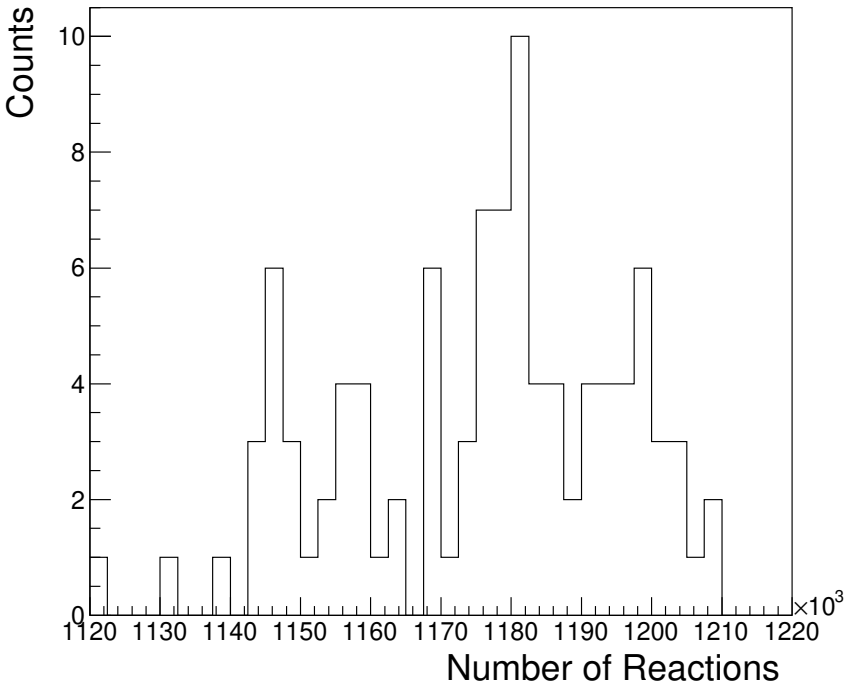

Figure C.3: Number of reactions for the $Z_1 + Z_2 = 91$ spallation-fission channel. This distribution was obtained by repeating the reaction selection with different detection conditions and cuts, as explained in the text.

C.7 TPat Efficiencies

C.7.1 Spallation-Evaporation Case

This calculation is similar to what was done for the TWIN MUSIC efficiency uncertainty calculation. The minimum energy cut to consider a heavy fragment traveling through the TWIN MUSIC detector was randomized at the same interval as before.

C.7.2 Spallation-Fission Case

As explained before, the fission-like region in Fig. C.2 was used to select fission events, with proper smearing in the limits.

C.8 Some Cross-Sections Distributions

Each one of the distributions calculated for the observables and correction factors used in the cross-section calculation was used in the cross-section calculation repetition by extracting random values from those distributions. The mean of each one of the obtained distributions was used as a final value for the cross-section measurement. The standard deviation of the distribution was used as a measure of the associated uncertainty. Fig. C.4 represents the result of these calculations for the spallation-evaporation case, with combined BERT and INCL libraries.

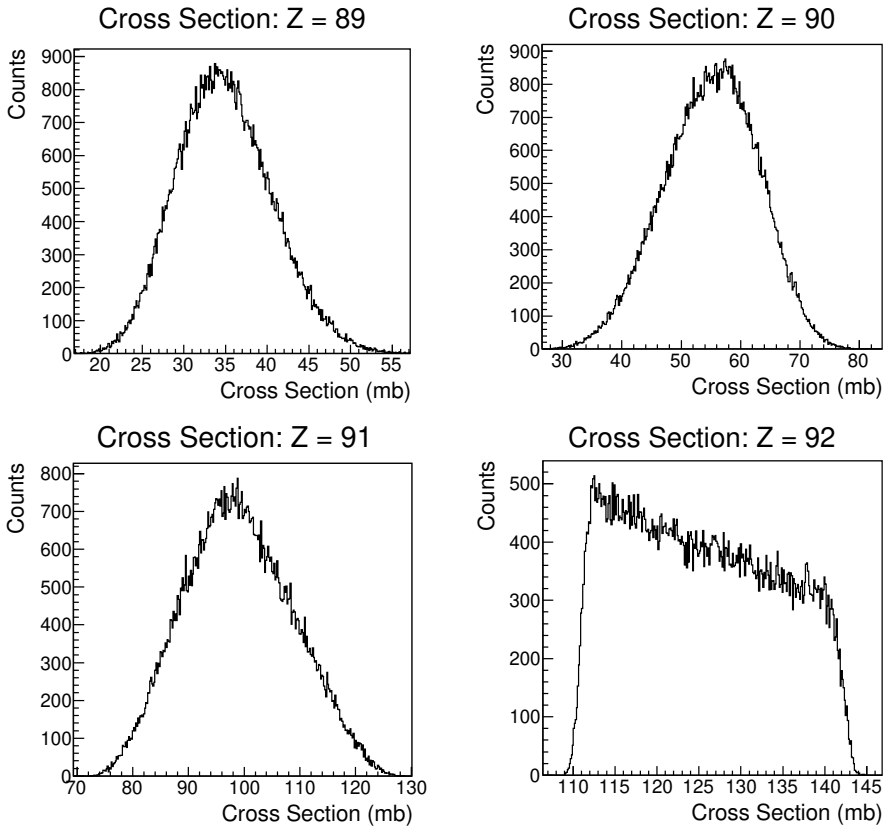

Figure C.4: Example of cross-section distributions, for the spallation-evaporation case, using the Bertini Geant4 library for efficiency calculations.

List of Materials

Note: this list was carefully obtained by A. Graña-González,
Total thickness up to the TWIN MUSIC = 1297,85 mg/cm2
Total thickness up to the target = 1068,282 mg/cm2

Name	**Matter**	ρ **(g/cm^3)**	**Thick. (mg/cm^2)**	**Thick. (cm)**
Window	Fe	7,874	158,03	0,0201
Foil	Mylar	1,38	15,19	0,011
Air	Air	0,001205	160,27	133
TPC Foil	Kapton	1,42	19,88	0,014
TPC Gas	Ar	0,00166	4,65E-2	0,028
Window	Fe	7,874	79,29	0,0101
Air	Air	0,001205	18,07	15
MWPC0 Window	Mylar	1,38	1,67	0,0012
MWPC0 Gas	$ArCO_2$	0,00171	0,34	0,2
MWPC0 Pads	Mylar	1,38	1,67	0,0012
MWPC0 Gas	$ArCO_2$	0,00171	0,86	0,5
MWPC0 Central Cathode	Ar	0,001662	2,01E-3	0,0012
MWPC0 Gas	$ArCO_2$	0,00171	0,86	0,5
MWPC0 Window	Mylar	1,38	1,67	0,0012
Air	Air	0,001205	11,75	9,75
TRIM Window	Mylar	1,38	3,46	0,0025
TRIM Field Cage	Mylar	1,38	3,46	0,0025
TRIM CO_2	CO_2	0,001842	1,29	0,7
TRIM CH_4	CH_4	0,0006	16,8	28
TRIM CF4	CF4	0,00372	14,14	3,8
TRIM Ar	Ar	0,001662	55,51	33,4

Name	Matter	ρ (g/cm^3)	Thick. (mg/cm^2)	Thick. (cm)
TRIM Field Cage	Mylar	1,38	3,46	0,0025
TRIM Stripper	Nb	8,57	60,68	0,0071
TRIM Field Cage	Mylar	1,38	3,46	0,0025
TRIM Field Cage	Mylar	1,38	3,46	0,0025
TRIM Stripper	Nb	8,57	60,68	0,0071
TRIM Field Cage	Mylar	1,38	3,46	0,0025
TRIM Field Cage	Mylar	1,38	3,46	0,0025
TRIM Window	Mylar	1,38	3,46	0,0025
Air	Air	0,001205	15,06	12,5
Sci Window	Mylar	1,38	6,92	0,005
Sci 1st Half	BC400	1,032	154,5	0,075
Sci 2nd Half	BC400	1,032	154,5	0,075
Sci Window	Mylar	1,38	6,92	0,005
Air	Air	0,001205	68,69	57
Vacuum Chamber Window	Steel	8	40,64	0,0051
LH_2 Window	Mylar	1,38	17,26	0,0125
LH_2 Target	LH_2	0,0708	106,2	1,5
LH_2 Window	Mylar	1,38	24,85	0,018
Target Isolation	Mylar	1,38	6,91	0,005
Vacuum Chamber	Air	1E-10	1,13E-5	113
Vacuum Chamber Window	Steel	8	40,64	0,0051
Air	Air	0,0012	33,74	28
MWPC1 Window	Mylar	1,38	1,66	0,0012
MWPC1 Gas	$ArCO_2$	0,00171	0,34	0,2
MWPC1 Strips	Mylar	1,38	1,66	0,0012
MWPC1 Gas	$ArCO_2$	0,00171	0,86	0,5
MWPC1 Strips	Mylar	1,38	1,66	0,0012
MWPC1 Gas	$ArCO_2$	0,00171	0,51	0,3
MWPC1 Window	Mylar	1,38	1,66	0,0012
Air	Air	0,0012	5,42	4,5
TWIM Window	Mylar	1,38	3,46	0,0025

Resumo da Tese

Este traballo de tese céntrase no análise dun procedemento experimental innovador levado a cabo nas instalacións do GSI (Darmstadt, Alemaña), no contexto da colaboración R^3B (Reaccións con Feixes Radioactivos Relativistas). A medida realizada en marzo de 2021 formou parte do programa experimental de R^3B dentro da denominada Phase-0 do GSI-FAIR.

O experimento R3B é unha colaboración internacional actualmente composta por 255 membros rexistrados. O setup, que está actualmente en construción, ten como obxectivo realizar estudos en cinemática inversa con feixes exóticos relativistas, con enerxías que van desde centos de MeV ata máis de 1 GeV. O dispositivo está deseñado para funcionar como un montaxe experimental versátil con capacidades de medida en réxime de cinemática completa, onde se pode levar a cabo un variado programa de física. Realizáronse experimentos en astrofísica nuclear, ecuación de estado, modelo de capas e estrutura nuclear, fisión e correlacións de curto alcance.

Este experimento foi unha proba de concepto na que se combinaron dous procesos ben coñecidos en física nuclear: reaccións de espalación e knockout (arranque dun ou varios nucleóns) e procesos de fisión nuclear. Deste xeito, a fisión nuclear foi inducida por este tipo de reaccións. A diferenza de outros experimentos ben coñecidos nos que reaccións de espalación foron usadas para inducir fisión [32, 33, 34], neste caso o uso dos detectores da colaboración SOFIA (Studies on Fission with Aladdin) xunto co emprego dos detectores CALIFA e AMS, permitiron correlacionar a enerxía de excitación do proceso cos observables típicos na fisión nuclear: carga e masa dos fragmentos de fisión.

E.1 Obxectivo da Tese e Dispositivo Experimental

E.1.1 Supresión dos Efectos de Capa e Reparto de Enerxía dos Fragmentos de Fisión

Os efectos da estrutura nuclear introdúcense como unha corrección nos modelos de fisión nuclear para ter en conta os efectos das capas nucleares na fisión a baixa enerxía. Estes efectos de capa dilúense á medida que a enerxía de excitación do núcleo fisiónante crece. Por iso, é importante coñecer que tipo de atenuación se debe aplicar a estes efectos de estrutura para que os modelos usados sexan capaces de reproducir os datos experimentais obtidos.

Esta función de atenuación soe representarse como un factor multiplicativo á corrección por efectos de capas nucleares,

$$E = E_{LDM} + S(E^*)\delta E, \tag{E.1}$$

onde E_{LDM} é a enerxía obtida usando o modelo macroscópico de gota líquida, δE é a corrección por efectos de capa e $S(E^*)$ é a función usada que depende da enerxía de excitación.

Ao longo dos anos, diversas formas funcionais para esta función de amortiguamento foron propostas, desde funcións puramente exponenciais, cuxa constante se axusta cos datos experimentais [26]:

$$S(E^*) = \exp(-E^*/E_0), \tag{E.2}$$

a cuxa constante se axusta cos datos experimentais, a funcións máis complexas, como a proposta por Randrup [27]:

$$S(E^*) = \frac{1 + e^{-E_1/E_0}}{1 + e^{(E^*-E_1)/E_0}}, \tag{E.3}$$

que inclúe dous parámetros axustables, E_0 e E_1.

Propuxéronse diversas teorías para explicar os yields de fisión observados e a evaporación de neutrones producida polos fragmentos de fisión, baseadas na repartición de enerxía entre os pre-fragmentos de fisión. Recentemente, en [28], unha explicación baseada no aumento de entropía do sistema foi capaz de explicar a multiplicidade de neutrones evaporados a diversas enerxías de excitación.

Para probar todas estas ideas, dun xeito experimental, sería necesario un mecanismo de reacción para inducir a fisión e un dispositivo experimental co que:

- Medir distribucións de carga e masa dos fragmentos de fisión con gran precisión.
- Medir a enerxía de excitación do sistema fisionante.
- Inducir un amplo rango de enerxías de excitación.

E.1.2 Reaccións Quasi-free en Núcleos Pesados

As reaccións quasi-free foron extensamente estudadas para isótopos de masa lixeira e media, permitindo estudos detallados da estrutura de núcleos exóticos. Sen embargo, a caracterización deste proceso de reacción aínda non foi estudada para íons pesados inestables, só para obxectivos estables en cinemática directa [31]. Campañas experimentais en GSI na década dos anos 90 permitiron o estudo de residuos de espalación, pero sen información sobre os nucleóns dispersos antes da evaporación ou fisión. O estudo destas reaccións en núcleos pesados daría unha idea de como este método podería ser utilizado para estudar propiedades de íons pesados.

Estes dous puntos presentados aquí iniciaron a busca dun novo método para estudar reaccións de espallamento-fisión e espallamento-evaporación en íons pesados, que é o tema principal deste traballo de tese.

E.1.3 A Medida, Detectores Empregados y Software

A medida proposta para este experimento consistiu en ións de ^{238}U impactando a 540 AMeV no albo de protóns. Tras un proceso de knockout dun único protón, que pode determinarse mediante a medida da carga dos dous fragmentos de fisión en coincidencia, o ángulo relativo entre o par dispersado pode medirse, e a enerxía de excitación pode obterse utilizando un cálculo de masa invariante:

$$\begin{pmatrix} E_b \\ 0 \\ 0 \\ p_{bz} \end{pmatrix} + \begin{pmatrix} m_t c^2 \\ 0 \\ 0 \\ 0 \end{pmatrix} = \begin{pmatrix} E_1 \\ p_{1x}c \\ p_{1y}c \\ p_{1z}c \end{pmatrix} + \begin{pmatrix} E_2 \\ p_{2x}c \\ p_{2y}c \\ p_{2z}c \end{pmatrix} + \begin{pmatrix} E_R \\ p_{Rx}c \\ p_{Ry}c \\ p_{Rz}c \end{pmatrix}, \tag{E.4}$$

onde os subíndices denotan a partícula (b=feixe, 1=primeiro protón, 2=segundo protón, t=albo e R=remanente). Neste cálculo, supónse que o feixe ten só unha componente de momento nunha dirección. Se o momento dos dous protóns é medido, e o momento do feixe entrante é coñecido, entón pode empregarse un calculo de masa invariante para determinar

a enerxía de excitación do núcleo remanente:

$$I_m^2 = \left(\sum E\right)^2 - \left|\sum pc\right|^2$$
$$= (E_b + m_p c^2 - (E_1 + E_2))^2 - (p_{1x}c + p_{2x}c)^2 - (p_{1y}c + p_{2y}c)^2 - (\sqrt{E_b^2 - m_b^2 c^4} - (p_{1z}c + p_{2z}c))^2 \tag{E.5}$$

Esta masa invariante, I_m, corresponde entonces á masa do remanente despois da reacción, e a enerxía de excitación pode calcularse entón restándolle a masa en repouso do remanente:

$$E^* = I_m - m_R c^2. \tag{E.6}$$

No caso dun proceso quasi-free, a excitación dada ao remanente corresponde a excitacións de unha única partícula-buraco. Se o protón eliminado interacciona co resto dos nucleóns, este proceso de rescattering aumenta a enerxía de excitación debido ás múltiples colisións nucleón-nucleón

O setup experimental empregado para o experimento presentarase aquí. Varias Multiwire Proportional Chambers (MWPC) foron usadas con propósito de rastrexar o feixe e os fragmentos de fisión. O tempo de voo dos fragmentos obtívose usando o muro de tempo de voo (ToFWALL). As coordenadas espaciais e a enerxía dos nucleóns despois do proceso de espalación foron medidas usando os detectores CALIFA e AMS. A TWIN MUSIC empregouse para reconstruír a carga dos residuos de espalación e de fisión. NeuLAND instalouse ao final do setup co propósito de realizar medidas de multiplicidade de neutróns. Con esta configuración, logrouse unha medida cinemática completa do proxectil e dos produtos da reacción. Este dispositivo se resume na Figura E.1.

- Multiwire Proportional Chambers (MWPC): Compostas por un volume de gas recheo de pads alternos, que dan posición en X e Y. Varios destes detectores foron usados para facer tracking do feixe, mentres que os instalados ao final do setup foron usados para atopar o camiño percorrido polos fragmentos de fisión.

- Plastic scintillator: Un plástico centelleador, con dous PMTs instalados en ambos extremos. A sinal deste detector foi usada en combinación co ToFWALL para atopar o tempo de voo das partículas.

- AMS: Detector de silicio estripeado, que funciona como aparato de medida das coordenadas angulares dos protóns saíntes da reacción. No experimento instaláronse seis destes detectores, cunha capa de ouro na parte frontal para atenuar o efecto dos electróns delta.

- CALIFA: Calorímetro/espectrómetro da colaboración R^{3}B. No momento de realizar o experimento constaba de 1504 cristais centelleadores instalados, rodeando a zona do branco. Estes cristais inorgánicos están compostos de CsI(Tl). O detector cubría unha zona de 22° a 88°.

- Albo de protóns: O branco de reacción, composto dunha cápsula de Mylar que encerraba o hidróxeno en estado líquido. Este branco tiña unha lonxitude de 1.5 cm.

- TWIN MUSIC: Cámara de ionización altamente segmentada, dividida en 4 seccións con 16 ánodos cada unha. Este detector permite a identificación dos fragmentos de fisión en carga, e tamén a posición do vértice de reacción na coordenada Z.

- GLAD: O dipolo da colaboración. Permite realizar unha medida da masa dos fragmentos produto da reacción.

- ToFWALL: Composto por 20 plásticos centelleadores dispostos verticalmente ao final do setup. Con este detector construíuse o trigger de fisión e medíuse o tempo de voo dos fragmentos.

- NeuLAND: Espectrómetro de neutróns de gran aceptancia. Utilízase para atopar a multiplicidade e enerxía dos neutróns que se producen nas reaccións baixo estudo.

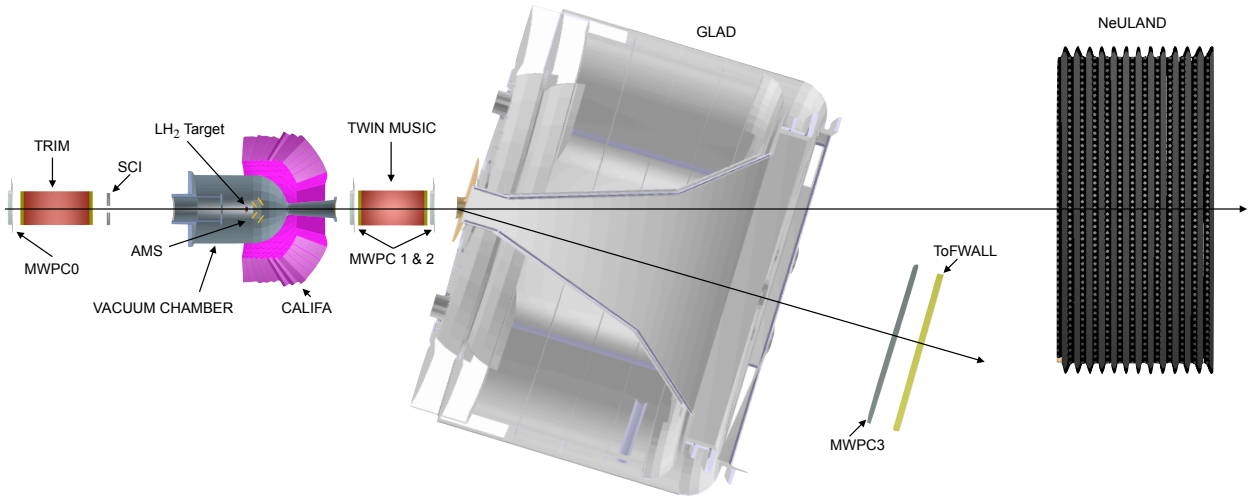

Figure E.1: Configuración experimental. As distancias non están á escala.

Para a análise de datos e a obtención de simulacións realistas, empregouse o framework R3BRoot. R3BRoot é a ferramenta estándar para análise de datos e simulacións dentro da colaboración R3B. Baseado en tarefas de FairRoot e Geant4, conta con características destacadas: escrito en C++ e orientado a obxectos, o código está optimizado para ser rápido, eficiente e fiábel. Conta cunha comunidade activa en GitHub que resolve preguntas, problemas e engade novo código, verificado polos desenvolvedores. Proporciona as mesmas ferramentas e estruturas de datos para a simulación e os datos experimentais. Os datos dos detectores almacénanse en estruturas de datos que se transforman mediante tarefas, o que facilita a comparación entre os resultados de experimentos e simulacións. A calibración, o mapeo e os parámetros de simulación xestiónanse de maneira eficiente e precisa, utilizando ferramentas herdadas das tarefas de FairRoot. Ofrece conexións con Geant4, Geant3 e outros motores de transporte de partículas, o que permite ao usuario adaptar os requisitos físicos da simulación utilizando as listas de física admitidas.

E.2 Análise de Datos e Simulacións

E.2.1 Simulación dos canles de reacción

A simulación dos diferentes canles de reacción consistiu en dous componentes clave: a entrada que contenía a información das partículas primarias e a simulación realista dos diferentes detectores e materiais pasivos relevantes para o análise experimental realizado neste traballo. As partículas e ións de entrada xeráronse por INCL e ABLA07, e estas trazas primarias propagáronse a través do montaxe simulado. Neste punto, a simulación realista da resposta do detector permitiu unha comparación precisa co montaxe experimental real. Cada un destes subsistemas de detección (a cámara de reacción, AMS e CALIFA) incluíu non só as partes activas senón tamén todas as partes pasivas (envoltorios ou soportes, por exemplo) que foron relevantes para reproducir os datos obtidos no experimento. A xeometría da cámara de reacción, baseada en deseños CAD, colocouse rodeando o branco de reacción. O sistema AMS-branco engadiuse dentro desta cámara de reacción e alinouse axeitadamente. Finalmente, o detector CALIFA encerrou estes dous sistemas. Cada detector alinouse de maneira precisa, coas medidas de AMS tomadas na Cova C como referencia. O vértice de reacción das partículas xeradas para cada evento simulado aleatorizouse dentro da rexión do branco.

E.2.2 Aliñamientos e Calibracións

Primeiramente, os detectores CALIFA e AMS foron aliñados coa axuda do modelo STEP resultante do escaneado con láser da rexión do obxectivo. Este escaneado permitiu aliñar cada un dos seis detectores AMS con respecto ao obxectivo de reacción, usando o modelo de referencia do detector. Esta medida tamén serviu para aliñar o CALIFA.

Neste traballo realizaronse tres calibracións: unha calibración para o CALIFA usando fontes gamma, unha subtracción de pedestais para o AMS e unha calibración da TWIN MUSIC para os fragmentos pesados procedentes de residuos de espalación.

Os resultados da calibración do CALIFA cunha fonte de ^{60}Co mostraron que a resolución obtida para o detector foi do 5,03% para os cristais no rango gamma e do 5,15% para os cristais no rango de protóns. Estes resultados están moi próximos aos requisitos técnicos do detector na proposta técnica do mesmo.

A subtracción de pedestais para o AMS realizouse usando datos sen feixe, nos que o sinal de cada strip puido ser caracterizado para a súa posterior extracción nos eventos co feixe. Estes pedestais axustáronse a distribucións gaussianas, strip por strip. Para obter sinais válidos no detector cando se rexistraba unha reacción, a cada enerxía de cada strip restóuselle a media de cada pedestal máis un número fixo de sigmas, neste caso, tres.

A calibración da TWIN MUSIC para fragmentos pesados realizouse usando eventos co feixe atravesando o volume activo do detector. A enerxía de todos os ánodos foi aliñada, e puido ser atopada unha correlación entre a traxectoria reconstruída polas MWPCs, situadas antes e despois deste detector, para obter unha correlación entre o tempo de drift e a carga depositada. Con este procedemento ademais descubriuse a presenza de estados de carga, cuxa contribución tivo que ser avaliada usando o software CHARGE [70].

E.2.3 Selección de Eventos

Para caracterizar os dous tipos de reacción estudados neste traballo, empregáronse certas condicións respecto dos sinales detectadas nos diferentes detectores do setup. Estas condicións variaron dependendo de se se trataba de reconstruír a reacción ou contar eventos para o posterior cálculo de seccións eficaces. En resumo:

- Para as reaccións de espalación-fisión, empregouse a condición de dúas sinalizacións

de alta enerxía en CALIFA, xunto con dous fragmentos de fisión detectados na TWIN MUSIC e dúas sinalizacións no ToFWALL. A condición de dúas sinalizacións en CALIFA substituíuse pola dunha única sinal debido á maior eficiencia obtida para esta condición, o que acarreaba unha menor incerteza.

- Para as reaccións de espalación-evaporación, empregouse a condición de dúas sinalizacións de alta enerxía en CALIFA, xunto con un fragmento de alta carga detectado na TWIN MUSIC. A condición de dúas sinalizacións en CALIFA substituíuse pola dunha única sinal debido á maior eficiencia obtida para esta condición, o que acarreaba unha menor incerteza, ao igual que no caso anterior.

E.2.4 Reconstrucción do Albo

Para a reconstrución do target, empregouse un procedemento baseado na formación de clusters con strips no detector AMS. Eses clusters permitiron a reconstrución en tres dimensións de todas as posibles traxectorias, incluíndo aquelas producidas pola alta multiplicidade de electróns delta. A pesar de todos os estudos levados a cabo e da presenza das láminas de ouro diante dos planos de silicio, a alta presenza destes electróns delta fixo que non fose posible reconstruír o punto de reacción evento a evento. De este estudo, as extraéronse as seguintes conclusións:

- Os ángulos de CALIFA tiveron que ser usados para extraer as coordenadas angulares dos nucleóns dispersados na reacción. A insuficiente resolución deste detector traduciuse nunha pobre resolución para a enerxía de excitación.

- Os detectores de silicio estriados non son adecuados para a reconstrución do vértice de reacción no caso de usar feixes con unha carga alta, como no caso do uranio. Este resultado foi unha das causas polas que comezaron a investigarse outras tecnoloxías, como os detectores de píxeles ALPIDE, que substituirán a AMS no futuro como tracker para a colaboración R^3B.

E.2.5 Reconstrución do Punch-Through

Para extraer de maneira correcta a enerxía de excitación do proceso de fisión, primeiro é necesario reconstruír a enerxía daqueles protóns que non foron detidos completamente en CALIFA. O alto número de reaccións de rescattering traduciuse nunha alta enerxía transferida aos protóns saíntes, de xeito que practicamente ningún protón era completamente detido no material activo de CALIFA. Para tratar de reconstruír estas reaccións, usáronse

dous métodos.

O primeiro deles consistiu en avaliar a enerxía depositada en cada cristal de CALIFA por unha serie de protóns simulados usando INCL. Desta maneira, puido extraerse unha correlación entre a enerxía dun cluster en CALIFA e a enerxía do protón simulado. A través desta correlación, puido observarse que un gran número de sinais provén de reaccións nucleares dentro dos cristais, ademais dos típicos procesos de punch-through.

Debido á dificultade para reconstruír a enerxía dos protóns usando este método, optouse por desenvolver un método de reconstrución baseado no uso de redes neuronais. Para iso, construíuse un software, SoKAI, que permitiu realizar esta tarefa. Mediante o uso de datos simulados, adiestrouse a rede para que fose capaz de reconstruír a enerxía mediante a información de entrada de CALIFA: enerxías dos clusters, ángulos, componentes da luz dentro do cristal de maior enerxía e desviacións angulares. A resposta da rede foi satisfactoria, e obtívose unha resolución razoable para esta enerxía, ademais dunha reconstrución razoable das distribucións cinemáticas de reacción.

E.2.6 Reconstrución da Enerxía de Excitación

O emprego de CALIFA como método de reconstrución dos cuadrimomentos dos protóns fixo que a resolución en enerxía de excitación se vira afectada, con un valor polo menos dúas veces maior do esperado antes do experimento. Esta resolución foi cuantificada usando os métodos de reconstrución anteriormente explicados, e mediante o uso de simulacións, obtívose un valor medio de uns 30 MeV (FWHM) para o valor desta resolución.

E.3 Resultados e Conclusións

Os resultados da análise foron estudados en bo acordo co comportamento agardado dado polos modelos teóricos utilizados, INCL e ABLA07.

Para as reaccións de espalación-fisión, o ángulo de apertura reconstruído usando CALIFA mostrou unha clara distribución de rescattering. Este proceso dominaba sobre o mecanismo quasi-free e estaba asociado cunha maior enerxía de excitación para o remanente despois de sucesivas colisións nucleón-nucleón dentro do núcleo. A enerxía de excitación reconstruída mostrou unha clara correlación con este ángulo de apertura.

A pesar dos amplos cortes de enerxía de excitación que se tiveron que realizar, puido levarse a cabo un estudo da evolución da carga dos fragmentos de fisión con este observable. Variacións de modelos para o código ABLA07 mostraron que unha fase superfluída desprazada xunto cunha función exponencial estándar, cun valor de atenuación dos efectos de estrutura de $E_0 = 40$ MeV e a fórmula de Randrup con valores $E_0 = 15$ MeV e $E_1 = 20$ MeV describían de maneira consistente e precisa os yields de carga observados.

As medidas de seccións eficaces mostraron un bo acordo cos cálculos teóricos. A maior disparidade observouse para o sistema fisionante Z1 + Z2 = 92, con polo menos un neutrón arrincado do ión entrante. O valor medido para esta sección eficaz foi de 297 ± 9 mb, bastante diferente do valor teórico de 344 mb. Esta discrepancia podería deberse á resposta simulada de CALIFA para os neutrones. O resto das seccións eficaces medidas estiveron en bo acordo cos cálculos teóricos. Levouse a cabo unha estimación da contribución do proceso de quasi-free para o canal Z1 + Z2 = 91, obtendo un valor de 3 ± 0.1 mb, unha pequena contribución ao proceso total que é consistente co ángulo de apertura observado para a distribución completa do ángulo de apertura.

Tamén se estudaron os canais de espalación-evaporación. A falta de reconstrución do vértice de reacción complicou a análise, e tivéronse que utilizar modelos para ter en conta as reaccións provintes do centelleador de plástico na entrada do setup. Sen embargo, puido observarse unha distribución quasi-free, asociada cos residuos Z = 92 e Z = 91 despois dos procesos de evaporación. Tamén observáronse e corrixíronse estados de carga na entrada do TWIN MUSIC mediante o uso do modelo CHARGE. As seccións eficaces estiveron en bo acordo coas medidas previas no FRS en GSI. A partir destes cálculos, obtivéronse resultados máis pequenos para as reaccións Z = 92 e Z = 91, que en principio poderían estar asociados cos factores de quenching de arranque dun único nucleón xa observados. Sen embargo, realizouse un cálculo teórico para os datos obtidos no FRS, e non se atoparon indicios relacionados con este factor de quenching.

Bibliography

[1] O. Hahn and F. Strassmann. Concerning the Existence of Alkaline Earth Metals Resulting from Neutron Irradiation of Uranium. *Nature*, 1939.

[2] L. Meitner and O.R. Frisch. Products of the Fission of the Uranium Nucleus. *Nature*, 1939.

[3] N.Bohr and J.A. Wheeler. The Mechanism of Nuclear Fission. *Physical Review*, 1939.

[4] G. Gamow. Mass defect curve and nuclear constitution. *Proceedings of the Royal Society of London*, 1930.

[5] C.F.V. Weizsäcker. Zur theorie der kernmassen. *Zeitschrift für Physik A Hadrons and Nuclei*, 1935.

[6] A.V. Karpov, A. Kelic, and K-H. Schmidt. On the topographical properties of fission barriers. *J. Phys. G: Nucl. Part. Phys*, 2008.

[7] M. Goeppert-Mayer. On Closed Shells in Nuclei. II. *Phys. Rev*, 1949.

[8] O. Haxel, J. H. D. Jensen, and H. E. Suess. On the "Magic Numbers" in Nuclear Structure. *Phys. Rev.*, 1949.

[9] S. G. Nilsson. Binding states of individual nucleons in strongly deformed nuclei. *Kgl. Danske Videnskab. Selskab., Mat.-fys Medd*, 1955.

[10] Yiman Yan. *Study of fission of exotic actinides by relativistic reactions*. PhD thesis, Université Paris-Saclay, 2017.

[11] V.M. Strutinsky. Shell effects in nuclear masses and deformation energies. *Nuclear Physics A*, 1967.

[12] C.M. Polikanov et al. Nuclear Shape Isomers. *Sov. Phys. - JETP 15*, 1962.

[13] K. S. Krane. *Introductory Nuclear Physics*. Wiley, 1991.

[14] Ulrich Brosa, Siegfried Grossmann, and Andreas Müller. Nuclear Scission. *Physics Reports*, 1990.

[15] Ulrich Brosa, Siegfried Grossmann, and Andreas Müller. Four Channels in the Fission of 252Cf. *Z. Naturforsch*, 1986.

[16] M. Meneguzzi, J. Audouze, and H. Reeves. The production of the elements Li, Be, B by galactic cosmic rays in space and its relation with stellar observations. *Astronomy and Astrophysics*, 1971.

[17] Felix Fernandez-Alonso and David L Price. Neutron Scattering – Applications in Biology, Chemistry, and Materials Science. *Experimental Methods in the Physical Sciences*, 2017.

[18] L. Atar et al. Quasifree (p,2p) Reactions on Oxygen Isotopes: Observation of Isospin Independence of the Reduced Single-Particle Strength. *Physical Review Letters*, 2018.

[19] V. Panin et al. Exclusive measurements of quasi-free proton scattering reactions in inverse and complete kinematics. *Physics Letters B*, 2016.

[20] T. Aumann, C. A Bertulani, and J. Ryckebusch. Quasifree (p,2p) and (p,pn) reactions with unstable nuclei. *Physical Review C*, 2013.

[21] Valerii Panin. *Fully exclusive measurements of quasi-free single-nucleon knockout reactions in inverse kinematics*. PhD thesis, Technische Universität Darmstadt, 2012.

[22] O. Chamberlain and E. Segrè. Proton-Proton Collisions within Lithium Nuclei. *Phys Rev*, 1952.

[23] J. B. Cladis, W. N. Hess, and B.J.Moyer. Nucleon Momentum Distributions in Deuterium and Carbon Inferred from Proton Scattering. *Phys. Rev*, 1952.

[24] A.S. Goldhaber. Statiscical Models of Fragmentation Processes. *Physics Letters*, 1974.

[25] P. Díaz Fernández et al. Quasifree (p, pN) scattering of light neutron-rich nuclei near N = 14. *Physical Review C*, 2018.

[26] A. V. Ignatyuk, K. K. Istekov, and G. N. Smirenkin. The Role of Collective Effects in the Systematics of Nuclear Level Densities. *Sov. J. Nucl. Phys.*, 1979.

[27] J. Randrup and P. Moller. Energy dependence of fission-fragment mass distributions from strongly damped shape evolution. *Physical Review C*, 2013.

[28] K.-H. Schmidt and B. Jurado. Entropy Driven Excitation Energy Sorting in Superfluid Fission Dynamics. *Physical Review Letters*, 104, 2010.

[29] E. Pellereau et al. Accurate isotopic fission yields of electromagnetically induced fission of 238U measured in inverse kinematics at relativistic energies. *Physical Review C*, 2017.

[30] D. Ramos Doval. *Fragment Distributions of Transfer- and Fusion-Induced Fission from* $^{238}U+^{12}C$ *Reactions Measured Through Inverse Kinematics*. PhD thesis, University of Santiago de Compostela, 2016.

[31] T. Noro et al. Experimental study of (p, 2p) reactions at 392 MeV on ^{12}C, ^{16}O, ^{40}Ca and ^{208}Pb nuclei leading to low-lying states of residual nuclei. *Progress of Theoretical and Experimental Physics*, 2020.

[32] M. Bernas et al. Fission-residues produced in the spallation reaction ^{238}U + p at 1 AGeV. *Nuclear Physics A*, 2003.

[33] B. Fernández-Domínguez et al. Nuclide cross-sections of fission fragments in the reaction ^{208}Pb + p at 500 AMeV. *Nuclear Physics A*, 2005.

[34] J. Benlliure et al. Isotopic production cross sections of fission residues in ^{197}Au-on-proton collisions at 800 AMeV. *Nuclear Physics A*, 2001.

[35] J.L Rodríguez-Sánchez et al. Complete characterization of the fission fragments produced in reactions induced by ^{208}Pb projectiles on proton at 500 AMeV. *Physical Review C*, 2015.

[36] The GSI Homepage. https://www.gsi.de.

[37] NUSTAR Database. https://www.r3b-nustar.de/member/db/.

[38] E. Pellereau et al. Accurate isotopic fission yields of electromagnetically induced fission of ^{238}u measured in inverse kinematics at relativistic energies. *Physical Review C*, 2017.

[39] D. Cortina-Gil et al. CALIFA, a Dedicated Calorimeter for the R3B/FAIR. *Nuclear Data Sheets*, 2014.

[40] H Álvarez-Pol et al. Performance analysis for the CALIFA Barrel calorimeter of the R3B experiment. *Nuclear Instruments and Methods in Physics Research A*, 2014.

[41] The R3B Collaboration. Technical Report for the Design, Construction and Commissioning of The CALIFA Barrel: The R3B CALorimeter for In Flight detection of γ-rays and high energy charged pArticles, 2011.

[42] 3M. https://www.3m.com/3M/en_US/p/d/b5005047091/.

[43] G. García-Jiménez et al. Study of scintillation properties and performance of CsI(Tl) detectors over time. *Nuclear Instruments and Methods in Physics Research A*, 2023.

[44] Hamamatsu. https://www.hamamatsu.com/eu/en/product/optical-sensors/apd/si-apd/S8664-1010.html.

[45] AMCRYS. http://www.amcrys.com/.

[46] Berkeley Nucleonics. https://www.berkeleynucleonics.com/cesium-iodide.

[47] FEBEX. https://www.gsi.de/en/work/research/experiment_electronics/data_processing/embedded_software/febexsoftware.

[48] MBS. https://www.gsi.de/en/work/research/experiment_electronics/data_processing/data_acquisition/mbs.

[49] M. Feijoo. *Fission Dynamics Investigated in Inverse Kinematics in Reactions Induced by Relativistic 236U Projectiles*. PhD thesis, University of Santiago de Compostela, 2021.

[50] Paloma Díaz Fernández. *An investigation into quasi-free scattering of light neutron-rich nuclei around N=14*. PhD thesis, Universidade of Santiago de Compostela, 2013.

[51] E. Pellereau et al. SOFIA: An innovative setup to measure complete isotopic yield of fission fragments. *EPJ Web of Conferences*, 62, 2013.

[52] K. Boretzky et al. NeuLAND: The high-resolution neutron time-of-flight spectrometer for R3B at FAIR. *Nuclear Instruments and Methods in Physics Research A*, 2021.

[53] R3B GitHub Repository. https://github.com/R3BRootGroup/R3BRoot.

[54] FairRoot Group. https://fairroot.gsi.de/index.html.

[55] Geant4 Collaboration. https://geant4.web.cern.ch/.

[56] W. McCulloch and W. Pitts. A Logical Calculus of Ideas Immanent in Nervous Activity. *Bulletin of Mathematical Biophysics*, 1943.

[57] F. Rosenblatt. The Perceptron: A Probabilistic Model For Information Storage And Organization in the Brain. *Psychological Review*, 1958.

[58] A. G. Ivakhnenko and V. Lapa. Cybernetic Predicting Devices. *CCM Information Corporation*, 1973.

[59] G.E. Hinton D.E. Rumelhart and R.J. Williams. Learning representations by back-propagating errors. *Letters to Nature*, 1986.

[60] D. P. Kingma and J. Lei Ba. Adam: A Method for Stochastic Optimization. *Published as a conference paper at ICLR*, 2015.

[61] D.Mancusi et al. Improving the description of proton-induced one-nucleon removal in intranuclear-cascade models. *Physical Review C*, 2015.

[62] A. Boudard et al. Intranuclear cascade model for a comprehensive description of spallation reaction data. *Physical Review C*, 2002.

[63] A. Boudard et al. New potentialities of the Liège intranuclear cascade model for reactions induced by nucleons and light charged particles. *Physical Review C*, 2013.

[64] S. Leray et al. Extension of the Liège Intra Nuclear Cascade model to light ion-induced collisions for medical and space applications. *Journal of Physics, Conference Series*, 2013.

[65] A. Kelic, M. V. Ricciardi, and K-H. Schmidt. ABLA07 - towards a complete description of the decay channels of a nuclear system from spontaneous fission to multifragmentation. *Joint ICTP-IAEA advanced workshop on model codes for spallation reactions*, 2008.

[66] sigma 3D GmbH. https://www.sigma3d.de/.

[67] B. Pietras et al. First testing of the CALIFA Barrel Demonstrator. *Nuclear Instruments and Methods in Physics Research A*, 2013.

[68] G. F. Knoll. *Radiation Detection and Measurement*. Wiley, 1979.

[69] ATIMA. https://www.isotopea.com/webatima/.

[70] CHARGE. http://web-docs.gsi.de/~weick/charge_states/.

[71] C. Anderson, G. McKinney, J. Tutt, and M. James. Delta-ray Production in MCNP 6.2.0. *Physics Procedia*, 90:229–236, (2017).

[72] M. Bendel et al. iPhos, a new technique for the CALIFA CsI(Tl) calorimeter. *Journal of Physics: Conference Series*, 587, (2015).

[73] T. von Egidy and D. Bucurescu. Systematics of Nuclear Level Density Parameters. *Physical Review C*, 72, 2006.

[74] A. V. Voinov et al. Nuclear excitations at Constant Temperature. *Physical Review Letters*, 79, 2009.

[75] A. A. Naqvi, F. Käppeler, F. Dickmann, and R. Müller. Fission fragment properties in fast-neutron-induced fission of ^{237}Np. *Physical Review C*, 34, 1986.

[76] K. Hirose et al. A key role of multi-chance fission for the description of fission-fragment mass distributions at high energies. *Physical Review Letters*, 119, 2017.

[77] S. Tanaka et al. Effects of multi-chance fission on isotope dependence of fission fragment mass distributions at high energies. *Physical Review C*, 100, 2019.

[78] M.G. Itkis et al. Assymetric Fission of the Pre-Actinide Nuclei. *Zeitschrift für Physik A*, 320, 1985.

[79] K.-H. Schmidt, B. Jurado, and C. Amouroux. General description of fission observables - GEF model. *JEFF-Report 24, Data Bank, Nuclear-Energy Agency, OECD*, 2014.

[80] P. Möller et al. Heavy-element fission barriers. *Physical Review C*, 79, 2009.

[81] J. Taïeb et al. Evaporation residues produced in the spallation reaction ^{238}U + p at 1 AGeV. *Nuclear Physics A*, 724, 2003.

[82] J. Díaz-Cortés et al. Systematic reduction of the proton-removal cross-section in neutron-rich medium-mass nuclei. *Physics Letters B*, 811, 2020.

[83] V. Vaquero et al. Inclusive cross sections for one- and multi-nucleon removal from Sn, Sb, and Te projectiles beyond the N = 82 shell closure. *Physics Letters B*, 795, 2019.

[84] T. Aumann et al. Quenching of single-particle strength from direct reactions with stable and rare-isotope beams. *Progress in Particle and Nuclear Physics*, 118, 2021.

[85] H. T. Johansson. *Hunting Tools Beyond the Driplines*. PhD thesis, Chalmers University of Technology, 2010.

This thesis work focuses on investigating proton-induced reactions on ^{238}U in inverse kinematics, taking advantage of the R^{3}B/ SOFIA setup. Nuclear fission was induced after knockout processes, with scattered nucleons being analyzed using the CALIFA calorimeter. Innovative reconstruction algorithms were developed for CALIFA to extract the process's excitation energy through an invariant mass approach which was then correlated with fragment charge yields and compared with theoretical models across various physics model configurations. Furthermore,cross-sections for spallation-fission and spallation-evaporation channels were measured. The obtained data demonstrate good agreement with previous measurements and theoretical calculations.